CHEMICAL REVIEWS

pubs.acs.org/CR

Review

Probing and Manipulating Noncovalent Interactions in Functional Polymeric Systems

Jingsi Chen,[†] Qiongyao Peng,[†] Xuwen Peng, Hao Zhang, and Hongbo Zeng*

Cite This: https://doi.org/10.1021/acs.chemrev.2c00215

Read Online

ACCESS | Metrics & More | Article Recommendations

ABSTRACT: Noncovalent interactions, which usually feature tunable strength, reversibility, and environmental adaptability, have been recognized as driving forces in a variety of biological and chemical processes, contributing to the recognition between molecules, the formation of molecule clusters, and the establishment of complex structures of macromolecules. The marriage of noncovalent interactions and conventional covalent polymers offers the systems novel mechanical, physicochemical, and biological properties, which are highly dependent on the binding mechanisms of the noncovalent interactions that can be illuminated via quantification. This review systematically discusses the nanomechanical characterization of typical noncovalent interactions in polymeric systems, mainly through direct force measurements at microscopic, nanoscopic, and molecular levels, which provide quantitative information (e.g., ranges, strengths, and dynamics) on the binding behaviors. The fundamental understandings of intermolecular and interfacial interactions are then correlated to the macroscopic performances of a series of noncovalently bonded polymers, whose functions (e.g., stimuli-responsiveness, self-healing capacity, universal adhesiveness) can be customized through the manipulation of the noncovalent interactions, providing insights into the rational design of advanced materials with applications in biomedical, energy, environmental, and other engineering fields.

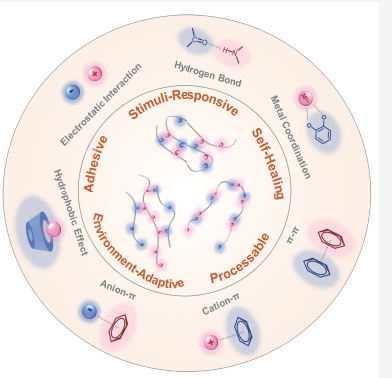

CONTENTS

Received: March 31, 2022

1. INTRODUCTION

1.1. Nature of Noncovalent Interactions

Unlike covalent bonds that involve the sharing of electrons between atoms within a molecule, noncovalent interactions occur between "distinct" units of one molecule (intramolecular) or different molecules (intermolecular), where the electron charge distributions of the involved atoms are barely changed. While the short-range covalent bonds are mainly responsible for the formation of individual molecules, noncovalent interactions can act at long distances ranging from several angstroms (e.g., van der Waals forces, electrostatic interactions, hydrogen bonding, π interactions) to hundreds of nanometers (e.g., hydrophobic interactions), which extensively participate in constructing molecule clusters and complex structures of macromolecules.[1,2] As noncovalent interactions usually exhibit reversibility, weak specificity, and moderate directionality,[3] they can act as regulating forces in many chemical and biological processes, including molecular recognition,[4] self-assembly of nanomaterials,[5] molecule−surface interactions, stabilization of biomacromolecules,[6] and enzyme catalysis.[7] For example, hydrogen bonding and $\pi-\pi$ stacking play key roles in constructing the double helix structure of DNA by directing the assembly of nucleic acids,[8] and hydrophobic interactions dominate the binding of many small-molecule ligands to their cognate protein receptors.[9] The unique features of noncovalent interactions also provide them numerous opportunities to be exploited in research areas such as supramolecular chemistry, biochemistry, pharmaceutics, and materials science, facilitating the design of functional materials and the development of new technologies.

In polymeric systems, noncovalent interactions mainly exhibit two effects: (1) control the conformation of polymer chains via regulating the intramolecular and intermolecular interactions; (2) serve as recognition motifs to direct the assembly of building blocks, leading to the formation of supramolecular structures (Figure 1). With the rapid development of supramolecular chemistry over the last decades, noncovalent interactions have been widely used to assist the synthesis procedure of polymer materials, whose shapes, sizes, and structures can be finely tuned.[10,11] Novel optical, physicochemical, mechanical, and biological properties are therefore endowed in these systems compared to the conventional ones only consisting of covalent bonds, greatly promoting the development of advanced materials and devices with desired functionalities for practical applications. For instance, taking advantage of the high reversibility of noncovalent interactions, the developed polymers have the potential to be easily processed and recycled,[12] and more importantly, they can be endowed with the ability to repair themselves after damage, which is commonly called "self-healing" and of great significance to extend the durability of materials, especially for those susceptible to damage or applied in poorly accessible areas.[13] Noncovalent interactions also contribute to or even govern the interfacial forces between polymers and other surfaces that are in close contact.[14] Marine organisms such as mussels and sandcastle worms can rapidly and tightly attach to diverse solid substrates like rocks, metal, and wood in turbulent seawater, where a variety of noncovalent interactions (e.g., electrostatic interactions, hydrogen bonding, metal coordination, π interactions) are recognized to play a key role in the strong adhesion between the secreted adhesive proteins and the foreign surfaces.[15] The revealed chemistry has inspired the design of a series of biomimetic materials with robust underwater adhesion, ranging from coacervates to hydrogels and coatings, which can be applied as tissue adhesives, drug delivery carriers, pollutant adsorbents, and so on.[16,17]

Although various types of noncovalent interactions have been identified depending on the nature of interacting species, they are generally governed by electrostatic interaction, polarization, dispersion, steric repulsion, and charge transfer.[3] Therefore, the binding of one site can easily influence the binding of the neighboring site, either enhancing or weakening the affinity of each other, which is called cooperativity or anticooperativity.[18] The cooperative/anticooperative effect can occur within one type of noncovalent interaction, and a typical example is hydrogen bonding. As a single hydrogen bond is usually considered weak, multiple hydrogen-bonding arrays have been extensively employed to direct the self-assembly of stable structures, in which triple, quadruple, or even sextuple hydrogen bonds can form between two complementary moieties.[19] The binding strength of the array is not only determined by the number of hydrogen bonds formed (primary electrostatic interaction) but also highly dependent on the arrangement of the donor (D) and acceptor (A), which induces secondary electrostatic interaction.[20,21] Additional stabilization arises when donors and acceptors are located on different moieties (DD-AA), while the alternate sequence of donor and acceptor in each molecule (DA-AD) causes destabilizing effect. Some binding motifs involve a combination of different types of noncovalent interactions, which work cooperatively to produce stable and specific associations. Macrocycle-based host−guest interactions have drawn great research interest in molecular recognition because of their high specificity, which is attributed to a variety of noncovalent interactions.[22] Normally, the formation of the inclusion complexation is dominated by the shape and size fit between the host cavity and guest molecule, whose stability can be cooperatively enhanced by hydrophobic interactions, the formation of hydrogen bonds, and maximized van der Waals forces via conformational adjustment of the guest molecule.[23,24] Similar cooperativity has also been detected in other systems such as catechol chemistry[25] and aromatic compounds.[26,27]

Because of the inherent dynamic nature and relatively low energy, noncovalent interactions can be readily perturbed by the changes of the surrounding environments, showing response to a variety of physical (e.g., temperature, light, electric/magnetic field), chemical (e.g., solvent type, pH, ionic strength, redox agent) and biological (e.g., enzymes) stimuli.[28−30] For example, the effect of a solvent can be significant for many noncovalent interactions, because hydrophobic interactions are totally

https://doi.org/10.1021/acs.chemrev.2c00215
Chem. Rev. XXXX, XXX, XXX−XXX

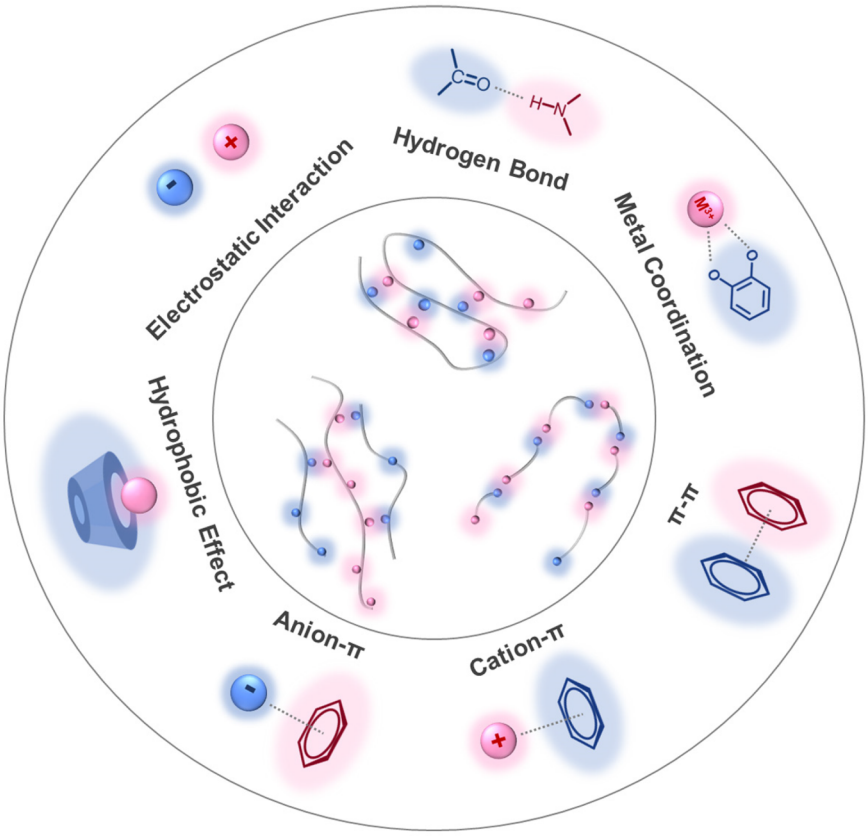

Figure 1. Typical intramolecular and intermolecular noncovalent interactions in polymeric systems.

solvent-driven and the strengths of ion pairs, hydrogen bonds, and polar interactions are all highly dependent on the medium.[31] The adjustment of the noncovalent interactions which are triggered by external stimuli would lead to changes in structures and functions of the resultant polymeric materials, and the stimuli-responsive property, which is also known as environmental adaptability, is the basis for the development of various "smart" materials such as controlled drug delivery vehicles, shape-memory materials, and sensing devices.[32−35] It should be noted that although many polymers only or mainly involve a specific type of noncovalent interaction, developing polymeric materials which combine more than one type of interaction has emerged as a hot topic.[36,37] In such systems, the functional arrays are orthogonally conjugated without disrupting the specificity and thermodynamics of each other, thus the polymers can be multiresponsive, which are capable of maintaining their integrity and precisely adjusting their properties in response to a broad range of environmental stimuli.[38]

1.2. Experimental Quantification Techniques

Experimentally quantifying noncovalent interactions (e.g., strengths, lengths, stoichiometry, association/dissociation constants) and identifying the influence of different environmental factors not only are of fundamental interest to elucidate the structures and properties of polymers but also lay the foundation for the development of materials with practical applications. Much effort has been devoted to addressing noncovalent interactions via a variety of theoretical, computational, and experimental approaches. Several reviews are available on providing theoretical understandings of noncovalent interactions in different states (e.g., gas phase, solution, solid state),[39−41] and in other reviews, the computational methods used to analyze and predict noncovalent interactions are summarized, including Quantum Monte Carlo,[42] semiempirical quantum mechanical methods,[43] wave function theory,[44,45] and density function theory,[46,47] which are not the focus of this review. The present review will mainly discuss the probing of noncovalent interactions and the elucidation of their mechanisms by experimental techniques, especially based on the measurements in polymeric systems.

1.2.1. Structural and Thermodynamic Approaches. A wide range of analytical methods are available for assessing the structures and binding affinities of noncovalent complexes, among which X-ray crystallography, spectroscopic analysis, and isothermal titration calorimetry (ITC) are the most conventionally used, providing useful information and insights of the interactions from different aspects. X-ray crystallography offers visualization of the position of atoms and their bonding arrangements in solid-state crystals, revealing the lengths, stoichiometries, and strengths of the interactions based on the atomic-level structural information.[48] It has been a powerful tool to study noncovalent interactions (e.g., hydrogen bonding, protein−ligand interactions) in biological molecules such as proteins, DNA, and drugs but requires the formation of crystals with reasonable quality and size.[49−51] Complementing the characterization of solid structures, spectroscopic techniques (e.g., X-ray emission spectroscopy (XES), X-ray absorption fine structure (XAFS) spectroscopy, infrared (IR) spectroscopy, nuclear magnetic resonance (NMR) spectroscopy, ultraviolet−visible (UV−vis) spectroscopy, and fluorescence spectroscopy) have been widely used to detect noncovalent interactions and identify the local structures of molecules in solutions and amorphous materials, where the variations of electronic

https://doi.org/10.1021/acs.chemrev.2c00215
Chem. Rev. XXXX, XXX, XXX−XXX

Table 1. Typical Parameters and Features of Different Force-Measuring Techniques

	Length scale	Force sensitivity	Spatial resolution		Typical systems	Features
			Normal	Lateral		
SFA	Macroscopic (10 mm)	10^{-8} N	<0.1 nm	~1 μm	Large particles, flat or curved surfaces	Measures absolute surface separation, surface deformation, local geometry, and contact area
AFM	Microscopic, nanoscopic (10 nm ~10 μm)	10^{-12}–10^{-11} N	~0.1 nm	1 nm	Colloids, biological cells, nanoparticles, macromolecules	Allows surface imaging and molecular manipulation with high lateral resolution
AFM-SMFS	Nanoscopic, atomic (0.1–1 nm)	10^{-12}–10^{-11} N	~0.1 nm	1 nm	Small molecules, intermolecular and intramolecular bonds	Detects individual bond strengths
OT	Microscopic, nanoscopic, atomic (0.1 nm ~10 μm)	10^{-14} N	0.2 nm	0.2 nm	Biological cells, organisms, macromolecules, small molecules	Provides high force sensitivity and manipulates particles in a noninvasive way

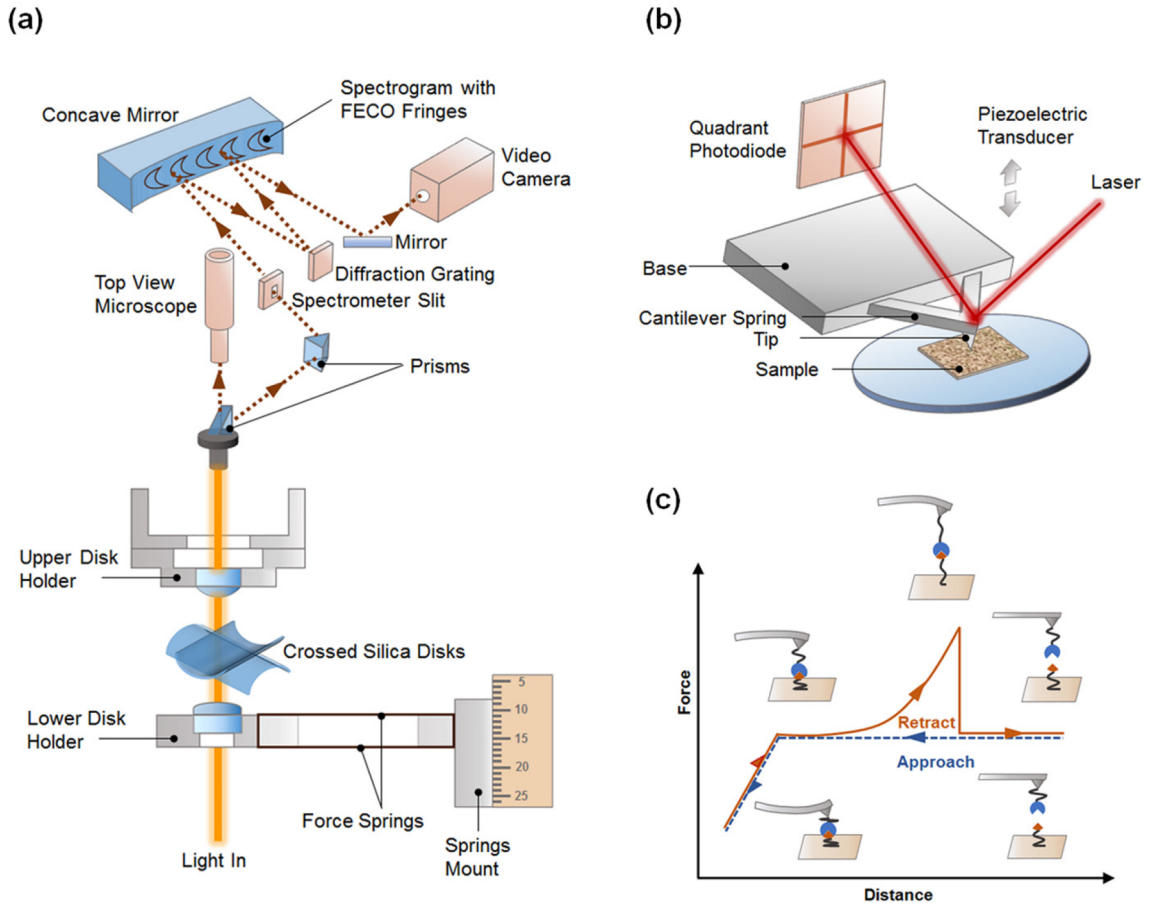

Figure 2. Schematic illustrations of typical experimental setups of (a) SFA and (b) AFM for intermolecular and surface force measurements. (c) Working principle and representative force–distance curve of AFM-SMFS (single-molecule force spectroscopy) for the measurement of interactions between two bonded molecules.

transitions, electron spin states, nuclear spin states, molecular rotations, and molecular vibrations in atoms and molecules can be probed via different techniques.[52−54] While a single spectrum generally offers qualitative data of bond formation, spectroscopic (including NMR, UV–vis, fluorescence) titrations have been commonly employed to estimate the binding affinity, where the concentrations of the unbonded species and bonded complexes are determined by the physio-chemical signals (e.g., intensity).[55−57] It should be noted that only equilibrium binding constants can be obtained, and for complexes with multiple binding sites, the maximum stoichiometry must be predetermined.[58] ITC directly measures the heat absorbed (endothermic reaction) or released (exothermic reaction) along with complex formation, which is of particular interest for studying noncovalent interactions in biological and polymeric systems as it gives access to the entire thermodynamic profile at equilibrium, including binding affinity, Gibbs free energy, enthalpy, entropy, and stoichiometry.[59] Sum frequency generation (SFG) spectroscopy and surface plasmon resonance (SPR) are surface/interface sensitive characterization techniques with ultrafast time resolution, which can provide information on the dynamics of the binding processes. SFG generates vibrational spectra of ordered species at interfaces, and it is mainly used to monitor the changes in molecular structure, orientation and conformation of the ordered monolayers.[60,61] SPR detects the binding process between the surface-

https://doi.org/10.1021/acs.chemrev.2c00215
Chem. Rev. XXXX, XXX, XXX–XXX

immobilized reactants and the species in solution, which can identify the formation, equilibrium, and reversibility of the complexes, revealing binding affinity and kinetics between the molecules.[62]

1.2.2. Direct Force Measurements. The nature and range of the force laws (i.e., force as a function of distance, F(D)) of noncovalent interactions can be determined by direct force measurements between two surfaces as a function of surface separation, which was originally demonstrated by Derjaguin and co-workers in 1954 by measuring attractive van der Waals forces between a glass hemisphere and a flat surface.[63] Since then, a variety of force-measuring techniques have been developed to evaluate the interactions between macroscopic surfaces, microscopic particles, and nanoscopic molecules, such as surface forces apparatus (SFA), atomic force microscopy (AFM), the osmotic pressure (OP) technique, optical tweezers (OT), total internal reflection microscopy (TIRM), microcantilevers, and micropipettes. Because of their different ranges, resolutions, and sensitivities, these techniques can provide reliable measurements to different subjects with appropriate force magnitudes, lengths, and time scales. For example, the OP technique detects the osmotic pressure of a solution between two macroscopic surfaces and can only be used for ordered colloidal structures (e.g., lipid bilayers), while OT and microcantilevers are able to distinguish sub-pico-Newton forces, which are generally applied to the study of single-molecule and single-bond interactions.[64] Although the principle of force measurement is quite straightforward, the real challenge lies in the accurate determination of weak forces and the measurement and correlation of absolute surface separations between the objects. SFA, AFM, and OT can provide control and measurement of surface forces and separations over a wide range with high force sensitivities and spatial resolutions (Table 1), which have become the most commonly employed force-measuring techniques for the quantification of intermolecular and surface interactions in diverse systems.

1.2.2.1. Surface Forces Apparatus (SFA). The SFA is a well-established technique that allows in situ and real-time measurements of interaction forces, absolute surface separation, and local geometry of two interacting surfaces under various conditions (e.g., vacuum, vapors, and liquids).[65−67] A typical SFA setup is schematically illustrated in Figure 2a, which contains two crossed cylindrical silica disks (with a radius of ∼2 cm) that are generally covered by a semireflective layer of silver back-coated on a thin mica sheet. Mica serves as the most common substrate in SFA measurements because of its transparency, atomic smoothness, and versatility for surface modification; alternative materials such as silica, sapphire, gold, metal oxides, and polymer films have also been explored.[68,69] The samples can be immobilized on the curved substrates or dispersed in the solution, and the force measurements are realized by driving one disk to approach and retract from the other disk. During this process, the two surfaces can come into contact or only be separated by a confined thin fluid film. The absolute surface separation, thickness of the confined film, contact area, and surface deformation of the interacting surfaces can be monitored with multiple beam interferometry (MBI) using fringes of equal chromatic order (FECO), where the shapes and separation distances of the surfaces are reflected from the shapes and positions of the interference fringes. On the basis of the movement of the driven surface and the changes of absolute separation between the surfaces, the deflection of the cantilever spring (with a spring constant in the range of ∼100 to >2000 N/m) is determined and used for the calculation of the interaction forces by Hooke's law. Although the direct visualization of interfacial phenomena is realized with a relatively low lateral resolution (∼1 μm), the normal resolution (resolution of separation distance) of an SFA can reach <0.1 nm with a force sensitivity of $\sim 10^{-8}$ N, providing quantitative information on a variety of fundamental interactions occurring between two macroscopic surfaces, such as van der Waals forces, electrostatic interactions, hydrophobic forces, and ligand−receptor interactions.[70−72] Besides normal movement, the surfaces can also be sheared laterally, allowing friction tests as well as rheology measurements of the confined thin fluid films.[73,74]

1.2.2.2. Atomic Force Microscopy (AFM). Since its first introduction in the early 1980s, AFM has become one of the most widely used techniques for surface characterization, which offers surface imaging, force measurements, and molecular manipulation at the atomic level under diverse conditions.[75] The force measurement principle of AFM is similar to that of the SFA, where the interaction forces are determined through a cantilever deflection using Hooke's law. However, in AFM, the forces are generated between a microscopic/nanoscopic probe and a surface rather than between two macroscopic surfaces. Although sharp AFM probes (with radius of 10−100 nm) with a pyramidal geometry have been extensively exploited for surface imaging because of the high lateral resolution, colloidal probes are generally preferable for the quantification of surface interactions, as the well-defined geometry of the colloidal particles can provide precise force results based on contact mechanics models.[76] The colloidal probes are prepared by attaching microsized (radius of 0.1−10 μm) particles such as silica, gold, and polymer spheres to the tipples cantilevers,[77] and the particles can be easily modified with different chemical groups. As shown in Figure 2b, in a typical force measurement, the AFM probe is driven by a piezoelectric transducer to approach, contact with, and retract from the substrate, during which the deflection of the cantilever is detected by the position displacement of the laser beam reflected from the back of cantilever using a quadrant photodiode. The spring constant of the cantilever is usually calibrated by the Hutter and Bechhoefer method, which generally ranges from 0.05 to >1 N/m.[78] Therefore, with a distance resolution of ∼0.1 nm, the force sensitivity AFM can readily reach $\sim 10^{-11}$ N. A major difference between the SFA and AFM is how the surface separation/interaction force is determined. The SFA possesses advantages in the direct measurement of absolute surface separation, surface deformation and contact area; however, material choice is relatively limited in this approach as the surfaces or thin films often need to be transparent or semitransparent. Although there is no requirement for material transparency in AFM experiments, it should be noted that the separation distance of the probe and substrate is not directly measured but inferred from the displacement and deflection of the cantilever, which is likely to deviate from the absolute separation, especially for soft surfaces with nonnegligible deformations (e.g., soft polymers).[79] For the study of molecular and surface interactions, the SFA and AFM usually serve as complementary approaches. While an SFA is generally used for quantifying physical forces between surfaces with defined contact areas and the capability for measurements close to or under thermodyanmic equilibrium conditions, AFM measurements are intrinsically dynamic and better suited to investigate events on a molecular scale.[80]

https://doi.org/10.1021/acs.chemrev.2c00215
Chem. Rev. XXXX, XXX, XXX−XXX

1.2.2.3. Atomic Force Microscopy-Based Single-Molecule Force Spectroscopy (AFM-SMFS). Because of the high spatial resolution and force sensitivity, AFM enables direct force measurements of individual bonds at the single-molecule level, which is primarily utilized to study the noncovalent interactions within one molecule (intramolecular) or between a pair of interacting molecules (intermolecular). This technique, known as AFM-SMFS, has been demonstrated to be a powerful tool for investigating various chemical and biological phenomena, including molecular assembly, molecule adsorption, DNA base-pairing, and protein folding.[81−83] Figure 2c schematically illustrates the principle of AFM-SMFS for the detection of intermolecular interactions between two bonded moieties. In general, both the sharp AFM tip and the substrate are functionalized with one of the groups, respectively, via either physisorption or chemisorption with a flexible polymer linker. While physisorption is widely utilized because of the simple sample preparation, chemisorption provides a better performance because of the robust attachment. During a typical force measurement cycle, the cantilever suspended above the substrate first approaches the surface, allowing molecules on the tip to interact with the functionalized surface, which induces specific interactions and leads to the formation of a single-molecule bridge between the tip and substrate. Then the retraction of the AFM tip will result in the elongation of the polymer bridge followed by bond rupture at a certain point, showing a gradual increase and a sudden drop of the force−distance curve. For the detection of intramolecular interactions, the macromolecules (e.g., proteins) are normally absorbed/immobilized on the substrate and then captured and extended by the AFM tip. The regime showing the increasing attractive force is related to the stretching of the polymer chain, which is usually used to examine the characteristics (e.g., contour length, elasticity) of the extended polymer.[84,85] The maximum force is referred to as "rupture force" and normally employed for the investigation of molecular interactions, whose binding ranges, kinetics, and affinities are commonly revealed by Bell−Evans analysis.[86,87] As the Bell−Evans theory predicts a simple (i.e., linear) relationship between rupture force and log-loading rate, it has been most widely employed for data analysis in dynamic force spectroscopy. However, it should be noted that the linear trend predicted by the Bell−Evans model is only effective for irreversible bond ruptures that are measured at relatively high loading rates (i.e., far-from-equilibrium regime), and when highly dynamic interactions are detected at low loading rates, nonlinearity would appear because of the rebinding of the functional groups, which is referred to as near-equilibrium regime. To address this limitation, Friddle and co-workers introduced a new parameter (i.e., equilibrium force for bond rupture) to modify the Bell−Evans equation, which was successfully used to describe the full evolution of the force spectra.[88] Even at high loading rates, deviations from the Bell's theory could also be observed because of the change of energy barrier distance, and Szabo et al. derived a generalization of Bell's equation by considering the position change during pulling.[89] The main limitation of AFM-SMFS is the relatively high stiffness of AFM cantilevers, with which the low force ranges associated with many biological processes are difficult to achieve.

1.2.2.4. Optical Tweezers (OT). OT, also known as optical traps, are unique scientific techniques that can apply localized and precise optical forces to hold and move microscale dialectic particles without mechanically touching them.[64,90] This technique usually employs a visible or near-infrared (NIR) laser beam with a wavelength in the range of 0.5−1 μm, which is strongly focused to a tiny region by passing through a high numerical aperture objective, generating three-dimensional optical gradients with the highest intensity at the center of the beam. When a particle presents near the beam focus, the gradient force tends to drive the particle toward the center and focus of the beam, forming an optical trap to prevent the particle from diffusing away.[91] As any dielectric particle near the focus of the beam can be traped, the solution that contains freely diffusing colloidal samples must be kept at an extremely low concentration to prevent the simultaneous trapping of a large number of particles.[92] Besides particle manipulation, OT has also been used to conduct accurate force measurements, as the optical force applied on the particle is proportional to its displacement from the trap center. The position of the particle can be monitored by recording the deflection of the laser beam with a photodiode detector, yielding a spatial resolution of ∼1 nm, and the trap stiffness (i.e., spring constant) is obtained by calibration.[93] Because of the noninvasive nature, OT has gained special research interest in manipulating biological cells and organisms, and the ultrahigh force sensitivity (10^{-14} N) allows this technique to detect interactions of polymers and biomolecules at the single molecular level.[94] However, as the small molecules (such as protein, RNA) of interest cannot interact significantly with the trapping light, in most OT experiments, they need to be attached to microscopic particles (e.g., silica or polystyrene with radius >100 nm) through linker molecules.[95] Although OT provides noninvasive force measurements, the high intensity at the optical trap can cause local heating and the resultant thermal gradients in the vicinity. Moreover, photodamage of the trapped specimens may occur, which might be minimized by exchanging the oxygen in the medium with an inert gas.[96]

The force-measuring techniques can not only provide the force laws of specific interactions but also reveal the mechanical properties (e.g., viscoelasticity, modulus, adhesion, deformation, friction) of the detected materials at the microscopic/nanoscopic/molecular level, which are directly correlated to the structures and bulk performances of the materials. These nanomechanical properties can be either directly obtained from the force curves or extracted by fitting parts of the force curves using contact mechanics models. For example, in AFM measurements, the maximum attractive force obtained during tip retraction can be used to indicate the surface adhesion, and the elastic modulus of the sample surface was calculated by applying a particular model of contact mechanics.[97] The classical and most commonly used models are developed by Hertz (Hertz model), Derjaguin Müller and Toporov (DMT model), and Johnson Kendall and Roberts (JKR model), which describe the surface deformation and adhesion between two elastic surfaces. For soft and viscoelastic systems, more complicated interaction models have been proposed with the consideration of the viscous responses of the surfaces.[98] Over the last two decades, nanomechanical characterization has been extensively employed to study intermolecular and surface interactions, especially noncovalent interactions, in diverse chemical and biological systems, contributing to the in-depth understanding of the interfacial phenomena and interaction mechanisms. The fundamental study of the noncovalent interactions significantly promotes the development of functional materials, whose properties and functionalities can be designed and modulated based on the tunable interactions. This review aims to provide a systematic overview of important noncovalent interactions

https://doi.org/10.1021/acs.chemrev.2c00215
Chem. Rev. XXXX, XXX, XXX−XXX

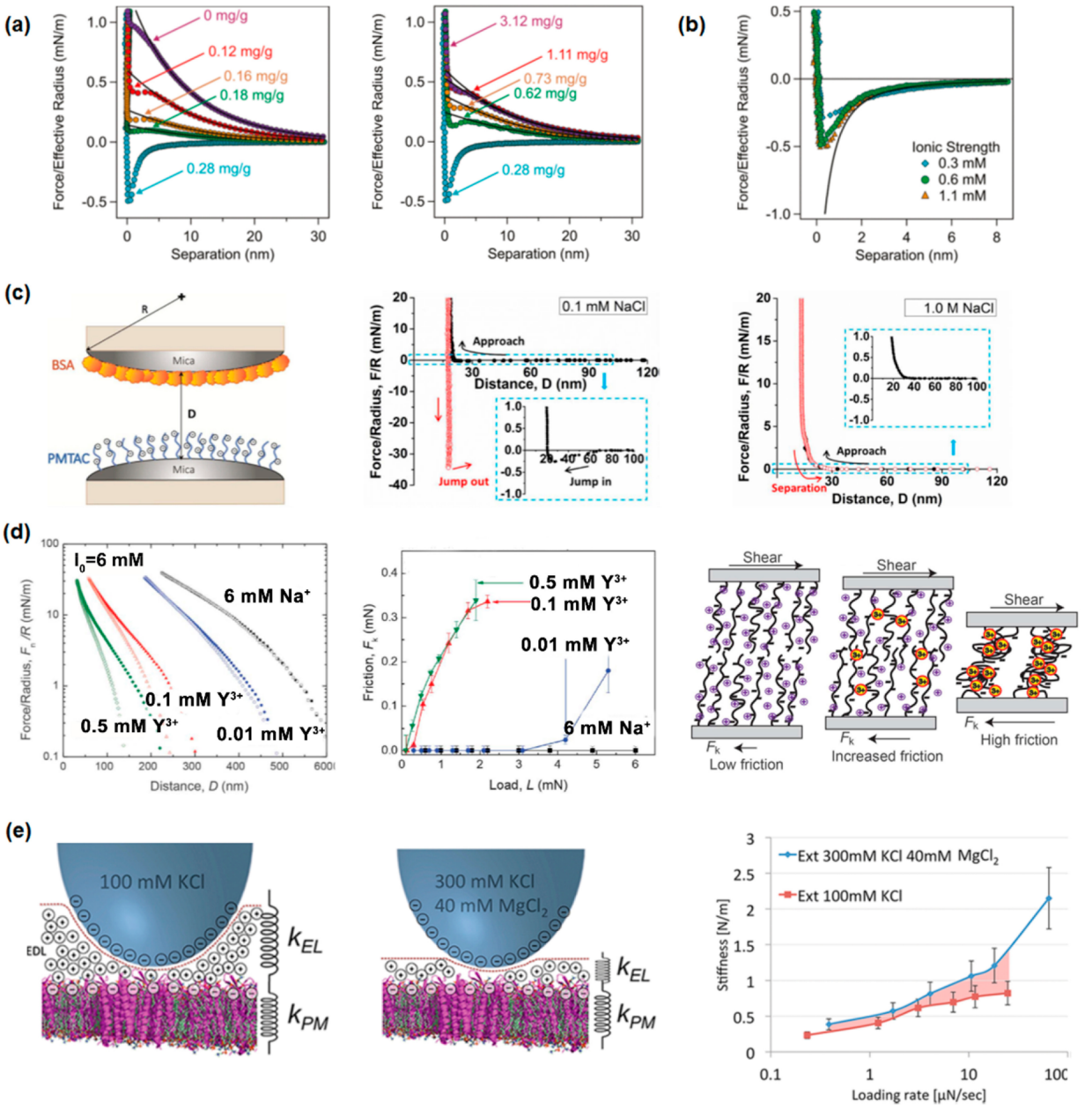

Figure 3. Force−distance curves between sulfate latex particles (a) at various LPEI concentrations (fitted with Poisson−Boltzmann theory) and (b) at different KCl concentrations in the presence of 0.28 mg/g LPEI (fitted with van der Waals theory). Reproduced with permission from ref 105. Copyright 2011 American Chemical Society. (c) Schematic of surface force measurements conducted between a PMTAC brush coating and a BSA coating and the force−distance profiles obtained in 0.1 mM and 1.0 M NaCl solutions. Reproduced with permission from ref 114. Copyright 2017 Elsevier. (d) Normal force−distance curves, friction forces and schematics of sliding of apposing PSS brushes in solutions (6 mM ionic strength) with 0.6 mM NaCl, 0.01 mM, 0.1 mM, and 0.5 mM $Y(NO_3)_3$. Reproduced with permission from ref 119. Copyright 2017 American Association for the Advancement of Science. (e) Schematics and the measured stiffness of purple membranes at low (100 mM KCl) and high (300 mM KCl, 40 mM $MgCl_2$) electrolyte concentrations. Reproduced with permission from ref 122. Copyright 2013 American Chemical Society.

employed in polymeric systems. We first discuss the quantification of various types of noncovalent interactions in polymeric systems, including van der Waals forces, electrostatic interactions, metal coordination, hydrogen bonding, π/cation/anion−π interactions, hydrophobic interactions, and cooperative interactions, with a focus on how the interaction mechanisms are experimentally discovered and demonstrated using force-measuring techniques (i.e., nanomechanical analysis). The revealed binding mechanisms are then correlated to the structures and functionalities of a broad range of polymer materials, ranging from microscopic colloids, two-dimensional films to bulk coacervates and hydrogels, offering inspirations for the design and optimization of materials and technologies with cutting-edge applications.

2. NANOMECHANICS OF NONCOVALENT INTERACTIONS IN POLYMERIC SYSTEMS

In this work, the nanomechanics or nanomechanical properties of noncovalent interactions mainly refer to the force laws and thermodynamic characteristics of these interactions.

https://doi.org/10.1021/acs.chemrev.2c00215
Chem. Rev. XXXX, XXX, XXX−XXX

2.1. van der Waals Forces and Electrostatic Interactions

van der Waals forces arise from the interactions of the rotating or fluctuating electric dipoles, which are present in all phenomena driven by molecular and surface interactions. In practice, only a few systems solely involve van der Waals forces. When molecules and surfaces are immersed in water or other media with high dielectric constants, they are generally charged and accompanied by the formation of an electric double layer consisting of counterions close to the surface. The resultant electrical double layer forces will act together with van der Waals forces to determine the overall interactions of the colloids/surfaces, which is referred to as classical Derjaguin−Landau−Verwey−Overbeek (DLVO) theory. Unlike van der Waals forces that are generally attractive (except for cases such as a mineral solid−water−air system), the double layer interactions can be attractive for surfaces bearing opposite charges or repulsive for similarly charged surfaces. Therefore, the net DLVO force can either be attractive or repulsive as a function of the separation distance, depending on the surface potentials and solution conditions (e.g., pH, electrolyte type and concentration).[99] As a fundamental framework to rationalize the long-range interactions between colloidal particles and interfaces in aqueous solutions, the DLVO theory has been widely used to evaluate colloidal stability and their aggregation/dispersion behavior, which facilitates the illumination of many chemical and biological processes, including polymer adsorption, fabrication of multilayers, protein binding, and cell adhesion.[100,101] It should be noted that when surfaces carrying polymers or biomolecules approach each other, their interactions generally could not be fully described by the DLVO theory because of the presence of other non-DLVO forces, such as polymer bridging, polymer-mediated steric forces, hydrophobic interactions, and hydration forces, which should also be considered to address the limitation of the DLVO theory.

2.1.1. Polyelectrolyte-Modified Surfaces. Polyelectrolytes are polymers possessing ionizable repeating units, which can be classified as anionic, cationic, and ampholytic according to the nature of the carried charges. Polyelectrolytes can interact with a broad range of neutral or charged surfaces/particles/molecules and have been extensively used for surface modification, providing good control of surface properties such as wetting, adhesion, lubrication, and biological resistance.[102,103] The fabrication of polyelectrolyte-modified surfaces can be facilely realized by the direct adsorption of polyelectrolytes to oppositely charged surfaces, which is dominated by electrostatic attraction, and the interactions between the polyelectrolyte-coated surfaces generally follow the DLVO theory, where non-DLVO forces, including steric forces and polymer bridging, may also make a contribution. The adsorption process of cationic polyvinylamine (PVAm) on negatively charged glass surfaces was examined by an SFA.[104] In the absence of a polymer, the interactions between the two surfaces were dominated by the long-range double-layer repulsion, and the addition of 1 ppm PVAm in the solution could neutralize the surface charge by polymer adsorption, leading to the vanishment of repulsion and the appearance of long-range attraction. It was noted that the detected attractive force was substantially stronger than the van der Waals force, which was attributed to the bridging of polymers when they were absorbed on both surfaces. With the further adsorption of PVAm, the surfaces would be overcompensated and positively charged, and electrostatic repulsion and steric repulsion from the adsorbed polymer chains would dominate the surface interactions. Similarly, the interactions between negatively charged sulfate latex particles in the presence of cationic linear poly(ethylene imine) (LPEI) were investigated using colloidal AFM, with forces varying from repulsive to attractive and then back to repulsive with the increase of polymer concentration (Figure 3a).[105] The attractive forces measured at the isoelectric point (with 0.28 mg/g LPEI) were totally governed by van der Waals forces and insensitive to ionic strength, suggesting a high homogeneity of the absorbed polymer layer (Figure 3b). However, in many cases, the adsorption of polyelectrolytes would result in heterogeneous surface charge distributions because of the formation of polymer patches, and the electrostatic patch−charge interactions contributed to the additional attraction exceeding van der Waals forces.[106,107] Polyelectrolyte multilayers are formed by alternating adsorption of polycations and polyanions, which has found a wide range of engineering and biomedical applications.[103] The self-assembly process of poly(allylamine) hydrochloride/poly(styrenesulfonate) sodium salt (PAH/PSS) multilayer was deciphered by measuring the interactions of symmetric and asymmetric surfaces.[108] It was found that the adsorption of polyelectrolyte to an oppositely charged polyelectrolyte layer was dominated by the long-range electrostatic attraction, generating localized ion pairs and inversing the surface charge. The further adsorption was controlled by a balance among electrostatic repulsion, short-range attraction because of ion-pair formation, and short-range electrosteric repulsion caused by the extended polymer segments in the solution.[109]

Besides physical adsorption, polyelectrolytes can be chemically anchored to surfaces at high grafting densities, showing stretched "brush" structures in contrast to coil configurations because of the osmotic pressure created by the counterions immobilized inside the brushes.[110] The interactions between two particles grafted by strong polyelectrolyte brushes poly(2-(methacryloyloxy)ethyltrimethylammonium chloride) (PMTAC) were detected by OT, and only weak electrostatic interactions in the range of a few $\mu N \cdot m^{-1}$ were measured.[111] The calculated surface charge density was only 4% compared to fully dissociated PMTAC, indicating the majority of the Cl^- counterions were immobilized in the dense polymer brushes. The conformation and properties of the polyelectrolyte brushes are highly dependent on the surrounding environment, including temperature, pH, and ionic strength. The pH effect on the contact mechanics between cationic poly[2-(dimethylamino)ethyl methacrylate] (PDMAEMA) brushes and anionic poly(methacrylic acid) PMAA brushes was studied using AFM.[112] At a neutral pH, the strong electrostatic attraction between the two oppositely charged surfaces resulted in a large contact area and adhesion force, while either a high or a low pH could induce the solvation of one of the surfaces, generating an osmotic pressure to resist deformation. Thus, both the adhesion and the contact area were reduced. Typically, an increase of the salt concentration induces the screening of electrostatic interactions, which impairs polymer stretching.[113] The salinity-regulated property has been applied to control the adsorption and desorption of biomolecules, and the interactions between a PMTAC-grafted surface and a bovine serum albumin (BSA) coating were examined.[114] As shown in Figure 3c, when the NaCl concentration was 0.1 mM, the oppositely charged surfaces jumped into contact around a separation of 60 nm upon approaching, and a strong adhesion was detected during separation. However, in a 1.0 M NaCl solution, the electrostatic attraction was greatly suppressed, accompanied by an eliminated

https://doi.org/10.1021/acs.chemrev.2c00215
Chem. Rev. XXXX, XXX, XXX−XXX

adhesion because the steric repulsion between the surfaces overwhelmed the van der Waals forces. Besides salt concentration, the type of ions also plays an important role in the structure of the polyelectrolyte brushes. A study on the anion-specific behavior of cationic poly(2-diisopropylamino)ethyl methacrylate (PDPA) brushes revealed that kosmotropic acetate (strong hydration, high charge density) could significantly promote the swelling of PDPA by inducing high osmotic forces, while the effect of chaotropic thiocyanate (poor hydration, low charge density) was not obvious.[115] Tirrell and co-workers performed SFA measurements on PSS brushes in the presence of multivalent counterions, indicating that divalent cation (e.g., Mg^{2+}, Ca^{2+}, Ba^{2+}) exhibited specific ion effects on the shrinkage of PSS depending on the size and hydration state, and the introduction of trivalent cation Y^{3+} resulted in abrupt shrinkage of the brushes.[116] The structural change greatly influences the lubrication properties of the polymer brushes, which plays a critical role in many technical and biological applications. Normally, polyelectrolyte brushes are postulated to show excellent wear resistance and low friction, ascribed to the counterion osmotic pressure and the hydration layer around the polymer segments.[117] The friction coefficients measured between sulfonated polyelectrolyte brushes could be lower than 0.0006−0.001 in pure water.[118] Although the excellent lubrication could be maintained in monovalent salt solutions (e.g., 6 mM NaCl) for PSS brushes, the addition of only 0.01 mM Y^{3+} would reduce the range of repulsion and increase the friction force at a relatively high load (>3 mN), which resulted from the electrostatic bridging medicated by the multivalent ions that enhanced chain interpenetration of the apposing brushes (Figure 3d).[119] The further increase of Y^{3+} concentration (0.1 and 0.5 mM) induced strong hysteresis of the repulsion and a rapid increase of friction even at a very low load (0.2 mN), attributed to the collapse of the brushes into pinned-micelle-like structures. Divalent cations Ca^{2+} and Ba^{2+} also exhibited similar trends with quantitative differences.

2.1.2. Protein Surfaces. Proteins usually exhibit net charges because of the charged groups carried by individual amino acids, which play a critical role in their interactions with other objects. Butt determined the local surface charge of purple membranes (75 wt % bacteriorhodopsin and 25 wt % lipids) using a scanning force microscope.[120] By comparing the force curves obtained on bare alumina (with a known charge density) and purple membrane-absorbed alumina substrates, the surface charge of the purple membrane was estimated to be -0.05 C/m^2. For AFM imaging or force measurements conducted in solutions, as the tips usually carry charges, they tend to interact with the charged protein surfaces via electrostatic interactions, influencing the results (e.g., image resolution, height, modulus) obtained by AFM characterization. For example, a patterned catalase film was imaged using a silicon nitride AFM tip in sodium phosphate buffers at different pH and salt concentrations, where the force−distance curve obtained at each condition was in good agreement with the DLVO theory, indicating the interactions were dominated by electrostatic and van der Waals forces.[121] It was found that stable images could only be obtained when electrostatic repulsion existed between the tip and protein surface, and the screening of the electrostatic double layer (at high salt concentration or pH around isoelectric point) could lead to higher image resolution as well as a decrease in the measured height of the protein. Medalsy and Müller demonstrated that the electrostatic repulsion between the AFM tip and the purple membranes also influenced the measured nanomechanical properties of the proteins.[122] As shown in Figure 3e, at the loading rate of ∼10 μN/s, the detected mechanical stiffness of the purple membrane was lowered by ∼40% (from ∼1.3 to 0.8 N/m) with an enhanced electrostatic double layer repulsion (from 300 mM KCl, 40 mM $MgCl_2$ to 100 mM KCl). It was because that the total mechanical stiffness (k_{total}) was contributed by both the purple membrane (k_{pm}) and the electrostatic double layer (k_{el}), where k_{pm} was much higher than k_{el}. In the presence of a lower electrolyte concentration, the k_{total} probed by AFM was dominated by the softer electrostatic repulsion resulting from the thicker electrostatic double layer. The adhesion of proteins to surfaces was highly dependent on their surface charges, and a study on the adhesion between symmetric proteins layers (BSA or apoferritin) indicated that strong adhesion forces could only be detected near the isoelectric point of the proteins and at high ionic strength, demonstrating the important contribution of electrostatic interactions.[123] However, the AFM adhesion measurements conducted between lysozyme molecules and TiO_2 surfaces revealed that the solution condition could change the charged state of the proteins, which altered the apparent or effective size of the protein molecule. In this case, the adhesion was regulated by the contact area between the proteins and surfaces rather than the electrostatic interaction.[124] Besides their interactions with other molecules or surfaces, the mechanical stability of single proteins can also be affected by electrostatic interactions, which was demonstrated by AFM-SMFS of protein GB1 with two histidine residues.[125] With the pH changing from 8.5 to 3, the unfolding force of the protein was decreased from 115 to 76 pN, attributed to the increased electrostatic repulsion between the positively charged histidines.

2.2. Metal−Ligand Coordination

2.2.1. Structure of Coordination Complexes. Metal−ligand coordination occurs between a metal ion and the surrounding array of organic molecules, which are known as coordination center and ligands, respectively, yielding metal-containing compounds that are referred to as coordination complexes. In polymer science, metal−ligand coordination attracts special research interest because the generated coordination polymers can combine the properties of organic polymers with the specific features (e.g., optical, magnetic, dielectric, and catalytic) of metals.[126] Metal−ligand coordination is fundamentally an acid−base reaction, where the metal ions are viewed as Lewis acids that can accept at least one pair of electrons and the ligands are Lewis bases to donate electron pairs to metal ions. The nature and strength of the coordination bonds can be semiquantified by hard−soft acid−base theory, which classifies the acids and bases into hard (small and non-polarizable) and soft (large and polarizable) categories.[127] Hard acids bind strongly to hard bases with the formation of ionic bonds, while soft acids bind strongly to soft bases via covalent bonds. For interactions between hard acids−soft bases or soft acids−hard bases, relatively weak and dynamic coordination bonds can be generated. Because of the large variety of metal ions (especially transition metals) and ligand motifs (e.g., amine, pyridine, imidazole, nitrile, carboxylate, phosphonate), the binding strength can be readily modulated within a wide range (∼25%−95% of a covalent bond).[128] The structure of coordination complexes is largely determined by the coordination number, which denotes the number of donor atoms attached to the metal center. Although the formation of most coordination bonds is thermodynamically favorable, the

https://doi.org/10.1021/acs.chemrev.2c00215
Chem. Rev. XXXX, XXX, XXX−XXX

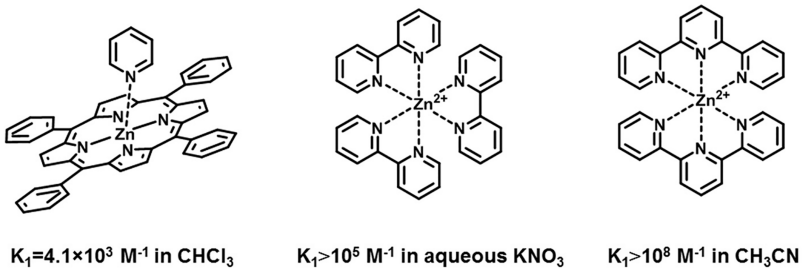

Figure 4. Typical examples of Zn^{2+}–pyridine complexes formed with monodentate, bidentate, and tridentate ligands.

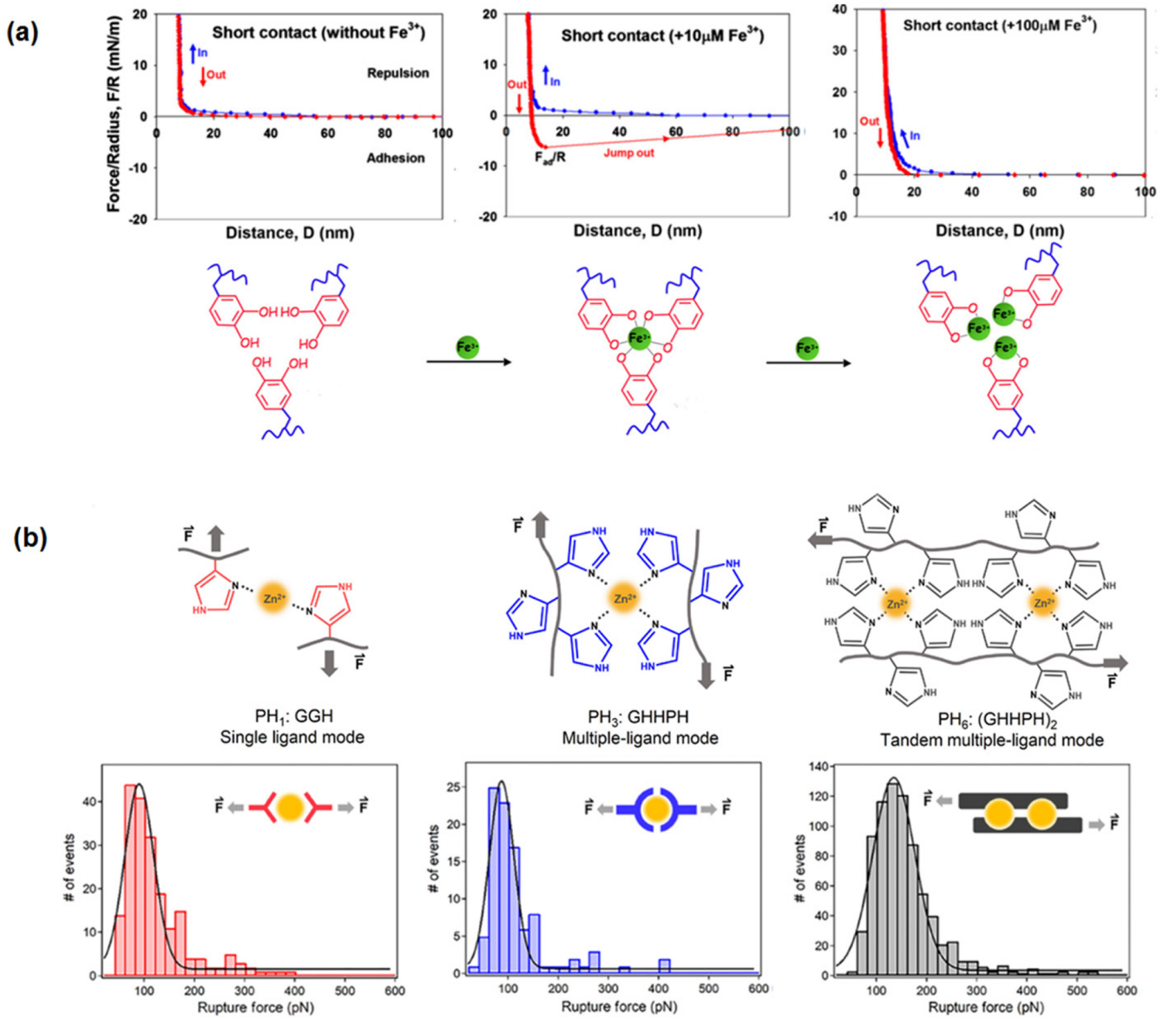

Figure 5. (a) Force–distance curves of symmetric mfp-1 films at different concentrations of Fe^{3+} and the corresponding catechol–Fe^{3+} coordination. Reproduced with permission from ref 72. Copyright 2010 National Academy of Sciences. (b) Rupture force histograms of histidine-containing peptide–Zn^{2+} complexes formed by single ligand coordination, multiple ligands chelation, and two multiple ligands chelation arranged in tandem. Reproduced with permission from ref 142. Copyright 2020 American Association for the Advancement of Science.

coordination number cannot increase indefinitely because of the steric effects between ligands and the repulsion between electrons donated by different ligands.[129] The most common coordination numbers are 2, 4, and 6, leading to linear, square planar/tetrahedral, and octahedral geometries, respectively. Compared to monodentate ligands that only form one coordination bond with metal ions, many ligands are able to bind to the metal centers through several donor atoms, which are referred to as multidentate ligands and the formed complexes are called chelate complexes. Generally, the chelate complexes

https://doi.org/10.1021/acs.chemrev.2c00215
Chem. Rev. XXXX, XXX, XXX–XXX

derived from multidentate ligands are much more stable than those prepared with monodentate ligands, with typical examples depicted in Figure 4. When different types of pyridine-containing ligands coordinated to Zn^{2+}, the binding constant for the first ligand (K_1) dramatically increased from ~10^3 M^{-1} for the single coordination bond to >10^8 M^{-1} with the tridentate chelating ligand.[130−132]

2.2.2. Metal−Catechol Coordination. Metal−catechol coordination is one of the most well-known interactions occurring in marine mussels, where the high extensibility and hardness of mussel byssal threads are postulated to be contributed by the robust and dynamic coordination bonds between Fe^{3+} and the catechol-like amino acid 3,4-dihydroxyphenylalanine (DOPA).[133] Catechol is a bidentate ligand that can bind Fe^{3+} via one, two, or three moieties, depending on the molar ratio of metal ions and ligands as well as the pH of the solution. The catechol−Fe^{3+} coordination was quantitatively investigated by Zeng and co-workers using an SFA, with an examination of the interaction behaviors between two positively changed mussel foot protein-1 (mfp-1) films at various Fe^{3+} concentrations.[72] As shown in Figure 5a, without the presence of Fe^{3+}, no attraction and adhesion were detected between the films, but the introduction of only a low concentration (10 μM) of Fe^{3+} could result in robust bridging of the surfaces with an adhesion energy of 4.3 mJ/m^2, which was ascribed to the formation of tris-catechol−Fe^{3+} complexes. However, the further increase of Fe^{3+} (100 μM) would induce the tris-complexes to transform into mono-catechol−Fe^{3+} complexes, and the bridging adhesion was abolished. The effect of pH on the coordination of Fe^{3+} and catechol groups was also studied, with surface adhesion and cohesion characterization of mussel adhesive proteins.[134] When the pH of the Fe^{3+} solution increased from 3 to 8, the cohesion energy between two in vivo residue-specific DOPA-incorporated recombinant foot protein fp-3F (drfp-3F) protein films was significantly enhanced from 0.5 to 2.1 mJ/m^2, with the surface adhesion (to mica) reduced by over 90%. It was because the tris-catechol−Fe^{3+} was favored at a high pH, which facilitated the cohesion because of intermolecular bridging and sacrificed the surface adhesion. The mechanical properties of the catechol−Fe^{3+} complexes were also investigated at the single-molecule scale by stretching a single-chain polymeric nanoparticle held by catechol−Fe^{3+} bonds.[135] The results revealed that the rupture force of the catechol−Fe^{3+} complexes was in the range of 100 to 250 pN, much weaker than covalent bonds (>1 nN) and stronger than typical hydrogen bonding or hydrophobic interactions (<150 pN). With the modulation of Fe^{3+} concentration and solution pH, the free energy landscapes underlying the ruptures of both bis- and tris-complexes were detected, where the rupture forces of the bis-complexes were almost twice of that of the tris-complexes but both structures showed similar energy barriers. It was possibly ascribed to the different geometries (tetrahedral of bis and octahedral of tris) of the complexes that influenced their unbinding pathways. Besides Fe^{3+}, catechol is also able to coordinate with other metals (e.g., Cu, Zn, Al), and its interaction with vanadium (in the form of V^{3+} and VO^{2-}) was investigated. At the same ion concentration, the cohesion measured between two recombinant mfp-1 films in the presence of V is much higher than that with Fe, following the trend of V^{3+} > VO^{2-} > Fe^{3+}, and the formation of tris-catechol−V complexes could occur at much lower pH values (e.g., pH = 4).[136] Lee et al. detected the interactions of an individual catechol group on a Ti surface by SMFS, and the measured rupture force suggested a dissociation energy of ~93 kJ/mol, attributed to a strong catechol−Ti coordination.[137] This coordination was also demonstrated to be regulated by solution pH. With the increase of pH from 3 to 7.5, the binding between one catechol group and the TiO_2 surface would change from two hydrogen bonds to one hydrogen bond and one coordination bond, and finally two coordination bonds.[138]

2.2.3. Metal−Histidine Coordination. Besides metal−catechol coordination, the interactions between histidine groups and divalent cations also contribute to the tough and self-healing behavior of mussel byssus, which is mainly ascribed to metal−imidazole coordination and possibly facilitated by interactions between metal ions and amine/carboxylate groups.[139] Harrington and co-workers employed colloidal AFM to measure the adhesion between two histidine-rich protein surfaces in the presence of Ni^{2+}, which could be greater than 0.3 mJ/m^2.[140] Similar to metal−catechol coordination, the bridging effect because of histidine−Ni^{2+} complexation was also affected by metal ion concentration and solution pH. An SMFS study on a bihistidine-containing protein GB1 demonstrated the stability of the protein could be greatly enhanced with the introduction of 4 mM Ni^{2+}, showing an increased unfolding force from ~120 to ~240 pN. However, the addition of 300 mM imidazole reduced the unfolding force back to the previous level because of its competition with histidine residues.[141] Recently, a series of histidine-rich peptides were designed to form different coordination structures with Zn^{2+}, and the mechanical stabilities of these complexes were examined in detail.[142] As presented in Figure 5b, three types of binding motifs could interact with Zn^{2+} and form complexes via different modes, which were single ligand coordination, multiple ligands chelation, and two multiple ligands chelation arranged in tandem, respectively. The rupture forces of these structures were measured to be 90, 87, and 135 pN, with calculated off-rate constants of 9.49, 2.91, and 0.56 s^{-1}, respectively. Therefore, compared to single ligand coordination, the multiple ligands chelation was less dynamic, and the tandem arrangement of two chelation sites would significantly improve the mechanical stability of the complex, because of the simultaneous break of the two sites upon bond rupture.

2.2.4. Other Types of Metal−Ligand Coordination. Pyridine ligands, including monopyridine, bipyridine, and terpyridine, are widely used to form coordination complexes, which can bind to a variety of metal ions via the electron pair donated by nitrogen. The interactions of two types of monodentate pyridine ligands with a pincer Pd metal center were detected, showing similar dissociation pathways with different rates. It suggested that the transition state geometry of the coordination complexes was not affected by the specific structures of the pyridines.[143] The unbinding force of two terpyridine ligands bridged by a ruthenium ion was detected, yielding a rupture force of 95 pN at a loading rate of 1 nN/s.[144] It should be noted that the bis-terpyridine complex was only formed in the presence of Ru^{2+}, and Ru^{3+} could coordinate with only one terpyridine moiety. However, the same ligand was found to be capable of coordinating with osmium ions in the forms of both Os^{2+} and Os^{3+}, and the redox state of the central metal ion could influence the binding strength.[145] At the fully oxidized state, the unbinding force of the bis-terpyridine−Os^{3+} complex was measured to be as high as 190 pN, which was weakened to 80 pN for the fully reduced bis-terpyridine−Os^{2+}. When measured at an open circuit (a mixture of Os^{2+} and Os^{3+}),

https://doi.org/10.1021/acs.chemrev.2c00215
Chem. Rev. XXXX, XXX, XXX−XXX

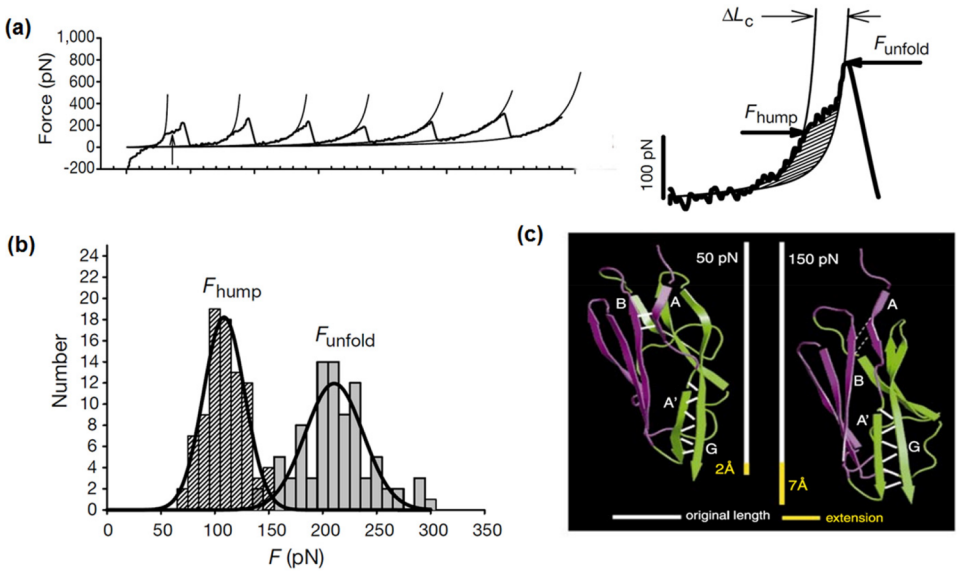

Figure 6. Unfolding of a titin-like polyprotein containing tandem repeats of immunoglobulin domains I27. (a) Typical force−extension curve showing a sawtooth pattern and a hump. (b) Histogram with Gaussian fits for hump force and unfolding force, and (c) structures of I27 module simulated at forces at 50 and 150 pN. Reproduced with permission from ref 155. Copyright 1999 Springer Nature.

the coordination bonds ruptured at around 100 pN, comparable to the terpyridine−Ru system.

Thiolate ligands are regarded as soft Lewis bases that bind strongly to transition metals. Li and co-workers detected the mechanical unfolding events of rubredoxin, which consisted of an FeS_4 center with one iron atom bounded by four cysteinyl sulfur atoms. The bond rupture occurred at ∼200 pN with a very broad distribution, suggesting the coordination bond is much more labile than typical covalent bonds.[146] Later, the chemical reactivity of the Fe-thiolate coordination was studied at different solution conditions. It was found that the rupture force was evidently lowered (from 211 to 160 pN) when the pH changed from 7 to 5 because of the protonation of the metal site, and the addition of a nucleophilic ligand (SCN^-) impaired the mechanical stability of the FeS_4 center because of ligand substitution.[147] Besides the unfolding studies, the folding process of rubredoxin was recently investigated using OT, taking advantage of the superb force resolution of this technique.[148] Compared to the unfolding forces that were usually higher than 40 pN, the forces detected during refolding were generally below 10 pN. Moreover, the reconstruction of the FeS_4 center was highly dependent on the coordination state of Fe−thiolate in the unfolded protein, which could only be facilitated by the two-coordinate Fe site rather than mono-coordinated Fe.

2.3. Hydrogen Bonding

A hydrogen bond is a dipole−dipole interaction occurring between an electronegative atom (e.g., oxygen, nitrogen, chlorine, fluorine) and a hydrogen atom that is covalently bound to a similar electronegative atom. Hydrogen-bonding interaction ubiquitously exists in biological systems and plays an essential role in various biological processes such as DNA pairing and protein folding. Because of the tunable affinity, fair directionality, and reversibility, single or multiple hydrogen-bonding arrays have evolved as one of the most developed approaches to generate synthetic supramolecular polymers, where the binding strength between the complementary units is governed by the number of hydrogen bonds formed, nature of donors and acceptors, arrangement of donor/acceptor sites, and the type of solvent.[19,149] In general, hydrogen bonds are favored in nonpolar environments, and polar media, especially water, can greatly weaken the hydrogen-bonding strength between the bonded units, by providing competitive hydrogen bonds with the dissolved hydrogen-bond donors and acceptors.[39]

2.3.1. Hydrogen-Bonded Biomolecules. Base pairing (i.e., adenine−thymine (A−T), cytosine−guanine (C−G)) in the DNA duplex is one of the most well-known molecular recognition events in nature, which is dominated by hydrogen bonding. The first direct force measurements between the complementary strands of DNA were performed by Lee and co-workers using AFM, in which the single-stranded DNA oligonucleotides with complementary sequences were covalently immobilized on the tip ($(ACTG)_5$) and surface ($(CAGT)_5$), respectively.[150] These oligonucleotides did not contain self-complementary regions and allowed the binding between each other by forming 20, 16, 12, 8, and 4 base pairs. Four populations of adhesive forces of 1.52, 1.11, 0.83, and 0.48 nN were detected. As the nonspecific interactions between the noncomplementary strands were measured to be 0.38 nN, the first three obtained forces were supposed to correspond to the unbinding of the DNA complexes with 20, 16, and 12 base pairs. To detect the binding strength of specific base pairs, Boland and Ratner prepared self-assembled monolayers from each of the four DNA base derivatives respectively and measured the interactions between two monolayers with all 16 combinations.[151] Only when the opposite base-pair coatings (i.e., A−T and C−G) interacted with each other, a large attractive force as well as a hydrogen-bonding force could be detected, while the other combinations only consisted of nonspecific attractive force. When the enthalpy (7.5 kJ/mol) and distance (0.2 nm) of a single hydrogen bond were assumed, the hydrogen-bonding forces of each A−T and C−G pairs were simply estimated to be 125 and 188 pN, respectively. The direct quantification of a single base pair was realized by stretching a DNA strand with an alternating A−T or C−G sequence.[152] As these strands could pair themselves to form hairpin structures because of their self-

https://doi.org/10.1021/acs.chemrev.2c00215
Chem. Rev. XXXX, XXX, XXX−XXX

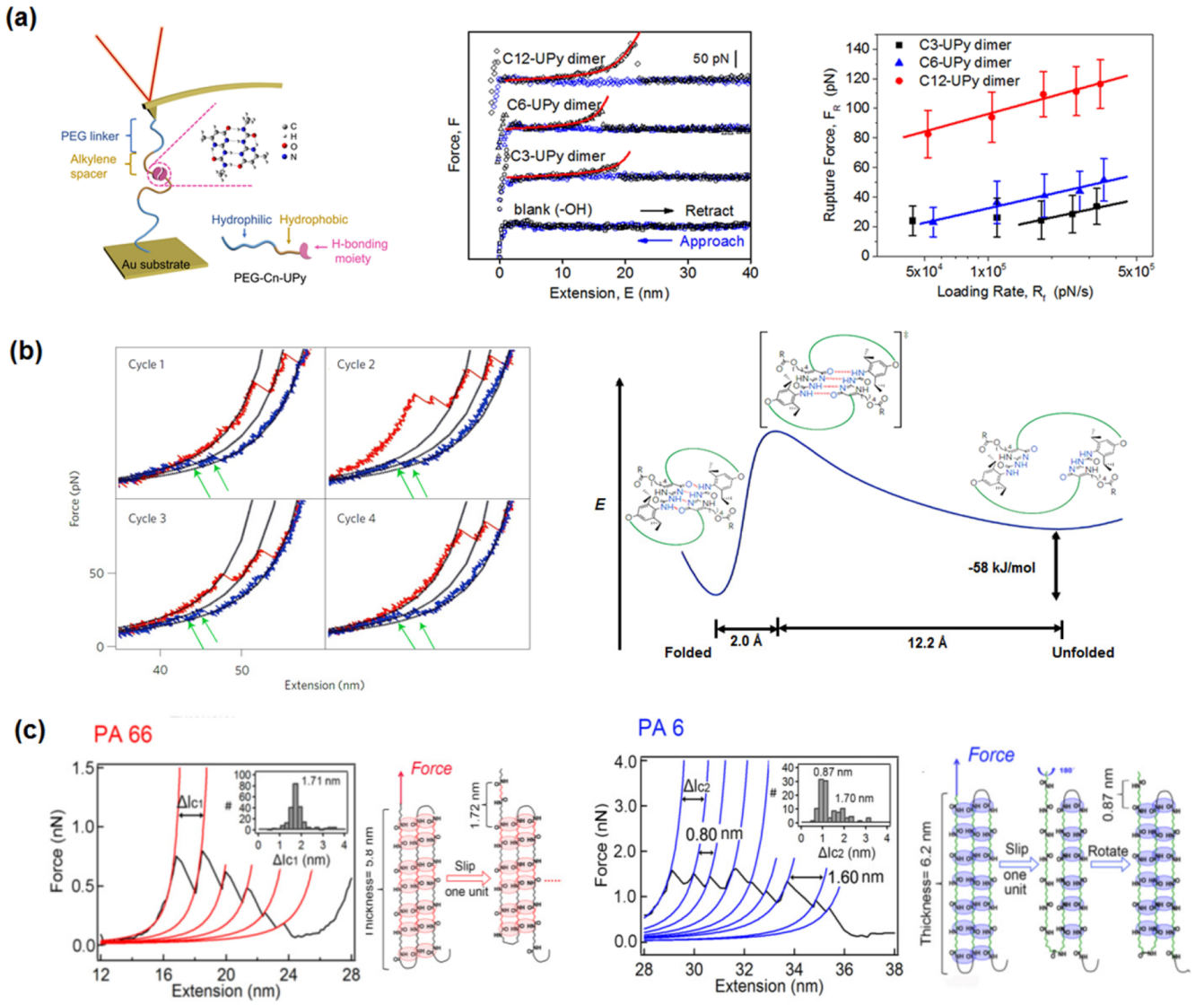

Figure 7. (a) Schematic experiment setup, force−extension curves, and loading rate dependence of the most probable rupture forces of the interactions between Cn−UPy (n = 3, 6, and 12) dimers. Reproduced with permission from ref 164. Copyright 2019 American Chemical Society. (b) Representative force curves during extension (red) and retraction (blue) cycles, and the constructed potential energy landscape for UPy dimer unfolding. Reproduced with permission from ref 165. Copyright 2014 Springer Nature. (c) Force−extension curves of PA66 and PA6 and the schematics of the change of hydrogen-bonding networks in the single crystals. Reproduced with permission from ref 173. Copyright 2018 American Chemical Society.

complementary nature, a plateau would appear in the force curve upon extension, corresponding to the force required to unzip the individual base pairs. The unzipping force was found to be 9 pN for the A−T sequence and 20 pN for the C−G sequence. The mechanical unzipping of a double-strand DNA molecule with thousands of base pairs was also examined by OT at a low stretching velocity (close to thermal equilibrium), and the opening of the double helix was observed to occur around 10−15 pN with a rapid fluctuation and an amplitude of ∼10%, which was because of the differences in the pairing and stacking of different base pairs, reflecting the sequence dependence of DNA unzipping.[153]

The secondary structure of proteins has been known to be regulated by hydrogen bonding between the neighboring amino acids, among which the α-helix is held together by hydrogen bonds nearly parallel to the long axis of the helix and the β-sheet is bounded by hydrogen bonds between adjacent β-strands that are nearly perpendicular to the polypeptide chains. The secondary structure of poly-L-lysine (PLL) was proved to play an important role in its cohesion behavior, as the cohesion energy measured between two symmetric films prepared from β-sheet PLL was four times higher than that prepared from α-helix PLL.[154] It was because the β-sheet conformation provided a larger number of lysine side chains on the opposing surfaces for hydrogen bonds formation. The cohesion energy was reduced with an increase of ionic strength, attributed to the impaired hydrogen-bonding capability of the amine groups. The unfolding of titin modules containing tandem repeats of immunoglobulin domains (e.g., I27) was detected by AFM-SMFS.[155] As presented in Figure 6a,b, besides the characteristic sawtooth patterns with rupture forces of ∼200 pN, a "hump"(∼100 pN) was observed before the first peak with an ∼0.7 nm extension of each domain. Along with steered molecular dynamics (SMD) simulations, it was demonstrated

https://doi.org/10.1021/acs.chemrev.2c00215
Chem. Rev. XXXX, XXX, XXX−XXX

that the hump correlated to a transition state because of the rupture of the two hydrogen bonds bridging the A and B β-strands, while the large rupture force corresponded to the full unfolding of the I27 module with the breakage of six hydrogen bonds stabilizing the A′ and G β-strands (Figure 6c). In SMFS studies, the stability of protein was not only dependent on the number and position of hydrogen bonds but also affected by the direction of the applied force. When a protein E2lip3 was pulled in the direction perpendicular to the hydrogen bonds (shear geometry), the unfolding force was measured to be 177 pN; however, when the direction of applied force was parallel to the hydrogen bonds (unzipping geometry), the unfolding force could not be detected as it was below the sensitivity of the instrument.[156] A similar phenomenon was also proved in a protein containing the src SH3 domain that was stretched by OT at a much lower pulling rate (near equilibrium). The unfolding forces were determined to be 35 and 14 pN for the shear and unzipping geometries, respectively.[157]

Polysaccharides are rich in hydroxyl groups and oxygen atoms. Therefore, they tend to form networks via extensive intermolecular and intramolecular hydrogen bonds. The intramolecular hydrogen bonding of amylose was investigated by examing the elasticity of individual molecules in solvents with different dielectric constants.[158] It was found that when the extension of each pyranose ring was above 0.5 nm, the slope of the force curves (related to the polymer rigidity) increased with a lower dielectric constant, which was ascribed to the formation of hydrogen bonds between adjacent sugar rings in nonpolar environments, and the differences disappeared when the hydroxyl groups were substituted by acetates. Comparing the free energies of amylose stretching in water and dimethyl carbonate, the energy of each intramolecular hydrogen bond was estimated to be 6.3 kJ/mol. It should be noted that in water, the force curves of amylose displayed a fingerprint plateau, and this feature gradually vanished with the decrease of water content in the mixed solvent, which was likely related to the coordinated hydrogen bonds provided by water molecules.[159] A SMFS study on hyaluronan (HA) in aqueous solutions demonstrated that HA behaved like a random coil at an elevated temperature (46 °C) but became semirigid at room temperature, attributed to the intramolecular hydrogen bonds that generated directly between the polar groups of polymer or by water bridges.[160]

2.3.2. Hydrogen-Bonded Synthetic Polymers. For the fabrication of synthetic supramolecular polymers, a single hydrogen bond is usually not strong enough and multiple hydrogen-bonding arrays are extensively exploited. Among them, the 2-ureido-4[1H]-pyrimidinone (UPy) group is pre-eminent because of its strong dimerization ability through quadruple hydrogen bonds and easy accessibility via a one-step reaction.[161] Zeng and co-workers elaborately investigated the surface self-adhesion of poly(butyl acrylate) (PBA) copolymers carrying different amounts of the UPy comonomer (4% and 7.2%).[162] Compared to pure PBA with a surface energy of 34 mJ/m^2, the strong hydrogen bonding between UPy groups increased the surface energies of the prepared polymers to 45−56 mJ/m^2. The adhesion force was greatly dependent on the UPy content and environment conditions (i.e., temperature, humidity), which affected the strength of hydrogen bonding and viscoelastic properties of the polymers. The unbinding strength of a single UPy−UPy dimer was directly detected by AFM-SMFS, showing a rupture force of >145 pN in nonpolar hexadecane.[163] As solvents with high polarity, especially water, are well-known to impair the pairwise interactions of the hydrogen-bonded arrays, the unbinding of the UPy dimers was also quantified in an aqueous environment, and the cooperative effect of hydrophobic interactions was evaluated by adding different lengths of alkylene spacers beside the UPy group (Figure 7a).[164] It was confirmed that the rupture forces measured in water were much lower than that detected in nonpolar environments but could be enhanced with the increased length of the hydrophobic spacers. When the number of carbon atoms of the alkylene spacer increased from 3 to 12, the unbinding energy barrier was improved from 21 to 34 kJ/mol in water, but still lower than ∼50 kJ/mol determined in nonpolar solvents. Chung et al. designed a polymer containing several UPy dimers with a double closed loop architecture, thus enabling cyclic detection of both unfolding and refolding processes by pulling and retraction.[165] As presented in Figure 7b, sawtooth patterns appeared on both extension and retraction force curves with a significant hysteresis, correlated to the large energy dissipation of the bulk material. The energies associated with the unbinding and rejoining events could be calculated based on the rupture and rejoining forces, yielding an asymmetric energy diagram with a short pathway (0.2 nm) toward rupture and a broad pathway (1.2 nm) toward redimerization, with an equilibrium free energy of 58 kJ/mol (in toluene). Besides the detection of isolated dimers, the stretching of single-chain polymeric nanoparticles assembled via a series of hydrogen-bonding units (UPy or benzene-1,3,5-tricarboxyamide (BTA)) was also realized. In this way, not only the dimerization energy of UPy could be measured (44 kJ/mol) but also the stacking energy of BTA was obtained (36 kJ/mol) in a cooperative fashion.[166] The Hamilton receptor (HR) is a hydrogen-bonding motif employed in molecular recognition that can bind barbiturates/cyanurates via six hydrogen bonds.[167] The rupture force of HR−barbituric acid was determined to be 172 pN by AFM-SMFS in tetrahydrofuran, but the force for the dissociation of HR−cyanuric acid in water was only 17 pN measured by OT and decreased by 1−2 pN when one of the hydrogen-bonding sites were blocked. The discrepancy arose from the differences in pulling rates, geometries, and solvents.[168,169] Besides the coordination ability to metals, the catechol group is also capable of forming hydrogen bonds with diverse hydrophilic surfaces. When catechol-functionalized acrylic polymers were immersed in metal-free water, metal-chelating was inhibited and the underwater adhesion of the polymer films was dominated by hydrogen bonding. By subtracting the adhesion force of fully oxidized quinone surfaces (100 mN) from that of unoxidized catechol surfaces (700 mN), the adhesion contributed by pure hydrogen bonding was calculated to be 600 mN in SFA measurements.[170]

Besides intermolecular recognition, intramolecular hydrogen bonding was also detected mainly by investigating the elasticity of single-polymer chains. In poly(vinyl alcohol) (PVA), the intramolecular hydrogen bonds between adjacent hydroxyl groups led to a remarkable deviation of the force−extension curve from that of polyethylene, and the long plateau was attributed to the additional energy consumed by the spatial geometry change of the hydroxyl groups.[171] In a vacuum, the average energy of hydrogen bonding increased with the degree of alcoholysis (DA), which was determined to be 4.75, 3.46, and 2.87 kJ/mol for PVA with DA of 99%, 88%, and 80%, respectively, suggesting the synergistic enhancement between the intramolecular hydrogen bonds. Similarly, the intramolecular hydrogen bonds of poly(*N*-isopropylacrylamide) (PNIPAm) were examined, yielding binding energy of 3.72

https://doi.org/10.1021/acs.chemrev.2c00215
Chem. Rev. XXXX, XXX, XXX−XXX

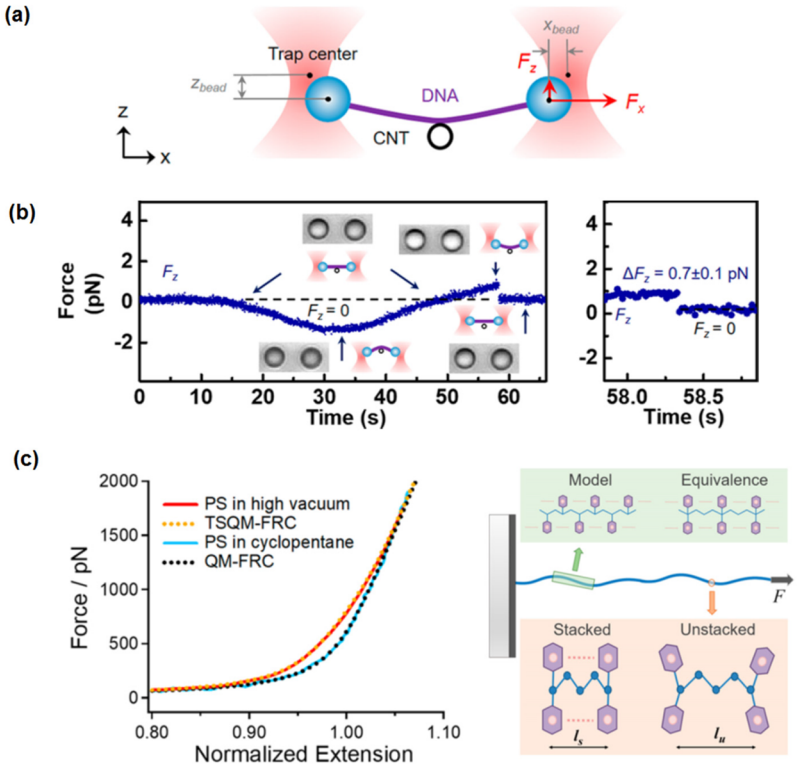

Figure 8. (a) Schematic of a suspended CNT transistor combined with dual-trap optical tweezers and (b) force applied to the right bead in the z direction during DNA approaching to and retracting from the CNT surface. Reproduced with permission from ref 184. Copyright 2018 American Chemical Society. (c) Typical force−extension curves of PS obtained in high vacuum and cyclopentane, and the schematic of the $\pi-\pi$ stacking transition under an external force. Reproduced with permission from ref 185. Copyright 2019 American Chemical Society.

kJ/mol in a vacuum, which rapidly dropped to 1.76 kJ/mol in a nonpolar solvent (nonane) and could not be determined in polar solvents.[172] A polyamide (PA) can form crystal structures with hydrogen-bonded networks, where the intramolecular bonding structures were revealed by detecting the stick−slip motion in PA66 and PA6 single crystals.[173] As presented in Figure 7c, the average gap between the sawtooth peaks of PA66 was 1.71 nm, close to the contour length of a repeat unit (1.72 nm), confirming the break and reformation of hydrogen bonds with the shift of one repeat unit. For PA6, the distance between the peaks showed two major distributions (0.87 and 1.70 nm), corresponding to the length of one and two repeat units. It was evident that the direct shift of two repeat units could result in the formation of a new hydrogen-bonding network; however, when the polymer chain shifted only by one repeat unit, it was capable of rotating 180° to reconstruct the multiple hydrogen bonds.

2.4. π Interactions

2.4.1. $\pi-\pi$ Interactions. The $\pi-\pi$ interactions denote the attraction between neutral and closed-shell aromatic rings, which are prominent in aromatic systems and contribute to the stabilization of DNA/protein structures, molecular recognition in self-assemblies, and molecular packing in crystals.[174,175] The geometries of the $\pi-\pi$ interactions can be roughly classified into three categories: edge-to-face/T-shaped, parallel-displaced, and parallel-stacked. Normally, a benzene-type molecule possesses a quadrupole moment with a negative potential above both sides of the ring and a positive potential around the peripheral atoms. When such two molecules interact with each other, they tend to adopt T-shaped or parallel-displaced configurations. If an aromatic ring is attached with atoms/groups with high electronegativity, the electron cloud above the ring will be withdrawn to the periphery, resulting in a reversal of the quadrupole moment, and the parallel-stacked configuration is preferred when the electron-deficient aromatic ring interacts with an electron-rich aromatic ring, which is known as $\pi-\pi$ stacking.[176] Although the physical origins of $\pi-\pi$ interactions have been revealed by numerous computational studies and their bonding strengths were evaluated by some experimental approaches based on the averaging of ensemble data,[177,178] the direct nanomechanical studies of $\pi-\pi$ interactions are relatively limited, possibly because this type of interaction usually works synergistically with other interactions (e.g., hydrogen bonding, hydrophobic interactions, electrostatic interactions) and is easily affected by environmental disturbance.

Zhang et al. probed the $\pi-\pi$ interaction between a pyrene molecule and graphite surface in water, yielding an unbinding force of ∼55 pN without loading rate dependence and an estimated unbinding energy of ∼26 kJ/mol.[179] The molecular interactions between a cationic aromatic dye (methylene blue) and graphene oxide (GO) were also investigated, indicating that although the attraction was dominated by electrostatic interactions at a neutral pH, $\pi-\pi$ interactions played a vital role in acidic conditions. The methylene blue molecules could adsorb on the GO surface via both parallel-stacked and T-shaped configurations.[180] By peeling single-stranded DNA (i.e., polycytosine, polythymine, polyademine, polyguanine) from single-crystal graphite, Vezenov and co-workers quantified the $\pi-\pi$ interactions of DNA bases with a flat graphite surface, where the characteristic plateaus represented the peeling of the homopolymer from the surface and the abrupt jumps denoted the complete detachment of one or more polymer chains. The estimated average binding energy per nucleotide of the four

https://doi.org/10.1021/acs.chemrev.2c00215
Chem. Rev. XXXX, XXX, XXX−XXX

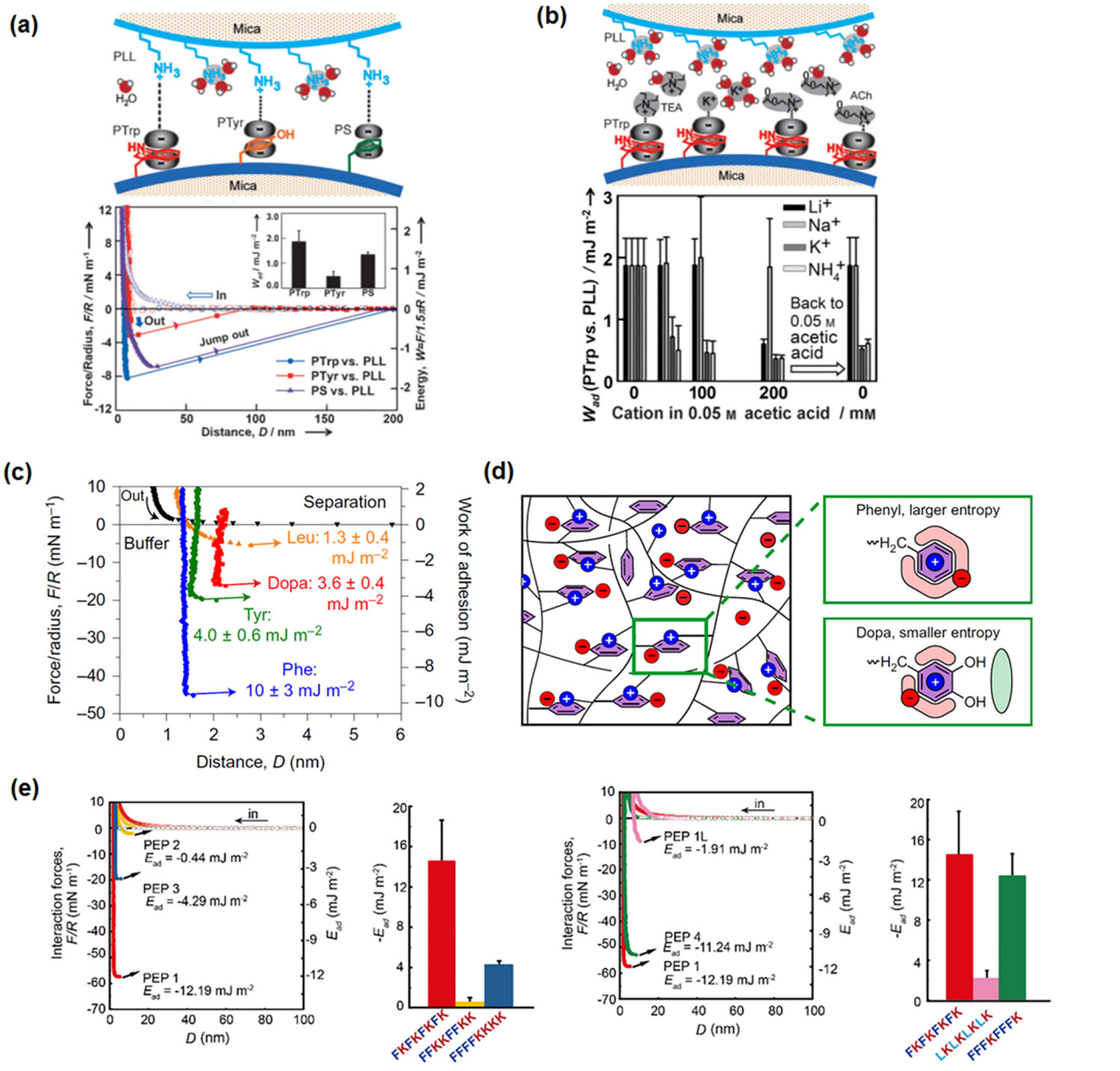

Figure 9. (a) Schematics of cation−π interactions and typical force−distance curves with corresponding interaction energies between PLL and different aromatic polymers (PTrp, PT yr, and PS). (b) Schematics of the hydrated cation effects and the energy changes between PLL and PTrp films with the addition of different cations. Reproduced with permission from ref 190. Copyright 2013 John Wiley & Sons. (c) Representative force−distance curves and the corresponding work of cohesion of symmetric films coated with different lysine- and aromatic-rich peptides. (d) Schematics of the anion complexation with positive cation−π binding pairs in lysine- and aromatic-rich peptides films. Reproduced with permission from ref 191. Copyright 2017 Springer Nature. (e) Typical force−distance profiles and corresponding adhesion energies of symmetric peptide films with different sequences of amino acids (lysine and Phe). Reproduced with permission from ref 196. Copyright 2021 American Chemical Society.

bases followed the order of T > A > G > C (11.3, 9.9, 8.3, and 7.5 k_BT, respectively), which did not scale with the size of the bases and was likely because of the different conformations of the DNA backbones on graphite.[181,182] However, the binding strengths of these DNA strands to single-walled carbon nanotubes (SWCNTs) showed a different ranking of A > G > T > C, with corresponding binding energies of 38.1, 33.9, 23.3, and 17.1 k_BT, respectively. Compared to that with flat graphite, the enhanced interactions of DNA bases with curved SWCNTs were attributed to the spontaneous curvature of DNA, which led to preferred binding to curved surfaces.[183] To obtain direct force measurements between two individual aromatic rings in the near-equilibrium regime, a CNT force sensor was designed by combining a suspended CNT with dual-trap OT.[184] As illustrated in Figure 8a, a DNA molecule was tethered between two polystyrene beads, whose movement was controlled by the dual-trap OT in the perpendicular direction to the CNT, and the forces along both the x and z directions were recorded. When the DNA tether was pushed down toward the CNT, the force in the z direction started to increase negatively after the contact and then decrease during the following lifting up of DNA. By further pulling the DNA tether up from the CNT, the force gradually increased in the positive z direction and finally exhibited a sudden drop, suggesting a complete detachment of DNA from the CNT surface (Figure 8b). The detected unbinding forces were distributed into three groups: 1.2, 3.3,

https://doi.org/10.1021/acs.chemrev.2c00215
Chem. Rev. XXXX, XXX, XXX−XXX

and 4.8 pN, which corresponded to the binding of 1 to 3 nitrogenous bases to the hexagonal CNT sidewall, and the binding free energy between a single base and CNT was estimated to be 13.1 k_BT.

Besides the $\pi-\pi$ interactions occurring on graphitic surfaces, the intrachain $\pi-\pi$ stacking in a single polystyrene (PS) crystal was studied.[185] It was found that in a high vacuum, the force curve of PS during stretching strongly deviated from that in cyclopentane (i.e., freely rotating chain) because of the $\pi-\pi$ stacking formed among every-other phenyl groups (E-type) (Figure 8c). In a free-state PS crystal, 91% of the phenyl groups participated in this type of configuration. Upon stretching, the geometry of phenyl groups would experience a transition from the E-type to an adjacent (A-type) stacking state, leaving only 4% of E-type stacking at an external force of 1600 pN. By fitting the force curve, the strength of each E-type stacking was estimated to be 2.9 kJ/mol, which was much lower than that for a benzene dimer, attributed to the longer center-of-mass distance between the stacked phenyl groups.

2.4.2. Cation$-\pi$ Interactions. The term "cation$-\pi$ interaction" was proposed by Dougherty to describe the noncovalent attraction occurring between the face of an electron-rich π system (e.g., benzene, phenol, indole, imidazole) and the adjacent cations (e.g., Li^+, Na^+, K^+, NH_4^+) or molecules carrying positive charges (e.g., lysine, arginine, histidine).[186] The association between an ion and an electric quadruple was primarily governed by electrostatic interactions, while inductive interactions contributed to the attraction of ions to large and polarizable π systems.[187] Therefore, the strength of cation$-\pi$ interactions has been demonstrated to exceed other aromatic interactions (e.g., $\pi-\pi$ interactions), and the binding energies in the gas phase could be rationalized by an electrostatic model. Normally, stronger cation$-\pi$ interactions were expected from aromatic species with higher negative electrostatic potentials (contributed by electron-donating substituents) and cations with smaller sizes and larger charge densities. For example, the association free energies of the alkali metals with benzene in the gas phase decreased in the order of $Li^+ > Na^+ > K^+$.[188] However, in aqueous solutions, this order was found to be inversed and followed the trend of $K^+ > Na^+ > Li^+$, which was in good accordance with the Hofmeister series. It suggested that the degree of cation hydration played an important role in the cation$-\pi$ interactions in aqueous media. As larger monovalent cations tended to possess more fragile hydration shells, they could overcome the screening effect of the hydration shell more easily and bind closely to the hydrophobic π-species.[189]

The first nanomechanical characterization of cation$-\pi$ interactions in an aqueous environment was conducted by Zeng and co-workers using an SFA, building a model system to elucidate the impact of different cations and aromatic residues.[190] As presented in Figure 9a, cationic PLL bearing positively charged NH_3R^+ moieties was deposited on one mica surface, and the other mica surface was coated with one of the three aromatic polymers: poly L-tryptophan (PTrp), poly L-tyrosine (PTyr), and polystyrene (PS), providing aromatic side groups of indole, phenol, and benzene, respectively. The adhesion energies between PLL and the three aromatic polymers followed the order of PTrp > PS > PTyr (1.8, 1.3, and 0.5 mJ/m^2, respectively), generally consistent with the quadrupole moments of the π systems (indole > benzene ≈ phenol). The interactions between different monovalent cations (i.e., Li^+, Na^+, K^+, NH_4^+, NH_3R^+) and indole were subsequently investigated by injecting the cations between PLL and PTrp surfaces (Figure 9b), where the affinity trend of the hydrated cations to PTrp was measured to be $Li^+ < Na^+ < K^+ < NH_4^+ < NH_3R^+$, indicating that the monovalent cation$-\pi$ interactions in aqueous media were dominated by the hydration degree of the cations rather than the cation charge density. Later, the underwater cohesion of three types of lysine- and aromatic-rich peptides were quantitively investigated, with an increased hydroxylation degree of the aromatic side groups, namely phenylalanine (Phe), tyrosine (Tyr), and DOPA.[191] Figure 9c indicates that all three peptides exhibited strong cohesion mediated by cation$-\pi$ interactions, with measured adhesion energies of 10.0, 4.0, and 3.6 mJ/m^2, respectively, which was comparable to or even stronger than the metal coordination-mediated adhesion of mussel-mimic proteins. It should be noted that the energy of the cation$-\pi$ complexation was pronouncedly weakened by the hydroxylation of the aromatic residues, contradictory to the calculations of binary cation$-\pi$ systems, therefore, a ternary cation$-\pi-$anion interaction model was proposed, where anions were required to complex with the positive cation$-\pi$ pairs to avoid the strong repulsion between each pair and stabilize the whole system (Figure 9d). Because of the presence of the electronegative hydroxyl groups, the number of anion-favored binding sites (pink area) was reduced, leading to a decreased configurational entropy within the films and thus the reduced cohesion energy. Ternary $\pi-$cation$-\pi$ interactions were experimentally confirmed by detecting the assembly behaviors and cohesion forces of π-conjugated poly(catechol) coatings with the coexistence of K^+.[192] It was found that in the absence of K^+, the poly(catechol) coating formed by in situ polymerization of catechol was quite smooth, with a surface roughness of 0.32 nm and a cohesion energy of 0.14 mJ/m^2, while the gradual increase of the K^+ concentration (from 10 to 250 mM) could correspondingly result in larger aggregates of poly(catechol) and enhance the adhesion between the symmetric coatings (surface roughness of 3.32 nm and adhesion energy of 4.98 mJ/m^2 with 250 mM K^+). These phenomena were ascribed to the formation of ternary $\pi-K^+-\pi$ complexes as binary $K^+-\pi$ interactions could not contribute to the cohesion between the two films. However, a further increase of K^+ concentration (600 mM) would induce a transition of the binding mode from ternary complexes to binary pairs, undermining the adhesion because of the lack of bridging.

Mussel foot proteins provide excellent platforms for the study of cation$-\pi$ interactions as most of them are rich in cationic (e.g., lysine) and aromatic (e.g., Trp, Tyr, DOPA) amino acids. Although the underwater adhesion of mussel foot proteins was transitionally attributed to DOPA-mediated interactions (e.g., covalent bonds, metal coordination, hydrogen bonding), cation$-\pi$ interactions were proved to play a dominant role in DOPA-deficient foot proteins. For example, for the Trp-rich mussel foot protein from *Perna viridis* (pvfp-1), the adhesion energy between the two symmetric films could be >2.3 mJ/m^2, and for a Tyr-containing recombinant *Mytilus* foot protein (rmfp-1), the symmetric adhesion was measured to be 2.9 mJ/m^2. In both cases, the adhesion strength decreased with the increase of K^+ concentration, demonstrating K^+ could effectively compete with the lysine$-\pi$ interactions in the proteins.[193,194] Recently, the antisynergitic effect of amine-catechol pairs on underwater cation$-\pi$ interactions was reported in a series of mussel-mimic model peptides.[195] It was found that when the aromatic group (i.e., DOPA, Phe, Tyr) and the cationic lysine were separated by a linker of two glycine moieties, the cohesion of the protein films would be significantly enhanced compared

https://doi.org/10.1021/acs.chemrev.2c00215
Chem. Rev. XXXX, XXX, XXX−XXX

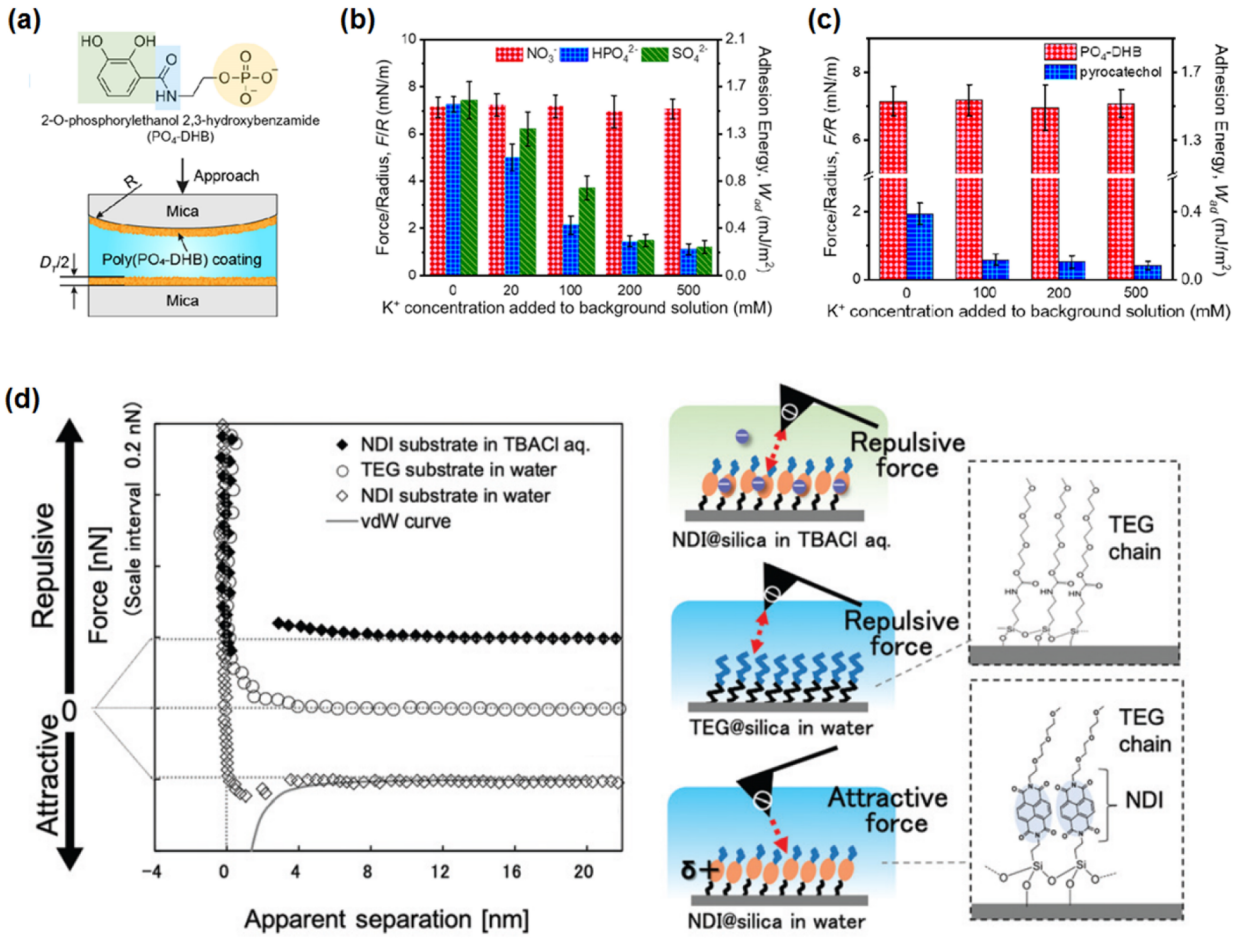

Figure 10. (a) Molecular structure of PO_4-DHB and the schematic of SFA measurement with two opposing poly(PO_4-DHB) films. (b) Adhesion changes between poly(PO_4-DHB) films with the addition of different anions and (c) adhesion changes between poly(PO_4-DHB)/poly(pyrocatechol) films with increased K^+ concentration. Reproduced with permission from ref 201. Copyright 2020 American Chemical Society. (d) Typical force curves of TEG or NDI-modified substrates interacting with a negatively charged AFM probe in aqueous solutions. Reproduced with permission from ref 202. Copyright 2021 The Royal Society of Chemistry.

to that of proteins with flanking lysine and aromatic residues. Combining the results with Raman spectra, the authors proposed that in a flanked protein, the positively charged lysine was located near the aromatic ring, thus undermining the association of this pair with another lysine group (intermolecular interaction) because of the relatively strong electrostatic repulsion between the amines. The sequence-dependent adhesive properties were also probed in another class of engineered short peptides.[196] As shown in Figure 9e, peptides PEP 1−3 possessed identical lengths and compositions, which only differed in the sequence of lysine (K) and Phe (F). PEP 1 consisting of alternating K and F residues exhibited the strongest adhesion energy of 14.5 mJ/m^2, while the adhesion energies of PEP 2 and 3 composed of blocks of more than one F or K groups were only 0.5 and 4.2 mJ/m^2, respectively. As the decrease of the number of K residues (PEP 4) did not lead to an obvious change of the adhesion, it was suggested that the strength of cation−π interactions was mainly dependent on the binding efficiency of the lysine groups, which was affected by the surrounding Phe. When positively charged lysine was isolated and flanked by hydrophobic Phe, the binding of water molecules to the cationic amine would be impeded, resulting in a more labile hydration shell to favor intermolecular interactions.

2.4.3. Anion−π Interactions. In addition to the well-known $\pi-\pi$ and cation−π interactions, attractive interactions between anions and aromatic molecules were recently recognized by theoretical calculations, occurring between negatively charged species and electron-deficient heteroaromatic rings.[197,198] As counterparts to cation−π interactions, anion−π interactions are also governed by electrostatic interactions and ion-induced polarization, but with relatively smooth potential energy surfaces. Therefore, the anions are not only located above the ring centroid but also can reside in the same plane or over the periphery of the aromatic ring.[199] Compared to cation−π interactions, the prediction of the strength of anion−π interactions is more complicated because of the large variety of polyatomic anions, whose charge density, size, shape, geometry, polarity, and hydration state can contribute to the stability of anion−π complexes.[200] As a newly proposed interaction, only a few studies provide experimental identification of anion−π interactions. Zeng and co-workers quantitively probed the anion−π interactions in a bioadhesive-mimic compound 2-O-phosphorylethanol 2,3-hydroxybenzamide (PO_4-DHB), which consisted of an anionic phosphate ester and a π-conjugated catechol moiety (Figure 10a).[201] In saline buffer solutions (pH 8.4), the PO_4-DHB was polymerized into poly(PO_4-DHB) coatings on the mica surfaces

https://doi.org/10.1021/acs.chemrev.2c00215
Chem. Rev. XXXX, XXX, XXX−XXX

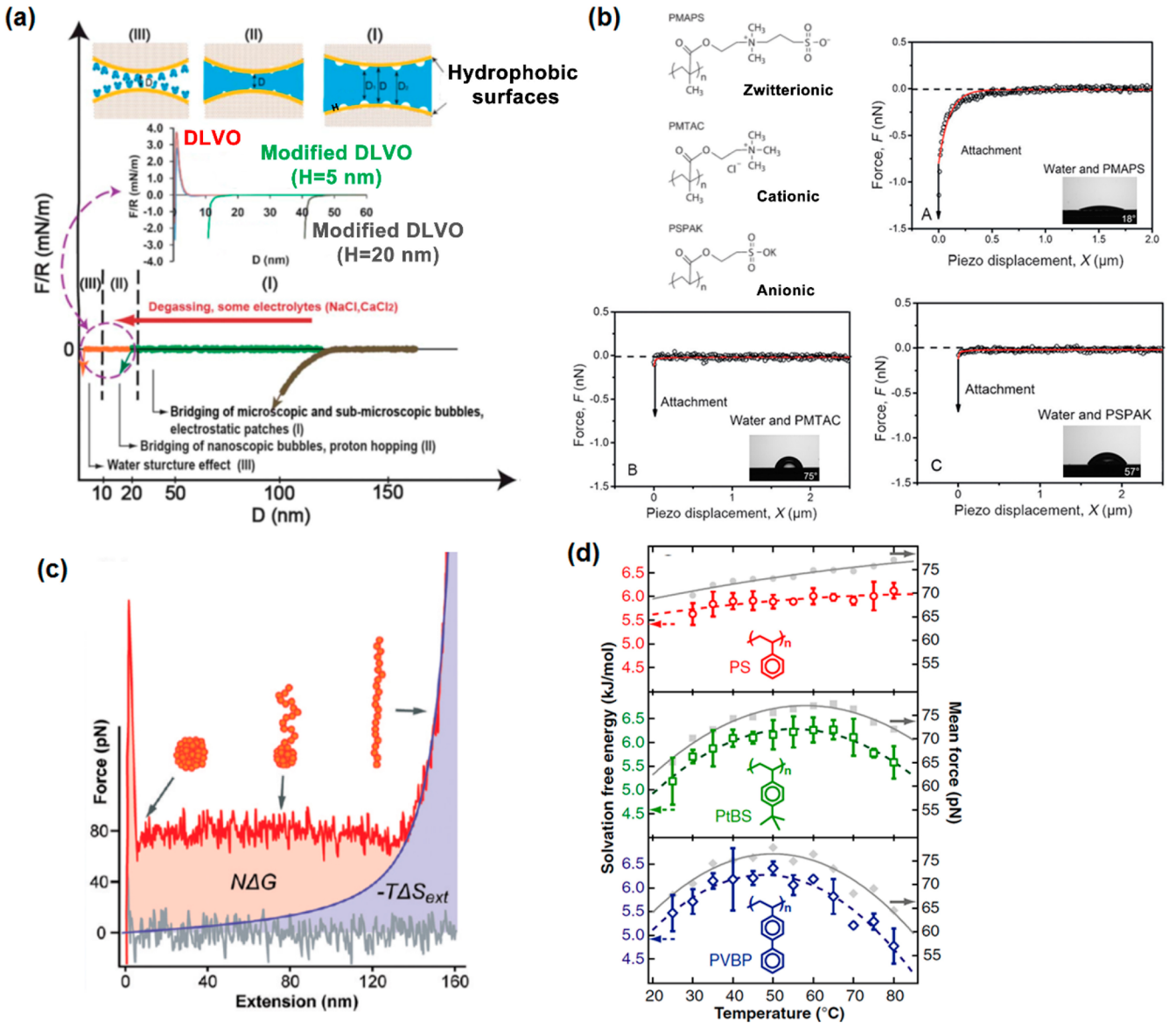

Figure 11. (a) Proposed three-regime hydrophobic interaction model with DLVO and modified DLVO force profiles for two PS surfaces interacting in 100 mM electrolyte. Reproduced with permission from ref 208. Copyright 2012 The Royal Society of Chemistry. (b) Molecular structures of zwitterionic PMAPS, cationic PMTAC, anionic PSPAK and their interactions with a water droplet as well as water contact angles in toluene. Reproduced with permission from ref 212. Copyright 2016 John Wiley & Sons. (c) Typical force−extension curve of a collapsed PS nanosphere in water showing a force plateau followed by entropic elastic stretching. (d) Temperature dependencies of the plateau force and hydration free energy per monomer in PS, PtBS, and PVBP. Reproduced with permission from ref 214. Copyright 2011 National Academy of Sciences.

in an SFA, and the adhesion energy between the symmetric coatings was measured to be ∼1.5 mJ/m^2 after 1 h of deposition. Inhibition experiments were conducted using NO_3^-, HPO_4^{2-}, and SO_4^{2-} as competing anions to phosphate ester in the solution (Figure 10b), and the affinity of these anions to the catecholic groups was found to obey the order of phosphate ester > HPO_4^{2-} > SO_4^{2-} > NO_3^-. As the attractive force between the electron-rich aromatic moieties and anions were expected to be weak, the robust adhesion detected in this system was ascribed to the enhanced anion−π interactions because of the presence of cations on the other side of the π system, where stronger cation−π interactions led to higher stability of the anion−π complexes. Compared to poly(pyrocatechol) coatings that only allowed the formation of cation−π pairs, the bridging effect of anion−π interactions in poly(PO_4-DHB) coating resulted in its strong adhesion with cation concentration insensitivity (Figure 10c), postulated to contribute to wet adhesion of marine organisms. Akamatzu et al. prepared a surface modified with an electron-deficient aromatic molecule naphthalenediimide (NDI) and examined its interactions with a negatively charged AFM probe.[202] As illustrated in Figure 10d, in pure water, only repulsive forces were detected on the substrate modified with hydrophilic triethylene glycol (TEG) groups, while the surface functionalized with NDI molecules exhibited an attraction of ∼0.1 nN at a separation of 3−4 nm, owning to anion−π interactions. The introduction of halide anions could suppress the attraction to some extent because of the competing effect, with an inhibition trend of Cl^- > Br^- > I^-. According to the peak periodicity of the attractive force

https://doi.org/10.1021/acs.chemrev.2c00215
Chem. Rev. XXXX, XXX, XXX−XXX

distribution, the interaction of a single anion−π pair was speculated to be ∼40 nN.

2.5. Hydrophobic Interactions

The term hydrophobic interactions or hydrophobic effects is commonly used to describe the strong attraction (beyond the expected van der Waals interactions) between nonpolar molecules in aqueous environments, resulting in aggregates or clusters of such hydrophobic moieties with rearranged structures of the surrounding water molecules. Because a large number of natural and synthetic polymers bear abundant nonpolar moieties, hydrophobic interactions have been proved to play prominent roles in a variety of biological phenomena and engineering processes associated with aqueous solution interfaces, including the folding of protein segments, the association of proteins and small molecules, the self-assembly of micelles/vesicles/membranes, the adsorption of molecules/particles on surfaces, etc.[71,203] Although the exact physical mechanism of intrinsic hydrophobic interactions has not been fully revealed, it is well-accepted that the association of hydrophobic solutes in water is entropy-dominated.[3,204] When a nonpolar molecule without a hydrogen-bonding capability is introduced into water, the original hydrogen-bonding network of the interfacial water molecules will be disrupted and lead to a rearrangement of these water molecules into an ordered hydration shell. As the entropy loss accompanied by the restricted mobility of water molecules is thermodynamically unfavorable, the nonpolar molecules tend to aggregate together to minimize the hydrophobic surface area exposed to water, lowering the solvation free energy of the system. For interactions between two hydrophobic surfaces, the situation is more complicated because of the interference from some "pseudo-hydrophobic interactions", such as bridging of microscopic or nanoscopic bubbles and electrostatic interactions resulting from the charge fluctuations on surfaces.[205,206] The accurate quantification of hydrophobic interactions at the nano and molecular scale is critical to establish an understanding of the nature of hydrophobic interactions in many interfacial, colloidal, and biophysical pathways.

2.5.1. Hydrophobic Interactions between Polymer Surfaces. The early nanomechanical studies on interfacial hydrophobic interactions were generally conducted between two surfaces that were hydrophobized via physical adsorption of surfactant molecules, suggesting an exponential decay of hydrophobic force with surface separation.[207] Despite the ease of preparation, these self-assembled monolayers could be susceptible to solution conditions (e.g., temperature, salinity) and bring difficulties to data interpretation. Therefore, stable hydrophobic surfaces prepared with inherent hydrophobic polymers provide an alternative approach to the investigation of hydrophobic interactions. By directly measuring the interactions between two physically adsorbed PS surfaces in electrolyte solutions, Faghihnejad and Zeng revealed the important role of the dissolved gas in the interfacial interactions and proposed a three-regime interaction model (Figure 11a).[208] Above a separation distance of ∼20 nm, the attraction was mainly caused by the capillary briding because of the coalescence of microscopic and submicroscopic bubbles or electrostatic interactions, while the attractive force detected in the intermediate regime (∼10 to 20 nm) was ascribed to the briding of nanobubbles or possibly enhanced proton hopping in water, where spontaneous cavitation of water was observed even in degassed solutions. Within a few nanometers of separation, the interaction was considered to be related to the water structure changes near the surface. The following study on the interactions between an air bubble and a PS surface also confirmed the existence of interfacial nanobubbles in solutions of low and intermedium salinity (≤100 mM NaCl), which could stabilize the confined thin water film and lead to non-DLVO repulsion but were greatly suppressed at high salinity (≥500 mM NaCl).[209] When hydrophobic polymers were bonded to substrates via chemical reactions, stable and smooth hydrophobic surfaces could be obtained, and the effect of pre-existing nanobubbles could be eliminated in some systems. By characterizing the interactions between poly(dimethylsioxane) (PDMS) surfaces in water, a general interaction potential of the hydrophobic interactions was established, where the interaction energy exponentially decayed with a decay length (a key parameter relating to the range of hydrophobic interactions) of 0.3−2 nm, providing a quantitative description of the attraction between hydrophobic polymer films in addition to the classical DLVO theory.[210] In this study, the hydrophobic interactions were speculated to be originated from the density depletion forces, water molecule orientation, and hydrogen-bonding corrections, which could be weakened with the introduction of amphiphilic solvents (e.g., tetrahydrofuran). Although surface hydrophobicity has been traditionally postulated to dominate the hydrophobic interactions (i.e., hydrophobic force range monotonically increases with surface hydrophobicity), by modulating the nanoscale structure and chemistry of the surface, Cui et al. discovered that surfaces with similar hydrophobicity could exhibit distinctly different ranges of hydrophobic interactions with an air bubble, while surfaces with different hydrophobicities could possess a similar range of hydrophobic interactions.[209] It suggested that the water structuring effect (directly related to hydrophobic interactions) was highly dependent on the heterogeneity of the surface nanoscale structure and chemistry, which was facilitated on a crystalline-like surface (low heterogeneity) and weakened on an amorphous or liquid surface (high heterogeneity). The impact of surface chemical heterogeneity on hydrophobic interactions was also investigated by Ma et al., using an AFM to characterize how hydrophobic interactions between alkyl-functionalized surfaces changed with proximally immobilized cations.[211] It was found that when 40% of the terminal methyl groups on the substrate were replaced by ammonium, hydrophobic interactions could still be detected, and the strength was doubled (pull-off force increased from 0.8 to 1.9 nN) with the protonation of the amine groups (pH decreased from 10.5 to 7). However, further turning ammonium into guanidinium would diminish the hydrophobic interaction below the detectable range of the instrument, indicating that the effect of the cationic groups on the solvation shells of the neighboring (∼1 nm) nonpolar domains was ion-specific. It is worth noting that resembling hydrophobic interactions, long-range hydrophilic interactions were reported between water droplets and hydrophilic polyelectrolyte surfaces in a nonpolar media.[212] As shown in Figure 11b, when a water droplet approached one of the three types of polyelectrolyte surfaces (i.e., zwitterionic poly(3-[dimethyl(2-methacryloyloxyethyl) ammonium] propanesulfonate) (PMAPS), cationic poly(2-(methacryloyloxy)-ethyl trimethylammonium chloride) (PMTAC), and anionic poly(3-sulfopropyl acrylate potassium) (PSPAK)) in toluene, a strong attraction could be detected before the final water attachment on the surface. The strongest attraction was measured on zwitterionic PMAPS with a force range up to 1

https://doi.org/10.1021/acs.chemrev.2c00215
Chem. Rev. XXXX, XXX, XXX−XXX

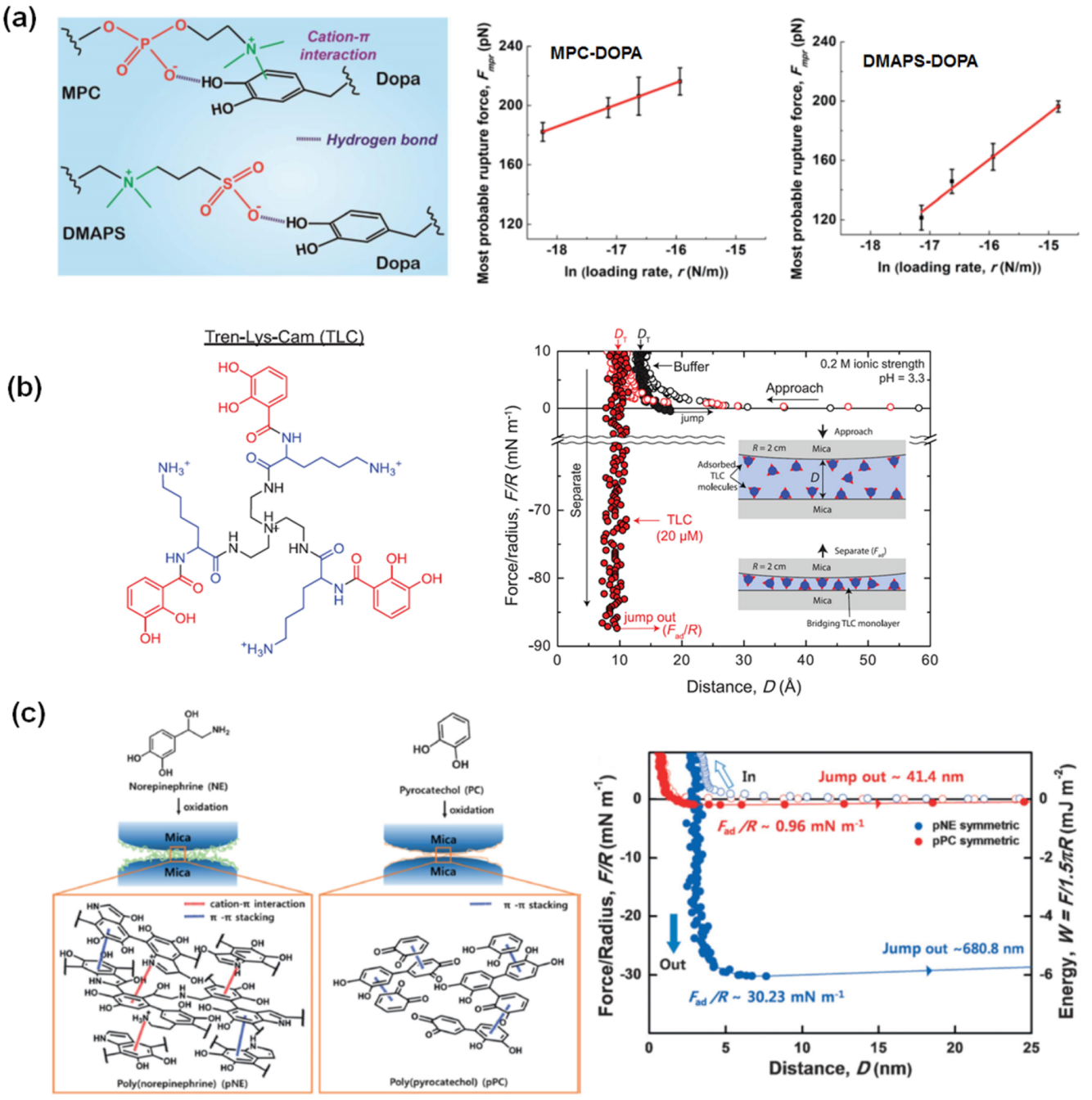

Figure 12. (a) Binding mechanisms of MPC−DOPA and DMAPS−DOPA interactions and the corresponding loading rate dependence of the most probable rupture forces. Reproduced with permission from ref 221. Copyright 2019 The Royal Society of Chemistry. (b) Structure of a siderophore analog TLC and the typical force−distance curves between two mica surfaces with or without the TLC-mediated adhesion. Reproduced with permission from ref 222. Copyright 2015 American Association for the Advancement of Science. (c) Schematic illustrations of the interaction mechanisms and typical force−distance curves of symmetric poly(catecholamine) and poly(catechol) films. Reproduced with permission from ref 225. Copyright 2018 John Wiley & Sons.

μm while the cationic PMTAC and anionic PSPAK exhibited weaker attractions to the water droplet within 200 nm. The strength of the attractive force directly correlated to the hydrophilicity of the polymers (the water contact angles of PMAPS, PMTA, and PSPAK in toluene were 18°, 75°, and 57°, respectively) and was ascribed to the dipolar interactions induced by the large dipole moment of polyelectrolytes.

2.5.2. Hydrophobic Interactions within Single Polymers. From the thermodynamic point of view, the free energy of a hydrophobic interaction is the change of the hydration free energy of the system before and after the interaction. Therefore, to elucidate the hydrophobic interactions within polymers at the molecular scale, Li and Walker performed SMFS studies on the hydration behaviors of single PS chains in aqueous solutions, which collapsed into nanospheres because of the hydrophobic interactions between the nonpolar side groups.[213] When the PS chain was stretched from the collapsed state to the extended state in water, a force plateau region of ~80 pN appeared before

https://doi.org/10.1021/acs.chemrev.2c00215
Chem. Rev. XXXX, XXX, XXX−XXX

the entropic elastic region, corresponding to the energy required to hydrate the exposed monomers along the polymer chain (Figure 11c). The force measurements were conducted in a series of water−ethanol and water−salt mixtures, and by excluding the entropic contribution from the stretching of a freely jointed chain, the solvation free energy per monomer could be estimated, showing a linear dependence on the interfacial energy between PS and the solvent. In the following study, the authors revealed that although the solvation free energy of PS could be evaluated by the macroscopic interfacial energy, the hydration behavior of the stretched polymer was not controlled by interfacial thermodynamics (hydration free energy scales with the solvent-accessible surface area) but resembled those of small molecules (hydration free energy scales with the volume of the molecule).[214] As shown in Figure 11d, the hydration free energies of three different types of hydrophobic polymers (i.e., PS, poly(4-*tert*-butylstyrene) (PtBS), and poly(4-vinylbiphenyl) (PVBP)) were thoroughly examined, strongly dependent on both temperature and the size of the monomer, which were signatures for the hydrophobic hydration of small molecules (<1 nm). The overall hydration free energy per monomer within a polymer chain was ∼6 kJ/mol, much lower than that of free monomers (20−30 kJ/mol), because strong hydrophobic interactions still existed between the neighboring side groups even in a stretched polymer chain. The hydration free energies of the collapsed PS nanospheres were also evaluated, showing a cubic dependence of the radius when the particle is less than ∼1 nm and turning to a square dependence for larger paritlces.[215] By investigating the single-chain mechanics of nature cellulose (NC) in different solvents, it was found that although the insolubility of NC in water was conventionally postulated to result from the dense hydrogen-bonding network, hydrophobic interactions should also play a vital role.[216] In nonpolar octane, a single NC behaved like a freely jointed chain, while it adopted a globule conformation in water and showed a long force plateau during stretching (∼85 pN at 20 °C and increased monotonically with the increase of temperatue), similar to the stretching collapsed PS spheres. This hydration behavior was ascribed to hydrophobic effect as well as the crystallization of the molecule.

2.6. Cooperative Interactions

As a variety of polymers and biomacromolecules contain more than one type of motif that can noncovalently interact with other objects and the complex structures of many interacting groups allow the coexistence of different types of noncovalent interactions, cooperativity or anticooperativity can arise among these noncovalent interactions, which strongly impacts the binding strength and plays a critical role in controlling the structure and function of the resultant complexes. Mussel-inspired chemistry and host−guest complexation are typical systems involving the cooperative effect of different noncovalent interactions.

2.6.1. Mussel-Inspired Chemistry. The strong and wet adhesion of marine mussels to diverse substrates has been the subject of extensive scientific research over the last few decades. Since the first report by Waite and Tanzer,[217] DOPA has been recognized as the key component responsible for the versatile adhesion of mussel foot proteins (mfps), while other charged (e.g., lysine, histidine, phosphate) and hydrophobic (e.g., tyrosine, phenylalanine, leucine) residues also make a contribution.[17,218] Besides the mentioned metal coordination, cation−π, and anion−π interactions, DOPA also allows the presence of other noncovalent interactions when interacting with a variety of molecules and surfaces, including hydrogen bonding, $\pi-\pi$ interactions, and hydrophobic interactions, where the types of interactions depend on the features of the interacting objects. For example, DOPA can form bidentate coordination and hydrogen bonds to mineral and oxide surfaces, as well as hydrophobic interactions on some polymer surfaces.[219] The binding energies of a single DOPA moiety to a wide range of organic and inorganic surfaces were evaluated by SMFS, yielding a strong interaction to TiO_2 (29 k_BT) because of bidentate hydrogen bonding plus metal coordination, and medium-strong interactions within the range of 13−17 k_BT to OH, NH_2 and COOH-terminated surfaces arising from monodentate hydrogen bonding, and weak interactions (9 k_BT) to gold (charge transfer or polarizability of the π system) and alkyl-functionalized surfaces (hydrophobic interactions).[220] Although superhydrophilic zwitterionic groups are famous for their antifouling properties because of the tightly bound water molecules, Xie et al. reported that DOPA could effectively bind to zwitterions via cation−π interactions and/or hydrogen bonding, where the binding strength and mechanism was strongly dependent on the orientation of the dipole moment.[221] Figure 12a shows the rupture forces when pulling a single DOPA molecule from two types of zwitterionic surfaces (i.e., 2-methacryloyloxyethyl phosphorylcholine (MPC) and (methacryloyloxy)ethyl]dimethyl-(3-sulfopropyl) ammonium hydroxide (DMAPS)) at different loading rates, revealing that the interaction energy of DOPA with MPC (19.4 k_BT) is much stronger than that with DMAPS (10.8 k_BT). The difference was ascribed to the opposite dipole orientations of the two molecules, where the structure of MPC allowed the cooperativity of cation−π interactions (ammonium cation and aromatic ring) and hydrogen bonding (phosphate and catecholic −OH) when it interacted with DOPA, but only hydrogen bonding (sulfonate and catecholic −OH) could occur for DMAPS−DOPA binding.

In some mussel foot proteins (e.g., mfp-3 and mfp-5), DOPA and positively charged lysine residues are generally positioned adjacent to each other along the protein backbone, and the role of the close proximity was illuminated by an SFA using a siderophore and its analogs that contained paired catechol and lysine groups.[222] As presented in Figure 12b, when two bare mica surfaces were brought into contact in the buffer solution (50 mM acetate buffer and 150 mM KNO_3), an intervening compressed film with a thickness of 1.3 nm was detected along with neglectable adhesion, because of the formation of hydration layers on the interfaces. By injecting Tren-Lys-Cam (TLC) molecules into the solution, the compressed film thinned to 0.9 nm with a dramatic increase of the adhesion (∼15 mJ/m^2), suggesting a monolayer of TLC was generated by replacing the hydrated K^+ and acted as the bridge between the surfaces. Interestingly, the existence of either catechol or cationic ammonium alone could only result in very weak adhesion (<2 mJ/m^2), demonstrating a synergistic interplay between catechols and lysines, where cationic lysines effectively breached the hydrated salt layers on the mineral surfaces, thus facilitating the bidentate binding of catechol residues to the substrates. This cooperativity is not unique to amine cations, as enhanced adhesion was still detected by replacing lysines with arginines that bore guanidinium cations, but the catechol−cation synergy of guanidinium was less effective than that of ammonium.[223] Although it was originally postulated that the proximity of the paired catechol and cationic functionalities was critical for the

https://doi.org/10.1021/acs.chemrev.2c00215
Chem. Rev. XXXX, XXX, XXX−XXX

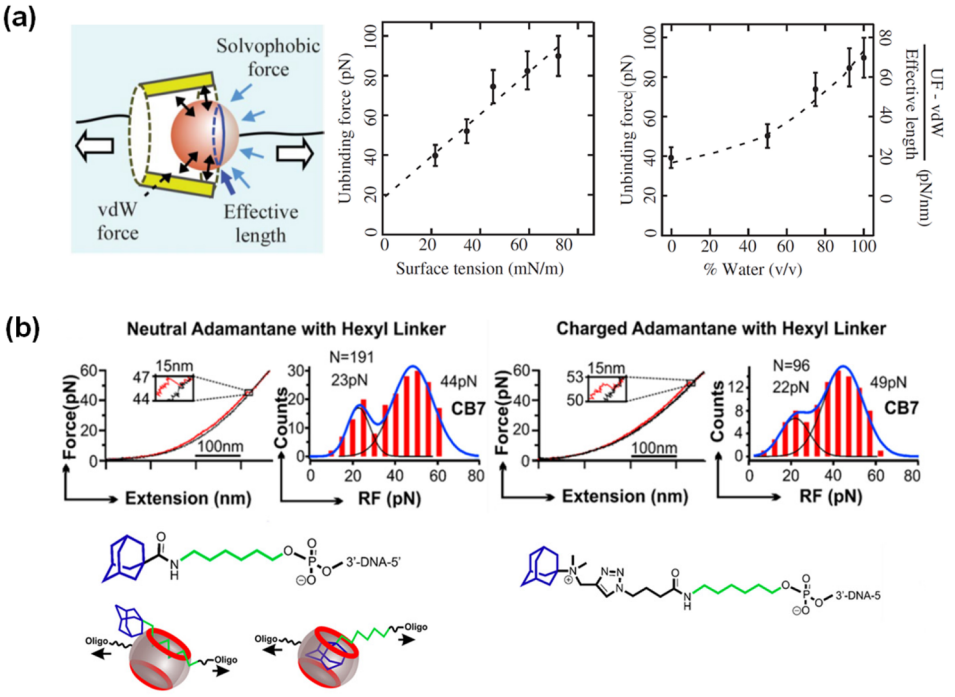

Figure 13. (a) Schematic illustration of the van der Waals and solvophobic forces during the unbinding of the β-CD/adamantane complex and the measured unbinding forces as a function of the surface tension or mixing ratio of solvents. Reproduced with permission from ref 230. Copyright 2006 American Physical Society. (b) Typical force−extension curves and histograms of rupture forces for the unbinding of CB[7]/neutral adamantane and CB[7]/charged adamantane pairs. Reproduced with permission from ref 234. Copyright 2019 American Chemical Society.

robust wet adhesion to other substrates, several studies unraveled that the adjacency of the cationic and aromatic residues was not necessary for their cooperative binding[32,193,194] and no cutoff distance existed between the moieties. By only increasing the intramolecular catechol−lysine spacing (the molecular weight remained constant) with the zero to two glycine residues, the adhesion force barely changed, however, if the increase of spacing was accompanied by increased molecular weight, the adhesion would be progressively reduced because of the lowered density of binding groups.[25] A series of adhesive polymers was prepared by copolymerizing catechol and lysine-rich monomers.[224] When catechol and amine groups were coupled together in the same monomer (i.e., in close proximity), the stretching of a single polymer exhibited a rupture force of 430 pN, and the separation work for the detachment of an AFM colloidal probe from the polymer-coated substrate was 9.72×10^{-16} J. When the catechol and amine functionalities were decoupled into different monomers (i.e., the functional groups were randomly distributed along the polymer backbone with different spacings), these corresponding values were only slightly decreased to 351 pN and 8.76×10^{-16} J, respectively, indicating that adhesion synergy between catechol and amine could be established without the proximity of these groups.

The coexistence of catechol and cationic residues can not only promote the interfacial adhesion but also boost the cohesion of polymers because of the enhanced cation−π interactions. The catechol−amine cooperativity was proved in a poly(catecholamine) coating, where the cohesion energy between two symmetric poly(catecholamine) films was measured to be 6.4 mJ/m^2, 30 times higher than that of poly(catechol) films (0.2 mJ/m^2) without the presence of charged primary amines (Figure 12c).[225] The robust cohesion was mainly contributed by the amplified cation−π interactions along with π−π stacking, while only π−π interactions were allowed in poly(catechol) film. Similarly, by introducing primary amine groups to polydopamine (PDA), the very weak cohesion between pure PDA coatings was significantly enhanced to 5.7 mJ/m^2 because of the synergistic effect between PDA and amines, and the cohesion energy could be further modulated by tuning the content and position of the amine groups.[226]

2.6.2. Host−Guest Complexation. Host−guest complexation is a type of molecular recognition involving unique structural relationships between two or more molecules (i.e., encapsulation of one within another), which generally combines a series of noncovalent interactions (e.g., hydrogen bonding, electrostatic, hydrophobic, and van der Waals interactions) and is largely dependent on the size, shape, and geometry of the molecules. Among diverse host−guest systems, macrocyclic-based host−guest complexation is most commonly employed in supramolecular chemistry because of its high specificity, where the large cavity volume of the host molecule (e.g., cyclodextrins (CD), cucurbiturils (CB), calixarenes) can accept one or more small organic guests mainly based on the size and shape complementarity.[22,227] CDs are water-soluble cyclic oligosaccharides composed of six to eight glucose units linked by α 1−4 glycosidic bonds, creating a cone shape with a hydrophilic exterior and a relatively hydrophobic cavity. The complexation behaviors of β-CD (seven glucose units) to different types of guest molecules, namely ferrocene, aniline, toluidine, *tert*-butylphenol, and adamantane, were detected by SMFS between a self-assemble monolayer of β-CD and guest molecule-functionalized AFM tips, showing rupture forces of 55, 39, 45, 89, and 102 pN respectively for each individual host−guest pair, which mainly arose from hydrophobic interactions and van der Waals forces.[228,229] Although the rupture forces varied with different geometries of the guest molecules, they were

https://doi.org/10.1021/acs.chemrev.2c00215
Chem. Rev. XXXX, XXX, XXX−XXX

independent of the loading rates, suggesting fast complexation/decomplexation of the host−guest systems. Later, the contribution of the hydrophobic interactions and intrinsic van der Waals forces to the complexation of β-CD and adamantane was distinguished by examing the unbinding forces of the host−guest pair in a series of methanol−water mixtures.[230] As shown in Figure 13a, the rupture force of the complex exhibited a linear relationship with the surface tension of the solvent, indicating the unbinding of the host−guest system at the single-molecule scale could be directly related to the wetting of the molecules, with an effective length (1.07 nm) comparable to the size of adamantane. By extrapolating the linear relationship to zero surface tension, the van der Waals force between the two molecules was determined to be 18 pN, which was 25% of the rupture force in water and 50% of that in methanol, suggesting the host−guest complexation in water was dominated by hydrophobic interactions. Pandey et al. used OT to characterize the interactions of a single β-CD/cholesterol pair and found that the binding strength is dependent on the direction of the cholesterol molecule inserted in the β-CD cavity.[231] When the hydroxyl end of cholesterol entered the wide opening of β-CD, the majority of the hydrophobic rings were buried inside the cavity, showing rupture forces with a center at 41 pN, while the inclusion of the cholosterol through the alkyl end only yielded a value of 32 pN because of the reduced hydrophobic and van der Waals interactions.

CBs are pumpkin-shaped macrocyclic molecules containing methylene-bridged glycoluril units, which also possess hydrophilic exteriors and hydrophobic cavities. Besides hydrophobic and van der Waals interactions, the carbonyl groups at the portals can provide additional binding to guest molecules, especially cations, through ion−dipole interactions and hydrogen bonding, greatly enhancing the binding affinity of CBs.[232] A SMFS study reported a 26 pN unbinding force for separating a positively charged phenyl guest from CB[7], which was reduced to 18 pN when the charged group was removed, demonstrating ion−dipole interactions contributed to the host−guest complexation.[233] The mechanical stabilities of CB[7]/adamantane host−guest complexes were thoroughly investigated by OT, where both neutral and positively charged adamantane guests were employed and coupled with an adjacent hexyl group (Figure 13b).[234] When the host−guest complexes were forced apart, two populations of rupture forces were observed, among which the major population was ascribed to the direct inclusion of adamantane into CB[7], increasing from 44 pN for neutral adamantane to 49 pN for charged adamantane because of additional ion−dipole interactions. The average values of the minor population for both complexes were comparable (22 and 23 pN, respectively), resulting from the hydrophobic interactions between the hexyl group and the CB[7] cavity. Although this type of interaction was relatively weak, it could help to bring adamantane and CB[7] into close proximity and facilitate the formation of the CB[7]/adamantane pairs, leading to increased binding probability and enhanced complex stability.

3. BUILDING FUNCTIONAL SOFT MATERIALS VIA TUNABLE NONCOVALENT INTERACTIONS

On the basis of the nanomechanics of various noncovalent interactions in polymer systems, the molecular interactions within polymeric systems could be modulated by diverse factors such as the type of monomers, the length of the polymer chain, the concentration of functional groups, and the environmental conditions, which lay the foundation for the design of functional polymeric materials. It has received increasing attention for fabricating diverse functional soft materials encompassing colloidal systems, films and membranes, coatings, coacervates, and hydrogels, through modulating single or cooperatively multiple noncovalent interactions. These functional materials built with tunable noncovalent interactions show wide applications in many fields, such as drug delivery and releasing, substances detection and separation, tissue engineering, flexible electronics, and wastewater treatment. The following subsections introduce various functional soft materials by correlating design strategies of utilizing noncovalent interactions with desirable applications.

3.1. Colloidal Systems

3.1.1. Responsive Nanoparticles (RNPs). A colloidal system usually refers to a two-phase mixture, where one divided phase is uniformly dispersed in a second continuous phase.[235,236] The dispersed colloidal particles are available from various materials like metals, minerals, polymers, proteins, etc., and can range from nanometers to micrometers. Besides the large specific surface areas and facile surface modification of colloidal particles, RNPs have attracted extensive research interest because of their versatile size- and environmental-dependent properties, which are able to change their optical, photothermal, ultrasonic, electrical, and magnetic properties in the response of specific stimuli, holding great potential in applications of biomedical and environmental engineering. The commonly employed stimuli can be broadly classified into two categories: exogenous incentives including light, temperature, ultrasound, electricity, and magnetic field; and endogenous stimulants such as pH, enzyme, reactive oxygen species (ROS), hypoxia, and redox potential. The design, fabrication, and application of RNPs usually rely on the combination of multiple covalent and/or noncovalent intermolecular interactions, where the manipulation of the noncovalent ones would be elucidated and summarized in this section.

Polymers and biomacromolecules have been most frequently employed to fabricate RNPs because of the substantial choices of building blocks and modification methods, and the assembly as well as application of RNPs can be controlled via various noncovalent intermolecular interactions including hydrophobic interactions, electrostatic interactions, host−guest interactions, hydrogen bonding, ligand−receptor interactions, $\pi-\pi$ interactions, etc. Hydrophobic interactions play a significant role in constructing RNPs by directing the association of hydrophobic moieties of polymers or biomacromolecules to form particles, micelles or polymersomes, which enable the encapsulation of hydrophobic drugs and allow the on-demand release of the drugs because of the dissociation of self-assemblies upon specific stimuli. For polymers whose hydrophobic moieties and hydrophilic chains are linked with cleavable bonds, the hydrophobic interaction-driven assembled micelles or polymersomes could be facilely dissociated by disrupting the cleavable bonds. For example, when hydrophobic doxorubicin (DOX) was decorated on the end of a hydrophilic pectin chain via an acyl hydrazone bond, the polymers were able to self-assemble into micellar nanoparticles and encapsulate hydrophobic dihydroartemisinin (DHA). Because of the cleavage of acyl hydrazone bonds upon acid environments, DOX and DHA molecules could be simultaneously released with the dissociation of the micellar NPs.[237] Another widely exploited cleavable bond is azo bond, where an azobenzene derivative can be reduced to two separated aniline derivatives under hypoxic

https://doi.org/10.1021/acs.chemrev.2c00215
Chem. Rev. XXXX, XXX, XXX−XXX

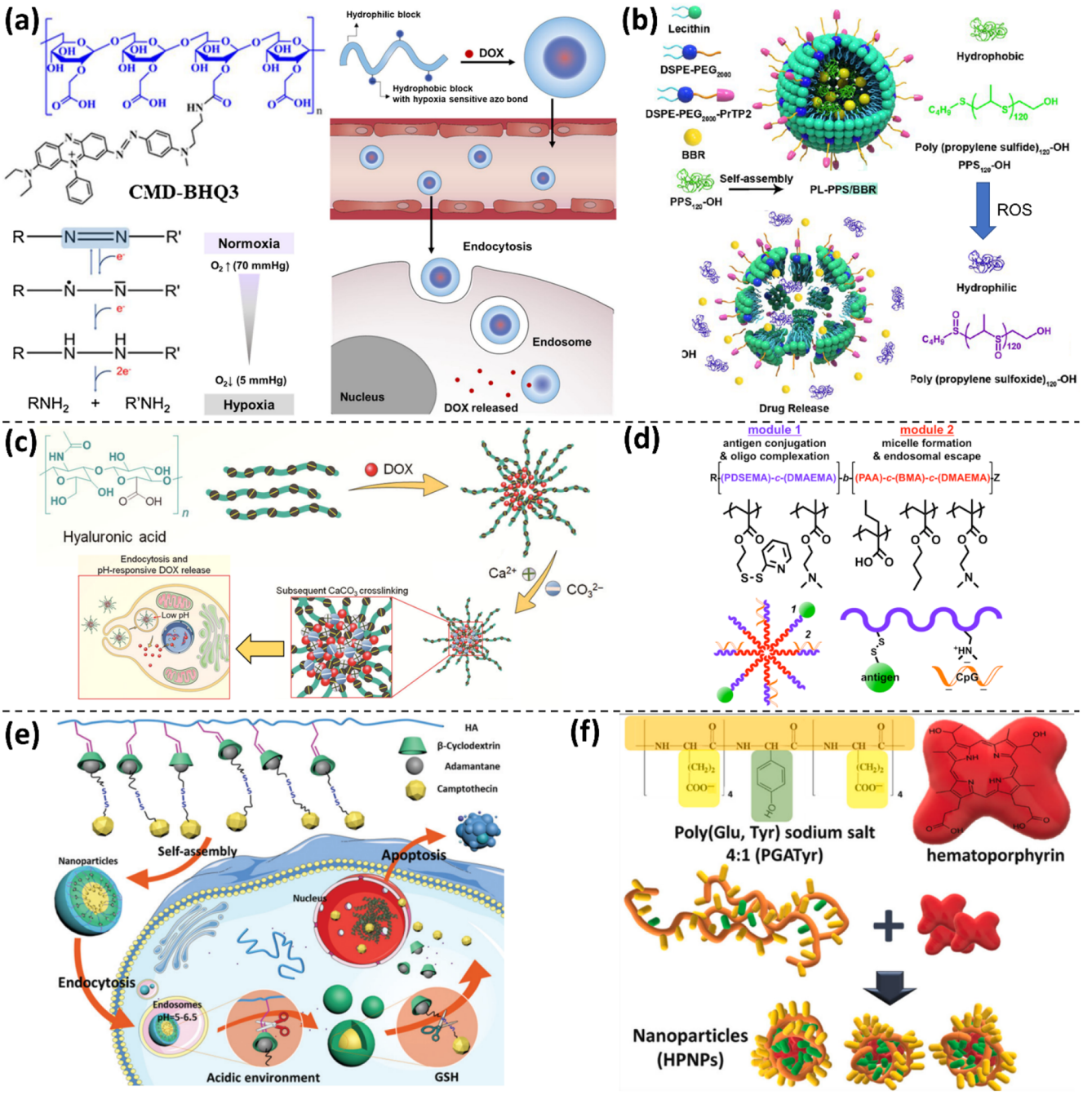

Figure 14. Polymeric RNPs assembled by noncovalent molecular interactions. (a) Hydrophobic interaction-driven NPs enter cell via endocytosis, followed by the collapse of the NPs because of the cleavage of the azobenzene bonds in the hypoxia environment inside the cell. Reproduced with permission from ref 238. Copyright 2018 Elsevier. (b) NPs assembled by hydrophobic interactions among hydrophobic drugs (poly(propylene sulfide)$_{120}$-OH (PPS_{120}-OH) and berberine (BBR)) and the hydrophobic blocks of the amphiphile block copolymers (lecithin, DSPE(1,2-distearoyl-*sn*-glycero-3-phosphoethanolamine)-PEG (poly(ethylene glycol))$_{2000}$, DSPE-PEG_{2000}-PrTP2 (Prestin-targeting peptide 2)). The NPs are dissociated by the hydrophobic−hydrophilic transition of the PPS_{120}-OH caused by ROS. Reproduced with permission from ref 243. Copyright 2021 American Chemical Society. (c) Electrostatic interaction-driven NPs between cationic DOX molecules and negatively charged hyaluronate (HA), which are further cross-linked by the addition of $CaCO_3$ and dissociate with the dissolution of $CaCO_3$ core at acid environment. Reproduced with permission from ref 248. Copyright 2018 Springer Nature. (d) Micellar vaccine NPs enabled by the synergy of hydrophobic interactions, electrostatic interactions, and ligand−receptor interactions. Reproduced with permission from ref 252. Copyright 2013 American Chemical Society. (e) NPs associated by the synergy of hydrophobic interactions and host−guest interactions. Reproduced with permission from ref 257. Copyright 2017 The Royal Society of Chemistry. (f) NPs assembled by hydrophobic interactions and $\pi-\pi$ interactions. Reproduced with permission from ref 258. Copyright 2021 Elsevier.

environment. For instance, hydrophilic carboxymethyl dextran (CMD) was functionalized with hydrophobic black hole quencher 3 (BHQ3) molecule side chains containing azo bonds, which self-assembled into nanoparticles (NPs) with a hydrophilic CMD shell and a hydrophobic BHQ3 core that loading DOX via hydrophobic interactions (Figure 14a). Hypoxia led to the reduction of the azo bond and the departure of hydrophobic moieties from the side chains of CMD

https://doi.org/10.1021/acs.chemrev.2c00215
Chem. Rev. XXXX, XXX, XXX−XXX

backbones, resulting in the destruction of NPs and the release of DOX.[238] Diblock copolymer poly(lactic acid) (PLA)-azobenzene-poly(ethylene glycol) (PEG) formed polymersomes in an aqueous medium because of the hydrophobic interactions among hydrophobic PLA blocks, whose cores were laden with anticancer drugs gemcitabine and erlotinib. A hypoxic environment induced the breakage of the azo bond linkers between PLA and PEG blocks, followed by the disintegration of the polymersomes as well as the release of the anticancer drugs.[239] Polymers containing self-immolative monomers with hydrophobic groups such as quinone-methide moieties could self-assemble into polymeric NPs but disassemble upon specific stimuli (e.g., light) via a cascade of reactions, leading to complete depolymerization.[240] Another way to collapse hydrophobic interaction-directed NPs is converting the hydrophobic moieties to be hydrophilic. It was reported that diblock copolymers with a hydrophilic block and a tertiary amine-containing hydrophobic block could assemble into micellar NPs, which would dissociate under acidic environments because of the charge repulsion within the hydrophobic cores caused by the protonation of the tertiary amines.[241] Hydrophilic CMD backbones modified with hydrophobic 2-nitroimidazole derivative side chains could conjugate into NPs with hydrophobic cores being able to encapsulate DOX, which would collapse under hypoxic conditions with the reduction of nitro groups into amino groups.[242] Some diblock and/or triblock polymers, such as lecithin, lipid-PEG, Pluronic PEG-poly(propylene glycol) (PPG)-PEG, composed of both hydrophilic and hydrophobic blocks, have been extensively employed to assist the fabrication of RNPs. The hydrophobic blocks of these diblock or triblock polymers interact with the responsive polymers to form the hydrophobic cores of NPs, which would then be disassembled with the change of specific stimuli like ROS (Figure 14b),[243] glutathione,[244] hypoxia,[245,246] and cooling.[247] Electrostatic interaction is also utilized to frame RNPs. It was reported that cationic DOX molecules could interact with negatively charged hyaluronate (HA) with anionic carboxyl groups via electrostatic interactions and generate NPs, which could be further cross-linked by subsequently adding Ca^{2+} and CO^{3-} (Figure 14c). The release of DOX was proposed to be attributed to the acid-responsiveness of $CaCO_3$ in the cores.[248] Another work demonstrated that an anionic insulin-heparin aggregate could be protected in harsh stomach acid environment by coated with positively charged chitosan (CS), which teneded to dissociate in the basic environment of the mucus layer ascribed to the deprotonation of the positively charged groups.[249] Positively charged poly(ethylenimine) (PEI) conjugated with NIR fluorochrome Cy5.5 and protein kinase A peptide motif could interact with negatively charged poly(aspartic acid) to form polyelectrolyte complex NPs. Upon protein phosphorylation, negative charged phosphate destroyed the balance of electrostatic interaction to induce the solubilization of polyelectrolytes, where the separated Cy5.5 moieties exhibited strong NIR fluorescence for imaging protein kinase activities.[250] Besides the exploration of one type of noncovalent interaction, RNPs enabled by the synergy of two or more noncovalent intermolecular interactions have been widely investigated. The cooperation of hydrophobic interactions and electrostatic interactions have been employed, sometimes assisted by ligand−receptor interactions for specific binding. For example, in a diblock copolymer, the hydrophilic block not only contained pyridyl disulfide groups (pyridyl disulfide ethyl methacrylate, PDSEMA monomer) for the decoration of thiolated protein antigen but also possessed cationic dimethylaminoethyl methacrylate (DMAEMA) monomers for the electrostatic complexation with negatively charged nucleic acid adjuvant, while the pH-responsive hydrophobic block (copolymerization of acrylic acid (AA), butyl methacrylate (BMA), and DMAEMA monomers) impelled the assembly of micellar vaccine NPs. The NPs could collapse to expose the membrane-destabilizing core to promote the antigen delivery and enhance the immune response (Figure 14d).[251,252] A recent study presented that the positively charged hypoxia-targeting NIR dye (Cy7) moieties linked with a hydrophobic antitumor agent gambogic acid (GA) and negatively charged surfactins could generate nanoparticles via hydrophobic interaction among GA moieties and alkyl chains of surfactins. The positively charged Cy7 groups were immobilized in the hydrophilic corona of the NPs through electrostatic interaction with the anionic ends of the surfactins, and they would be released by interacting with organic anion-transporting polypeptides on the cytomembrane.[253] Redox-responsive NPs composed of a cationic lipid/anionic siRNA complex-containing hydrophobic poly(disulfide amide) core and a lipid-PEG shell could undergo fast intracellular siRNA release through rapid degradation of disulfide bonds triggered by the highly concentrated glutathione (GSH) in the cytoplasm.[254] Pluronic F127 (PEG-PPG-PEG) with two end groups modified with chitosan self-assembled into micelles via hydrophobic interaction among PPG blocks with curcumin molecules encapsulated. These micellar NPs were positively charged under mind hyperthermia of 43 °C, offering them increased uptake by negatively charged nuclear membrane via electrostatic interactions to enhance the delivery of curcumin to target cancer cells.[255] The synergy of hydrophobic interaction and host−guest interaction was also studied. Hydrophilic comb shaped supramolecular copolymer could be generated by mixing sodium alginate (SA) with β-CD side chains and methoxypolyethylene glycol (mPEG) end-capped with uncharged hydrophobic ferrocene (Fc) through host−guest interaction between β-CD and Fc. The addition of α-CD would turn the comb-shaped copolymer into a coil−rod structure through the host−guest inclusion of α-CD with mPEG, leading to the self-assembly of NPs with a hydrophobic associated rod core and a hydrophilic coiled shell. The loaded bovine serum albumin (BSA) could be released with presence of H_2O_2 which induced the dissociation of Fc-β-CD by oxidizing Fc to Fc^+.[256] Similarly, an amphiphile supramolecular copolymer was obtained by mixing β-CD-modified HA and camptothecin (CPT) that was functionalized by the guest molecule adamantane (ADA) via a disulfide bond. The dissociation of the hydrophobic CPT core was induced by the breakage of the disulfide bonds resulted from the presence of an acid environment and a high concentration of GSH (Figure 14e).[257] The combinations of hydrophobic and $\pi-\pi$ interactions, hydrophobic and ligand−receptor interactions, electrostatic and ligand−receptor interactions, etc. were also investigated. Copolymer poly(L-glutamic acid-L-tyrosine) can form NPs with hematoporphyrin (HP) via hydrophobic and $\pi-\pi$ interactions among benzene rings of tyrosine and aromatic rings of HP (Figure 14f). Upon the digestion of polyglutamate by a proteolytic enzyme, cathepsin B, the size of the NPs gradually reduced with the release of the loaded drug.[258] A dandelion-like NP with a hydrophilic PEG corona end-capped with bradykinin receptor 1 (B1R) for tumor detection and a hydrophobic core comprising interacted poly(aspartic acid), DOX and adenosine-5′-triphosphate ATP aptamer could enter into cancer cells and release anticancer DOX assisted by B1R

https://doi.org/10.1021/acs.chemrev.2c00215
Chem. Rev. XXXX, XXX, XXX−XXX

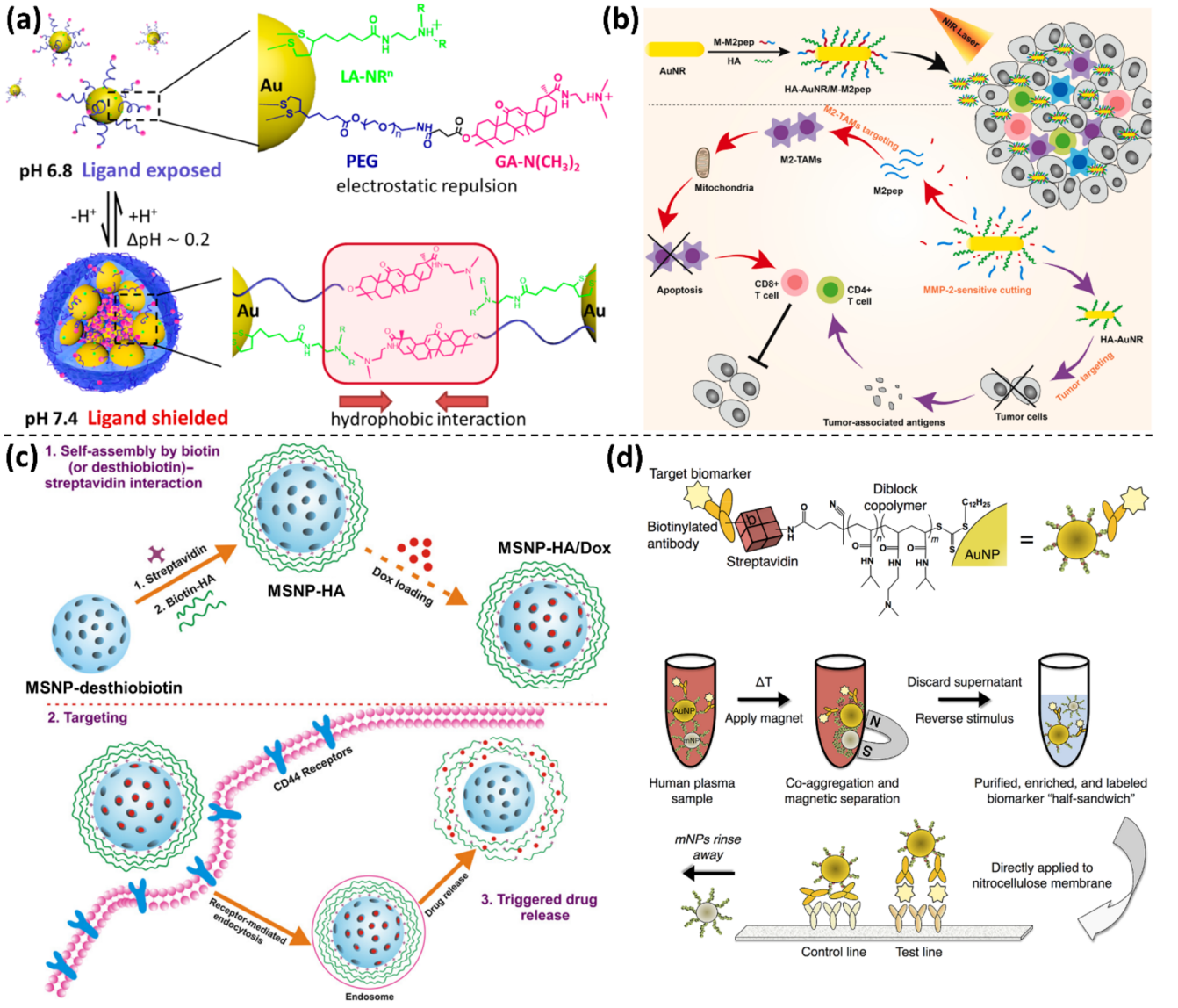

Figure 15. Inorganic NPs-based RNPs and the related noncovalent interactions. (a) Assembly and dissociation of functionalized AuNPs enabled by the modulation of electrostatic interactions. Reproduced with permission from ref 262. Copyright 2014 American Chemical Society. (b) AuNRs modified with HA and matrix metalloproteinase-2 (MMP2)-responsive M2pep fusion peptides (M-M2pep). Reproduced with permission from ref 265. Copyright 2021 Elsevier. (c) DOX-loaded MSNPs encapsulated by complexes of streptavidin and biotin-modified HA can enter cell via ligand–receptor interactions between HA and CD44 receptor. Reproduced with permission from ref 269. Copyright 2016 American Association for Cancer Research. (d) Thermal- and magnetic-responsiveness are integrated by combining biomarker-targeted PNIPAm-modified AuNPs with PNIPAm-coated iron oxide magnetic NPs (mNPs). Reproduced with permission from ref 274. Copyright 2012 American Chemical Society.

and ATP.[259] Positively charged PEI conjugated with hydrophobic photosensitizer pheophorbide A (PheoA) could complex with negatively charged antigen ovalbumin (OVA) to generate NPs which was able to strengthen antigen-specific $CD8^+$ T cell immune response for cancer immunotherapy.[260] Apart from polymer- and biomacromolecule-based RNPs, a novel metal–metal-to-ligand coordination was reported to direct controllable and imageable self-assembly of small molecules. In the square-planar platinum(II) complex, the metal–metal-to-ligand charge transfer states were enabled by directional metallophilic interaction, face-to-face $\pi-\pi$ interaction, and directional N–H hydrogen bond interaction between neighboring platinum(II) compound molecules.[261]

Gold NPs (AuNPs) are popular building blocks for the construction of RNPs taking advantage of their multiple nanoshapes (sphere, rod, shell, etc.), specific physical properties, and chemically active surface for modifications. It was reported that AuNPs thiolated with lipoyl tertiary amines (LA-NR^n) and PEG-glycyrrhetinic acid (GA)-$N(CH_3)_2$ chains could self-assemble into nanoaggregates with hydrophobic GA-$N(CH_3)_2$ groups buried inside the assembly at physiological conditions (Figure 15a). When exposed to the acidic tumor environment, the assemblies would disperse into single AuNPs stabilized by electrostatic repulsion because of the protonation of tertiary amines, with GA acting as ligands for targeting tumor cells.[262] AuNPs simultaneously decorated with Au–S linkages and mercaptoalkanoic acid groups exhibited ligand configuration-associated photoluminescent variation in response to pH. To be specific, the carboxyl groups were deprotonated at high pH and the polymers extended as molecular brushes to stabilize the NPs

https://doi.org/10.1021/acs.chemrev.2c00215
Chem. Rev. XXXX, XXX, XXX–XXX

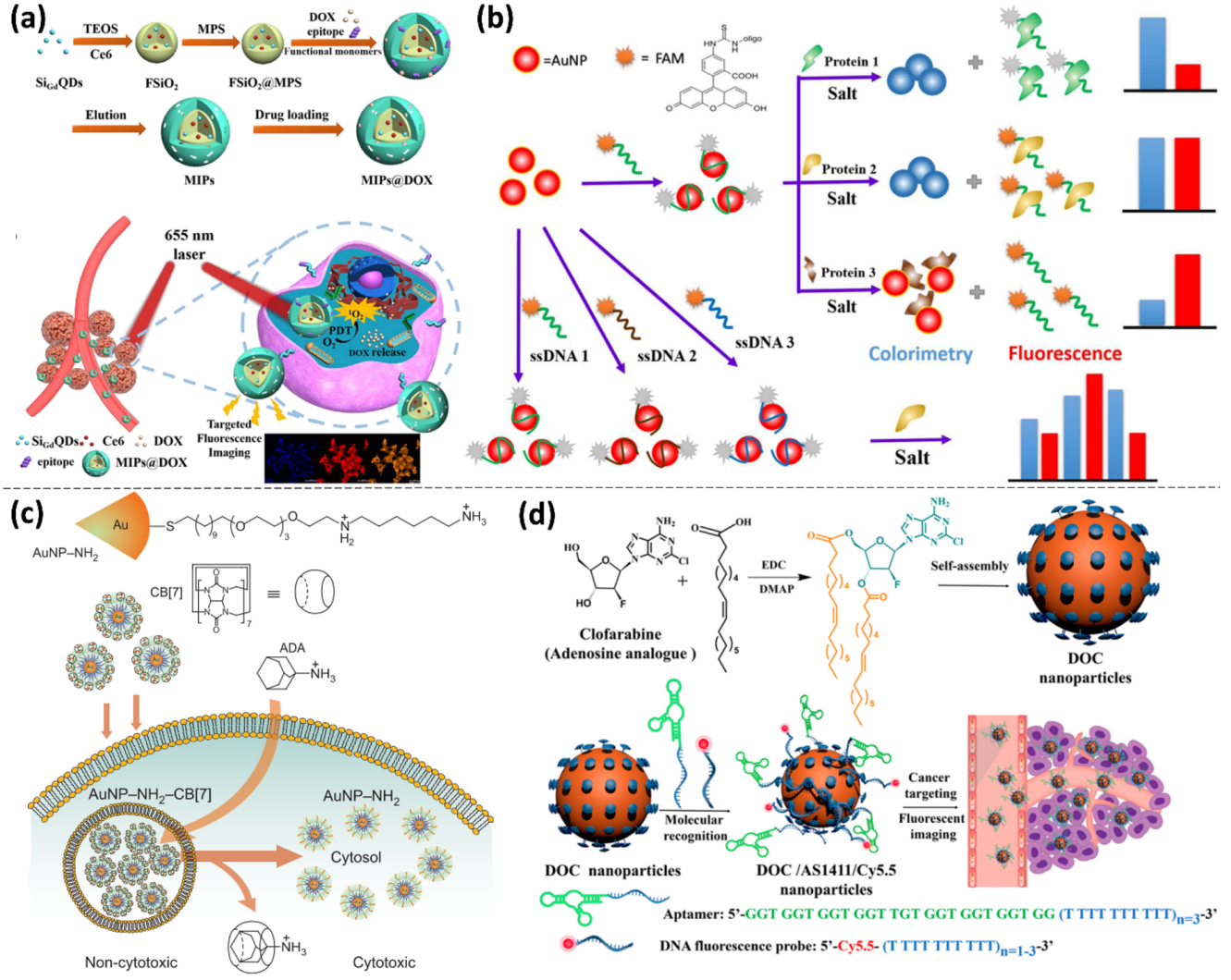

Figure 16. NPs with recognition ability. (a) NPs with recognition ability derived from customized sites of MIPs. Reproduced with permission from ref 278. Copyright 2020 American Chemical Society. (b) AuNPs absorbed with ssDNA act as a multidimensional sensor for protein discrimination. Reproduced with permission from ref 290. Copyright 2015 American Chemical Society. (c) Competing recognition of CB[7] on ADA over diaminohexane activates the cytotoxic property of the diaminohexane-terminated AuNPs. Reproduced with permission from ref 294. Copyright 2010 Springer Nature. (d) DOC NPs were anchored with tailor-made aptamer for the recognition of protein overexpressed on the surface of tumor cells and fluorescent probe for the monitoring of the NPs. Reproduced with permission from ref 296. Copyright 2017 American Chemical Society.

by electrostatic repulsion. However, a low pH would protonate the carboxyl groups and the molecular brushes collapsed because of the van der Waals interactions between the polymers and AuNPs.[263] AuNPs could also undergo chemically/electrochemically reversible molecular template-directed self-assembly based on host–guest interactions between the π-electron-deficient cyclobis(paraquat-*p*-phenylene) tetracationic cyclophane ($CBPQT4^+$) host and the π-electron-rich diethylene glycol-disubstituted tetrathiafulvalene (TTF-DEG) guest, providing an approach to precisely manipulate the molecular templates at the nanoscale.[264] Au nanorods (AuNRs) were modified with HA and metalloproteinase-2 (MMP2)-responsive M2pep fusion peptides (M-M2pep) to target tumor cells and realize precise tumor photothermal therapy (PTT) upon NIR light irradiation (Figure 15b). Via ligand–receptor interactions, released M2pep and HA-AuNRs could attack immunosuppressive M2-type tumor-associated macrophages (TAMs) and induce immunogenic cell death, respectively, to elicit antitumor immunity.[265] Optomechanical actuator (OMA) NPs composed of an AuNR core and a temperature-responsive PNIPAm shell were demonstrated to enhance myoblast differentiation and muscle growth in vitro and in vivo via cyclic strain induced by the heat-dependent volume transition, where PNIPAm chains experienced cyclic coil–globule transitions through the formation and collapse of hydrogen bonds between backbone amide C=O and N–H groups.[266,267]

Other NPs such as silica NPs and Fe_3O_4 NPs also have been harnessed individually or cooperatively to construct RNPs via the manipulation of noncovalent intermolecular interactions. For example, by tuning the distance between charged silica NPs via electrostatic interactions, RNPs with various structural colors could be obtained.[268] Mesoporous silica nanoparticles (MSNPs) have attracted extensive research attention because of their well-defined structures and tunable pore size, which are excellent carriers of responsive moieties and/or drugs. DOX-loaded MSNPs encapsulated by complexes of streptavidin and biotin-modified HA could enter cancer cells via receptor-mediated endocytosis (ligand–receptor interaction between

https://doi.org/10.1021/acs.chemrev.2c00215
Chem. Rev. XXXX, XXX, XXX–XXX

HA and a cluster of differentiation protein such as CD44 receptors), after which the drug release would be triggered with the presence of hyaluronidase and intracellular biotin (Figure 15c).[269] Redox-responsive peptides were anchored on the surface of MSNPs via disulfide bonds, which served as tumor-targeting ligands and gatekeepers of the loaded DOX.[270] Fe_3O_4 NPs are usually utilized taking advantage of their magnetic responsiveness. Generally, they are functionalized with charged polymers and then brought into contact with oppositely charged membranes or cells. The corresponding assembly could respond to specific magnetic fields to act as antifouling surface coating,[271] where the adsorbed foulants could be detached from the membrane facilitated by magnetic fields.[272] Thermal- and magnetic-responsiveness could be integrated into one platform by mixing biomarker-targeted PNIPAm-modified AuNPs with PNIPAm-coated iron oxide magnetic NPs, which could be combined with each other upon heating (above the lower critical solution temperature (LCST) of PNIPAm) (Figure 15d). The aggregated NP system could be facilely separated and collected using a magnet for rapid purification, enrichment, and detection of biomarkers in human plasma.[273,274] Multiresponsive hybrid NPs were fabricated by making use of silica NPs, Fe_3O_4 NPs, and AuNRs. Silica-coated Fe_3O_4 NPs were encapsulated within a thermoresponsive and negatively charged p(NIPAM-*co*-acrylic acid) hydrogel network, which electrostatically interacted with positively charged AuNRs to become hybrid NPs, exhibiting thermo-, pH-, photo-, and magneto-responsiveness for controlled drug delivery applications.[275]

3.1.2. Nanoparticles with Recognition Ability. Highly specific molecular recognition based on noncovalent interactions plays a vital role in diverse biological processes (e.g., transcription factors' specific recognition toward the certain sequence of DNA, specific catalysis of enzymes) and has inspired the development of NPs with recognition abilities,[276] which have applications in various fields such as separation, drug delivery, biosensors, bioimaging, and so on.[277] Several strategies have been exploited to fabricate NPs with a recognition ability, among which NPs with molecularly imprinting polymers (MIPs), functionalized AuNPs, and self-assembled polymeric NPs are the most commonly investigated ones.

MIPs are synthetic receptors with customized sites for target molecules.[277] They are usually linked to silica nanoparticles,[278−283] upconversion NPs,[284] Fe_3O_4 NPs,[285,286] and carbon dots (CDs).[287] Either in the fabrication of the NPs or especially in the recognition process of target molecules, noncovalent interactions play an essential role. As shown in Figure 16a, the formation of polymer imprinted NPs started with the production of silica NPs, which was generally obtained via the hydrolysis of alkyl silicates such as tetraethyl orthosilicate (TEOS) and the subsequent condensation of silicic acid in alcoholic solutions.[278,288] Herein, gadolinium-doped silicon quantum dots (Si_{Gd}QDs, the agent for fluorescent/magnetic resonance dual-imaging) and chlorin e6 (Ce6, photosensitizers being capable of emitting ROS under light irradiation for photodynamic therapy) were simultaneously doped within the silica NPs, followed by the surface coating of 3-methacryloxypropyltrimethoxysilane (MPS) to provide sufficient accessible vinyl for the subsequent polymerization. Sequentially, the epitope (YNCPNPTADCK) of the CD59 protein, which is usually overexpressed on the surface of solid tumors, and the antitumor agent DOX were added into the aqueous solution of functional monomers including NIPAm, *N*-*tert*-butyl acrylamide (TBAm), acrylamide (AAm), and cross-linker *N*,*N*-methylenebis(acrylamide) (BIS). The polymerization and subsequent elution endowed the imprinted polymer shell with tailor-made sites of epitope and DOX. The silica NPs with MIPs could recognize and bind the CD59 protein to enter the cancer cells, where the released DOX and Ce6 synergistically performed antitumor properties aided by the acid environment and laser irradiation. The recognition ability of the polymer imprinted silica NPs toward the CD59 protein and DOX was attributed to the noncovalent interactions including hydrogen bonding and van der Waals forces between the customized cavities of the imprinted polymers and the epitope or DOX molecules. The silica NP cores could be further etched out to receive the hollow MIPs, promoting the penetration of target molecules into the imprinted sites.[279] The imprinted polymer shells of NPs could be integrated into a membrane by decorating the NPs onto PDA-modified regenerated cellulose membranes, which was realized through bidentate hydrogen bonds and electrostatic interactions between the negatively charged surface of the NPs and the positively charged amine groups of the PDA.[281] In addition, the polymerization of vinyl monomers could be substituted by the self-polymerization of dopamine to form the MIPs.[283] Upconversion NPs could be coated by zeolite imazolate framework-8 (ZIF-8) because of the electrostatic interaction between the negatively charged surface of upconversion NPs and the cationic Zn^{2+} of ZIF-8. Because of the hydrogen bonding and van der Waals forces, the cavities suitable to accommodate target molecules (e.g., octopamine) could be framed via polymer imprinting on the ZIF-8-modified upconversion NPs.[284] Magnetic NPs with imprinted polymers were beneficial for the separation process after recognizing and binding enough target molecules such as glycoproteins.[285]

AuNPs have become one of the most popular templates for numerous functionalizations because of their unique optical, electrical, chemical, and catalytic properties. AuNPs and DNA sequences are favorable pairs as they can be facilely associated either via physical adsorption (van der Waals forces) or chemical bonds (thiol, disulfide, and bisdisulfide groups).[289,290] It was reported that the conjugates of AuNPs and dye-labeled DNA sequences could work as multidimensional sensors to recognize proteins with the exhibition of different combinations of UV absorption and fluorescence intensity, which was induced by aggregation and dispersion of AuNPs as well as quenching and dequenching of fluorescent dyes, respectively. As illustrated in Figure 16b, fluorescent dye carboxyfluorescein (FAM)-labeled single-stranded DNA (ssDNA) would be quenched once adsorbed on AuNPs via van der Waals forces. In the process of protein recognition, AuNPs would aggregate because of the screen of long-range electrostatic repulsion with the addition of salt and the competitive binding of the protein, and the fluorescence recovered through desorbing from the AuNPs (protein 2). Meanwhile, three Fe-containing proteins (e.g., hemoglobin, myoglobin, and transferrin) could also initiate the aggregation of AuNPs but quench the fluorescence with the presence of Fe, which corresponded to protein 1. In contrast, proteins including pepsin, bovine serum albumin (BSA), horseradish peroxidase (HRP), human serum albumin (HSA), trypsin, and egg white albumin (EA) exhibited higher affinity to AuNPs, preventing the AuNPs from aggregation and enhancing the fluorescence of the released FAM-labeled ssDNA (protein 3). Similarly, the variation of the ssDNA sequences would expand the discrimination ability of this sensor to proteins. In another work, bare AuNPs and citrate-stabilized AuNPs were separately brought to contact with different proteins ensued

https://doi.org/10.1021/acs.chemrev.2c00215
Chem. Rev. XXXX, XXX, XXX−XXX

with the addition of $HAuCl_4$ to trigger the growth of AuNPs. The resultant solution exhibited distinct colors, ascribed to the different growth modes of AuNPs caused by the variable interactions with different proteins, and the quantification via UV/vis spectra could be used to build a colorimetric response pattern map for protein recognition.[291] Citrate-stabilized AuNPs were also harnessed to detect glucose in rat brains.[292] Briefly, the high charge density of ssDNA adsorbed on AuNPs could suppress the salt-induced aggregation between the negatively charged citrate-modified AuNPs, but they tended to decompose into fragments by hydroxyl radicals generated from the Fe^{2+}-catalyzed Fenton reaction of H_2O_2, impairing the stabilizing capability. As H_2O_2 could be generated from glucose and O_2 in the presence of glucose oxidase, the amount of aggregated AuNPs could be quantified by UV/vis spectrometry and directly correlated to the concentration of glucose. Au−S bond is a widely used approach to the modification of AuNPs with desired functional groups.[293,294] For example, AuNPs were anchored with 4-amino-3-mercaptobenzoic acid (AMBA) through a thiol group and utilized to detect pesticide cyhalothrin. The AMBA-AuNPs showed specific recognition to cyhalothrin, demonstrated by the changes of color and UV/vis absorption compared with other pyrethroid pesticides. It was proposed that only cyhalothrin contained the trifluoromethyl groups which could facilely form hydrogen bonds with the amine and carboxyl groups of AMBA, thereby breaking the balance of the electrostatic repulsion among AuNPs and leading to the aggregation.[293] Besides the recognition-based detection and separation of certain substances, the recognition ability of functionalized AuNPs could also serve as a trigger to activate the therapeutic property of the AuNPs. As presented in Figure 16c, diaminohexane-terminated AuNPs (AuNP-NH_2, functionalized by Au−S bonds) could be decorated with a monolayer of cucurbit[7]uril (CB[7]) via the host−guest interaction between CB[7] and diaminohexane moieties, where the hydrophobic cavities of CB[7] circumvented the diaminohexane moieties to eliminate their therapeutic cytotoxicity. The host−guest complexes would dissociate after endocytosis with the addition of a competitive orthogonal guest molecule 1-adamantylamine (ADA, an antiviral or anti-Parkinsonian drug), thereby releasing the cytotoxic AuNP-NH_2.[294] The chiral recognition ability of L-tartaric acid-modified AuNPs on mandelic acid (MA) was studied,[295] with results showing that the addition of L-MA induced the aggregation of the tartaric acid-modified AuNPs while the addition of D-MA imposed no effect on the dispersion, indicating the recognition was controlled by the hydrogen-bonding interactions between L-tartaric acid-modified AuNPs and L-MA.

The polymeric NPs with a recognition ability are usually fabricated by the self-assembly of amphiphile polymers and modification with functional groups. For example, two oleic acid molecules were connected to the adenosine analogue clofarabine by an esterification reaction to form a prodrug 3′,5′-dioleoyl clofarabine (DOC), which could self-assemble into NPs enabled by hydrophobic interactions among alkyl groups of the oleic acid with a hydrophilic shell of clofarabine exposed to the surrounding environment (Figure 16d).[296] Then the designed aptamer (AS1411) and DNA fluorescence probe (Cy5.5) were simultaneously anchored onto the DOC NPs by forming multiple hydrogen bonds with clofarabine. After injection, the NPs were effectively accumulated at the tumor sites because of the specific aptamer−receptor interaction between the G-rich segment of the aptamer and the nucleolin protein overexpressed on the surface of the tumor cells, thereby demonstrating the antitumor property. Simillarly, ligands EXP3174 (ligand for the angiotensin-II type 1 receptor (AT1R)) and Ang-I (the pro-ligand angiotensin-I, which can be recognized by the angiotensin converting enzyme (ACE) and be converted into the active ligand angiotensin-II (Ang-II)) were linked to the amphiphile block polymer poly(lactic acid)$_{10k}$−poly(ethylene glycol)$_{5k}$ (PLA_{10k}-PEG_{5k}) ended with $-NH_2$ and −COOH groups (PLA_{10k}-PEG_{5k}-NH_2 and PLA_{10k}-PEG_{5k}-COOH), respectively.[297] The self-assembly of the polymeric micelles was initiated by the hydrophobic interaction among the hydrophobic PLA blocks while the ligands-capped hydrophilic PEG shells were faced toward the aqueous solution to interact with the AT1R and ACE receptors located on the surfaces of the target cells. The ligand−receptor interaction between Ang-I and ACE could convert Ang-I to Ang-II, which subsequently interacted with AT1R to actuate the endocytosis. Therefore, polymeric micelles can effectively serve as transporters into mesangial cells, holding great promises as drug carriers with viral cell recognition.

3.2. Films, Membranes, and Coatings

Films, membranes, and coatings play a crucial role in functional soft materials as they possess large surfaces that can be facilely tailored for various demands. All of them are generally built on substrates, where coatings usually adhere to the substrates while films and membranes sometimes could be free-standing. Surface modification is a widely used strategy to endow substrates with responsiveness and/or functionalities, which can be achieved via both chemical and physical approaches. Covalent functionalization commonly involves thiol chemistry (Au-SH), click chemistry (alkyne coating followed by azide−alkyne reaction), polymer brushes (initiator immobilization followed by polymerization of monomers), anchor molecules (silane, catechol, phosphate) followed by a polymer graft, 1-ethyl-3-(3-(dimethylamino)propyl)carbodiimide/*N*-hydroxysuccinimide (EDC/NHS) linker, and so on.[114,298−302] Physical approaches, from the perspective of surface morphology, usually include roughening (plasma etching and mechanical roughening) and patterning (lithography, direct-writing, 3D patterning), which would not be discussed in details in this review.[303] The following subsections would emphasize the approaches toward surface functionalization based on noncovalent molecular interactions, among which layer-by-layer assembly is first elucidated from the aspects of sensing, drug delivery, functional coatings, fuel cells, catalysis, packaging, water treatment, and so on. Adaptable films/membranes are then introduced by highlighting their applications in oil/water separation and bone regeneration. Adhesive layers that bridge substrates and functional coatings are also discussed.

3.2.1. Layer-by-Layer (LBL) Assembly. LBL assembly is a mature and widely used technique for the fabrication of multilayered composites (films, membranes, capsules, etc.) with controlled compositions and architectures at the nano- and microscales, which has been extensively exploited in various research fields such sensing, drug delivery, functional coatings, fuel cells, catalysis, packaging, water treatment, and so on.[304−306] Compared to the conventional Langmuir−Blodgett (LB) technique, which is dominant in the fabrication of nanostructured films/membranes, the LBL assembly exhibits overwhelming advantages in massive choices of the substrate regardless of their shape (plates, tubes, spheres, rods, etc.) or surface morphology (smooth, rough, porous, etc.).[307] More-

https://doi.org/10.1021/acs.chemrev.2c00215
Chem. Rev. XXXX, XXX, XXX−XXX

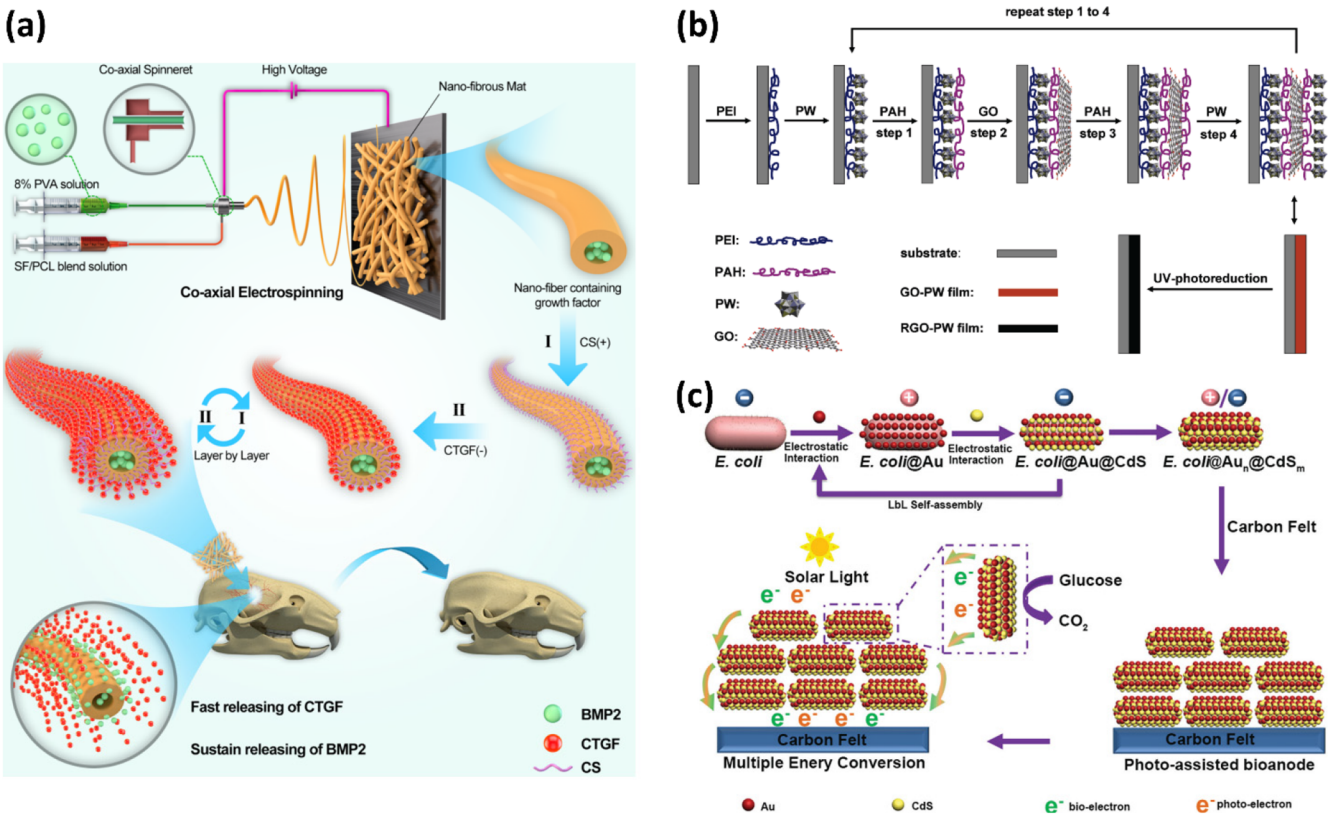

Figure 17. LBL assemblies for (a) drug delivery, (b) FETs/photodetector devices, and (c) microbial fuel cells (MFCs). (a) Dual-delivery of bone morphogenetic protein 2 (BMP2) and connective tissue growth factor (CTGF) through LBL assembly of core−shell nanofibers for promoting bone generation. Reproduced with permission from ref 311. Copyright 2019 American Chemical Society. (b) PW-rGO multilayer films fabricated by LBL assembly of anionic PW clusters and GO nanosheets as well as cationic PEI and PAH, followed by in situ UV-photoreduction of GO to rGO. Reproduced with permission from ref 321. Copyright 2011 American Chemical Society. (c) Surface of *E. coli* was modified by LBL assembly of positively charged PDDA-coated AuNPs and negatively charged photoresponsive CdS NPs, exhibiting higher power output than that without surface modification. Reproduced with permission from ref 323. Copyright 2021 The Royal Society of Chemistry.

over, LBL assembly is not confined to specialized instruments or amphiphile materials, which are required for the LB technique.[308] LBL assembly is mainly driven by strong electrostatic interactions, allowing the facile buildup of multilayers on charged surfaces via sequential adsorption of oppositely charged polyelectrolytes. Other noncovalent interactions including hydrogen-bonding interactions, host−guest interactions, hydrophobic interactions, biological specific ligand−receptor interactions also widen the flexibility of the LBL technique in the selection of materials,[308,309] including polymers, carbon nanotubes, 2D materials, clays, nanoparticles, dyes, metal oxides, proteins, peptides, nucleic acids, enzymes, and viruses.

The last two decades have witnessed a rapid increase of research regarding the modulation of various noncovalent interactions toward new fabrication strategies, functionalization methods, and applications of the LBL technique, especially in biomedical- and bioengineering-related fields such as drug delivery, tissue engineering, cell encapsulation, biosensors, biocatalysts, and biomimetics. For example, DNA- or protein-containing polyelectrolyte multilayers (PEMs) were built up on stainless steel microneedles via LBL assembly for the transdermal delivery of DNA- or protein-based therapeutics to skin. Stainless steel microneedles were first precoated with 10 bilayers of a multilayered film composed of positively charged linear poly(ethylene imine) (LPEI) and negatively charged sodium poly(4-styrenesulfonate) (SPS), terminated with a topmost layer of SPS, and then coated with alternating deposition of positively charged poly(β-amino ester)/bovine pancreatic ribonuclease A (RNase A) and negatively charged plasmid DNA/sodium SPS, respectively, until 16 bilayers were deposited.[310] Dual-delivery of osteogenic and angiogenic growth factors for the regeneration of bone tissue was accomplished through LBL assembly of core−shell nanofibers. The core with a negative surface charge was constructed by coaxial electrospinning of the bone morphogenetic protein 2 (BMP2)-containing poly(vinyl alcohol) (PVA) aqueous solution and silk fibroin/polycaprolactone (SF/PCL) blend solution, while the shell was fabricated via LBL assembly by alternatively depositing a positively charged chitosan (CS) solution and a negatively charged connective tissue growth factor (CTGF) solution (Figure 17a).[311] Drug release is generally conducive for tissue regeneration, while cell transplantation usually induces side effects like deleterious host responses, for which minimizing the transplant volume might be a feasible approach to attenuate the situation. It was reported that the intraportal islet transplantation through encapsulating individual pancreatic islets with conformal nanothin PEG-rich coating via LBL assembly could significantly reduce void volume as well as confer tailored bioactivity compared with microcapsules formed via various drop generating processes. The positively charged lysine moieties of poly(L-lysine)-*g*-poly-

https://doi.org/10.1021/acs.chemrev.2c00215
Chem. Rev. XXXX, XXX, XXX−XXX

(ethylene glycol) (biotin/PPB) electrostatically interacted with negatively charged cell surfaces and the subsequent alternating deposition of streptavidin (SA) and PPB through the receptor−ligand interaction resulted in the formation of LBL assembled coating of cell islets.[312] LBL assembly has also been applied in biosensing and biocatalysts. For instance, LBL-assembled graphene multilayer films were employed as enzyme-based biosensors for the detection of glucose and maltose because of their excellent electrocatalytic activity for H_2O_2, which was a common product of enzyme-catalyzed reactions. The sensors were fabricated by alternating deposition of positively charged poly(ethylenimine) (PEI) and negatively charged pyrene-grafted poly(acrylic acid)-modified reduced graphene oxide codissolved with the glucoamylase on glassy carbon electrodes.[313] Meanwhile, negatively charged 2D reduced graphene (RG) and 1D multiwalled carbon nanotubes (MWCTs) could be simultaneously incorporated into the interface of the LBL-assembled composite electrode, via electrostatic interactions with positively charged poly(diallyldimethylammonium chloride) (PDDA), leading to an electrochemical immunosensor (denoted as $(PDDA/RG/PDDA/MWCT)_n$/antihuman IgG (immunoglobulin G)) for the detection of IgG concentration in human serum.[314] LBL-assembled multilayers could also be constructed into nanotubes in the pores of a template membrane as a carrier of biocatalysts, where negatively charged poly(sodium styrenesulfonate) (PSS) and redox protein cytochrome c (cyto-c, involved in the cell respiration process and is a significant electron transfer agent during bio-oxidation, possessing a positive charge at pH below 10.4) were sequentially adsorbed onto the positively charged PEI-modified inner wall of the template membrane.[315] The LBL technique also serves as an economic, efficient, and facile approach toward biomimetic engineering such as artificial nacre, whose ordered brick-and-mortar arrangement of organic and inorganic layers is similar to lamellar bones, holding great potential as bone implants. The structure was constructed by sequential deposition of positively charged PDDA and negatively charged montmorillonite clay platelets, which were connected via strong attractive electrostatic and van der Waals interactions at the interfaces, and free-standing artificial nacre films were obtained by dissolving the supporting SiO_2 coating with HF solution.[316] By incorporating a layer of starch-stabilized Ag NPs to the artificial nacre, it could be endowed with antimicrobial properties.[317] The exquisite porous organic layers of nacre were imitated by LBL deposition of negatively charged poly(acrylic acid) (PAA) and positively charged poly(4-vinylpyridine) (PVP) on a glass substrate with the desired thickness, followed by etching out the PAA with a solution of pH 10. Further immersion in PVP induced the formation of nanopores by PVP dewetting through repulsive electrostatic interaction, and the final immersion in PAA enabled the PVP surface to be negatively charged for the subsequent growth of a smooth amorphous $CaCO_3$ mineral layer.[318]

With the rapid development of the information era, there are urgent demands for highly integrated chips aiming at large-scale data processing as well as power sources with high energy densities and small volumes for portability. The LBL assembly method can provide nanoscale accuracy of both material composition and architecture. It was demonstrated that wafer-scale semiconductor films with vertical compositions of atomic-scale precision could be acquired via LBL assembly facilitated by metal organic chemical vapor deposition (MOCVD). Two-dimensional building blocks of graphene and transition-metal dichalcogenides such as monolayer MoS_2, WS_2, and $MoSe_2$ one- and three-atom-thick were vertically stacked via van der Waals interactions, being able to be formulated into large-scale superlattice films, batch-fabricated tunnel device arrays, or band-engineered heterostructure tunnel diodes.[319] Oppositely charged reduced graphene oxide (rGO) sheets were employed to assemble multilayers held together by electrostatic interactions on interdigitated electrodes for the fabrication of solution-gated field-effect transistors (FETs) with high transconductance.[320] Negatively charged graphene oxide (GO) nanosheets and negatively charged polyoxometalate clusters ($H_3PW_{12}O_{40}$ (PW)) were able to be LBL assembled on the supporting substrates with the aid of positively charged PEI and poly(allylamine hydrochloride) (PAH) (Figure 17b). Because of the UV photoreduction and the photocatalytic activity of PW clusters, GO could be facilely converted to rGO with an enhanced conductivity, and the corresponding multilayered was utilized to fabricate FETs and photodetector devices.[321] As for batteries and fuel cells, all the cathodes, anodes, and electrolytes could take advantage of the LBL technique for higher performance. Sulfur as a conversion cathode has a higher theoretical capacity of 1672 mA h g^{-1} compared with the maximum capacity of ∼300 mA h g^{-1} for lithium-ion cathodes transition metal oxides, or phosphates. A nanostructured sulfur cathode was designed to strengthen the performance of Li−S batteries. The single sulfur particle was first embedded with hollow carbon nanospheres, which were then encapsulated into an ion-selective, flexible nanomembrane built up by LBL assembly of positively charged poly(diallyldimethylammonium chloride) (PDADMAC) and negatively charged poly(3,4-ethylenedioxythiophene)−poly(styrenesulfonate) (PEDOT:PSS) polyelectrolytes. The sequential adsorption of polyelectrolytes ended with PDADMAC and finally decorated the sulfur particles with conductive carboxyl-modified carbon.[322] Exoelectrogens hold great potential as bioanodes of photoassisted microbial fuel cells (MFCs) with surface modification of photoelectric materials. To avoid the poor conductivity of most photoelectric materials, the positively charged PDDA-protected conductive AuNPs and negatively charged 3-mercaptopropionic acid-modified photoresponsive CdS NPs were alternatively adsorbed onto the surface of *Escherichia coli* (*E. coli*) (Figure 17c). The photocurrent generated by the CdS layers upon solar light irradiation could transfer with the bioelectrons through the conductive AuNPs channel, enhancing the power output of the MFCs by 2.5-fold compared with unmodified *E. coli*.[323] As one of the most widely used polymeric ion conductors, PEG usually suffers from impairment of mechanical properties with the enhancement of ionic conductivity. Mechanically strong and self-healable solid electrolyte composite thin films with high lithium ion conductance of $2.3 \pm 0.8 \times 10^{-4}$ S cm^{-1} at 30 °C could be prepared by LBL self-assembly of PEG and PAA, where heat-induced covalent bonding between the terminal groups of PEO and the carboxyl groups of PAA and the hydrogen-bonding interaction between the etheric oxygens of PEO and the hydroxyl groups of PAA played a synergetic role.[324]

Functionalized coatings have attracted increasing attention in industrial fields such as clothing, food packaging, medical supplies, and construction materials, aiming at flame retardant/fire protection, healthy food packaging, antibacterial performance, anticorrosion, and so on, where the LBL technique provides an easy, cost-effective, and green way for surface nanostructuring. For instance, cationic starch and anionic poly(phosphoric acid) (PPA) solutions were alternatively

https://doi.org/10.1021/acs.chemrev.2c00215
Chem. Rev. XXXX, XXX, XXX−XXX

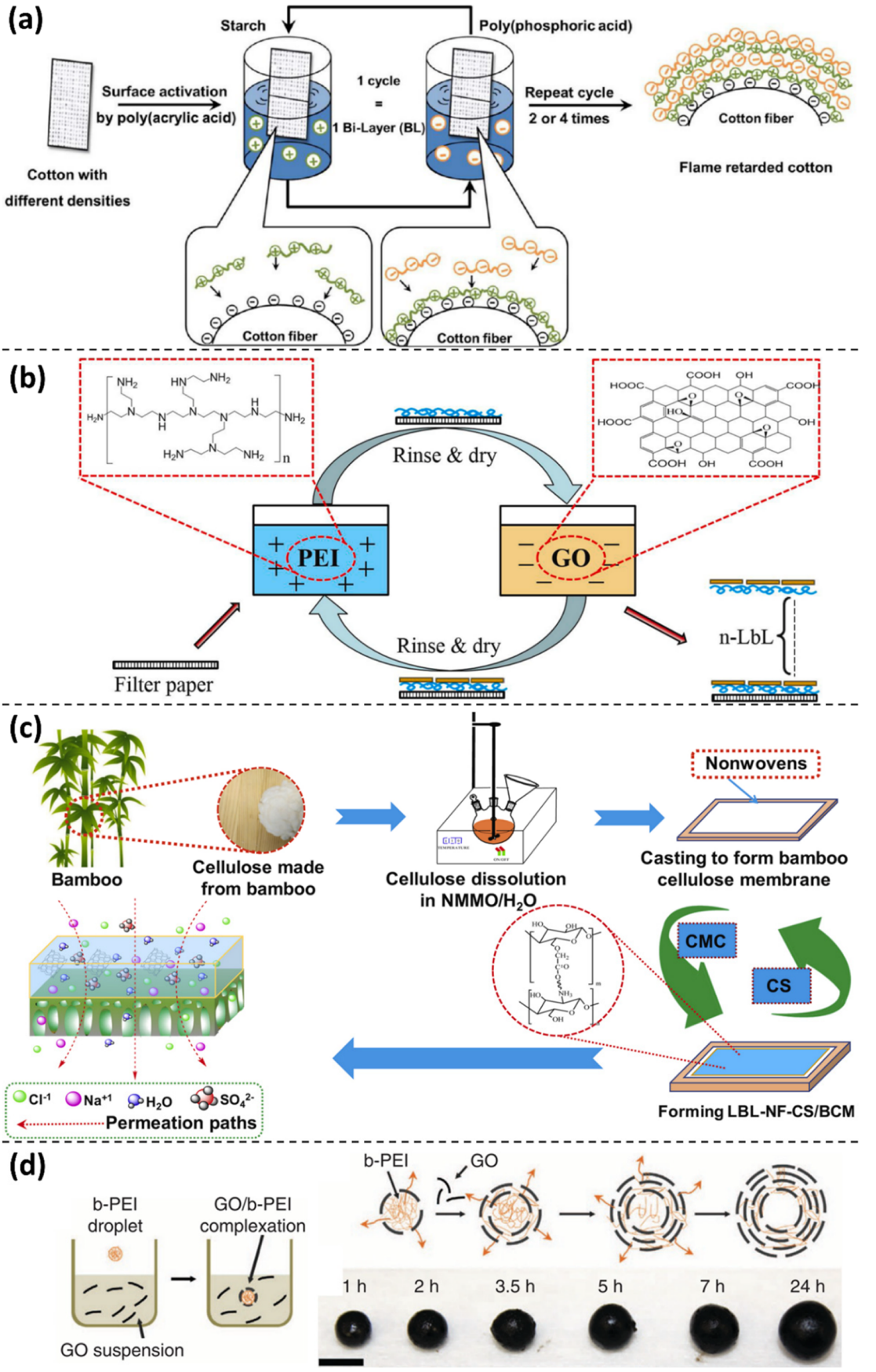

Figure 18. LBL assemblies for (a) cotton fire protection, (b) packaging of agriculture products, and (c) water treatment. (d) Novel LBL approach driven by diffusion. (a) Anionic PAA-treated cotton fabrics were modified with the fire-retardant LBL assembly of positively charged starch and

https://doi.org/10.1021/acs.chemrev.2c00215
Chem. Rev. XXXX, XXX, XXX−XXX

Figure 18. continued

negatively charged poly(phosphoric acid) (PPA). Reproduced with permission from ref 325. Copyright 2015 American Chemical Society. (b) Paper-based packaging materials functionalized by LBL assembly of cationic PEI and anionic GO showing capabilities of air barrier and water vapor permeability. Reproduced with permission from ref 330. Copyright 2021 Elsevier. (c) Bamboo cellulose-based nanofiltration membrane prepared by LBL assembly of anionic CMC and cationic CS for efficient sodium chloride removal. Reproduced with permission from ref 334. Copyright 2021 Elsevier. (d) LBL assembly of anionic GO nanosheets with controlled porous 3D macrostructures enabled by the diffusion of cationic branched PEI (b-PEI) (scale bar: 5 mm). Reproduced with permission from ref 340. Copyright 2014 Springer Nature.

dipped on poly(acrylic acid)-modified cotton fabrics to enhance the char forming ability of cellulose assisted by the dehydration ability of PPA (Figure 18a). It was reported that the deposition of only two bilayers could enable the cotton fabrics to self-extinguish a flame.[325] Similarly, positively charged chitosan and negatively charged phytic acid were alternatively coated on polyester/cotton blend fabrics to endow the substrate with eco-friendly flame retardant and dripping-resistant properties.[326] Besides, cationic PDDA, polyhedral oligomeric silsesquioxane or alumina-coated silica nanoparticles and anionic α-zirconium phosphate nanoplatelets could also be used to build flame retardant LBL-assembled multilayered coatings on textiles, respectively.[327] LBL-assembled colloidal multilayers, such as oppositely charged silica colloidal suspensions, could also be constructed to form fire protection coatings on fabrics.[328] When it comes to food packaging, the number of bilayers of LBL assembly plays a significant role, as it can influence the diffusion pathway of air. To build an excellent air barrier, anionic sodium montmorillonite clay and cationic polyacrylamide (PAM) were grown on a polyethylene terephthalate (PET) film with 30 clay−polymer bilayers, where the as-prepared transparent and microwaveable film possessed oxygen transmission rate (OTR) below the detection limit of commercial instrumentation (<0.005 cc/m^2/day/atm), holding great potential in the packaging of food and in flexible electronics.[329] Paper-based packaging materials treated with the LBL assembly technique could achieve an excellent air barrier and favorable water vapor permeability (WVP). It was demonstrated that 10 bilayers of LBL-assembled PEI and GO on a filter paper substrate could decrease air permeability by 99.99% as well as improve the WVP by 15.82% compared with the pristine substrate, being a good candidate for the preservation of agricultural products (Figure 18b).[330] Medical textiles and devices with antibacterial coatings are in urgent need to prevent healthcare-related infections, especially because of the COVID-19 epidemic since December 2019, because the SARS-CoV-2 virus would transmit via respiratory droplet-contaminated surfaces.[331] To address this issue, LBL assembly was exploited for the construction of antibacterial coatings on various surfaces. *N*-Halamines have been widely used as biocides ascribing to their superior antibacterial property against a broad spectrum of microorganisms through directly transferring oxidative halogen to cell membranes of microbials as well as being able to be simply replenished by aqueous chlorine exposure. Therefore, oppositely charged *N*-halamine copolymers could be repeatedly and sequentially deposited on the negatively charged bleached cotton fabrics to inactivate both *Staphylococcus aureus* (*S. aureus*) and *E. coli* O157:H7 within 15 min of contact time.[332] The corrosion of metals is one of the main destructive processes of metal structures, which would result in big economic losses. Although chromate-containing coatings can effectively provide corrosion protections, their applications are limited because the hexavalent chromium species have been demonstrated to be responsible for some diseases such as DNA damage and cancer. Hence, LBL assembly serves as an accessible approach to the fabrication of anticorrosive coatings with alternative layers. By the LBL technique, SiO_2-based nanoreservoirs were formed by alternating deposition of anionic PSS and cationic benzotriazole on cationic PEI-treated SiO_2 NPs, which were then incorporated into the matrix of a hybrid sol−gel protective coating to act as containers of corrosion inhibitors. Corrosion inhibitor benzotriazole exhibited prolonged release to damaged zones, endowing the protective coating with a self-healing ability.[333]

From the perspective of environmental engineering, both water treatment and gas monitoring (toxic, harmful, or humidity) have benefited from the LBL technique, by which multilayered membranes with desired functions can be fabricated via the manipulation of noncovalent interactions between various polyelectrolytes. An anionic carboxymethyl cellulose (CMC) solution and a cationic chitosan (CS) solution were sequentially sprayed onto a chitosan-incorporated bamboo cellulose-based membrane (BCM) until 15 bilayers were deposited, achieving a pore size of 2.2 nm (Figure 18c). The composite membrane exhibited a rejection rate of 36.11% against a 500 ppm of NaCl solution and a membrane flux of 12.08 L (m^2 h)$^{-1}$ under an ultralow pressure of 0.3 MPa, showing great potential for efficient sodium chloride removal.[334] Furthermore, the organic contaminants in saline wastewater could be readily purified by a hierarchical composite membrane with a robust omniphobic surface, which was fabricated via LBL assembly of cationic PDDA, anionic silica aerogel NPs, cationic PDDA, and anionic 1H,1H,2H,2H-perfluorodecyltriethoxysilane (FTCS) in sequence on a negatively charged polyvinylidene fluoride (PVDF) phase inversion membrane.[335] Forward osmosis (FO) membranes have attracted considerable attention in recent years because of their low energy consumption, as external pressures are not required during the purification process. When positively charged PAH and negatively charged GO nanosheets were alternately deposited on both sides of a negatively charged porous poly(acrylonitrile) (PAN) support, an LBL-assembled FO membrane was prepared and exhibited higher solute flux for ionic species than that for sucrose because of the swelling of the membrane in ionic solutions. The as-prepared FO membrane could be used to purify low ionic strength water with sugary draw solutions.[336] Nanofiltration (NF)-like FO membranes with good magnesium chloride retention were built up through the alternating deposition of cationic PAH and anionic PSS on negatively charged PAN.[337] LBL assembly has been demonstrated to serve as an intermediate template for the synthesis of metal oxide (e.g, In_2O_3) nanotubes with ultrahigh surface-to-volume ratios, generating excellent gas-sensing candidates. First, LBL assembly of cationic PDDA and anionic PSS was prepared on CNTs, which could absorb $InCl_3$ and citric acid onto the surface via electrostatic interactions. Porous and polycrystalline In_2O_3 nanotubes were attained through the reduction of In^{3+}, following the oxidation of In, and the final calcination of In_2O_{3-x}, showing a superior sensitivity to the detection of NH_3

https://doi.org/10.1021/acs.chemrev.2c00215
Chem. Rev. XXXX, XXX, XXX−XXX

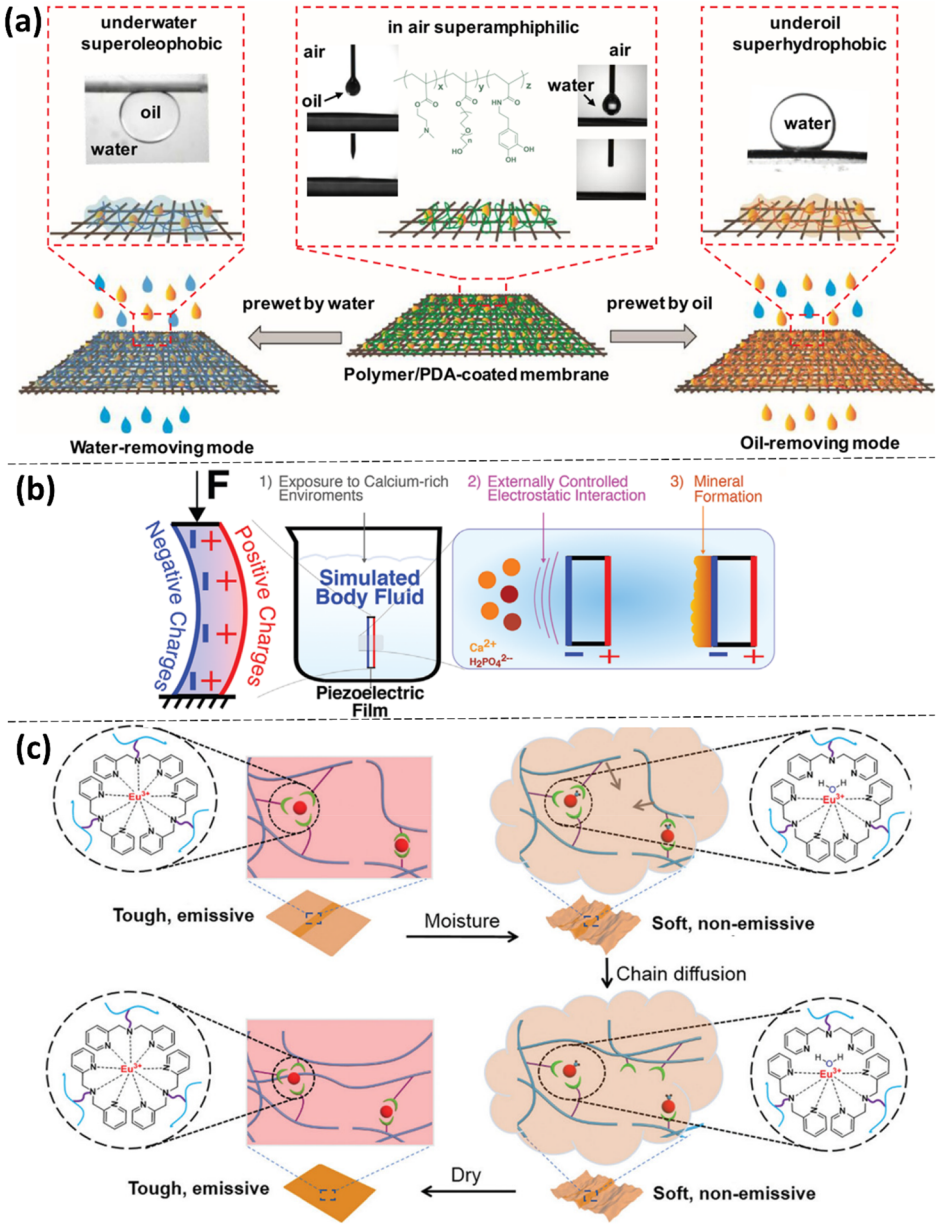

Figure 19. Adaptable films/membranes. (a) Polymer membrane with adaptable wettability enabled by prewetting of targeting oil or water. Reproduced with permission from ref 347. Copyright 2020 Elsevier. (b) Tunable mineralized film grown on the negatively charged surface of the piezoelectric PVDF film with loading-induced oppositely charged surfaces. Reproduced with permission from ref 348. Copyright 2020 John Wiley & Sons. (c) Polymer film with switchable mechanical and fluorescent properties enabled by metal coordination. Reproduced with permission from ref 349. Copyright 2020 The Royal Society of Chemistry.

(at 25 ppm).[338] Humidity monitoring was realized by measuring the resistance of two parallel metal electrodes that were vapor deposited on an LBL-assembled composite film, which was prepared by alternating deposition of cationic PEI and anionic carboxy group-decorated MWCNTs on a glass substrate.[339]

The development of the LBL technique has been accelerated via the manipulation of noncovalent interactions. For example, it was reported that diffusion-driven LBL assembly of GO nanosheets could enable the construction of functional macroscale architectures with controlled size and shape from tiny building blocks. In this case, droplets of a positively charged branched PEI solution were added into a suspension of negatively charged GO nanosheets, where a layer of PEI-GO complex formed around the droplets and further grew into a LBL 3D macrostructure driven by diffusion of PEI from the inner droplet to the outside (Figure 18d).[340] When neutral and hydrophobic materials are used as substrates for LBL assembly, harsh chemical or physical treatments are usually required to modify the surfaces with specific charged groups. To achieve substrate-independent deposition, mussel-adhesive-inspired catechol-containing and amine-rich polymers were employed, because of their robust adhesion on multifarious substrates through the synergy of bidentate hydrogen bonding and electrostatic interactions. It was demonstrated that catechol-functionalized cationic PEI and catechol-functionalized anionic HA could be alternatingly deposited on various untreated substrates such as poly(tetrafluoroethylene) (PTFE), polyethylene (PE), poly(ethylene terephthalate) (PET), polycar-

https://doi.org/10.1021/acs.chemrev.2c00215
Chem. Rev. XXXX, XXX, XXX−XXX

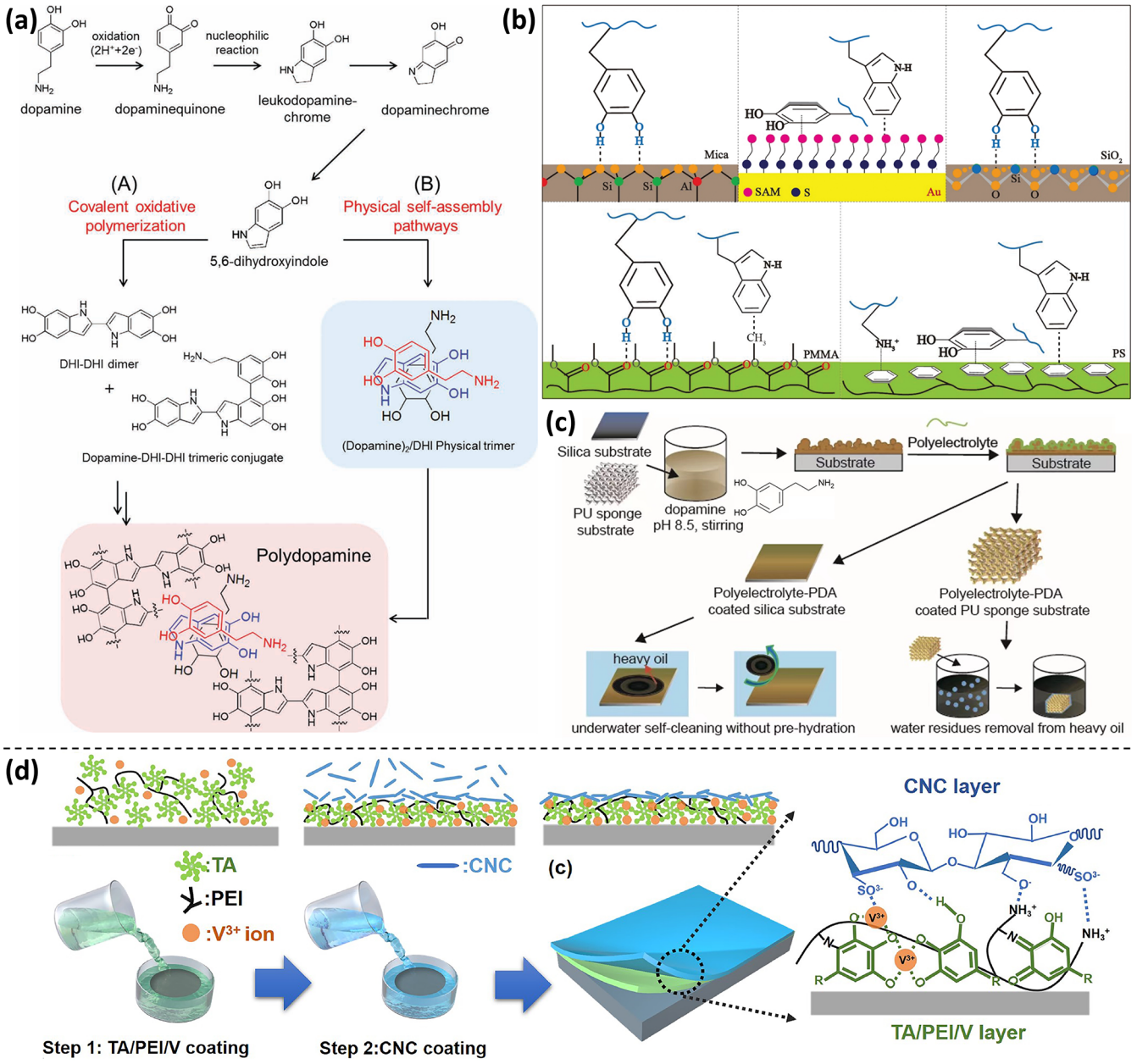

Figure 20. PDA and PDA-inspired coatings as adhesive layers in coating technology. (a) Proposed mechanism of the formation of PDA coating, involving covalent oxidation polymerization and noncovalent self-assembly. Reproduced with permission from ref 357. Copyright 2012 John Wiley & Sons. (b) PAD coating exhibits robust adhesion on various substrates such as mica, methyl-terminated self-assembled monolayers (SAMs), SiO_2, poly(methyl methacrylate) (PMMA), polystyrene (PS) via various physical noncovalent molecular interactions. Reproduced with permission from ref 358. Copyright 2019 The Royal Society of Chemistry. (c) PDA coating grafted with zwitterionic polyelectrolyte to serve as underwater self-cleaning substrate and sponge for removing water residues from heavy oil. Reproduced with permission from ref 360. Copyright 2018 Royal Society of Chemistry. (d) Film of TA/PEI/V^{3+} complexes serves as an adhesive layer for the deposition of cellulose nanocrystals (CNCs) toward an antifouling coating. Reproduced with permission from ref 371. Copyright 2021 John Wiley & Sons.

bonate (PC), poly(methyl methacrylate) (PMMA), Au, and SiO_x, in a stable and controllable way. Besides, the latent redox property of catechol could reduce metallic ions (e.g., Ag^+) into NPs, endowing the LBL-assembled multilayers with additional functions such as antibacterial activity and antifouling property.[341] Reiterative rinsing is generally inevitable during the LBL process in order to get rid of the excessive unstably absorbed components. To avoid the time-consuming and water-wasting operations, dewetting effect was introduced to the LBL method to provide the solid−liquid interfaces with self-cleaning ability, significantly reducing the time for the multilayer formation.[342] The LBL technique was also combined with electrodeposition toward the construction of superhydrophobic surfaces, which was realized by potentiostatically electrodepositing Ag aggregates on an LBL-assembled PDDA/PSS polyelectrolyte multilayer followed by chemisorption of a self-assembled monolayer of *n*-dodecanethiol.[343] To expand the materials for fabricating LBL-assembled multilayer films/membranes, hydrogen bonding (e.g., between PVA and PAA),[344] host−guest interactions (e.g., between cyclodextrin group and azobenzene group),[345] halogen bonding (usually involving a halogen as halogen bonding donor and a Lewis base

https://doi.org/10.1021/acs.chemrev.2c00215
Chem. Rev. XXXX, XXX, XXX−XXX

as halogen bonding acceptor)[346] have also been utilized to build LBL structures.

3.2.2. Adaptable Films/Membranes. Adaptable films/membranes are capable of switching their innate properties (e.g., wettability, stiffness) to accommodate the changes of environments, holding great promise for engineering and biological applications such as oil/water separation, bone regeneration, etc.[347−349] Zeng and co-workers designed an amphiphile synthetic copolymer membrane, which was deposited on a steel mesh with an intermediate PDA layer, showing adaptable wettability upon prewetting the membrane with water or oil.[347] As shown in Figure 19a, PEG side chains, catechol groups, and tertiary amine groups were simultaneously incorporated into the copolymer. When the membrane was prewetted by water, the hydrophilic PEG side chains, catechol groups, and ionized quaternary amine groups would be saturated by water, and the formed water film could prevent the penetration of oil, offering the membrane underwater superoleophobicity. In contrast, when the membrane was prewetted by oil, the hydrophobic dimethyl groups and aromatic rings would induce the generation of an oil film, impeding the interactions between water molecules and the polymer membrane and endowing the membrane with underoil superhydrophobicity. Therefore, the substrate-independent adaptable membrane could be applied to on-demand oil/water separation by facilely modulating the properties of the membrane surface. Likewise, catechol-rich tannic acid and diethylenetriamine were directly codeposited on a commercial polypropylene membrane to endow the membrane with switchable wettability, where the hydrophobicity of this membrane was induced by immersion in ethanol. It was proposed that the superhydrophilicity was caused by the deprotonation of the phenolic groups of tannic acid when soaked in water, and the superhydrophobicity of the membrane was driven by the strong hydrogen bonding between the protonated tannic acid and diethylenetriamine which would repel the penetration of water.[350] Apart from adaptable films/membranes with switchable wettability, some films/membranes could exhibit enhanced stiffness upon external stress.[348] Human tissues such as bone, teeth, and coral reefs are capable of adjusting their mechanical properties to resist external loading, and their adaptive properties have attracted numerous research interests in the development of biomimic self-stiffening materials.[348,351] Through imitating bone's control in adding or removing substances collected from surrounding media such as blood according to cellular signals, a piezoelectric polyvinylidene fluoride (PVDF) membrane was utilized as the substrate to build adaptable films. A PVDF membrane with oppositely charged surfaces induced by external bending force was immersed in a simulated body fluid (SBF). The mineralized film significantly accumulated on the negatively charged surface because of that the electrostatic interaction-driven adsorption of Ca^{2+} initiated the nucleation of hydroxyapatite and/or calcite depending on the composition of the SBF (Figure 19b). The strategy could not only stiffen films/membranes but also be able to construct graded materials by controlling the deformation of the piezoelectric PVDF film. On the contrary, some polymer films could soften themselves in response to the surrounding environment such as moisture, which have also benn utilized to modulate the mechanical property of polymer films.[349] For instance, a tough polymer film, poly(*n*-butyl acrylate-*co*-2-hydroxy-3-dipicolylamino methacrylate) (P(*n*BA-*co*-GMADPA)), was prepared via metal coordination between Eu^{3+} and dipicolylamine (DPA) groups (Figure 19c). When exposed to moisture, the polymer film would be softened via the dissociation of metal coordination and the generation of hydrogen bonds between Eu^{3+} and water molecules, which could restore the toughness after drying in N_2. The chain mobility-induced softening was usually accompanied by the reduction of the fluorescence intensity of Eu^{3+} ions, allowing accurate detection of the mechanical property by optical readout. Replacing the DPA groups with iminodiacetate (IDA) groups could also resulted in tough polymer films with moisture-endowed switchable mechanical and fluorescent properties.[352]

3.2.3. Adhesive Layer in Coating Technology. The adhesive layer plays an important role in constructing films/membranes on a certain substrate. For example, LBL deposition of polyelectrolytes usually requires the pretreatment of the substrates with charged substances, and metal or inorganic oxide substrates are generally linked to polymer coatings via thiols or silanes.[353,354] In 2007, Lee and Messersmith reported that PDA could act as a universal adhesive layer between various substrates and functional coatings, providing a versatile strategy for substrate-independent surface modification.[355,356] The formation of PDA was ascribed to the synergy of covalent polymerization and noncovalent self-assembly (numerous possible intermolecular interactions such as ionic, cation−π, $\pi-\pi$, quadrupole−quadrupole and hydrogen-bonding interactions) as illustrated in Figure 20a,[355,357] and the resultant coating could strongly bind to a variety of substrates (e.g., mica, methyl-terminated self-assembled monolayers (SAMs), SiO_2, poly(methyl methacrylate) (PMMA), polystyrene (PS)) via multiple noncovalent interactions such as bidentate hydrogen bonds, hydrophobic interactions, cation−π interactions, and/or $\pi-\pi$ interactions (Figure 20b).[358] Biomolecules can be covalently immobilized on PDA coatings through the reactions between PDA and the amine/thiol groups of the biomolecules.[359] A polyelectrolyte coating composed of zwitterionic polymer poly(3-[dimethyl(2-methacryloyloxyethyl)-ammonium]propanesulfonate) (PMAPS) was fabricated via Michael addition between the quinone groups of PDA and thiol groups of PMAPS (Figure 20c),[360] which exhibited a self-cleaning ability underwater and could separate water residues from heavy oil. Similarly, chitooligosaccharide (COS) was anchored onto a polyurethane (PU) membrane through an adhesive PDA layer, imparting the membrane with an enhanced antibacterial activity and cytocompatibility.[361] Lee and co-workers decorated growth factors and adhesive peptides with thiol and amine groups, which could be anchored to various substrates through a PDA coating, improving the differentiation and proliferation of human neural stem cell (NSC).[362] Noncovalent interactions are extensively exploited to immobilize polymer coatings on the PDA layer. A PDA-assisted hydroxyapatite formation (pHAF) method was reported as a universal strategy to mimic the biomineralization of bone tissue, where the PDA coating could enrich Ca^{2+} via metal coordination to promote its nucleation and growth in the form of hydroxyapatite crystals. The as-formed mineral layer showed the same alignment of crystals in bone tissues, holding great promise as the next-generation mineralized materials.[363] To simplify the coating process, a one-step surface modification strategy was presented, where the targeting molecules were mixed with dopamine in the solution and then deposited on the substrate via the polymerization of dopamine.[364,365] In addition to PDA, other catechol-containing materials including plant-derived tannic acid (TA), gallic acid, pyrogallol, catechin, epigallocatechin, epicatechin gallate, epigallocatechin gallate,

https://doi.org/10.1021/acs.chemrev.2c00215
Chem. Rev. XXXX, XXX, XXX−XXX

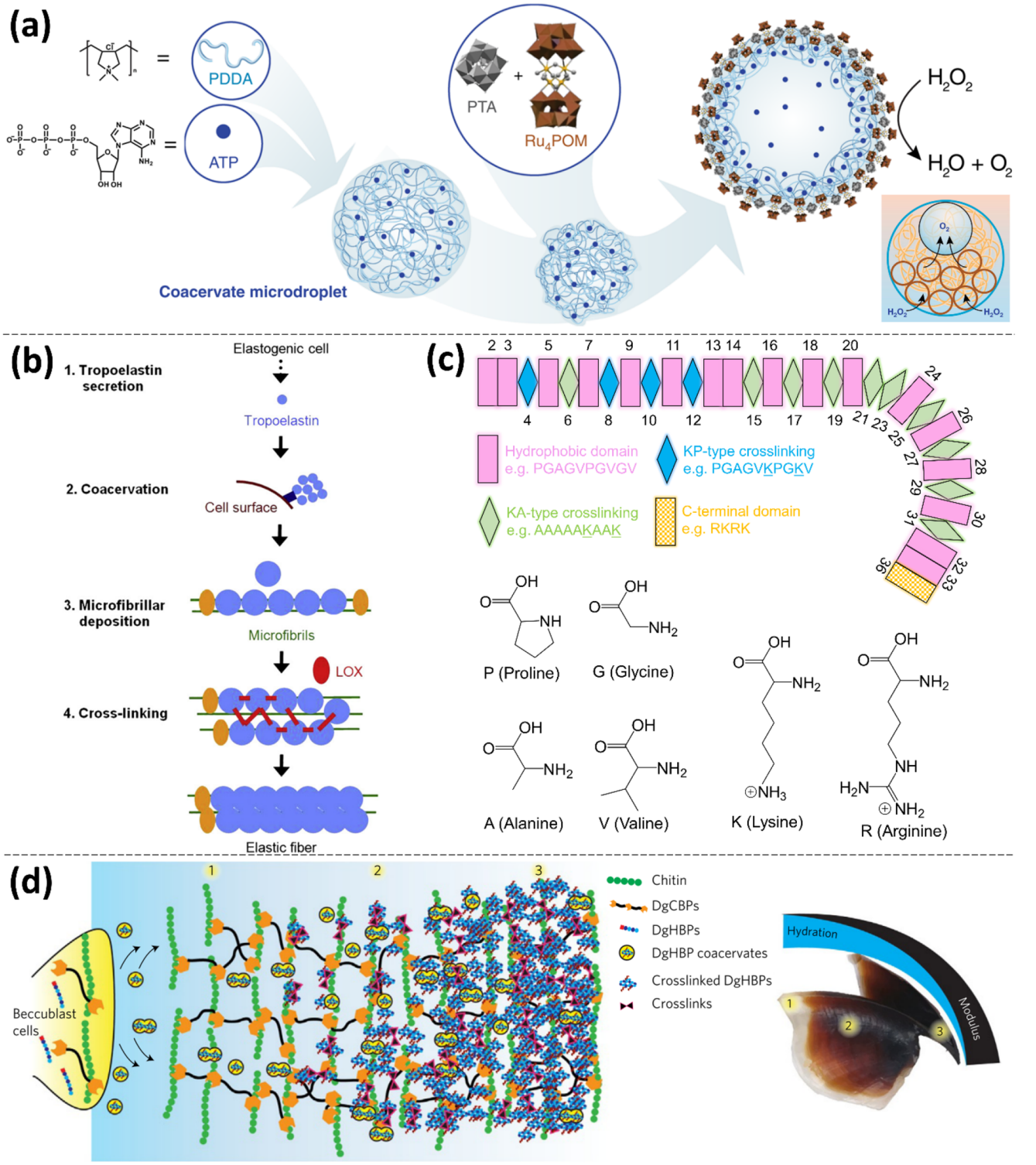

Figure 21. Coacervate-based biological tissues. (a) Coacervate droplets driven by electrostatic interaction between cationic PDDA and anionic ATP. The coacervate droplets were then circumvented by the membrane of polyelectrolyte complexes formed from positively charged PDDA and negatively charged PTA and Ru_4POM. The redox property of Ru_4POM could decompose H_2O_2 into H_2O and O_2. Reproduced with permission from ref 383. Copyright 2020 Springer Nature. (b) Transition processes of tropoelastin into an elastic fiber. Reproduced with permission from ref 378. Copyright 2011 Elsevier. (c) Exons sequence of the mature human tropoelastin and the molecular structures of some related amino acids. (d) Schematic mechanism of the formation of a squid beak. Reproduced with permission from ref 374. Copyright 2015 Springer Nature.

hydroxyhydroquinol, morin, bioderived neurotransmitter norepinephrine, and dihydroxybenzaldehyde have been explored as adhesive layers.[366,367] For instance, the neurotransmitter norepinephrine has been successfully employed as a substrate-independent surface modification reagent in a similar way to dopamine.[368] Zeng and co-workers developed a universal strategy for the construction of robust and antifouling coatings through a TA-containing adhesive layer, where the super-

https://doi.org/10.1021/acs.chemrev.2c00215
Chem. Rev. XXXX, XXX, XXX−XXX

hydrophilic cellulose nanocrystals (CNCs) were adsorbed on the intermediate adhesive layer of TA/PEI/V^{3+} via electrostatic interaction between sulfonate groups and PEI/V^{3+} as well as multiple hydrogen bonds between hydroxyl moieties and catechol groups (Figure 20d). Moreover, dopamine and catechol groups could be directly incorporated into polymers, simultaneously acting as an adhesive layer and a functional coating.[369,370]

3.3. Coacervate Systems

Coacervation is a liquid−liquid phase separation phenomenon, where the material-rich coacervate phase is dispersed in the material-sparse supernatant phase. The coacervate droplets were considered as possible protocells related to the origin of life, which could dynamically concentrate nutritious materials within certain bounded spaces[372] and protect nutritious substances from decomposition caused by UV radiation.[373] Coacervation has been demonstrated to play a significant role in constructing protoplasm, extracellular matrix, mechanical gradient materials (squid beak), skin, lung, blood vessels, sessile organisms' wet adhesives, and so on.[374−378] The driving force of coacervation has expanded from electrostatic interaction to various physical noncovalent interactions such as hydrophobic interaction, hydrogen bonding, and cation−π interaction, facilitating the development of diverse functional materials.[379] The following section focuses on the formation of coacervate-based biological tissues and adhesives with the modulation of noncovalent interactions.

3.3.1. Coacervate-Based Biological Tissues. Coacervation plays a vital role in the formation of diverse biological tissues such as organelles, protocells, skin, lungs, blood vessels, and mechanically gradient materials (e.g., squid beak). For example, P granules, as a membrane-less organelle to regulate germ cell biology across animal cells, were proposed to be generated by intracellular phase separation. It was demonstrated that the *Caenorhabditis elegans* protein LAF-1 (an RNA helicase) in P granules could undergo self-coacervation to form P granule-like droplets in vitro. Further sequence analysis revealed that the intrinsically disordered RGG domain of the LAF-1 protein was responsible for the coacervation. As the RGG domain simultaneously possessed abundant positively charged arginine and negatively charged aspartic acid and glutamic acid, the electrostatic interactions between them allowed the occurrence of the coacervation.[380] Because of the tunable phase separation enabled by sequence modification, the RGG domain derivatives were developed as responsive drug carriers.[381] A membrane-free protocell model was constructed with negatively charged low-molecular-weight mononucleotides such as nucleoside triphosphates and positively charged peptides like polylysine. The electrostatic interaction-driven nucleotide−peptide coacervate microdroplets could serve as an all-purpose paradigm to encapsulate energy-rich molecules, shedding light on the development of prebiotic metabolic building blocks.[372] Similarly, coacervation between anionic carboxymethyl dextran sodium salt (CM-Dex) and cationic polylysine resulted in a membrane-free protocell model, which could support isolated RNA catalysis, selectively concentrate ribozymes, and allow the exchanging of low-molecular-weight oligonucleotides.[382] A membrane-bounded protocell model with catalytic property was proposed by Mann and co-workers. The coacervate droplets were generated upon mixing positively charged polydiallyldimethylammonium chloride (PDDA) and negatively charged adenosine 5′-triphosphate (ATP) aqueous solutions (Figure 21a). Herein, the corresponding membranes were formed with the sequential addition of sodium phosphotungstate ($[PW_{11}O_{39}]^{7-}$, PTA) and a Ru(IV)-based polyoxometalate polyanionic catalyst $Na_{10}[Ru_4(\mu\text{-}O)_4(\mu\text{-}OH)_2(H_2O)_4(\gamma\text{-}SiW_{10}O_{36})_2]$ (Ru_4POM), which interacted with cationic PDDA to form a membrane of polyelectrolyte complexes. With the introduction of H_2O_2, it would be decomposed into H_2O and O_2 because of the redox active sites of the Ru_4POM, imitating the production of O_2 during photosynthesis.[383] Elastin is the key component of elastic fibers, which offers elasticity to various tissues including skin, lungs, blood vessels, etc. The precursor of elastin is a soluble tropoelastin secreted by elastogenic cells, which undergoes coacervation to aggregate as spherical globules on the cell surfaces, followed by the deposition on microfibrillar bundles and the further cross-linking into elastic fibers (Figure 21b).[378] As shown in Figure 21c, mature human tropoelastin is composed of 32 exons with alternating hydrophobic domains, KP-type cross-linking domains, and KA-type cross-linking domains, where the percentage of the hydrophobic domains is about 53%.[384] The KP-type and KA-type domains are critical for tropoelastin coacervate droplets to convert into fibrous elastic networks, while the hydrophobic domains are responsible for the coacervation process induced by temperature. The hydrophobic domains are rich in proline (P, hydrophobic), valine (V, hydrophobic), and glycine (G, hydrophilic for solubility in aqueous media) residues, which are usually arranged in the array of VPG or PGVG. Nose and co-workers verified that the synthesized dimeric elastin-like peptides (ELPs) analogue ($H\text{-}C(WPGVG)_3\text{-}NH_2)_2$ (W, tryptophan) could go through reversible and temperature-controlled coacervation at a critical concentration.[385] Tropoelastin with excellent biocompatibility was modified with methacryloyl, where coacervation could occur, and the coacervate would be formed at body temperature followed by photopolymerization to fulfill the function of a sealant.[386] Coacervation has been demonstrated to be a key procedure toward an elastin membrane, and recombinant ELPs were harnessed to investigate medial arterial calcification.[387] Both linear and dendritic/branched ELPs with the same number of GLPGL (L, leucine) pentamer repeat units possessed an intramolecular second structure transition in response to temperature and could undergo hydrophobic interaction-driven coacervation, where the dendritic ELPs required a higher temperature to induce the intramolecular second structure transition.[388] ELPs have also been widely exploited as drug carriers as they could be easily functionalized with both hydrophobic and hydrophilic blocks, encapsulating either hydrophobic or hydrophilic drugs because of the temperature-dependent hydrophobic interaction-driven coacervation or hydrophobic interaction-directed self-assembly.[389] Except for membrane-free organelles, protocells, and elastin, mechanical gradient materials such as squid beak (the difference of stiffness between dehydrated distal rostrum and the hydrated chitin of the soft beak base is 200 times) were found to be related with coacervation.[374,390] It was revealed that the squid beak contained two protein families. One of them was the *Dinomyrmex gigas* chitin-binding proteins (DgCBPs) responsible for the construction of chitin scaffolds, and the other one was the *D. gigas* histidine-rich beak proteins (DgHBPs).[374] The secreted DgHBPs could become a coacervate in seawater and directionally penetrate into the chitin scaffolds because of the innate low interfacial tension and shear thinning property of the coacervate (Figure 21d). The GHGXY (H, histidine; Y,

https://doi.org/10.1021/acs.chemrev.2c00215
Chem. Rev. XXXX, XXX, XXX−XXX

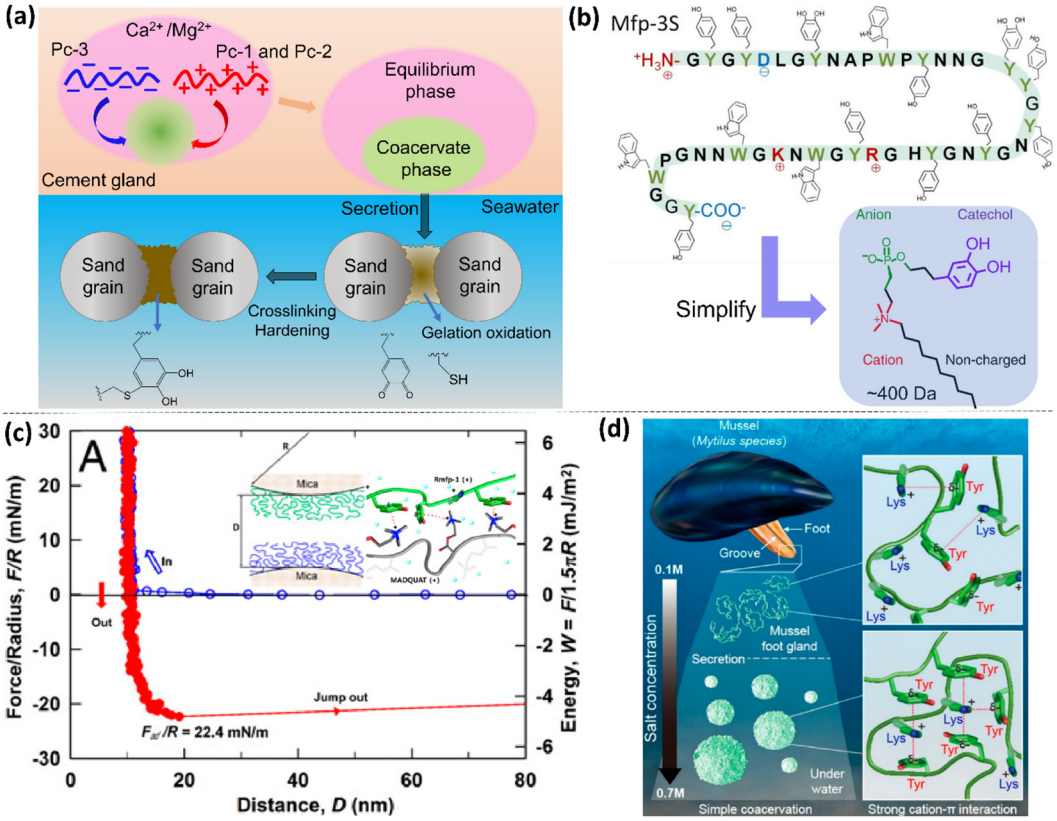

Figure 22. Coacervate adhesives of sessile organisms. (a) Formation process of sandcastle worm's wet adhesive. (b) Amino acid sequence of Mfp-3S and the structure of a designed simplified molecule mimicking Mfp-3 with dimethylamine, phosphate, catechol, and alkyl groups. Reproduced with permission from refs 397, 398. Copyright 2014 Elsevier. Copyright 2015 Springer Nature. (c) Force−distance profiles of the intermolecular interactions between Rmfp-1 film and MADQUAT film coated on mica surfaces. Reproduced with permission from ref 399. Copyright 2016 National Academy of Sciences. (d) Salt-triggered simple coacervation of Rmfp-1 enabled by strong short-range cation−π interactions between the amine groups of lysine and the aromatic rings of tyrosine. Reproduced with permission from ref 400. Copyright 2017 American Chemical Society.

tyrosine) motif of DgHBPs played a crucial role in coacervation, where the X usually denoted hydrophobic valine or leucine. It was proposed that the coacervation of the DgHBPs was first initiated by the hydrogen bonding between the hydroxyl groups of tyrosine and the deprotonated amine groups of histidine, strengthened by the hydrophobic interactions at specific pH and ionic conditions, and stabilized by the $\pi-\pi$ interaction between the hydrophobic aromatic rings of tyrosine.[391] The coacervation of an Alzheimer-related protein Tau was also reported, which generated aggregations of amyloid-promoting elements of Tau when the positively charged lysine-rich microtubule-binding domain of Tau interacted with the negatively charged surrounding molecules such as heparin or ribonucleic acids (RNA). Solid-like neurotoxic deposits were then formed via further cross-linking.

3.3.2. Coacervate Adhesives. Coacervation has been demonstrated to be a key process in the formation of wet adhesives secreted by sessile organisms,[376,392] which was first reported by Stewart et al. using oppositely charged polyacid and polybasic glue proteins secreted by sandcastle worms' glands.[393] Sequence analysis of the proteinous adhesive reveals that Pc-1 and Pc-2 proteins are positively charged with abundant glycine, lysine, and tyrosine groups, while Pc-3 proteins are rich in tyrosine and serine with a molar percentage of 60−90%, most of which are postphosphorylated into negatively charged phosphoryl groups. The tyrosine groups can be modified into DOPA moieties, some of which would react with cystine in Pc-1, Pc-2, and Pc-3 proteins, forming 5-*S*-cysteinyl−DOPA cross-links. As illustrated in Figure 22a, the separately secreted cationic Pc-1, Pc-2 proteins and anionic Pc-3 proteins interacted with each other within the cement glands at an acidic condition (pH ∼ 5) in the presence of Ca^{2+}/Mg^{2+}, yielding a coacervate phase via electrostatic interactions. Successively, the viscous proteinous coacervate was excreted out of the specific glands of the sandcastle worm to target positions, during which the gelation of the coacervate was induced by the lowered concentration of Ca^{2+}/Mg^{2+} as well as the oxidation of DOPA in the seawater (pH ∼ 8).[394] To mimic the formation of the wet adhesive, oppositely charged polyelectrolytes are employed, where the positively charged polymers were usually functionalized with amine groups while the negatively charged polymers generally contained phosphoryl and DOPA groups.[395,396] For example, DOPA-containing polyphosphate and polyaminated gelatin were utilized to form an adhesive coacervate with the addition of divalent cations (e.g., Ca^{2+}, Mg^{2+}). It was noted that the ratio of phosphate group, amine group, and divalent cations should be carefully maintained in a specific range to guarantee the balance of electrostatic interactions and prevent the formation of a solution, gel, or aggregates. The cured coacervate adhesive exhibited a shear strength up to 765 kPa between polished aluminum adherends, which was over twice that of the natural *Phragmatopoma californica* adhesive.[395] To further reinforce the adhesive strength of the synthesized coacervate, a second polymer network was introduced into the coacervate phase by

https://doi.org/10.1021/acs.chemrev.2c00215
Chem. Rev. XXXX, XXX, XXX−XXX

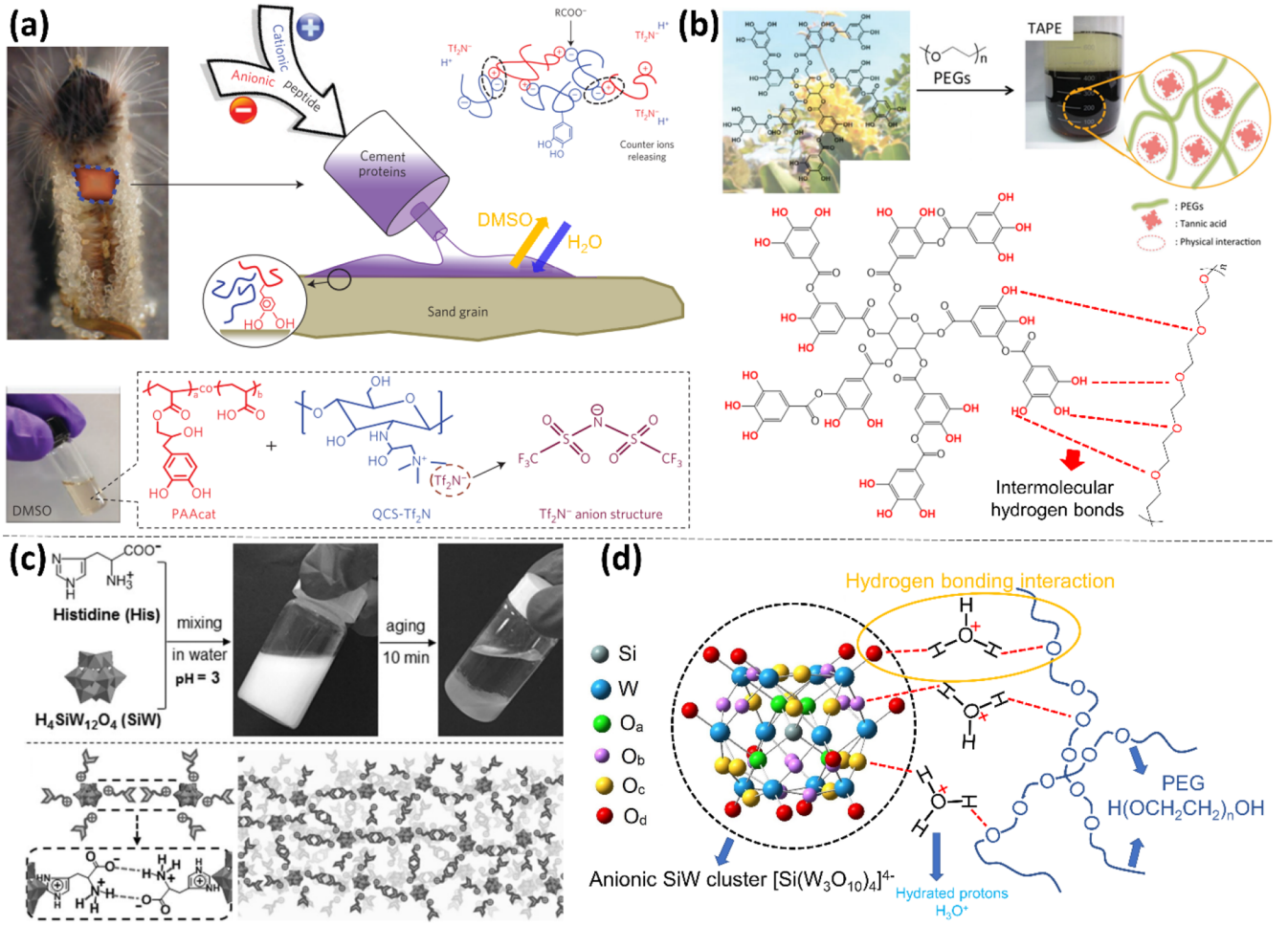

Figure 23. Sessile organism-inspired coacervate adhesives. (a) Electrostatic interaction-driven coacervate adhesive enabled by solvent exchange. Reproduced with permission from ref 401. Copyright 2016 Springer Nature. (b) Hydrogen bonding-actuated coacervation between tannic acid and PEG. Reproduced with permission from ref 403. Copyright 2015 John Wiley & Sons. (c) Coacervate adhesive based on the assembly of SiW and histidine via the synergy of electrostatic interactions and hydrogen bonding. Reproduced with permission from ref 405. Copyright 2017 John Wiley & Sons. (d) Coacervate adhesive formed from one-step mixing of SiW and PEG was driven by hydrogen-bonding interactions. Reprinted with permission from ref 406. Copyright 2020 John Wiley & Sons.

adding polyethylene glycol diacrylate (PEG-dA) monomers, leading to an elevated shear strength up to 1.2 MPa.[396] Israelachvili and Waite et al. reported that a mussel foot protein (mfp) Mfp-3S (Figure 22b) alone could undergo coacervation, which played a critical role in the formation of mussels' adhesive plaques.[397] Because of the pH and ionic strength dependence of the liquid−liquid phase separation, electrostatic interactions were considered as the main driving force for the self-coacervation of the Mfp-3S. Although Mfp-3S is a zwitterionic protein with abundant hydrophobic amino acid residues, it is generally positively charged, which can dissolve in a buffer solution with low pH and low monovalent salt concentration because of the long-range EDL repulsion. With the increase of ionic strength and pH, EDL repulsion would be screened and electrostatic interactions between oppositely charged groups would be maximized, resulting in the coacervation process. The contribution of hydrophobic interaction to the coacervation should not be overlooked considering the high percentage of hydrophobic amino acid residues. To reduce the complexity of the natural adhesive protein, a low-molecular-weight molecule with dimethylamine, phosphoryl, catechol, and hydrophobic alkyl groups was designed as depicted in Figure 22b to mimic Mfp-3.[398] As the imitated molecule bearing both hydrophobic and hydrophilic groups, its critical aggregation concentration (CAC) was investigated with a variable length of the alkyl tail. It was reported that the surfactant with ten carbons in the alky tail could spontaneously undergo liquid−liquid phase separation when the concentration was over 100 mg mL^{-1}. The driving force of the coacervation was ascribed to the synergy of hydrophobic interactions (among alkyl groups to initiate the self-assembly of micelles), electrostatic interactions (between zwitterionic domains for both micelle assembly and the physical cross-linking among micelles), and hydrogen bonding (bidentate hydrogen bonds between catechol groups for physical cross-linking among micelles). The resultant coacervate adhesive exhibited a strong wet adhesion of ∼50 mJ m^{-2}. Although electrostatic interactions between opposite charges have long been considered as the primary driving force for the coacervation of mfps, most of the known mfps are net positively charged and abundant in aromatic residues, and negatively charged mfp has not been reported.[399] For example, recombinant mfp-1 (Rmfp-1, $M(AKPSYPPTYK)_{12}$; M, methionine; S, serine; Y, tyrosine; T, threonine) is composed of equal molar amount (∼19.8%) of cationic lysine and aromatic

https://doi.org/10.1021/acs.chemrev.2c00215
Chem. Rev. XXXX, XXX, XXX−XXX

tyrosine. Therefore, cation−π interactions between the positively charged groups and aromatic rings can serve as an impetus to initiate coacervation. Similarly charged Rmfp-1 and poly(2-(trimethylamino)ethyl methacrylate) (MADQUAT) have been demonstrated to undergo coacervation in the presence of high-concentration sodium chloride, which was induced by the strong short-range cation−π interactions between the positively charged trimethylammonium group and the aromatic phenolic group of Rmfp-1 to overcome the electrostatic repulsion (Figure 22c). Furthermore, Zeng and Hwang et al. reported that cation−π interaction-enabled coacervation could occur within a single Rmfp-1, triggered by salt concentration at seawater level (>0.7 M) (Figure 22d), which screened the long-range electrostatic repulsion between positively charged amine groups.[400]

Inspired by the excellent adhesiveness of sessile organisms' coacervate, the coacervation phenomenon has been explored for the development of wet and underwater adhesives. For example, a catechol-modified PAA (PAAcat) and a quaternized chitosan ion-paired with bis(trifluoromethane-sulphonyl)imide (Tf_2N^-) (QCS-Tf_2N) were simultaneously dissolved in dimethyl sulfoxide (DMSO). After injection into water, the solvent exchange between DMSO and water triggered the deprotonation of the carboxyl groups of PAAcat, resulting in the formation of a coacervate via the electrostatic interactions between the anionic PAAcat and cationic QCS-Tf_2N (Figure 23a). The rapid setting of the coacervate phase was achieved by continuous solvent exchange, leading to a robust wet adhesion of 2 J m^{-2}.[401] To simplify the polymer synthesis, plant-derived sulfonate group-rich lignin was employed as the negatively charged component to form coacervate with a positively charged polyamidoamine epichlorohydrin (PAE-Cl, inexpensive industrial additive). The resultant coacervate could achieve an underwater adhesion up to 400 kPa after the ring-open cross-linking reaction between the azetinidium and amine groups, which was inhibited in acidic conditions and activated in neutral and basic environments.[402] Other noncovalent interactions such as hydrogen bonding have also been exploited for the fabrication of coacervate adhesives.[403,404] Lee and co-workers showed that plant-derived tannic acid could interact with linear and 4-arm PEG to generate a coacervate adhesive (TAPE) through the intermolecular hydrogen bonds formed between the hydroxyl groups of tannic acid and the etheric oxygens of PEG (Figure 23b). The as-prepared coacervate adhesive exhibited a wet adhesion strength up to 180 kPa between porcine skins without further cross-linking and successfully served as an effective hemostatic.[403] Zeng and co-workers improved the system by replacing the PEG/4-arm PEG with poly(ethylene glycol)$_{77}$-*b*-poly(propylene glycol)$_{29}$-*b*-poly(ethylene glycol)$_{77}$ (PEG-PPG-PEG, F68) micelles, where the hydrophobic core of the micelles offered additional cross-linking to enhance the mechanical property of the coacervate adhesive. The coacervate adhesive exhibited instant and repeatable underwater adhesion with adhesion strength up to 1.1 MPa on porcine skin and of 602.1 kPa on a poly(methyl methacrylate) (PMMA) substrate.[404] Inorganic materials have been harnessed to endow the coacervate adhesive with multifunctionalities such as an electrochromic property, an antibacterial property, a tunable optical property, and so on.[405−407] For example, Li and co-workers found that polyoxometalate silicotungstic acid $H_4SiW_{12}O_{40}$ (SiW) and amino acid histidine could self-assemble into coacervate adhesives through one-step mixing.[405] The positively charged imidazole groups of histidine could be absorbed onto the surface of SiW clusters via electrostatic interactions, while the protonated amine groups and deprotonated carboxyl groups of different histidine molecules interacted with each other by hydrogen bonds, leading to a self-assembly network of in coacervate phase (Figure 23c). The coacervate adhesive showed a wet adhesion strength of 38.3 kPa between copper plates and exhibited an electrochromic property because of the reduction-associated color change of the tungsten element. Zeng and co-workers reported that SiW and PEG could generate coacervate adhesives via one-step mixing.[406] The coacervation process was attributed to the hydrogen bonding between oxygens of SiW and etheric oxygens of PEG bridged by hydrated protons (Figure 23d). Because of the innate antibacterial property of SiW, the coacervate adhesive acted as an effective hemostatic with the capability to avoid microbial infection. When the linear PEG was replaced by poly(ethylene glycol)-*b*-poly(propylene glycol)-*b*-poly(ethylene glycol) (P123) micelles, the stability of the coacervate could be improved because of the stronger hydrogen-bonding interaction and the additional cross-linking endowed by the hydrophobic cores of the micelles.[407] Moreover, the adhesion strength was saliently raised from ∼100 kPa at wet conditions to ∼420 kPa obtained underwater. Besides the electrochromic property conferred by SiW, P123 micelles imparted thermoresponsiveness to the coacervate adhesive, yielding a promising candidate for energy-saving materials.

The design of coacervate adhesives is generally based on the manipulation of three types of noncovalent interactions (i.e., electrostatic interactions, cation−π interactions, and hydrogen-bonding interactions), and the characteristics of different coacervation strategies are summarized in Table 2. Inspired by the sandcastle worm, researchers have shown the electrostatic interaction-driven coacervation between two oppositely charged proteins generally requires complex polymer synthesis, where charged functional moieties such as amine and phosphate groups are introduced into different polymers.[395,396] Under this circumstance, the stoichiometry and pH adjustment of the two polyelectrolytes as well as the addition of salt should be delicately balanced to qualitatively tune the strength of the electrostatic interaction within the coacervate, otherwise, solutions, gels, or solid precipitates would be obtained. Herein, if the molecular interactions between the oppositely charged pairs of polyelectrolytes could be quantitatively measured under different environmental condictions, reasonable design of coacervate adhesives would have more reliable information to refer to. Meanwhile, DOPA has been incorporated into one of the two charged polyelectrolytes to facilitate the setting of the biological coacervate adhesives. However, as the setting process is irreversible, the repeatable adhesion is inaccessible. Cation−π interactions can not only drive coacervation between two like-charged polyelectrolytes but also induce coacervation within a single cationic polyelectrolyte, where the recombination of mussel foot proteins is usually involved to ensure the presence of both amine and phenol groups.[399,400] Compared with electrostatic interactions, cation−π interactions are less sensitive to pH adjustment. Therefore, the positively charged functional groups of these systems could remain cationic over a wide range of pH values. However, this stragtegy is restricted to acidic conditions because of the premature oxidation of DOPA in basic environments. Cation−π interactions are also highly sensitive to salt concentration because the long-range electrostatic repulsion between the positively charged polymers needs to be screened with a sufficient addition of salt to allow cation−π

https://doi.org/10.1021/acs.chemrev.2c00215
Chem. Rev. XXXX, XXX, XXX−XXX

Table 2. Typical Features of Different Coacervation Strategies

Involved noncovalent interactions	Inspiration	Coacervation components	Polymer synthesis	Stoichiometry	pH adjustment	Salt	Setting	Repeatability	Ref
Electrostatic interactions	Sandcastle worm	Two oppositely charged polymers	Complex polymer synthesis	Highly sensitive	Highly sensitive	Highly sensitive	Yes	No	395, 396
Cation−π interactions	Mussel	Two positively charged polymers or one positively charged polymer	Complex polymer synthesis	Highly sensitive	Sensitive	Highly sensitive	Yes	No	399, 400
Hydrogen bonding interactions	Prevalent interaction in living organisms	Generally nonionic polymers, commercially available	No	Sensitive	No	Sensitive but for the cohesion of the coacervate	No	Yes	403, 406, 408

interactions to occur. As a prevalent interaction in living organisms, hydrogen bonding has been widely applied in designing self-healing hydrogels attributed to its modulated strength, excellent biocompatibility, and a rapid association/dissociation behavior.[11] It has been reported that hydrogen-bonding interaction-driven coacervation can occur between pairs of commercially available products, such as tannic acid and PEG,[403] tannic acid and PVA[408] as well as SiW and PEG.[406] Generally, these coacervate adhesives can be acquired through simple one-step mixing without further treatment of the two counterparts, which could act as hydrogen donors and hydrogen acceptors during the coacervation process, respectively. The resultant coacervate adhesives can be facilely obtained over a wide range of mixing ratios and readily scaled up. Despite the existence of catechol groups, oxidation or cross-linking setting is dispensable to achieve wet/underwater adhesion as the cohesion of the coacervate adhesives can be easily tuned to be strong enough to support appropriate loading. The hydrogen donors, hydrogen acceptors, as well as catechol groups can provide reversible molecular interactions to bond the targeted surfaces repeatedly. Besides the approaches exploiting only one type of noncovalent interactions, more attention should be paid to the designs where two or more molecular interactions are involved.

3.4. Hydrogel Systems

Hydrogels are three-dimensional (3D) cross-linked polymer networks with a high content of water and have had applications in various fields, such as drug delivery, tissue engineering, wearable flexible electronics, and environmental engineering, because of their biocompatibility, easy fabrication, and facile tunability in mechanical and functional properties.[409,410] Both chemical and physical cross-linking strategies can be exploited for the construction of hydrogels, and this section only focuses on the development of functional (e,g., self-healing, adhesive, stimuli-responsive, adsorbent) hydrogels via noncovalent interactions.

3.4.1. Self-Healing Hydrogels. Inspired by the self-healing ability of living organisms, such as the healing of wounds in skin and the reparation of mussel byssal threads, the self-healing property has been pursued in lots of synthesized materials, which are expected to autonomously recover from damages induced by external forces, showing enhanced stability and extended lifespans.[411] Both dynamic covalent bonds (e.g., Schiff base imine bonds, disulfide bonds, phenylboronic ester complexation)[412,413] and noncovalent interactions (e.g., hydrogen bonding, hydrophobic interactions, host−guest interactions, metal−ligand coordination, electrostatic interactions, cation−π interactions, π−π stacking interactions) have been employed for the fabrication of self-healing hydrogels,[414,415] where the noncovalent interactions can bestow hydrogels with injectability and phase transition between a liquid-like state with high free volume and a low-free-volume solid state with elastic and plastic properties.[411]

Hydrogen bonding is one of the most prevalent noncovalent interactions for the construction of self-healing hydrogels, taking advantage of its biocompatibility, directionality, facilely tunable strength, and fast association/dissociation behavior.[19,416] Recently, hydrogen-bonding interaction-driven self-healing hydrogels have been prevailing in applications of flexible electronics because they can automatically self-heal from damages caused by frequent movements or unexpected breaks without external stimuli. For example, in situ polymerization of acrylic acid (AA) with the existence of ethylene glycol (EG)

AQ

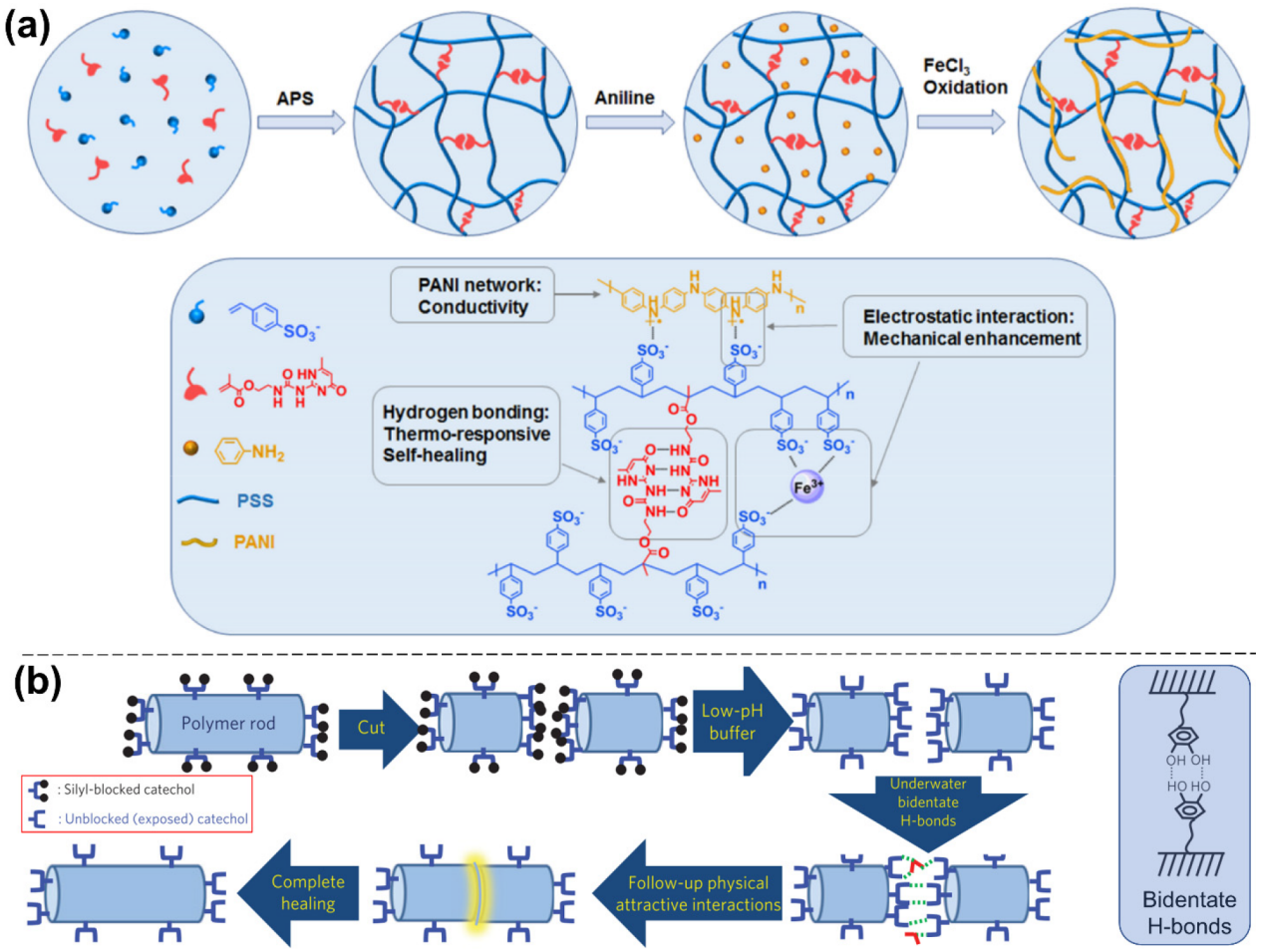

Figure 24. Self-healing hydrogels enabled by hydrogen-bonding interactions. (a) Preparation of a self-healing PANI/PSS-UPy hydrogel based on the formation of quadruple hydrogen bonds. Reproduced with permission from ref 409. Copyright 2019 American Chemical Society. (b) Polyacrylate and polymethacrylate hydrogels functionalized with mussel-inspired catechols showing underwater self-healing enabled by catechol-mediated interfacial bidentate hydrogen bonds. Reproduced with permission from ref 421. Copyright 2014 Springer Nature.

followed by the adsorption of KOH aqueous solution led to a self-healing hydrogel electrolyte for the fabrication of a flexible solid-state supercapacitor, which could retain 68% of its initial capacitance after 40 breaking/healing cycles because of the reconstruction of hydrogen bonds between carboxyl groups of poly(acrylic acid) (PAA) and hydroxyl groups of EG.[417] The abundant hydrogen bonds between hydroxyl side groups of PVA could impart the self-healing ability to a PVA-based hydrogel, which could further serve as the electrolyte of a zinc-ion battery when doped with zinc trifluoromethanesulfonate ($Zn(CF_3SO_3)_2$). The mechanical strength of the PVA hydrogel was enhanced by a facile freeze/thaw method with the formation of crystalline microdomains as cross-linkers.[418] The copolymerization of hygroscopic vinylimidazole(VI) monomer and hydroxypropyl acrylate (HPA) monomer in the $NaNO_3$ aqueous solution resulted in a p(VI-*co*-HPA) hydrogel electrolyte, where the integrated supercapacitor could restore its capacitance at temperatures ranging from +25 to −15 °C after 9 cycles of cut/healing. The self-healable capacitive performance was mainly ascribed to the hydrogen-bonding interactions between imidazole groups of VI and hydroxyl groups of HPA in addition to the ionic conduction and high mobility of polymer chains.[419] A conductive and self-healing nanocomposite hydrogel with an antifreezing property was prepared through the polymerization of oligo(ethylene glycol) methacrylate (OEGMA)-based monomers in a glycerol−water cosolvent with inorganic clay as physical cross-linkers and conductive ions. Because of the strong hydrogen-bonding interactions between polymer chains and clay, between polymer chains and glycerol/water molecules, as well as between glycerol and water molecules, hydrogel-based skin sensor with multifunctionalities including self-healing, antifreezing, and thermoresponsiveness was obtained.[420] The above-mentioned hydrogels were all constructed based on single hydrogel bonds, whose strength could be enhanced by the introduction of multiple hydrogen-bonding motifs including triple, quadruple, and sixtuple hydrogen-bonding arrays.[415] A stretchable, injectable, and self-healing conductive hydrogel was developed via incorporating quadruple hydrogen-bonding 2-ureido-4[1H]-pyrimidinone (UPy) groups as cross-linking points into a brittle polyaniline/poly(4styrenesulfonate) (PANI/PSS) network. The hydrogel could recover to the initial state within 30 s even after enduring a large strain of 1000% and preserve the identical relative resistance change and sensibility after 20 cyclic loading/unloading tests (Figure 24a).[409] When it comes to biomedical and environmental applications, self-healable hydrogels at wet or moist conditions are in pressing need. Israelachvili and Waite, etc. demonstrated that synthetic polyacrylate and polymethacrylate hydrogels functionalized with mussel-inspired catechols could undergo underwater self-healing enabled by catechol-

https://doi.org/10.1021/acs.chemrev.2c00215
Chem. Rev. XXXX, XXX, XXX−XXX

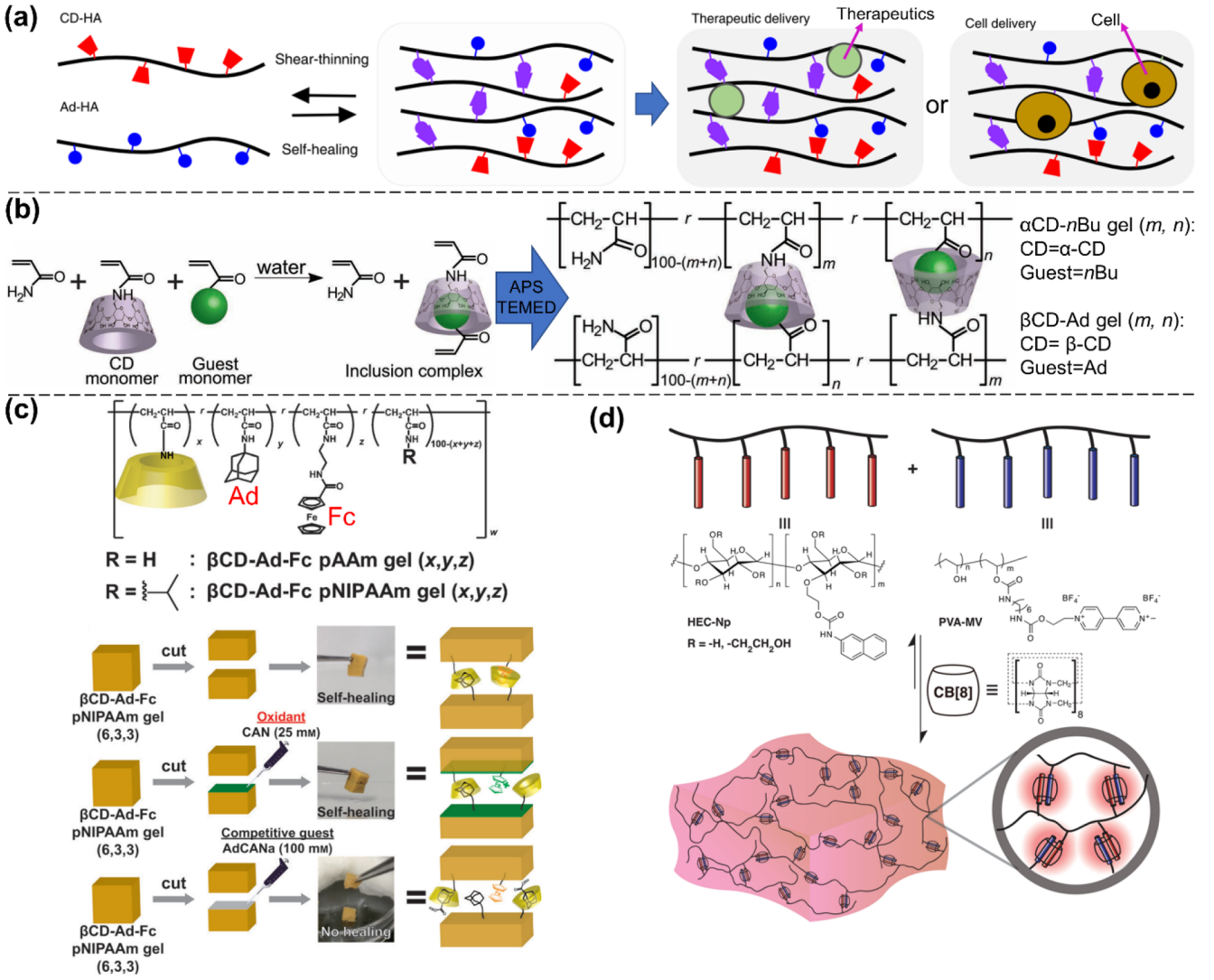

Figure 25. Self-healing hydrogels enabled by host−guest interactions. (a) Self-healing hydrogels driven by host−guest interaction between β-CD-HA and Ad-HA for the delivery of therapeutics and cells. Reproduced with permission from ref 433. Copyright 2017 Springer Nature. (b) Host (β-CD) and guest (*n*Bu or Ad) monomers were preorganized into inclusion complexes via host−guest interaction and then copolymerized with AM for the fabrication of self-healing hydrogels. Reproduced with permission from ref 438. Copyright 2013 John Wiley & Sons. (c) Acrylated host (β-CD) monomers and two different guest (Ad and Fc) monomers were simultaneously copolymerized in a hydrogel system, whose self-healing property was endowed by host−guest interaction between the host groups and the two guest moieties. Reproduced with permission from ref 441. Copyright 2015 John Wiley & Sons. (d) Supramolecular self-healing hydrogel prepared by adding CB[8] into the mixture of HEC-Np and PVA-MV aqueous solution. Reproduced with permission from ref 442. Copyright 2012 American Chemical Society.

mediated interfacial bidentate hydrogen bonds (Figure 24b).[421] Self-healing hydrogel also has been applied in filtration of water. The filtration membranes were coated with a self-healing hydrogel via in situ graft polymerization of 2-acrylamido-2-methyl-1-propanesulfonic acid (AMPS) onto microporous poly(ether sulfone) (PES) substrates, which could recover from damages caused during installation and operation. The self-healing ability was enabled by hydrogen bonding between AMPS side chains as well as molecular interdiffusion.[422] Some other studies focused on developing novel self-healing strategies of hydrogen-bonding interaction-driven hydrogels as well as improving the mechanical properties of the hydrogels.[423] For instance, a double network (DN) hydrogel was developed to optimize the balance between the mechanical strength and the self-healing property. The first network was hydrogen bond-associated entanglements of poly(acrylamide-*co*-acrylic acid) (PAM-*co*-PAA) and the second network was hydrogen-bonding interaction-driven PVA, which was reinforced through cyclic freezing/thawing. The hydrogel possessed a high strength of 1230 ± 90 kPa and toughness of 1250 ± 50 kJ m^{-3} with a sacrifice of the self-healing ability. The self-healing efficiency was evaluated by comparing the elongation at break for original and healed gel samples, where the hydrogel sample healed 12 h at 37 °C only exhibited a self-healing efficiency of 37%.[424] The incorporation of nanomaterials such as GO nanosheets into hydrogels was another strategy to fabricating self-healing and tough hydrogels. When acrylamide was in situ polymerized with the presence of GO nanosheets, massive hydrogen bonds were generated between the carbonyl groups of PAM and hydroxyl groups of GO, simultaneously endowing the hydrogel with a high strength of 580 kPa and a high elongation of 3300%. The hydrogels could reach a self-healing efficiency of 88% for tensile

https://doi.org/10.1021/acs.chemrev.2c00215
Chem. Rev. XXXX, XXX, XXX−XXX

strength and 98% for elongation by varying the concentration of GO.[425] The strength of hydrogen-bonding interactions within self-healing hydrogels could be modulated via optimizing the ratio of hydrophilic moieties to hydrophobic moieties. Copolymerization of *N*-acryloyl amino acid and *N*,*N*-methylenebis(acrylamide) monomers created rapid (within seconds) self-healing hydrogels, whose recovery degree was tunable through changing the side chain length (length of alkylene spacers) of *N*-acryloyl amino acid to mediate hydrogen bonds with minimal steric hindrance and hydrophobic collapse.[426]

Hydrophobic interactions have been utilized to build self-healing hydrogels inspired by the hydrophobic interaction-associated elastin, which is the main component of elastic, self-healable, hydrogel-like biological soft tissues including skin, blood vessels, and lungs.[378,427] Micelle copolymerization is commonly used in the fabrication self-healing hydrogels, where the hydrophobic monomers are encapsulated within the hydrophobic cores of micelles and the hydrophilic monomers are dissolved in the aqueous solution. The tightly entangled hydrophobic chains in the micellar cores serve as dynamic cross-linking sites to achieve the self-healing ability. It was reported that large hydrophobic monomers stearyl methacrylate (SMA/C18) or dococyl acrylate (C22) could be copolymerized with the hydrophilic acrylamide in a micellar solution of sodium dodecyl sulfate (SDS) to prepare self-healing hydrogels. A high concentration NaCl was required to induce the growth of micelles through shielding electrostatic interactions, allowing the high solubility of hydrophobic monomers within the hydrophobic cores of micelles. The as-prepared self-healing hydrogels could achieve an elongation up to 3600%, and the healed sample could also reach an elongation of 3580%.[428] The effects of hydrophobe size and surfactant concentration were further investigated, and the utilization of a hydrophobic monomer with an alkyl chain length of 18 carbon atoms led to the highest self-healing efficiency (88%) of the hydrogels. Moreover, hydrogels prepared with hydrophobic methacrylates exhibited a higher self-healing ability over those prepared with acrylates, as the constrained flexibility of backbones could set free more nonassociated hydrophobic blocks to mediate hydrophobic interactions. In addition, the self-healing ability of the hydrogels gradually disappeared along with the decrease of the SDS content.[429] When the poly(AM-*co*-SMA) hydrogel was doped with cellulose nanofiber (CNF)-stabilized MWCNTs, the tensile strength and electrical conductivity were enhanced with a compromised self-healing ability (77.2% of elongation recovery after healingfor 7 days). However, the as-prepared hydrophobic interaction-associated hydrogel exhibited an efficient electromagnetic interference (EMI) shielding performance of about 28.5 dB, holding great potential in the protection of precision electronics.[430] Surfactant-free hydrophobic interaction-associated self-healing hydrogels could be prepared via a controlled dehydration procedure. Specifically, benzyl methacrylate (B), octadecyl methacrylate (O), and methacrylic acid (MA) monomers were copolymerized in a solution and strong hydrophobic interaction among octadecyl groups was gradually initiated with the dehydration of the solution, generating a self-healing hydrogel. The cut interface of the hydrogel was capable of healing within 0.5 h, and perfect welding was achieved after 18 h.[431] Further incorporating PNIPAm nanogels into the polymer solution followed by controlled evaporation of water resulted in a hydrophobic interaction-driven self-healing hydrogel with thermoresponsive optical property. The addition of PNIPAm did not weaken the self-healing ability of the hydrogel but only enabled the hydrogel to exhibit heat-induced variation of transparency, which show potential applications as smart windows.[432]

Host−guest interactions can serve as a driving force for supramolecular assembly and the fabrication of self-healing hydrogels. For example, a self-healing hydrogel was generated by mixing β-CD-modified HA (β-CD-HA) and Ad-modified HA (Ad-HA), which was induced by the host−guest interaction between β-CD and Ad moieties. The high self-healing and shear-thinning efficiencies within seconds offered the hydrogel injectability and it could be loaded with therapeutics and cells (Figure 25a).[433] The self-healing hydrogels could serve as extruded inks and supportive scaffolds for 3D-bioprinting with high precision through modulating the grafting degree of HA and the concentrations of host/guest polymers.[433,434] Because of the biocompatibility of the polymers, the corresponding host−guest interaction-associated self-healing hydrogels hold great promise in biomedical applications. It was demonstrated that β-CD-modified alginate could interact with the aromatic residues of the methacrylated gelatin via a host−guest interaction, yielding a shear-thinning and self-healing hydrogel with potential applications in tissue engineering and cell/drug delivery.[435] In addition, β-CD-modified *N*,*N*′-dimethylacrylamide (DMA) and cholic acid (CA)-modified DMA could generate self-healing hydrogels suitable for injectable in situ gelling devices.[436] Some special inclusion complexes such as the inclusion of a β-CD macrocycle with an α-bromonaphthalene (α-BrNp) moiety could emit room-temperature phosphorescence (RTP) signals under specific excitation. Therefore, mixing poly(AM-*co*-β-CD) and poly(AM-*co*-α-BrNp) could result in a rapidly (within 1 min) self-healing hydrogel with phototriggered RTP responsiveness for smart soft materials, which could be further adjusted via competitive host−guest interaction between β-CD and Azo moiety through the addition of poly(AM-*co*-Azo).[437] Moreover, in order to get optimal self-healing efficiency of the host−guest interaction-enabled hydrogels, preorganizing host−guest pairs before polymerization could enhance their interaction opportunities. For instance, β-CD-modified and Ad-modified AM monomers or α-CD-modified and *n*-butyl acrylate (*n*-BuAc)-modified AM monomers formed inclusion complexes via host−guest interactions, respectively, followed by subsequent polymerization of inclusion complexes to yield host−guest interaction-driven self-healing hydrogels (Figure 25b).[438] A light-switchable self-healing hydrogel was prepared by polymerization of AM monomers and a host−guest macro-cross-linker assembled from a poly(β-CD) nanogel and azobenzeneacrylamide. The self-healing property of the hydrogel could be modulated by light as the azo moiety experienced trans−cis isomerization upon UV irradiation, where cis-state azo moieties were less favorable to β-CD cavities compared with those in the trans-state.[439] A three-arm supramolecule monomer associated by the host−guest interaction between isocyanatoethyl acrylate modified β-CD and a 2-(2-(2-(2-(adamantyl-1-oxy)ethoxy)ethoxy)ethoxy)ethanol acrylate guest monomer was polymerized, leading to a rapidly self-healing hydrogel with high mechanical strength and excellent biocompatibility.[440] Host and guest moieties could be also simultaneously copolymerized into the same polymer. When the β-CD monomer and two different guest monomers, Ad and Fc, were copolymerized, a hydrogel was generated, whose self-healing efficiency could be tuned by host−guest interactions between β-CD and Ad/Fc, respectively. The self-healing hydrogel exhibited

https://doi.org/10.1021/acs.chemrev.2c00215
Chem. Rev. XXXX, XXX, XXX−XXX

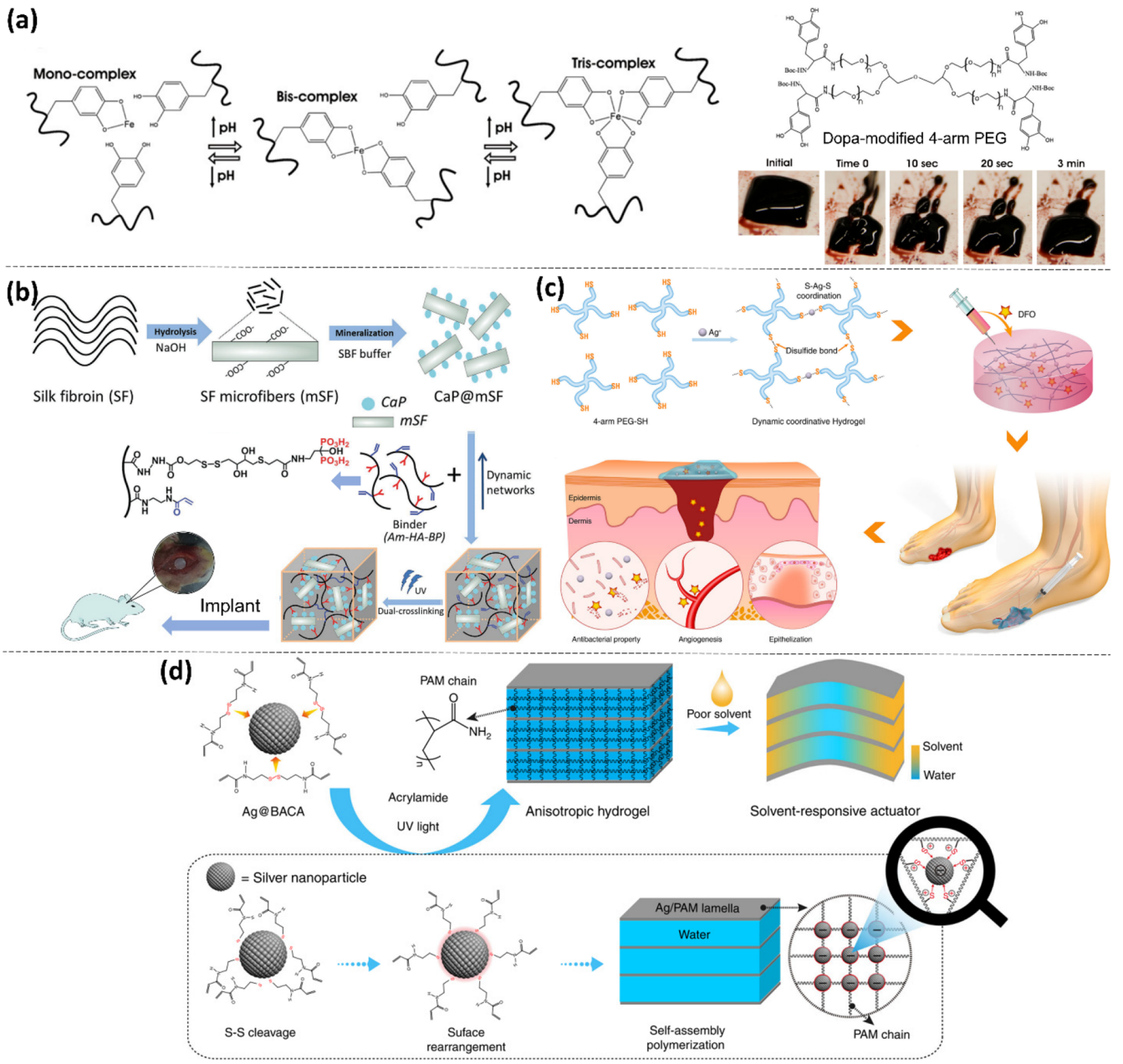

Figure 26. Self-healing hydrogels enabled by metal−ligand coordination. (a) Fe^{3+}−catechol complexes experience mono-, bis-, and tris-complex transitions with increasing pH. A self-healing hydrogel was generated based on the tris-catechol−Fe^{3+} coordination between DOPA-modified 4-arm PEG and Fe^{3+} at pH of about 12, which could recover from fracture within 3 min. Reproduced with permission from ref 446. Copyright 2011 National Academy of Sciences. (b) SF-based self-healing hydrogel for bone regeneration, where the chelation between Ca^{2+} and bisphosphonate ligands served as dynamic molecular interactions for self-healing. Reproduced with permission from ref 457. Copyright 2017 John Wiley & Sons. (c) Self-healing hydrogel prepared through mixing 4-arm-PEG-SH with $AgNO_3$, which could repair foot ulcers of type I diabetes via loading DFO. Reproduced with permission from ref 455. Copyright 2019 Springer Nature. (d) Self-healing hydrogel enabled by the RS-Ag coordination bonds. Reproduced with permission from ref 453. Copyright 2019 Springer Nature.

stimuli-responsiveness, which were light-responsiveness bestowed by Ad and redox-responsiveness endowed by Fc (its oxidized form is hydrophilic) (Figure 25c).[441] CB[*n*]s have been employed to formulate self-healing hydrogels through host−guest interactions with various guest moieties. Scherman and coworkers have made a significant contribute to CB[*n*]-related host−guest interaction-driven hydrogels toward multifunctionalities. Naphthalene (Np)-modified hydroxyethyl cellulose (HEC) and methyl viologen (MV)-modified PVA were mixed with CB[8] with a molar ratio of 1:1:1, where each CB[8] cavity could concurrently accommodate one electron-deficient guest MV and one electron-rich guest Np (Figure 25d). The as-prepared hydrogel exhibited rapid self-healing within a few seconds after being destructed by high-magnitude shear rate of 500 s^{-1}, and displayed multiple response to temperature, chemical potential, and competing guests.[442] The ternary self-healing hydrogel system could be improved by replacing Np-decorated HEC with cellulose nanocrystals (CNC)-modified Np-containing polymer brushes, leading to hydrogels with high storage modulus of more than 10 kPa and rapid sol−gel

https://doi.org/10.1021/acs.chemrev.2c00215
Chem. Rev. XXXX, XXX, XXX−XXX

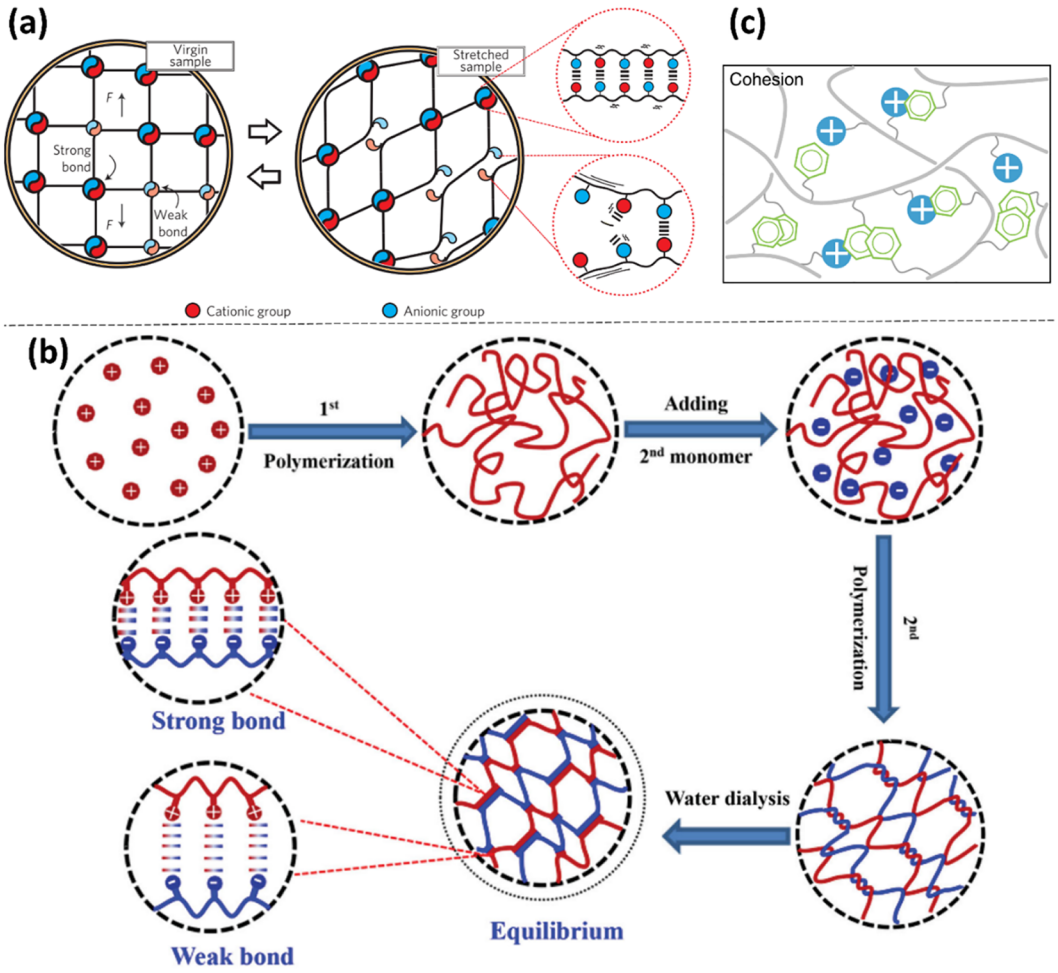

Figure 27. Self-healing hydrogels enabled by electrostatic interactions and cation−π interactions. (a) Copolymerization of oppositely charged monomers to generate self-healing polyampholyte hydrogels, whose elasticity was credited to the relatively strong ionic bonds while self-healing performance and capacity of dissipating energy were ascribed to those relatively weak bonds. Reproduced with permission from ref 460. Copyright 2013 Springer Nature. (b) Self-healing polyampholyte hydrogels were fabricated via a double network strategy, where the second charged monomer was in situ polymerized within the polymer network formed by the first monomer with an opposite charge. Reproduced with permission from ref 459. Copyright 2015 John Wiley & Sons. (c) Self-healing hydrogel based on cation−π interactions. Reproduced with permission from ref 462. Copyright 2019 Springer Nature.

transition within less than 6 s.[443] Through direct radical polymerization of AM monomers and inclusion complex monomers associated between CB[8] and polymerizable guest molecules (1-benzyl-3-vinylimidazolium), tough hydrogels (support object 2000 times of their weight) with extreme stretchability (elongation of 10000%) and fast room-temperature self-healing (self-healing efficiency of about 35% within 1 h) were obtained.[444]

Metal−ligand coordination has attracted increasing attention for the construction of self-healing hydrogels as metal-containing polymer networks are widespread in biology, especially in load-bearing biomaterials such as the *Mytilus* byssal cuticle.[445] Besides the widely studied Fe^{3+}−catechol coordination inspired by mussels,[446−449] other metal−ligand coordination interactions like Fe^{3+}/Al^{3+}−carboxylic group interaction,[449−452] metal−thiolate coordination (Ag/Au and −SH),[453−456] Ca^{2+}−bisphosphonate coordination[457] were also investigated. To circumvent ferric hydroxide precipitation, a mussel-inspired strategy of preorganizing Fe^{3+} in Fe^{3+}−monocatechol complexes at acidic pH could successfully protect Fe^{3+} to subsequently interact with DOPA via bis- and/or tris-catechol−Fe^{3+} complexes along with increasing the pH (Figure 26a). At a pH of about 12, a self-healing hydrogel was generated based on tris-catechol−Fe^{3+} coordination between DOPA-modified 4-arm PEG and Fe^{3+}, which could recover from a fracture within 3 min (Figure 26a). DOPA-PEG-based adhesives and coatings could be used in both dry and wet environments ascribing to the universal adhesion on various substrates of DOPA.[446] DOPA-functionalized polyallylamine and Fe^{3+} could adopt this strategy to form a self-healing hydrogel, which resumed from a destructive strain of 200% in less than 10 s.[447] Metal−ligand coordination between DOPA-modified chitosan and Fe^{3+} could engender a self-healing hydrogel, where genipin was introduced as cross-linkers to form covalent bonds with free amine groups of chitosan the enhance the mechanical property of the hydrogel with a reduced self-healing efficiency.[448] Free-radical polymerization of acrylic acid (AA) in the presence of Fe^{3+} was a facile way to fabricate self-healing hydrogels because of the dynamic and reversible metal−ligand coordination between Fe^{3+} and carboxylic groups of PAA.[450] Further incorporating polypyrrole (PPy)-grafted chitosan into the aqueous solution with Fe^{3+} prior to the

https://doi.org/10.1021/acs.chemrev.2c00215
Chem. Rev. XXXX, XXX, XXX−XXX

Table 3. Typical Self-Healing Hydrogels Based on Different Noncovalent Molecular Interactions

Involved noncovalent interactions	Design of polymer networks	Solvent	Available categories of materials	Salt	Factors affecting self-healing efficiency	Application	Ref
Hydrogen bonding	In situ polymerization of one kind of monomers at the presence of a specific substance (small organic molecules/inorganic nanomaterials); in situ polymerization of two different monomers; double-network polymer networks; or in situ graft polymerization of functional groups	Water or glycerol–water cosolvent	Substantial	Dispensable	Concentration of hydrogen bonds; bidentate, triple, quadruple, or sextuple hydrogen-bonding arrays; doping of nanomaterials; etc.	Electrolytes of flexible solid-state supercapacitors or ionic batteries; strain sensors; wet repair of tissues; filtration membranes; etc.	409, 415, 417–422, 424–426
Hydrophobic interactions	Micelle copolymerization of both hydrophobic and hydrophilic monomers, or polymerization with controlled dehydration if no surfactant	Water or with the presence of an amphiphilic cosolvent	Relatively less	High concentration or dispensable	Size and concentration of hydrophobic monomers; surfactant concentration; doping with nanomaterials; salt; etc.	Biological tissues; electromagnetic interference shielding	428–431
Host–guest interactions	Mixing of polymers with functional side groups being able to form host–guest interaction; polymerization of preorganized host–guest monomer pairs; copolymerization of host and guest moieties-contained monomers; mixing guest moieties-contained polymers with host molecules	Water	Relatively less	Dispensable	Graft degree of functional moieties on backbone polymers; pairing percentage and concentration of host–guest inclusion complexes; etc.	Drug/cell loading/delivery; tissue engineering; 3D-bioprinting; smart soft materials with responsiveness	433–444
Metal–ligand coordination	Mixing metal ions with polymer modified with specific ligands; polymerization of functionalized monomers in the presence of metal ions in water/polymer aqueous solution; polymerization of functionalized monomers in the presence of metal ions and functionalized nanomaterials	Water	Substantial	Unnecessary	Concentration of metal ions and ligands; incorporation of one or more metal–ligand coordination; etc.	Dry/wet adhesives; strain sensors; 3D-printed flexible electronics; electronic skin; biosensors; vessel sealant; mucoadhesive; tissue regeneration	446–458
Electrostatic interactions	Copolymerization of oppositely charged monomers to generate polyampholyte hydrogels; in situ polymerization of a charged monomer within the polymer network of another oppositely charged monomer	Water	Relatively less	Indispensable because of the saline softening effect	Various combinations of oppositely charged monomers; the fraction of dynamic weak bonds to total bonds	Focus on study of self-healing mechanisms	459–461
Cation–π interactions	Copolymerization of cationic and aromatic monomers	Organic	Relatively less	Indispensable	Various combinations and concentration of cationic and aromatic monomers, etc.	Underwater adhesives	32, 462, 463

https://doi.org/10.1021/acs.chemrev.2c00215
Chem. Rev. XXXX, XXX, XXX−XXX

polymerization of AA could confer the self-healing hydrogel good conductivity to be applied for human motion detection and 3D-printed flexible electronics. The hydrogel possessed high stretchability of 1500% and 100% mechanical recovery in 2 min because of the metal−ligand coordination between Fe^{3+} and carboxylic groups of PAA as well as NH groups of PPy.[451] The Fe^{3+}−catechols and Fe^{3+}−carboxylic groups coordinations were combined into one self-healing hydrogel by polymerizing AA in the presence of Fe^{3+} and DOPA-functionalized rGO nanosheets. Two separated parts of this hydrogel could heal overnight and recover 75% of the initial elongation of about 600%. The hydrogel displayed excellent biocompatibility considering that fibroblasts differentiated from human embryonic stem cells showed a flourishing living state on it, holding great potential as electronic skin and biosensors.[449] In addition, Al^{3+}−carboxylic coordination was used to fabricate a self-healing and photoluminescent hydrogel through introducing specific amounts of Al^{3+} and photoluminescent citric acid derivatives (PCADs) into carboxymethyl cellulose (CMC) polymer networks. The hydrogel was demonstrated to be an effective vessel sealant for solution leakage and mucoadhesive for stomach perforations.[452] Ca^{2+}−bisphosphonate coordination was employed to build a self-healing silk fibroin (SF)-based hydrogel for bone regeneration. Specifically, SF microfibers were first coated with a layer of calcium phosphate (CaP) particles, followed by interacting with bisphosphonate-functionalized polysaccharide binders (Figure 26b).[457] Recently, Ag-related metal−ligand coordination has been exploited to fabricate self-healing hydrogels with potential application in biomedical engineering mainly because of the innate antibacterial characteristic of Ag^{+}. For example, one step mixing of 4-arm thiolated PEG (PEG-SH) and $AgNO_3$ aqueous solutions resulted in an injectable and self-healing hydrogel with antibacterial property for diabetic skin wound repair, where doping the PEG-SH solution with angiogenic drug desferrioxamine (DFO) would further facilitate the wound healing (Figure 26c).[455] Similarly, replacing DFO with mangiferin liposomes (MF-Lip) within the above hydrogel enabled it to be conducive for the healing process of skin flap regeneration.[454] Furthermore, Ag NPs and a water-soluble and disulfide bond (S−S)-contained surface ligand N,N-bis(acryloyl)cystamine (BACA) could associate with each other through RS-Ag coordination between the highly active silver atoms on the surface of the Ag NPs and RS ligand, where the S−S bond cleaved upon the adsorption BACA onto Ag NPs (Figure 26d). UV irradiation initiated the uniform distribution of BACA on the surface of Ag NPs and induced the hydrophobization of Ag@BACA nanocomposite, because of surface energy change originated from the photothermal of Ag NPs and the dissociation of RS−Ag bonds at a high temperature. Within the Ag@BACA nanocomposite, Ag NPs served as electron acceptors while RS acted as electron donors, and the electrostatic repulsion among Ag NPs assisted by the hydrophobic interaction of the nanocomposite led to the 2D lamellar Ag NPs assemblies in single-nanoparticle thickness. Followed by the copolymerization with AM monomers, an anisotropic hydrogel with NIR irradiation- and low pH-mediated self-healing performance was fabricated, which afforded the hydrogel with great potential as a superior soft actuator.[453] Replacing Ag NPs with AuNPs and shifting AM monomers with NIPAM monomers also resulted in a hydrogel with a NIR-initiated self-healing property enabled by the dynamic RS−Au coordination interaction.[456] In addition, the newly discovered photodynamic Ru−Se coordination bond has been exploited for the preparation of visible-light-responsive self-healing hydrogels, which could experience reversible sol−gel transitions without side reactions upon cyclic mild visible-light irradiation and storage in the dark.[458]

Self-healing hydrogels driven by electrostatic interactions and other interactions (e.g., cation−π interactions) have been extensively explored. For the preparation of self-healing hydrogels driven by electrostatic interactions, a fast formation of inhomogeneous precipitation would be commonly observed because of a rapid complexation reaction between bulk aqueous solutions of polycations and polyanions.[459] To address this issue, Gong and co-workers employed the strategy of copolymerization of oppositely charged monomers to generate polyampholyte hydrogels, which simultaneously bear randomly spread cationic and anionic repeat groups, resulting in a a hierarchical distribution of ionic bonds with various bond strengths (Figure 27a). The elasticity of the hydrogels was credited to the relatively strong ionic bonds; the self-healing performance and the capacity of dissipating energy were ascribed to those relatively weak bonds (Figure 27a). The mechanical properties of these electrostatic interaction-driven self-healing hydrogels could be modulated over a wide range by utilizing various combinations of oppositely charged monomers.[460,461] However, these inhomogeneous polyampholytes hydrogels usually suffer from uncontrollable mechanical properties caused by globular conformation of polymer chains. To surmount these shotcomings, a double network approach was employed, where one charged monomer was first polymerized into a network with the subsequent in situ polymerization of another oppositely charged monomer (Figure 27b). The two interacted oppositely charged homopolymers with an extended coil polymer conformation were obtained to compose the electrostatic interaction-enabled self-healing hydrogels with controllable mechanical properties.[459] As a strong noncovalent interaction, cation−π interactions have attracted a lot of research attention for constructing self-healing hydrogels with underwater adhesiveness. As the aromatic monomer is hydrophobic, Gong and co-workers proposed a strategy for preorganizing cation−π interaction-associated monomer pair complexes to enable homogeneous distribution of divinyl-like or multivinyl-like monomers for subsequent polymerization (Figure 27c). Free radical polymerization of adjacent cationic−aromatic monomer pairs gave rise to underwater adhesive hydrogels, which were able to bind negatively charged surfaces in saline environments. Because of the dynamic feature of the cation−π interaction, these hydrogels could fully recover from 300% strain within 30 s.[462,463] The π−π interactions were also utilized for fabricating self-healing hydrogels. An amino-acid-based self-healing hydrogel was developed from 11-(4(pyrene-1-yl)butanamido)undecanoic acid and graphene/SWCNTs based on π−π interactions between the pyrene moieties and the π surface of the graphene/SWCNTs.[464]

Various types of noncovalent interactions have been introduced to construct self-healing hydrogels, which are summarized in Table 3. Among them, hydrogen bonding is primarily investigated because of the readily accessible pairs of hydrogen donors and hydrogen acceptors. The introduction of salts and/or other conductive nanomaterials generally will not impair the self-healing efficiency of the hydrogels, and when the nanomaterials were modified with hydrogen donors and/or hydrogen acceptors, the self-healing efficiency might be enhanced. Therefore, hydrogen-bonding-driven self-healing hydrogels have been extensively studied for the fabrication of flexible electronics including supercapacitors, ionic batteries,

https://doi.org/10.1021/acs.chemrev.2c00215
Chem. Rev. XXXX, XXX, XXX−XXX

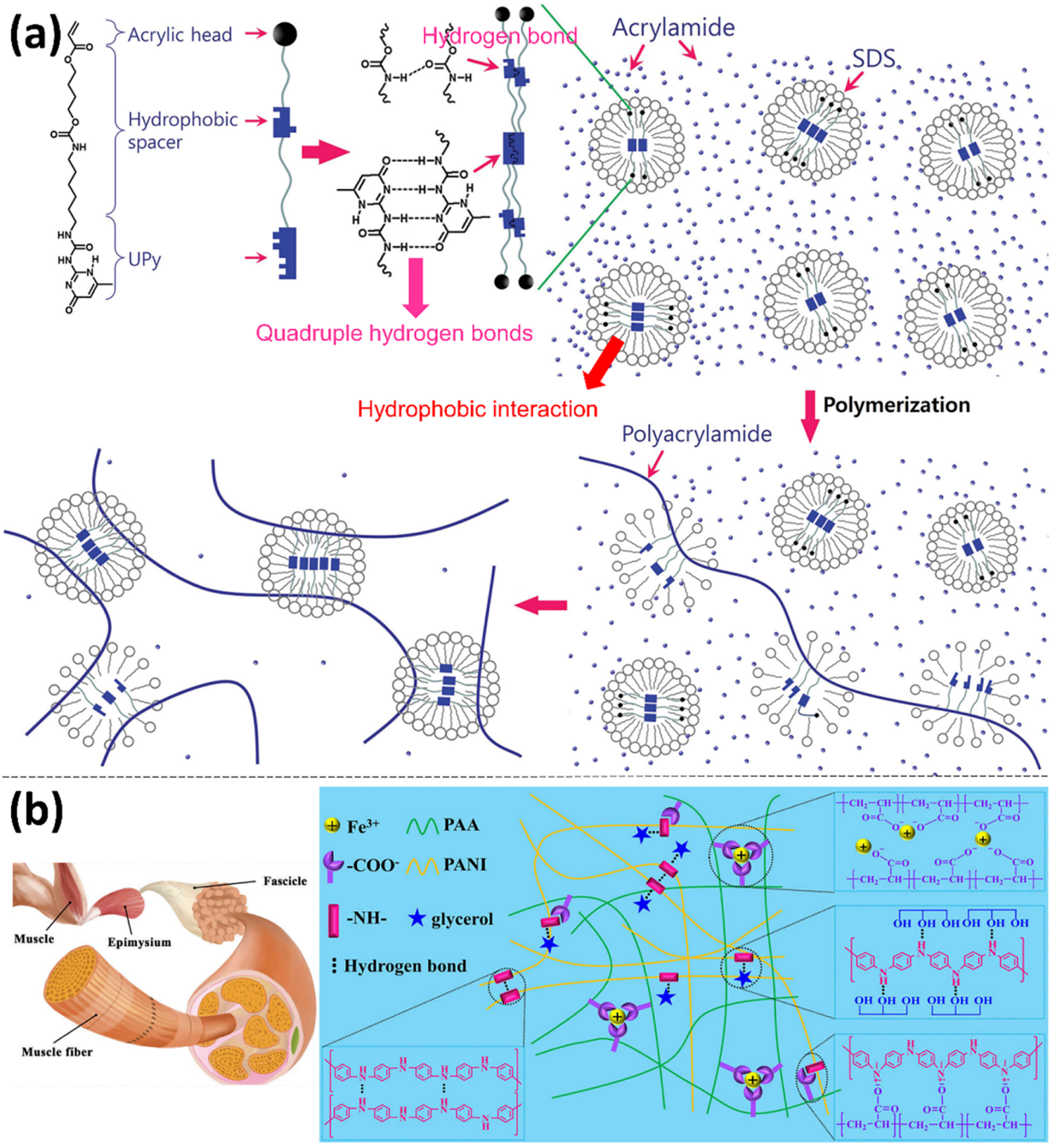

Figure 28. Self-healing hydrogels enabled by multiple noncovalent interactions. (a) Self-healing hydrogel formed via the synergy of hydrogen bonding and hydrophobic interactions. Reproduced with permission from ref 474. Copyright 2016 John Wiley & Sons. (b) Self-healing hydrogel enabled by the cooperation of metal coordination, hydrogen bonding, and electrostatic interactions. Reproduced with permission from ref 477. Copyright 2020 American Chemical Society.

strain sensors, biosensors, etc., where the electrical and/or ionic conductivity is indispensable, and the self-healing property could greatly enhance their life span. Although water-based self-healing hydrogels usually possess good biocompatibility, the weak water retention capability and antifreezing property would practically hinder their long-term usage. Strategies such as adding a high concentration of hygroscopic LiCl salt or wrapping the hydrogels with an elastomer as an outer layer have been proposed, but they are either expensive or complicated. Therefore, the development of water-free self-healing elastomers has become a promising strategy.[465−467] For example, bidentate urea hydrogen bonds, urethane hydrogen bonds, bidentate carboxylated hydrogen bonds, and quadruple hydrogen bonds between UPy moieties have been extensively studied for the fabrication of self-healing elastomers toward applications in flexible electronics such as soft robots,[468] e-skin,[469] triboelectric nanogenerators,[470] capacitive sensors,[471] etc. A major challenge for the preparation of self-healing hydrogels based on hydrophobic interactions is the poor solubility of hydrophobic monomers in aqueous solutions, which could be addressed by the formation of micelles or controlled dehydration. Host−guest interaction usually suffers

https://doi.org/10.1021/acs.chemrev.2c00215
Chem. Rev. XXXX, XXX, XXX−XXX

from the poor pairing percentage of the inclusion complexes, which may lead to low self-healing efficiency. Preorganizing host−guest monomer pairs before polymerization was brought up to tackle this problem. The design of self-healing hydrogels based on metal−ligand coordination also allows a wide range of choices in materials. However, when DOPA is involved, special attention should be paid to avoiding the preoxidation of the catechol groups. Directly mixing oppositely charged polyelectrolytes usually leads to the generation of precipitates attributed to the strong and unevenly distributed electrostatic interactions. Therefore, copolymerization of oppositely charged monomers to generate polyampholyte hydrogels as well as in situ polymerization of a charged monomer within the polymer network of another oppositely charged monomer are preferred. For cation−π interaction-enabled self-healing hydrogels, the poor solubility of the hydrophobic aromatic monomers requires organic solvents to be the polymerization medium. The corresponding self-healing hydrogels could be obtained after solvent exchange between organic solvent and water in the presence of sea-level salt.

Different types of noncovalent interactions can be combined into one hydrogel system to optimally satisfy various requirements of practical applications. Generally, the number and type of noncovalent interactions depend on the design strategy and materials used for the construction of hydrogels. The double network strategy is usually the preferable design method of a self-healing hydrogel as one polymer network could maintain the mechanical property of the hydrogel while the other one could work for self-healing. For example, a negatively charged sodium 4-vinyl-benzenesulfonate (NaSS) monomer and a positively charged *N*-(2-(methacryloyloxy)ethyl)-*N*,*N*-dimethylbutan-1-aminium bromide (MOBAB) monomer were copolymerized in an aqueous solution of soluble starch with the addition of GO nanosheets. The prepared hydrogel could restore its shear modulus from a destructive shear strain of 1000% within about 120 s, because of the reversible electrostatic interactions between the oppositely charged functional groups as well as hydrogel bonds among soluble starch, GO sheets, and P(NaSS-*co*-MOBAB) polymer chains.[472] Similarly, NIPAm and acrylated β-cyclodextrin (β-CD) were copolymerized in the presence of MWCNTs, followed by the in situ polymerization of pyrrole. The self-healing property of this hydrogel was endowed by dominant host−guest interactions and the weak hydrogen-bonding interactions between β-CD and NIPAm. The as-prepared hydrogel could recover its shear modulus immediately (less than 5 s) from a shear strain of 400%.[473] A single network hydrogel could also reach excellent self-healing efficiency with the combination of different types of noncovalent interactions. As shown in Figure 28a, acrylated UPy monomers with a hydrophobic spacer were encapsulated within the hydrophobic cores of the SDS micelles, which prevented the quadruple hydrogen bonds between the UPy moieties from dissociation in an external aqueous solution. Then the acrylated UPy monomers were copolymerized with the acrylamide monomers dispersed in the surrounding aqueous solution, resulting in a hydrogel cross-linked by interacted UPy moieties protected by SDS micelles. The corresponding hydrogel could retain its stretchability after healed within 30 s, ascribing to the quadruple hydrogen bonds between the UPy moieties and the single hydrogen bonds between the amide groups of the hydrophobic spacers.[474] Recently, self-healing hydrogels have been widely explored as wearable sensors, which usually required an appropriate balance among mechanical properties, self-healing efficiency, and conductivity. As mechanical properties are mainly guaranteed by strong covalent cross-linking, the self-healing efficiency generally relies on the synergy of multiple physical noncovalent interactions. Conductive compositions can be introduced to the systems via direct doping of metallic and carbon nanomaterials or in situ polymerization of conductive polymers.[475] It was reported that hydrophilic monomer AA, hydrophobic monomer lauryl methacrylate (LMA) could be copolymerized into a hydrogel via micellar polymerization with the presence of hexadecyl trimethylammonium bromide (CTMAB), followed by sequential dehydration. Then this dehydrated hydrogel was immersed in the mixture solution of aniline (ANI) and phytic acid (PA), after which ANI monomers were in situ polymerized into homogeneously distributed polyaniline (PANI) networks. The hydrogel possessed a high tensile strength of 0.9 MPa and a high stretchability of 2590% with a recovery of 72% (1866%) of the stretchability and 67% (0.6 MPa) of the tensile strength after healing for 72 h, because of the electrostatic interactions and hydrogen bonding between the abundant −N−H groups of PANI and −COOH groups of PAA, the electrostatic interactions between positively charged PANI and negatively charged PA, the hydrogen bonding between PANI networks, and the hydrophobic interaction among lauryl groups and the hydrophobic cores of SDS micelles.[476] Inspired by the fascicle-enhanced microstructure of human muscles, PANI nanofibers was mixed with PAA with addition of Fe^{3+} in the glycerol/water binary solvent, where the metal coordination (between Fe^{3+} and −COOH), electrostatic interactions (between −N−H groups of PANI and −COOH groups of PAA), and the hydrogen bonding (between −N−H groups of PANI and −COOH groups of PAA as well as between PANI networks) were responsible for the desirable mechanical property and the satisfactory self-healing ability (Figure 28b). The wedge-shaped hydrogel restored 91% (900%; original, 991%) of the stretchability and ∼70% (∼25 kPa; original, 36 kPa) of the tensile strength after healing for 6 h after breakage. Besides, the strong hydrogen bonding between glycerol and water inhibited the crystallization of water, which endowed the hydrogel with antifreezing property and self-healing ability under −26 °C.[477]

Although we have emphasized the importance of noncovalent interactions in the design of self-healing hydrogels, covalent bonds are omnipresent for all the systems. On the one hand, the functional groups able to generate noncovalent interactions are usually grafted to the ends or the side chains of the covalently bonded polymer chains, or be polymerized into polymer chains as part of monomer, or be a part of the polymer backbone. Small molecules and metal ions need to associate with covalently bonded polymers with counterpart functional groups to form a stable network. To further optimize the overall mechanical property of the self-healing hydrogels, a second polymer network can be introduced, where the cooperation and balance between the covalent and noncovalent bonds play an important role. For example, Gong and co-workers developed a double networks (DN) tough hydrogel by in situ polymerization of a loosely cross-linked second network in the presence of a first highly cross-linked network, where the first network was responsible for increasing the elastic stress while the second one contributed to withstand strain.[478] Compared with the single network PAAm hydrogel (break stress, 0.8 MPa; fracture strain, 84%) and PAMPS hydrogel (break stress, 0.4 MPa; fracture strain, 41%), the reported DN PAMPS (poly(2-acrylamido-2-methylpropanesulfonic acid)-PAAm hydrogel ex-

https://doi.org/10.1021/acs.chemrev.2c00215
Chem. Rev. XXXX, XXX, XXX−XXX

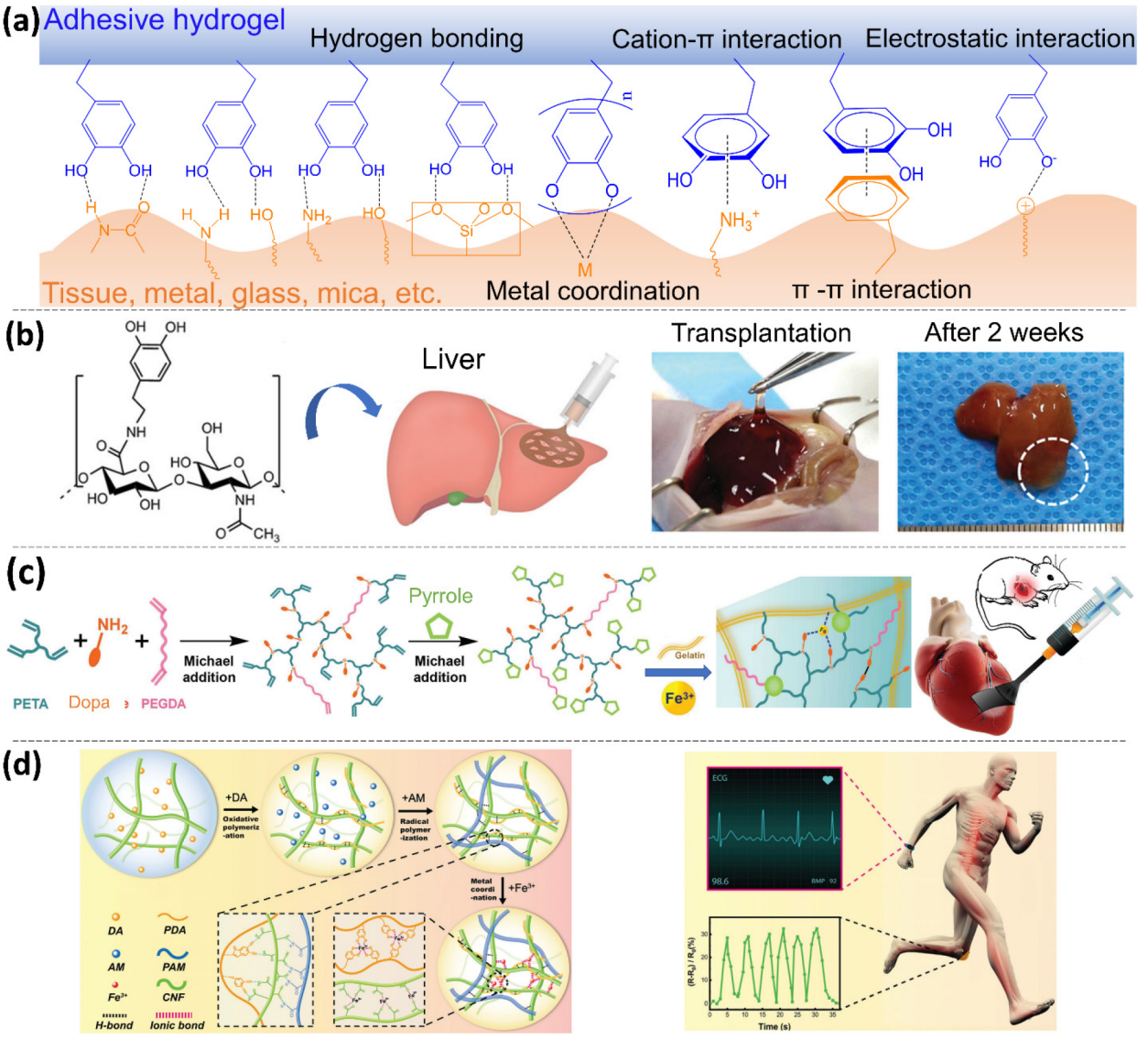

Figure 29. DOPA-based adhesive hydrogels. (a) DOPA-associated noncovalent interactions including hydrogen bonding, metal coordination, cation−π interactions, $\pi-\pi$ interactiosn, and electrostatic interactions. (b) Stem-cell loadable hydrogel tissue adhesive enabled by cross-linking of DOPA-functionalized HA. Reproduced with permission from ref 486. Copyright 2015 John Wiley & Sons. (c) Paintable and rapidly bondable hydrogel therapeutic cardiac patches through directly incorporating DOPA into the polymer hydrogel matrix via Michael addition. Reproduced with permission from ref 493. Copyright 2018 John Wiley & Sons. (d) DOPA was introduced into a hydrogel in the form of PDA polymer chains. The triple-network adhesive hydrogel was composed of PDA, CNF, and PAAm polymer networks, successfully serving as an epidermal sensor. Reproduced with permission from ref 494. Copyright 2020 The Royal Society of Chemistry.

hibited break stress of 17.2 MPa and fracture strain of 92%. However, the two networks of this kind of DN hydrogels were both covalently bonded, so the hydrogels could not recover from permanent fractures. Suo and co-workers addressed this problem by replacing the first network with reversible electrostatically cross-linked carboxylic groups of alginate and Ca^{2+}.[410] The resultant alginate-PAAm DN hydrogel showed extremely high stretchability of ~2300% and an enhanced rupture stress of 156 kPa with an extra self-healing property. The recoverable ability and mechanical strength are highly dependent on the molar ratio of the first to the second network and their cross-linking density, which involves the cooperation of covalent and noncovalent interactions.

3.4.2. Adhesive Hydrogels. Adhesive hydrogels have been widely utilized for wearable flexible electronics, wound dressing, hemostatics, and tissue repair/regeneration, because they can adhere to versatile substrates through harnessing both covalent bonds and noncovalent molecular interactions. Several design strategies (e.g., double networks hydrogels, nanocomposite-reinforced hydrogels)[475] and building blocks are available to construct adhesive hydrogels with specific functionalities and benign biocompatibility. The adhesive property is usually endowed by the outward/exposed functional groups on the surfaces of the hydrogels and in some cases achieved through the functionalization of the hydrogel surface.[479] The employed materials directly determine the types and strengths of the bindings between the adhesive hydrogels and the substrates. Covalent cross-linking of the interfaces usually associated with toxicity and side reactions as well as disposable permanence,[480]

https://doi.org/10.1021/acs.chemrev.2c00215
Chem. Rev. XXXX, XXX, XXX−XXX

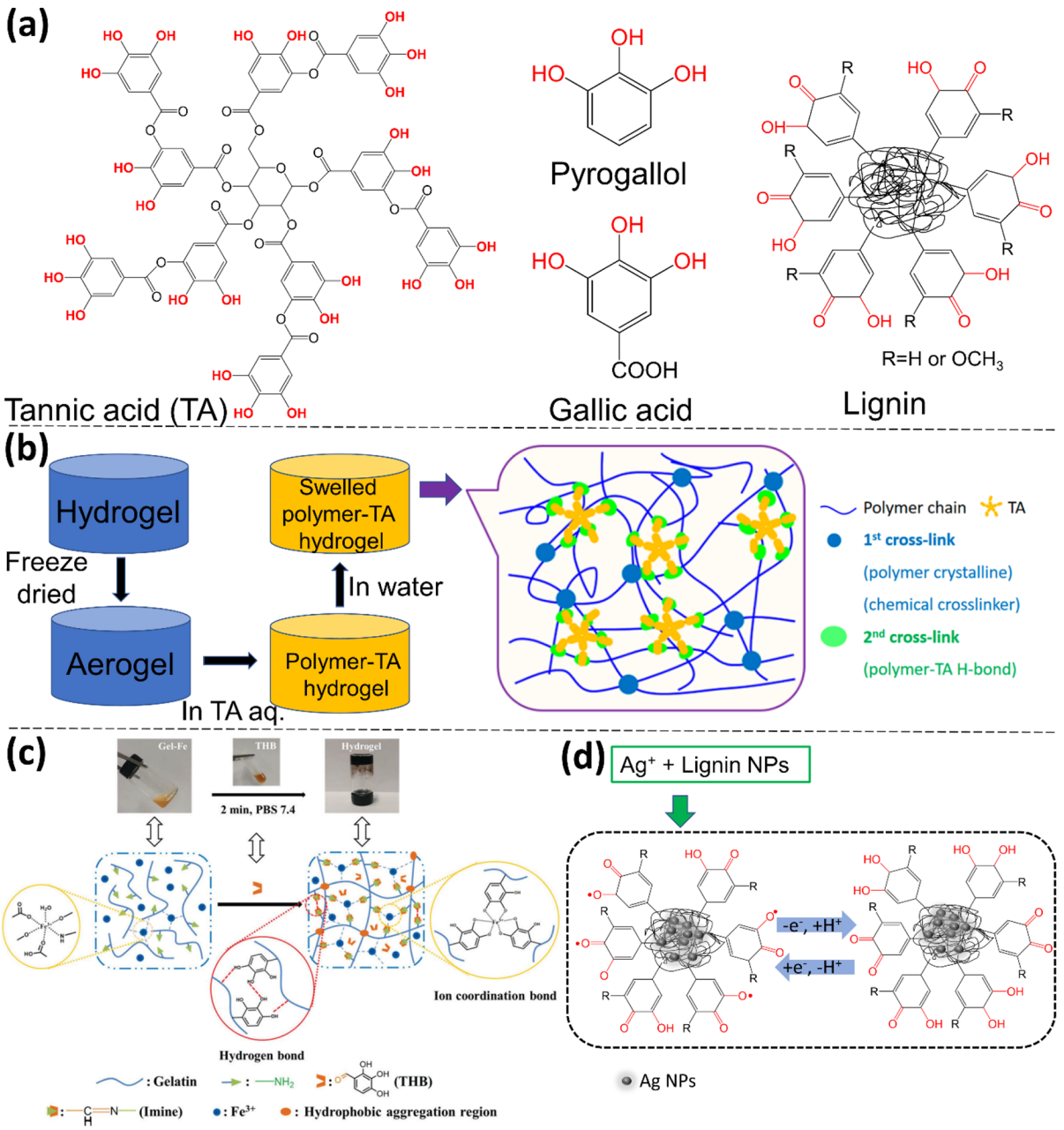

Figure 30. Plant-derived adhesive hydrogels. (a) Molecular structures of TA, pyrogallol, gallic acid, and lignin. (b) Facile and universal double-network strategy to make tough, swelling-resistant, self-healing and adhesive hydrogels. Reproduced with permission from ref 501. Copyright 2018 American Chemical Society. (c) Pyrogallol-contained adhesive hydrogel. Reproduced with permission from ref 502. Copyright 2020 The Royal Society of Chemistry. (d) Lignin-contained adhesive hydrogel with a dynamic catechol redox system aided by Ag^+. Reproduced with permission from ref 505. Copyright 2019 Springer Nature.

while noncovalent interactions elicit their advantages of biocompatibility, tunability, and reversibility.

Mussel-inspired adhesive hydrogels have attracted intensive research attention as they are effective in both dry and wet conditions, which are similar to sweaty skins and bleeding organs/tissues, providing imitable examples for the design of adhesive hydrogels, especially for biomedical applications. The key component of mussel's wet proteinous adhesives is DOPA, which is formed by post-translational modification of tyrosine. The catechol group of DOPA plays a vital role in bridging surfaces because of the formation of multiple noncovalent interactions including hydrogen bonding, metal−catechol coordination, electrostatic interactions, cation−π interactions, and $\pi-\pi$ aromatic interactions (Figure 29a).[16] One of the most frequently employed strategies to incooprate DOPA into hydrogel systems is grafting DOPA onto the polymer backbones such as alginate,[481] chitosan,[482−484] oxidized hyaluronic acid (OHA) or HA,[485,486] chondroitin sulfate,[487] and ε-polylysine.[488] For example, DOPA-grafted alginate, chondroitin sulfate, and regenerated silk fibroin (RSF) were cross-linked via oxidation by horseradish peroxidase (HRP), forming an injectable adhesive hydrogel that could load exosomes for endogenous cell recruitment and cartilage defect regeneration. Apart from DOPA-related adhesion on wet tissues, the presence

https://doi.org/10.1021/acs.chemrev.2c00215
Chem. Rev. XXXX, XXX, XXX−XXX

of deprotonated lysine and tyrosine in RSF strengthened the adhesion through establishing electrostatic interactions as well as phenolic hydroxyl group-involved hydrogen bonding, cation−π interactions, and $\pi-\pi$ interactions.[481] DOPA-modified quaternized chitosan was directly incorporated into a poly(D,L-lactide)-poly(ethylene glycol)-poly(D,L-lactide) (PLEL) hydrogel to endow the hydrogel with adhesiveness and antibacterial property. The positively charged trimethylammonium groups could enhance the tissue adhesion via electrostatic interactions.[482] DOPA-decorated chitosan was further modified with glycol moieties to enhance biocompatibility and alleviate its undesired immune responses.[484] DOPA-functionalized OHA, adipic acid dihydrazide-modified HA, and aldehyde-terminated Pluronic F127 were mainly cross-linked by dynamic covalent bonds via Schiff base reaction and an adhesive hydrogel was developed for skin wound dressing, where the unreacted catechol groups served as auxiliary noncovalent interactions for tissue adhesion since the oxidized catechol groups could generate covalent bonds with amine, imidazole and mercaptan groups on the biological substrates.[485] DOPA-functionalized HA could form a hydrogel via oxidative cross-linking, which worked as a stem-cell-encapsulated tissue adhesive with minimal invasion and improved angiogenesis while overcoming the tissue damage and hemorrhage of certain vulnerable organs caused by injection (Figure 29b).[486] Inspired by the polysaccharides/protein structure of natural epineurium matrices, DOPA-modified polylysine with maleimide groups and thiolated chitosan cross-linked via a Michael addition reaction, yielding a hydrogel as an effective tissue adhesive for peripheral nerve anastomosis.[488] The synergy between lysine and catechol could enhance the wet adhesion by surface salt displacement.[488,489] DOPA can also be directly copolymerized into polymer chains in the form of DOPA acrylamide/methacrylamide monomers. It was reported that the mixture of DOPA acrylamide, *N*-butyl acrylate (BA), acrylic acid (AAc) monomers and cross-linkers was photopolymerized into an adhesive conductive hydrogel in the presence of NaCl. The hydrogel worked well as wearable strain sensors for monitoring human motions including frowning, speaking, and bending.[490] DOPA methacrylamide and 3-(methacryloylamino) propyltrimethylammonium chloride were copolymerized and introduced into allyl cellulose with subsequent blue light-initiated polymerization. It was postulated that the existence of quaternary ammonium cationic groups could cooperate with catechol groups to reinforce tissue adhesion for wound dressing.[491] AAc and 3-((8,11,13)-pentadeca-trienyl)benzene-1,2-diol (UCAT) monomers were in situ polymerized within the polymer networks of chitosan. A hydrogel with strong and repeatable wet tissue adhesion was developed based on the synergy effect among catechol groups, negatively charged carboxyl groups, positively charged amine groups, and alkyl chains, which exhibited interfacial water-repelling property.[492] DOPA was also reported to be directly introduced into hydrogel polymer networks via Michael addition. DOPA and pyrrole molecules were sequentially introduced into the mixture of pentaerythritol triacrylate (PETA) and poly(ethylene glycol) diacrylate (PEGDA) via two-step Michael addition reactions with the formation of a hyperbranched polymer. This polymer was further cross-linked by Fe^{3+} in the presence of gelatin to generate a paintable and rapidly bondable conductive hydrogel as therapeutic cardiac patches (Figure 29c).[493] PDA is a frequently utilized composition of adhesive hydrogels. A triple-network adhesive hydrogel was composed of a cellulose nanofiber (CNF) network, an oxidatively polymerized PDA network, and a radically polymerized polyacrylamide (PAAm) network, which was further enhanced by addition of Fe^{3+} via metal coordination. This adhesive hydrogel was successfully applied as epidermal sensors (Figure 29d).[494] Acrylamide monomers were in situ polymerized in PDA solution to form adhesive hydrogel patches, which were simultaneously doped with extra-large pore mesoporous silica nanoparticles as drug carriers. The adhesive strength of the hydrogel was fortified by the multiple hydrogen bonds formed between silanol groups of the NPs and potential substrates.[495] An adhesive hydrogel was obtained through concurrently polymerizing AAc and acrylamide monomers in the PDA solution with the existence of a temperature-sensitive positively charged PNIPAm microgel (MR), which tackified the adhesiveness of the hydrogel by the concentration effect of weak bonds in the large cross-linking point of spherical MR.[496] Aside from homogeneously dispersing PDA chains within hydrogel matrices to endow adhesive property, PDA was also used to enhance the hydrophilicity of some hydrophobic inorganic materials such as rGO nanosheets,[497] talc nanoflakes,[498] and clay nanosheets.[499] Incorporation of the PDA-coated nanocomposite materials into hydrogels could not only impart catechol-based adhesiveness but also confer conductivity (rGO nanosheets), high stretchability (talc nanoflakes), or high toughness (clay nanosheets).

Plant-derived materials such as tannic acid (TA),[500,501] pyrogallol,[502] gallic acid,[503,504] and lignin[505] possess similar phenolic structures to that of DOPA (Figure 30a). Hence, they are also exploited as low-cost alternatives to fabricate hydrogels as adhesive moieties. For instance, in situ polymerized PAAc in the aqueous dispersion of tannic acid-coated cellulose nanocrystals (TA@CNCs) was further strengthened by Al^{3+} through metal coordination. The hydrogel served as wearable strain sensors on human skin without an inflammatory response and residual effect.[500] A facile and universal double-network strategy was utilized for the fabrication of tough, swelling-resistant, self-healing and adhesive hydrogels, taking advantage of the multiple hydrogel bonds between polymer chains and TA. The hydrogels such as poly(vinyl alcohol) (PVA) and polyacrylamide (PAAm) were first freeze-dried and then were immersed in TA aqueous solution to initiate the intermolecular hydrogen-bonding interaction toward double-network hydrogels, where the free catechol groups served as adhesive functional groups (Figure 30b).[501] A pyrogallol derivative 2,3,4-trihydroxybenzaldehyde (THB) was introduced into a Fe^{3+}-containing gelatin aqueous solution via the Schiff base reaction between the amino groups of gelatin and the aldehyde groups of THB, resulting in the generation of an adhesive hydrogel with antibacterial property for application of wound healing. The triple adjacent hydroxyl groups on the aromatic rings of THB enabled the hydrogel with adhesiveness through multiple noncovalent interactions akin to those of DOPA on various substrates (Figure 30c).[502] Alginate was modified by gallic acid through hydrogen bonds between hydroxyl groups and carboxyl groups, and then served as the first polymer matrix for in situ polymerization of the second polymer network, PAAc. If drugs like caffeine were loaded in the hydrogel at the gallic acid-modification step, the resulting hydrogel could act as an adhesive hydrogel for transdermal delivery. It was noted that the hydrogel exhibited an excellent adhesive strength of 74.7 kPa on aluminum foil, which was assumed to arise from the multiple catechol groups-enabled metal coordination.[503] Gallic acid could be grafted onto chitin nanofibers through 1-ethyl-3-(3-(dimethylamino)propyl) carbodiimide (EDC) chemistry

https://doi.org/10.1021/acs.chemrev.2c00215
Chem. Rev. XXXX, XXX, XXX−XXX

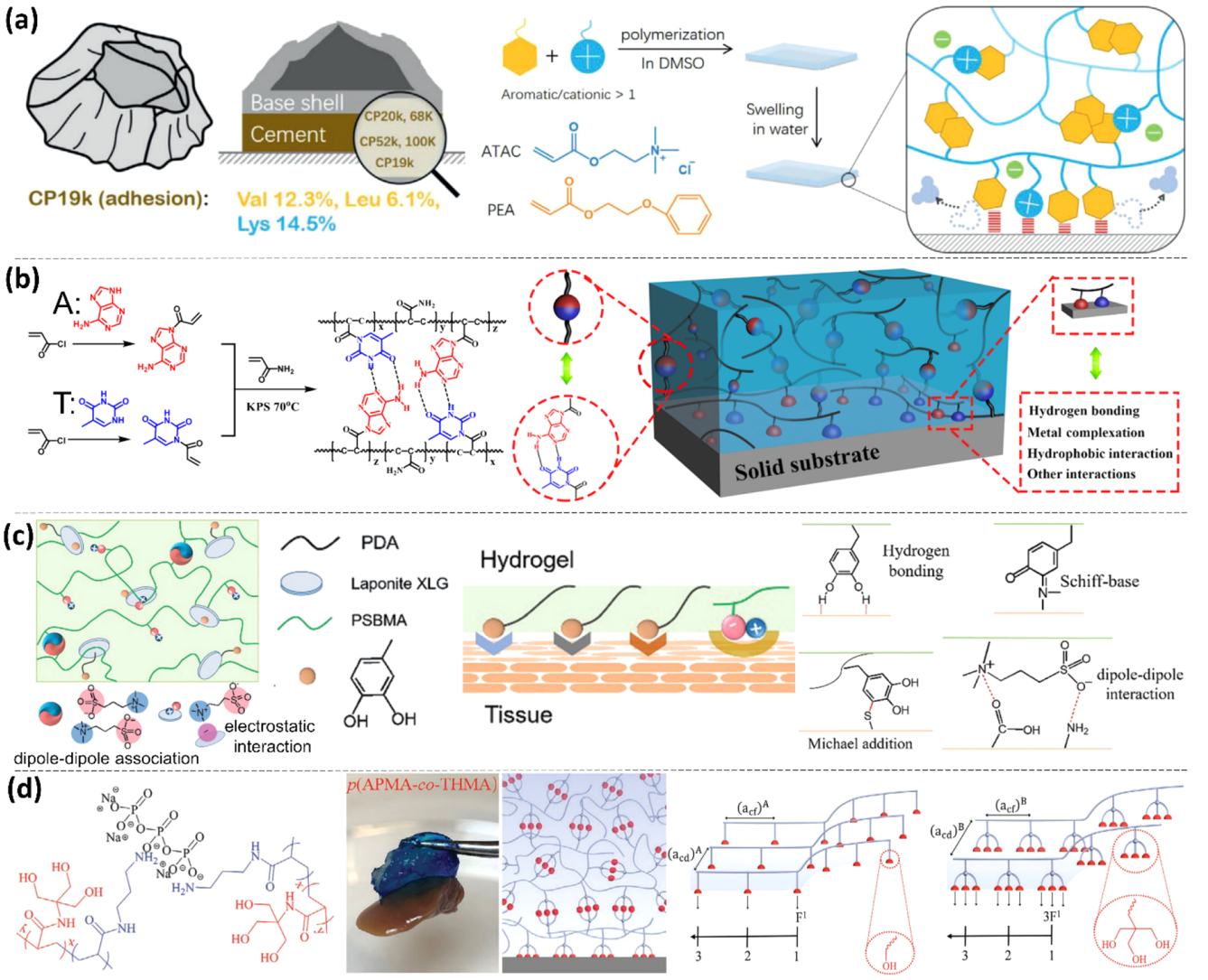

Figure 31. Design of adhesive hydrogels through manipulating noncovalent interactions. (a) Barnacle-inspired adhesive hydrogel through mimicking the composition of CP19k. Reproduced with permission from ref 463. Copyright 2020 John Wiley & Sons. (b) DNA-inspired adhesive hydrogel, which tackified the PAAm hydrogel by incorporation of acrylated A and T monomers. Reproduced with permission from ref 508. Copyright 2017 American Chemical Society. (c) Nanocomposite- and PDA-reinforced zwitterionic polymer hydrogel. Reproduced with permission from ref 510. Copyright 2020 The Royal Society of Chemistry. (d) Adhesive hydrogel with three hydroxy groups cluster-enabled triple hydrogen bonds. Reproduced with permission from ref 511. Copyright 2020 John Wiley & Sons.

between the amine groups of chitin and the carboxyl groups of gallic acid. Further cross-linking the gallic acid-modified chitin nanofibers by Fe^{3+} or sodium periodate $NaIO_4$ resulted in an adhesive hydrogel with enhanced cohesion and adhesion because of the multiple catechol groups of gallic acid.[504] It was reported the long-term wet adhesion of mussels on versatile substrates was enabled by the continuous secretion of a reductive protein, which maintained the dynamic equilibrium of catechol and quinone groups. Inspired by this, lignin was expected to continuously generate catechol groups under the aid of Ag^+ and the solar light in the ambient environment (Figure 30d). In detail, the phenolic hydroxyls or methoxy groups of lignin could reduce Ag^+ into Ag NPs, accompanied by the oxidation to redox-active quinone or hydroquinone. The Ag NPs could conversely generate electrons from surface plasmon resonance triggered by light in the ambient environment to convert the quinone or hydroquinone into catechol groups. When an aqueous solution of AA, Ag-lignin NPs, and pectin was polymerized into a hydrogel, the aqueous environment could continuously generate both catechol and quinone groups to retain long-term and repeatable adhesiveness.[505]

Other strategies have been also applied for developing adhesive hydrogels, such as polymerization and nanocomposite reinforcement. For example, inspired by barnacle cement proteins (CPs), one of which (CP19k) is composed of a high content of cationic lysine (Lys) as well as hydrophobic amino acids valine (Val) and leucine (Leu), it was envisioned that cationic and aromatic monomers could be polymerized into a hydrogel, mimicking barnacles' wet adhesion. Then cationic 2-(acryloyloxy)ethyl trimethylammonium chloride (ATAC) and aromatic 2-phenoxyethyl acrylate (PEA) monomers were copolymerized in dimethyl sulfoxide (DMSO), which converted into a hydrogel with subsequent swelling in water (Figure 31a). The as-prepared hydrogel elicited excellent repeatable wet adhesion on negatively charged, hydrophobic, and metal surfaces, suggesting that electrostatic interactions, hydrophobic

https://doi.org/10.1021/acs.chemrev.2c00215
Chem. Rev. XXXX, XXX, XXX−XXX

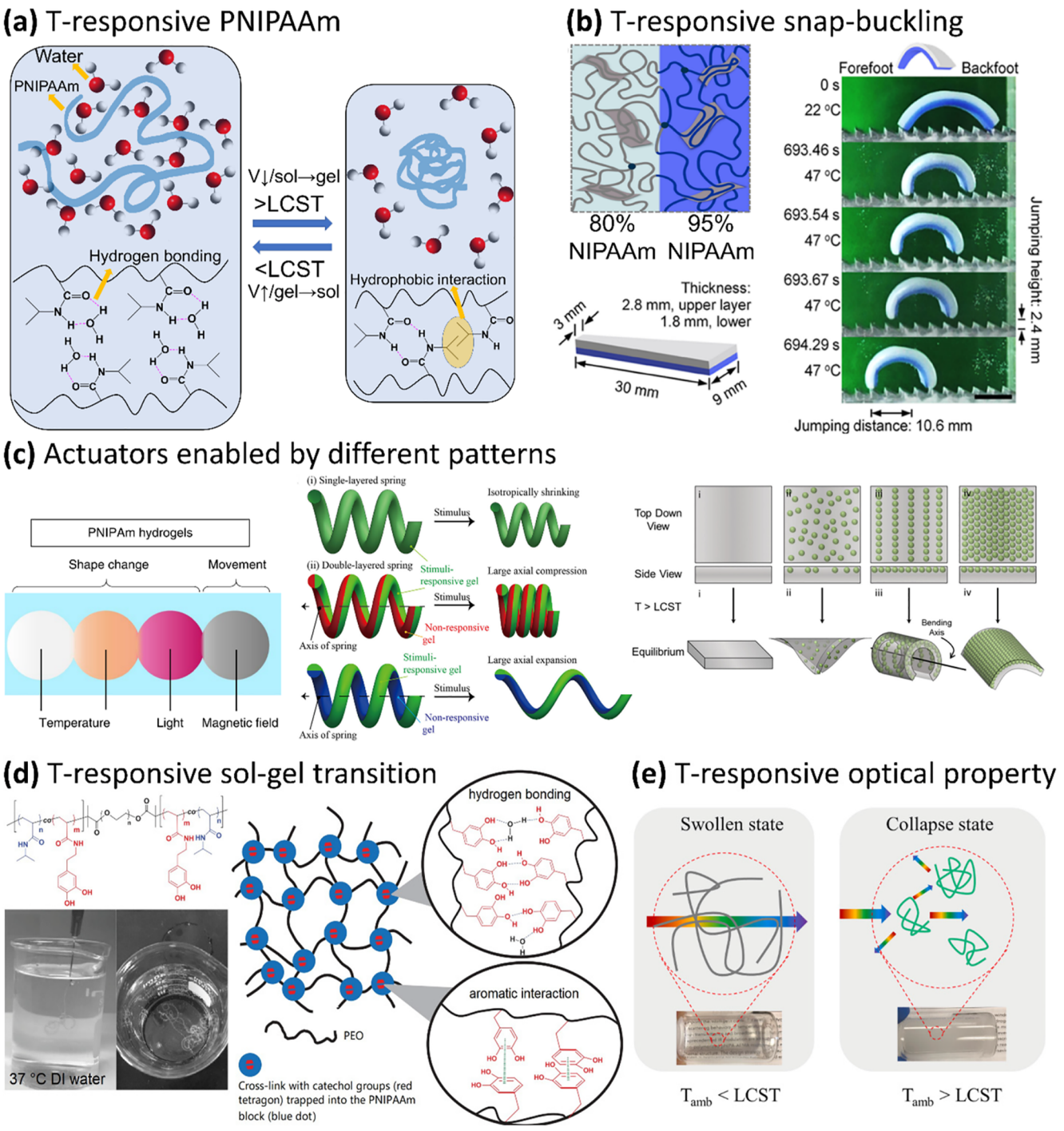

Figure 32. T-responsive hydrogels. (a) Reversible volume change or sol−gel transition of T-responsive PNIPAm hydrogel. (b) T-responsive snap-buckling fabricated with bilayer hydrogel containing different percentages of NIPAAm monomers. Reproduced with permission from ref 544. Copyright 2018 American Chemical Society. (c) T-responsive actuators constructed by hydrogels with different patterns. Left panel: Reproduced with permission from ref 550. Copyright 2020 Springer Nature. Middle panel: Reproduced with permission from ref 536. Copyright 2018 Elsevier. Right panel: Reproduced with permission from ref 546. Copyright 2016 John Wiley & Sons. (d) T-responsive sol−gel transition of a mussel-inspired triblock hydrogel with injectability. Reproduced with permission from ref 566. Copyright 2015 John Wiley & Sons. (e) Different solar light transmittance of T-responsive hydrogels because of the coil−globule transition of T-responsive polymers. Reproduced with permission from ref 547. Copyright 2021 Elsevier.

interactions, and cation−π interactions all played significant roles in achieving adhesion. It was noted that the adhesion to the negatively charged surface was the strongest, indicating the predominant role of electrostatic interaction. The hydrophobic aromatic groups were verified to be able to enhance the electrostatic interaction-bridged surfaces by inducing dehydration at the interface.[462,463] Inspired by DNA's stable double helix structure enabled by hydrophobic aromatic rings-protected multiple hydrogel bonds, nucleobases including adenine (A), thymine (T), guanine (G), cytosine (C), and uracil (U) have

https://doi.org/10.1021/acs.chemrev.2c00215
Chem. Rev. XXXX, XXX, XXX−XXX

been explored for constructing adhesive hydrogels.[506−509] For example, A and T were employed to tackify a PAAm adhesive hydrogel through copolymerization with AAm monomers in the form of acrylated monomers. The −C=O, $-NH_2$, and −N= groups were considered to contribute to both cohesion and adhesion of the hydrogel via multiple hydrogel bonds within the hydrogel (Figure 31b) and with various substrates (N, O, F, OH and/or $-NH_2$ functional moieties in the substrates). The −C=O and −N− groups could form a metal coordination via interacting with metal ions. The heterocyclic structure could generate hydrophobic interactions, $\pi-\pi$ interactions, and cation$-\pi$ interactions with hydrophobic groups, unsaturated (poly)cyclic molecules, and cations in the substrates, respectively, because of the hydrophobic and electron-rich aromatic rings. It was demonstrated that the A- and T-integrated PAAm hydrogel exhibited maximum peeling strength of 330 N m^{-1}, more than four times that of a pure PAAm hydrogel (70 N m^{-1}).[508] The adhesive strength of the zwitterionic poly[2-(methacryloyloxy)ethyl]dimethyl-(3-sulfopropyl) ammonium hydroxide (PSBMA) hydrogel was enhanced by incorporating PDA-modified laponite clay nanosheets into the hydrogel matrix because itself possessed low adhesion to various substrates because of weak ion−dipole and/or dipole−dipole interactions. The hydrogel firmly and repeatably adhered to a tissue substrate via Schiff base and Michael addition chemical cross-linking as well as hydrogen bonding and dipole−dipole physical interactions enabled by DOPA and zwitterionic groups (Figure 31c).[510] The copolymer of *N*-[tris(hydroxymethyl)methyl]-acrylamide (THMA) and *N*-(3-aminopropyl)methacrylamide hydrochloride (APMA) was converted into a hydrogel with the addition of a sodium tripolyphosphate (STTP) via ionically cross-linking between amine groups and phosphate groups (Figure 31d). The resulting p(APMA-*co*-THMA) hydrogel could firmly adhere to various substrates, especially to mouse liver, which is superior to a lot of hydrogen bonds-involved hydrogels such as pAPMA, poly(ethylenimine) (PEI), chitosan, PAAc, pTHMA, and poly(vinyl alcohol) (PVA), because of the intensive triple hydrogen bonds and the unique equal load sharing (ELS) configuration of the three hydroxy groups cluster.[511]

3.4.3. Stimuli-Responsive Hydrogels. Stimuli-responsive hydrogels have drawn great research interest because of their versatile applications such as controlled drug delivery,[512−529] protein delivery,[530] chemical-/biosensors,[531−539] actuators,[514,536,539−546] energy-saving smart windows,[547,548] disease diagnosis,[549] soft robotics,[545,550] 3D printing,[551] fluorescent printing,[552] antibacterial,[553,554] tissue engineering,[525,555] shape memory systems,[556] cell capture/release/harvest,[557−559] tunable surface wettability,[560,561] and so on. Basically, the stimuli can be classified into two categories: physical stimuli like light,[512,516,525,550,551,553,557] electric fields,[539,542,543] magnetic fields,[525,539,550] mechanical forces (shear, strain, artificial fracture),[551,562] and temperature (refs 515, 519, 521, 523−525, 531, 536, 540, 541, 544−546, 548, 549, 551, 552, 554, 555, 558, 559, and 561); and chemical stimuli including pH,[513−515,517,519,521,522,527,529,531,532,539,545,552,560,563] solvent changes,[531,541] gases,[533,564] ions,[513,528,556] enzymes,[516,522,526,534] reductants,[516,518] oxidants,[518] ROS,[555] saccharides,[558] and specific ligands/receptors.[520,530,535,537,538565] Extensive strategies are available for the fabrication of hydrogel matrices and the achievement of stimuli-responsive properties, and this section only summarizes hydrogels whose stimuli-responsiveness are based on noncovalent interactions. Physical stimuli and chemical stimuli could directly or indirectly affect/alter molecular structures or inter-/intramolecular interactions, among which temperature and pH are the most common triggers, usually inducing reversible volumetric changes or reversible sol−gel transitions via tuning noncovalent interactions.

Temperature (T) is one of the most common environmental variates, usually being employed as a trigger to initiate responses of thermosensitive ingredient-contained hydrogels. As the most studied thermally responsive polymer, PNIPAm can experience a rapid and reversible volume change at a critical temperature, that is, the LCST. At a low temperature (<LCST), the hydrophilic amide groups are well hydrated by water molecules via hydrogen-bonding interactions, which are weakened when the temperature is above the LCST while the hydrogen-bonding interaction between the amide groups as well as the hydrophobic interactions among the isopropyl groups play a predominant role in molecular interactions (Figure 32a). These variations of noncovalent interactions within the hydrogels resulted in the transition of polymer chains from hydrated coils to dehydrated globules, together with volume shrinkage of the hydrogels.[546,547,561,565] It has been demonstrated that this thermoinduced volume transition could be turned into mechanical energy to drive actuators, where the different deswellings of the two hydrogel layers lead to the desired bending direction. For example, it was reported that a snap-buckling was designed comprising two layers of PNIPAm-contained hydrogels but with different percentages of NIPAm monomers. Upon heat treatment in the water to above the LCST, the two layers of hydrogels exhibited different volume shrinkages, which gave rise to the hydrogel snap-buckling bending toward to the side with more NIPAAm monomers (Figure 32b). The accumulation of the bending deformation endowed the bilayer hydrogels with internal elastic energy, consequently engendering the jumping of the snap-buckling.[544] In another example, NIPAm was in situ polymerized within a polyaniline hydrogel to be a conductive photothermally responsive hydrogel. It could serve as a somatosensory actuator when bonded with a passive layer because of sensing endowed by conductive polyaniline and actuation (soft gripper in hot water) enabled by different shrinkages between the thermoresponsive PNIPAm hydrogel and the passive layer.[540] Various T-driven deformations could be achieved by pattern designs via microfabrication. For instance, multiresponsive connected PNIPAm hydrogel nanobeads were constructed through the photopolymerization of liquid bilayers-encapsulated aqueous pregel droplets, where AuNPs-incorporated PNIPAm hydrogel nanobeads enabled photothermal responsiveness while magnetic particles-doped PNIPAm hydrogel nanobeads served as a magnetic handle (Figure 32c left).[550] Spring-shaped actuators with tunable large deformations were made with the aid of simple capillaries and syringe pumps. The solution of poly(NIPAAm-*co*-acrylic acid) and alginate was extruded into a $CaCl_2$ solution to generate hydrogels with single-layered, double-layered, or inside−outside patterns (Figure 32c middle).[536] The assembly of diverse microparticle endoskeleton structures within the PNIPAm hydrogels could also direct various deformations of the hydrogels upon elevating the temperature above the LCST (Figure 32c right).[546] Besides actuators, PNIPAm hydrogels with T-associated volume changes could have applications in disease diagnosis, antibacterial materials, and cell harvesting. PNIPAm hydrogel microspheres could act as thermally responsive probes for mapping mechanical properties of tissues at cellular length

https://doi.org/10.1021/acs.chemrev.2c00215
Chem. Rev. XXXX, XXX, XXX−XXX

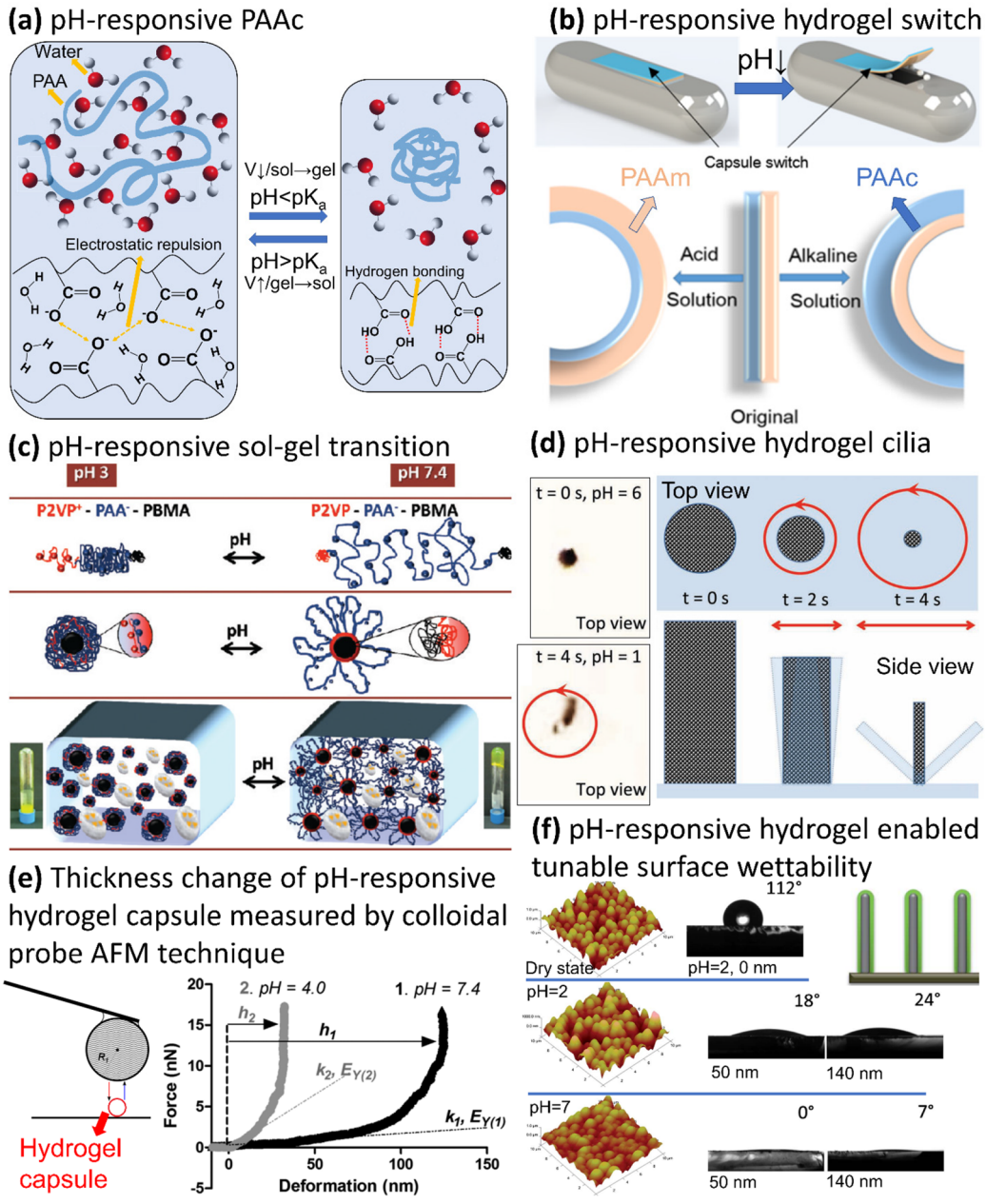

Figure 33. pH-responsive hydrogels. (a) Reversible volume change or sol−gel transition of the pH-responsive PAAc hydrogel. (b) Drug-loadable capsule with pH-responsive PAAc-PAAm bilayer hydrogel switch. Reproduced with permission from ref 514. Copyright 2020 American Chemical Society. (c) pH-responsive sol−gel transition of a triblock terpolymer P2VP-PAA-PnBMA. Reproduced with permission from ref 527. Copyright 2011 American Chemical Society. (d) pH-responsive hydrogel cilia shrunk with the decrease of pH and could rotate following the external rotating magnetic field because of the doping with iron particles. Reproduced with permission from ref 539. Copyright 2013 John Wiley & Sons. (e) Thickness change of the pH-responsive hydrogel capsule measured by colloidal probe AFM technique. Reproduced with permission from ref 563. Copyright 2013 American Chemical Society. (f) Poly(methacrylic acid-*co*-ethylene glycol diacrylate) hydrogel-coated VACNT array with tunable wettability at different pH values. Reproduced with permission from ref 560. Copyright 2012 The Royal Society of Chemistry.

scales. These microspheres injected into tissues kept at the compacted status but started to expand upon being cooled, whose degrees of expansion were dependent on the rigidity (soft or hard) of the surrounding tissues. The swelling percentages could be quantitatively associated with the stiffness of the surrounding tissue matrix by comparing the residual elasticities of the expanded PNIPAm hydrogel microspheres with those of the tissue phantoms.[549] Molecularly imprinting and removing β-lactamase molecules in the PNIPAm hydrogel could generate a hydrogel with T-responsive recognition toward β-lactamase (being able to hydrolyze the β-lactam ring to deactivate β-lactam antibiotics), which could bind β-lactamase expressed by bacteria while providing opportunities for β-lactam antibiotics to kill the bacteria. Subsequently, decreasing the temperature would make the PNIPAm hydrogel template swell, or in other words, shrink the imprinted sites to be no longer appropriate for binding lactamase, therefore being ready for the next cyclic utilization.[554] Replacing the β-lactamase with cell-adhesive peptide Arg-Gly-Asp-Ser (RGDS) enabled the surfaces of the molecularly imprinted PNIPAm hydrogel to be thermoresponsive cell

https://doi.org/10.1021/acs.chemrev.2c00215
Chem. Rev. XXXX, XXX, XXX−XXX

culture substrates. Cultured monolayer cell sheets would spontaneously detach from the substrates as lowering the temperature would turn the hydrogel surface from hydrophobic to hydrophilic and release the RGDS because of the changed shapes of the imprinted sites.[559] On the other hand, the sol−gel transition is a common phenomenon accompanied by the coil-to-globule transition of thermoresponsive polymers. T-sensitive polymers like PNIPAm and methylcellulose both undergo sol−gel transitions as elevating the temperature above their LCSTs, which is ascribed to reinforced intermolecular and intramolecular hydrogen-bonding interactions as well as hydrophobic interactions. This transition enables minimally invasive drug delivery or tissue injection with precise sites and/or controlled release of drugs.[523,524,555] Zeng and co-workers combined catechol functionalized PNIPAm and poly(ethylene oxide) (PEO) to form a thermoresponsive triblock copolymer, which could form a hydrogel once injected into 37 °C deionized (DI) water because of the thermosensitivity of PNIPAm. Meanwhile, the hydrogel possessed a self-healing property because of hydrogen bonding and aromatic interaction between catechol groups and an antibiofouling property because of the presence of PEO (Figure 32d).[566] This thermo-induced protection strategy was also used to ensure the close contact of cation and aromatic groups. Additionally, the coil−globule transition of thermoresponsive polymers is associated with transparency variations as the light would be greatly blocked when passing through the colloidal solution distributed with polymer globules (Figure 32e). Therefore, this characteristic was employed to design T-responsive energy-saving smart windows by incorporating a thermoresponsive hydrogel layer, which absorbed the heat of the solar radiation and turned opaque to resist further transmission, saving energy required for space cooling.[547,548]

As hydrogels are abundant with water and usually applied in aqueous environments, an ambient variate that can be conveniently tuned is pH. pH-responsive hydrogels are usually composed of weak polyelectrolytes, whose functional groups such as carboxyl groups or amine groups tend to protonate at pH values lower than their pK_a values, while they deprotonate at pH values higher than their pK_a values. Correspondingly, ionized functional groups extend the polymer networks of the hydrogels to exhibit swollen volumes because of the repulsive electrostatic interaction among likely charged ionized functional groups and dominant hydrogen-bonding interactions between hydrophilic ionized functional groups and water molecules. Conversely, protonated functional groups interact with each other with strong hydrogen bonding, leading to compacted polymer networks and shrunken volumes (Figure 33a).[514,517,539] Different volume changes of poly(acrylic acid) (PAAc)-polyacrylamide (PAAm) bilayer hydrogels in response to pH could be utilized to construct a drug-laden capsule with a pH-responsive hydrogel switch (Figure 33b). The switch was turned on when the capsule was in the acid environment in which the PAAc hydrogel layer shrunk while the PAAm hydrogel layer expanded. Inversely, the switch was turned off when the capsule was immersed in a basic medium.[514] This kind of drug carrier capsule could load and release both hydrophilic and lipophilic drugs via a hydrogel actuator switch, being different from hydrophilic hydrogels that release encapsulated hydrophilic drugs through direct diffusion from the bulky hydrogel.[517] Sometimes, pH would affect the self-assembly of polymers through modulating charged functional groups to be hydrophobic through protonation (Figure 33c).[527] Triblock terpolymer poly(2-vinylpyridine)-*b*-poly(acrylic acid)-*b*-poly(*n*-butyl methacrylate) (P2VP-PAA-PnBMA) self-assembled into spherical compact nanostructures dispersed in an aqueous solution with the hydrophilic corona formed through electrostatic interactions between positively charged P2VP chains and negatively charged PAA chains and the hydrophobic core generated via intermolecular hydrophobic interactions of the PBuMA blocks. However, it changed into flower-like micelles because of the hydrophobic interactions between the deprotonated P2VP and PnBMA blocks, which enabled the association of the hydrophobic core, while the repulsive electrostatic interactions between the negatively charged PAA chains induced them to expand to be the hydrophilic shell of the micelle. The overlapping of adjacent flower-like micelles to a certain extent resulted in the formation of 3D hydrogel networks. This pH-responsive sol−gel system was demonstrated to be a promising injectable drug delivery system.[527] Besides drug delivery, the pH-responsive hydrogels could also serve as biosensors. For instance, biomimetic cilia arrays with both motility and sensation could be achieved by making use of the pH-responsive PAAm hydrogel doped with iron particles. The PAAm hydrogel cilia arrays were first hydrolyzed in 2 M NaOH and then swelled from a square to a round shape in the cross section because of the repulsive electrostatic interactions among the ionized carboxyl groups which were converted from amine groups of PAAm under strong alkaline situation. When the pH dropped from 6 to 1, the cilia arrays shrunk in both cross section and length (the direction vertical to the substrate) and then started to rotate following the rotation of the external magnetic field because of the presence of the iron particles (Figure 33d).[539] Apart from the qualitative interpretation of pH-associated volume change of hydrogels from the perspective of intermolecular interactions, quantitative measurements were also demonstrated by the colloidal probe AFM technique.[563] As the pH decreased from 7.4 to 4.0, the film thickness h of the pendant-thiol-modified poly(methacrylic acid) hydrogel capsules decreased from h_1 to h_2 as the strong hydrogen-bonding interaction between the protonated carboxyl groups densified the hydrogel film. Correspondingly, the stiffness of the hydrogel film increased from $E_{Y(1)}$ to $E_{Y(2)}$ (Figure 33e). Besides, pH-responsive hydrogels can modify the wettability of surfaces as adjustable coatings.[560] Vertically aligned carbon nanotube (VACNT) arrays vapor-coated with a poly(methacrylic acid-*co*-ethylene glycol diacrylate) hydrogel changed from a pristine hydrophobic state with a water contact angle of 112° to a hydrophilic state with very small water contact angles (Figure 33f). The wettability of the hydrogel-coated surface could be further tuned via varying pH value and the thickness of the hydrogel coating. The patterned surface with a hydrogel coating of 50 nm exhibited superwettability (water contact angle = 0°) at a pH of 7, because of the appropriate porosity of the VACNT arrays and the superhydrophilicity induced by the ionization of the carboxyl groups, but it would become less hydrophilic in acidic conditions, attributed to the strong hydrogen bonding between the protonated carboxyl groups.

T-responsiveness and pH-responsiveness can coexist in pressing need with the increasing number of multifunctional smart materials. To this end, the generally used strategy is integrating T-responsive and pH-responsive functional groups into one hydrogel system. For example, NIPAm and AAc monomers were copolymerized into one hydrogel to endow the system with dual controllable drug release. A triblock copolymer with PNIPAm and PAAc end chains would self-assemble into

https://doi.org/10.1021/acs.chemrev.2c00215
Chem. Rev. XXXX, XXX, XXX−XXX

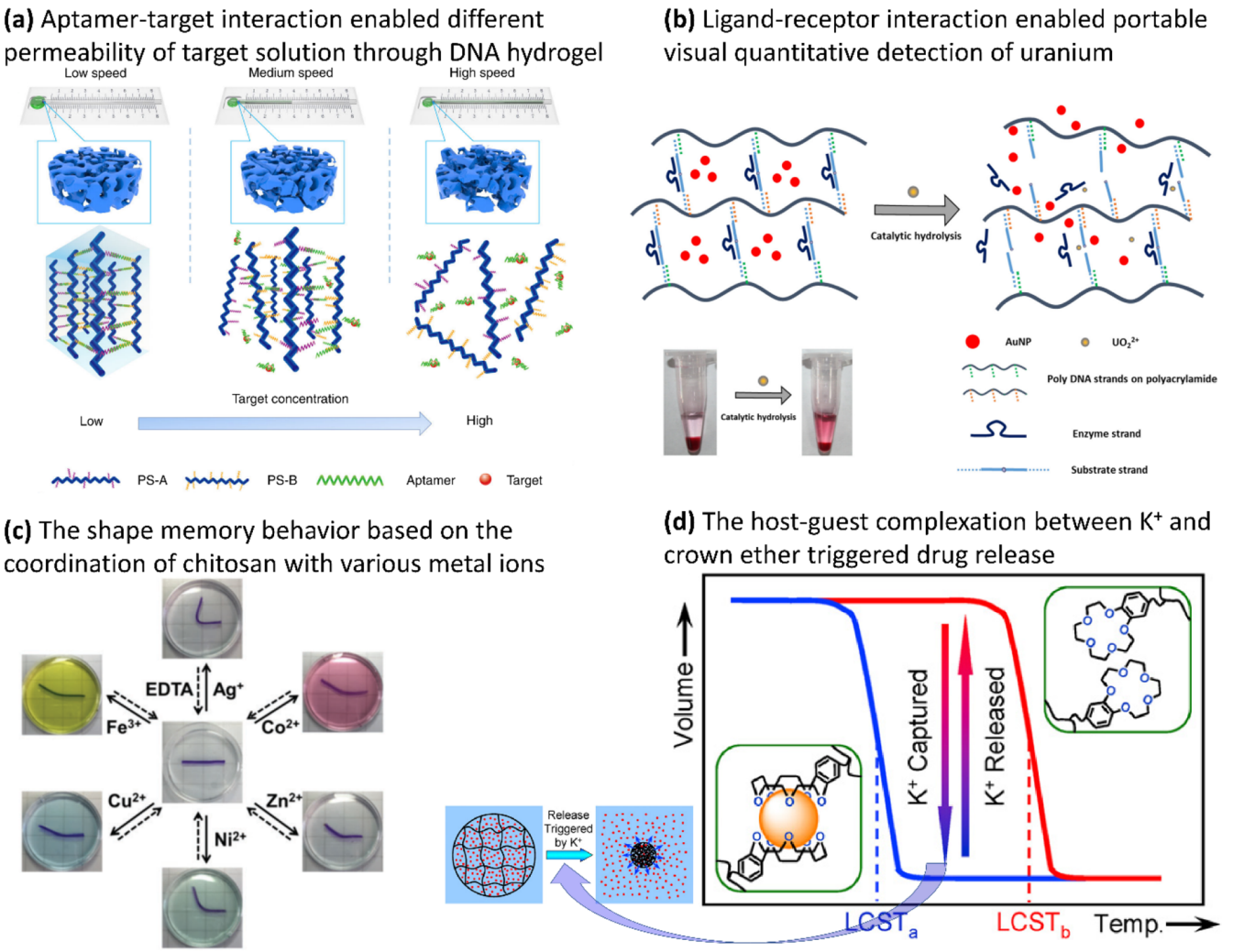

Figure 34. (a) Aptamer−target interaction enabled different permeability of target solution through DNA hydrogel. Reproduced with permission from ref 535. Copyright 2019 Springer Nature. (b) Ligand−receptor interaction enabled portable visual quantitative detection of uranium. Reproduced with permission from ref 537. Copyright 2016 Elsevier. (c) Deformation and recovery of stimuli-responsive hydrogels based on the coordination of chitosan with various metal ions. Reproduced with permission from ref 556. Copyright 2016 Royal Society of Chemistry. (d) Host−guest complexation between K^+ and crown ether triggered drug release. Reproduced with permission from ref 528. Copyright 2010 Elsevier.

micelles with a hydrophobic PNIPAm core and a hydrophilic PAAc shell when increasing the T to some extent. A subsequent decrease of pH transferred the micelles into a network structure with both PNIPAm and PAAc knots because of the strong hydrogen-bonding interactions among the protonated AAc groups and the hydrophobic interactions among the isopropyl groups. Further elevating T resulted in a more compacted network structure for drug loading, attributed to the reinforced hydrophobic interactions, and the drug release was initiated by the increase of pH, because of the partially collapse of the network structure induced by dissociation of the PAAc knots.[519] Decoupled thermo- and pH-responsive hydrogel microspheres could also be obtained by introducing cross-linkers formed through complexing polyethylene glycol (PEG)-based terminal bulky macromonomers with γ-cyclodextrin (γ-CD) into polymerization of NIPAAm monomers. The hydrogen bonds between the hydroxyl groups of γ-CD and the etheric oxygens of the macromonomers developed in acidic or neutral solutions would be impaired in alkali solutions, serving as manipulable noncovalent interactions for pH-responsiveness. This method could circumvent the uncontrollable volume shrinkage caused by attractive electrostatic interaction between deprotonated carboxyl groups and positively charged drugs.[521,567] It was proven that the pH-responsiveness of the pH and T dual-responsive hydrogel could be achieved through tuning the hydrogen-bonding interaction between the loaded drugs and the NIPAAm-contained polymer networks of the hydrogel. At a low pH, drugs released slower below the LCST of PNIPAm because of an enhanced hydrogen-bonding interaction between the protonated drugs and the polymer networks. While at a neutral pH, drugs were released faster below the LCST because the deprotonated drugs such as indomethacin were not inclined to form hydrogen bonds with the polymer networks.[515] Besides, double networks hydrogels incorporating p(NIPAAm-*co*-AAc) with sodium alginate and Ca^{2+} could realize T-/pH-responsive isotropic/anisotropic shrinkage/swelling of the hydrogels through modulating processing methods of the hydrogels.[545]

Hydrogels in response to other stimuli were also reported with the modulation of noncovalent interactions. A responsive DNA hydrogel was fabricated by connecting DNA strands PS-A and

https://doi.org/10.1021/acs.chemrev.2c00215
Chem. Rev. XXXX, XXX, XXX−XXX

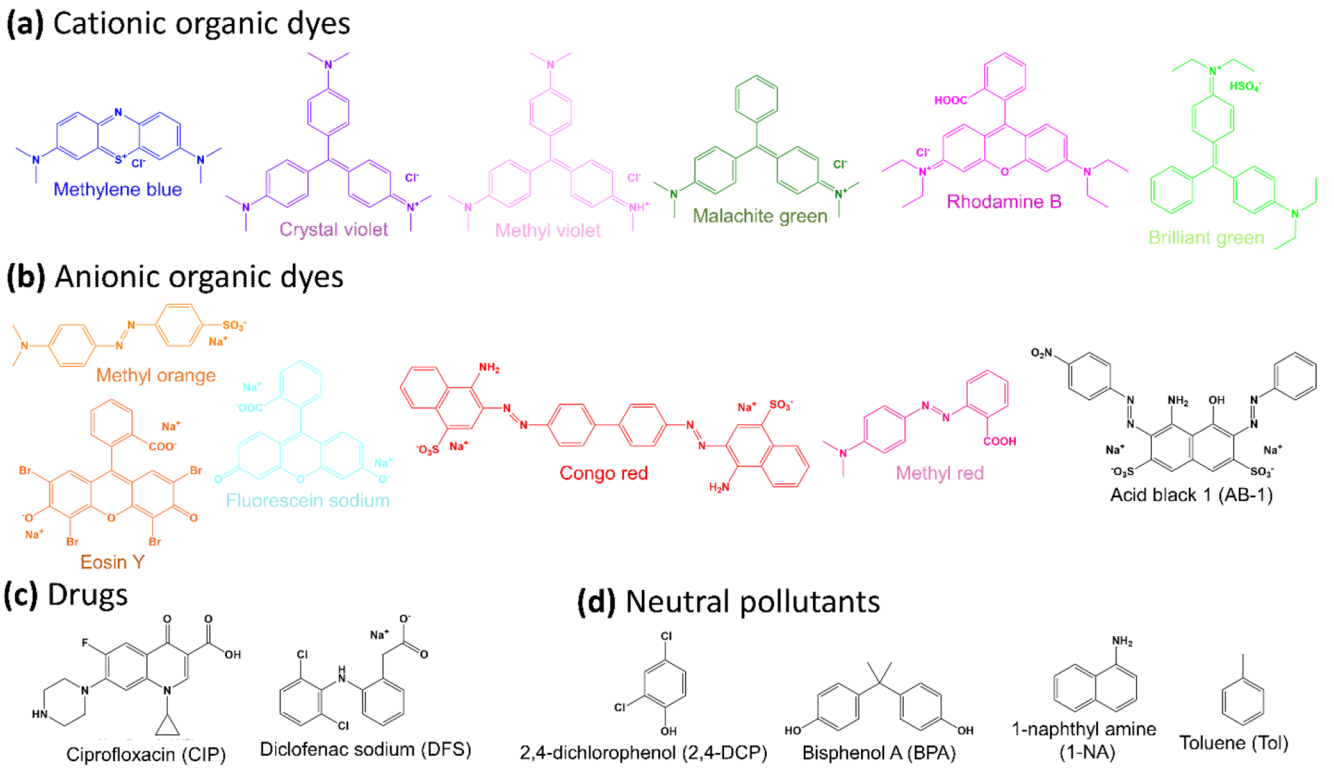

Figure 35. Molecular structures of typical examples of (a) cationic organic dyes, (b) anionic organic dyes, (c) some drugs, and (d) neutral pollutants.

PS-B with a cocaine aptamer as the cross-linker. In the presence of cocaine, the responsive DNA hydrogel would dissociate because of the competitive ligand−receptor interaction between cocaine and the cocaine aptamer, which would decrease the cross-linking density of the hydrogel and consequently increase the permeability of the hydrogel. Cocaine solutions of different concentrations could be quantitatively distinguished by comparing flow speed calculated from flow distance divided by flow time (Figure 34a).[535] Similarly, Pt NPs or Pt shell NPs with a Au core were loaded in the DNA hydrogel, which would release the NPs upon adding targets such as cocaine, ochratoxin A, and lead ion. Taking advantage of the catalytic property of the Pt NPs, H_2O_2 could be decomposed into O_2, whose corresponding pressure could be facilely read out via a pressuremeter and was proportional to the concentration of the target solution.[520,538] Ligand−receptor interaction was also employed for portable visual quantitative detection of uranium (existing as the most stable form of uranyl ion (UO_2^{2+}) in water). The DNAzyme complex was formed via the interacting substrate strand with the enzyme strand, which could cross-link DNA-grafted polyacrylamide into the DNA hydrogel and specifically recognize UO_2^{2+}. UO_2^{2+} dissociated the DNA hydrogel by cleaving the substrate strands and separating them from the enzyme strands, leading to the release of the AuNPs (Figure 34b). Dispersed AuNPs displayed a red color, which could be quantitatively measured by a developed volumetric bar-chart chip. The detection of UO_2^{2+} with different concentrations in water, therefore, could be correlated with the color of the dispersed AuNPs.[537] Metal coordination was utilized to induce deformation of hydrogel (in situ polymerization of acrylamide in the presence of chitosan and oxidized dextran) through adjusting the chelation interactions between the amino groups, the hydroxyl groups and the secondary amine groups of chitosan and various metal ions. The hydrogel could quickly recover to its original shape if being immersed in solutions of EDTA, oxalate, halide ions or H_2SO_4, which have a stronger affinity with these metal ions to replace their coordination with chitosan (Figure 34c).[556] Crown ether 15-crown-5 and K^+ could form host−guest complexes at a ratio of 2:1, which lowers the LCST of the poly(*N*-isopropylacrylamide-*co*-benzo-15crown-5-acrylamide) (P(NIPAM-*co*-B15C5Am)) from $LCST_b$ to $LCST_a$ (Figure 34d). Within the range of temperatures, the hydrogel could undergo isothermally volume shrinkage upon the recognition of K^+, which served as a trigger to release preloaded drugs.[528] In summary, noncovalent interactions have been a powerful tool for designing stimuli-responsive hydrogels, because of extensive choices of building blocks, facile tunability, easy controllability, benign biocompatibility, and so on.

3.4.4. Hydrogel Adsorbents. Hydrogel adsorbents are generally applied for the treatment of industrial/agricultural wastewater and domestic sewage discharged with diverse organic dyes, heavy metal ions, pesticides, and/or antibiotics/drugs, etc. Organic dyes are predominant components of tannery wastewater, which usually include both cationic dyes (Figure 35a) such as methylene blue (MB), crystal violet (CV), methyl violet (MV), malachite green (MG), rhodamine B (RhB), and brilliant green (BG) as well as anionic dyes (Figure 35b) such as methyl orange (MO), fluorescein sodium (FS), congo red (CR), methyl red (MR), acid black 1 (AB-1), and Eosin Y. In wastewater, heavy metals usually exist in the form of cationic ions including Pb^{2+}, Hg^{2+}, Cu^{2+}, Cd^{2+}, Ni^{2+}, La^{3+}, Ce^{3+}, Mn^{2+}, Zn^{2+}, Fe^{3+}, Cr^{3+}, Ag^+, U(VI), etc. In addition, antibiotic ciprofloxacin (CIP), the anti-inflammatory drug diclofenac sodium (DFS) as well as other drugs are present in domestic sewage through intake and excretion by human beings (Figure 35c). Inorganic nonmetallic ions ammonium-nitrogen (NH_4−N), NH_4^+, and $H_2PO_4^-$ tend to induce eutrophication of the water system. Besides, neutral molecules (Figure 35d) pesticide

https://doi.org/10.1021/acs.chemrev.2c00215
Chem. Rev. XXXX, XXX, XXX−XXX

Table 4. Adsorption Mechanisms and Maximum Adsorption Capacities of Various Hydrogel Adsorbents for Removal of Diverse Pollutants

Hydrogel components	Pollutants	Noncovalent interactions for adsorption	Maximum adsorption capacities	Ref
Calcium hydroxide nanospherulites, PAA, poly([2-(methacryloxy) ethyl]trimethyl ammonium chloride)	MB (+)	Electrostatic interaction	2249 mg g^{-1} in a 400 mg L^{-1} MB solution	576, 578
Tragacanth gum (TG), carboxyl-functionalized carbon nanotube (CFCNT)	MB (+)	Electrostatic interaction Hydrogen bonding $\pi-\pi$ interaction	1092 mg g^{-1} in a 50 mg L^{-1} MB solution	580
CS, BmImBr	MB (+)	Electrostatic interaction Hydrogen bonding Anion$-\pi$ and CH$-\pi$ interactions	4300 mg g^{-1} in a 20 mg L^{-1} MB solution	573
Wheat straw xylan, Fe_3O_4 NPs, in situ polymerized AA	MB (+)	Electrostatic interaction	120 mg g^{-1} in a 400 mg L^{-1} MB solution	588
Polydopamine (PDA), pullulan, epichlorohydrin (ECH), MMT	CV (+)	Electrostatic interaction $\pi-\pi$ interaction	112 mg g^{-1} in a 200 mg L^{-1} CV solution	590
Locust bean gum (LBG), in situ polymerized *N*,*N*-dimethyl acrylamide (DMAAm)	BG (+)	Electrostatic interaction	143 mg g^{-1} in a 50 mg L^{-1} BG solution	583
TiO_2 loaded 2-hydroxyethyl methacrylate cross-linked gum tragacanth	MG (+)	Electrostatic interaction $\pi-\pi$ interaction	28 mg g^{-1} in a 50 mg L^{-1} MG solution	581
Gellan gum-grafted-poly((2-dimethylamino) ethyl methacrylate)	MO (−)	Electrostatic interaction	25.8 mg g^{-1} in a 100 mg L^{-1} MO solution	592
Polycondensation using triethylenetetramine, acetone, and formaldehyde	AB-1 (−)	Electrostatic interaction	1756 mg g^{-1} in a 200 mg L^{-1} AB-1 solution	613
Covalent functionalization of cellulose nanowhiskers with GO	MB (+) RhB (+)	Electrostatic interaction $\pi-\pi$ interaction	123 mg g^{-1} (MB), 62 mg g^{-1} (RhB) in a 50 mg L^{-1} solution	587
GO nanosheets, CS, CMC, DADMAC, AMPSA	MB (+) MO (−)	Electrostatic interaction Hydrogen bonding $\pi-\pi$ interaction	124 mg g^{-1} (MB), 68 mg g^{-1} (MO) in a 50 mg L^{-1} solution	579
Triethylamine (TEA)- and ECH-modified starch, in situ polymerized AA	MB (+) CR (−)	Electrostatic interaction Hydrogen bonding van der Waals force	134 mg g^{-1} (MB), 65 mg g^{-1} (CR) in a 50 mg L^{-1} solution	582
Magnetic attapulgite, fly ash, in situ polymerized AA	Pb^{2+}	Metal coordination	38 mg g^{-1} in a 100 mg L^{-1} Pb^{2+} solution	599
Chitosan and PVA cross-linked by glutaraldehyde	Hg^{2+}	Metal coordination	585 mg g^{-1} in a 0.01 mol L^{-1} Hg^{2+} solution	605
Carboxyl groups-modified cellulose hydrogel	Cu^{2+}	Metal coordination Electrostatic interaction	268 mg g^{-1} in a 0.08 mol L^{-1} Cu^{2+} solution	614
Amino-functionalized starch/PAA hydrogel	Cd^{2+}	Metal coordination	256 mg g^{-1} in a 180 mg L^{-1} Cd^{2+} solution	604
PVA, polyethylene glycol dimaleate (PEGDMA), in situ polymerized AA	Pb^{2+} Ni^{2+}	Metal coordination	233 mg g^{-1} (Pb^{2+}), 165 mg g^{-1} (Ni^{2+}) in a 200 mg L^{-1} solution	593
SA-grafted PAM, GO	Pb^{2+}	Metal coordination	241 mg g^{-1} (Pb^{2+}), 69 mg g^{-1} (Cu^{2+}) in a 200 mg L^{-1} solution	594

https://doi.org/10.1021/acs.chemrev.2c00215
Chem. Rev. XXXX, XXX, XXX−XXX

Table 4. continued

Hydrogel components	Pollutants	Noncovalent interactions for adsorption	Maximum adsorption capacities	Ref
	Cu^{2+}			
Alginate and PEI cross-linked by ethylene glycol diglycidylether (EGDE)	Pb^{2+}	Metal coordination	345 mg g^{-1} (Pb^{2+}), 323 mg g^{-1} (Cu^{2+}) in a 100 mg L^{-1} solution	603
	Cu^{2+}			
In situ polymerization of AA in Jute aqueous solution	Pb^{2+}	Metal coordination	543 mg g^{-1} (Pb^{2+}), 402 mg g^{-1} (Cd^{2+}) in a ∼ 40 mg L^{-1} solution	597
	Cd^{2+}			
CMC with in situ polymerization of AA through high internal phase emulsions	La^{3+}	Metal coordination	382 mg g^{-1} (La^{3+}), 320 mg g^{-1} (Ce^{3+}) in a 400 mg L^{-1} solution	598
	Ce^{3+}	Electrostatic interaction		
Poly(sodium acrylate)-GO (PSA-GO) double network hydrogel	Cd^{2+}	Metal coordination	238 mg g^{-1} (Cd^{2+}), 166 mg g^{-1} (Mn^{2+}) in a 200 mg L^{-1} solution	602
	Mn^{2+}	Electrostatic interaction		
GO-embedded calcium alginate with further functionalization of PEI, hydrogel beads	Pb^{2+}	Metal coordination	602 mg g^{-1} (Pb^{2+}), 374 mg g^{-1} (Hg^{2+}), 181 mg g^{-1} (Cd^{2+}) in a 50 mg L^{-1} solution	575
	Hg^{2+}			
	Cd^{2+}			
Lignin extracted from rice husk, chitosan, and in situ polymerized AM	Pb^{2+}	Metal coordination	374 mg g^{-1} (Pb^{2+}), 197 mg g^{-1} (Cu^{2+}), 269 mg g^{-1} (Cd^{2+}) in a 200 mg L^{-1} solution	600
	Cu^{2+}			
	Cd^{2+}			
AA-modified soybean dregs with subsequent polymerization	Zn^{2+}, Fe^{3+}, Cu^{2+}, Cr^{3+}	Metal coordination	121 mg g^{-1} (Zn^{2+}), 79 mg g^{-1} (Fe^{3+}), 75 mg g^{-1} (Cu^{2+}), 42 mg g^{-1} (Cr^{3+}) in a 150 mg L^{-1} solution	601
		Electrostatic interaction		
L-Arginine, Ag NPs, rGO	U(VI)	Metal coordination	435 mg g^{-1} in a 200 mg L^{-1} U(VI) solution	596
AM-grafted CMC, porous carbon, citric acid-modified magnetite	MB (+)	Electrostatic interaction	222 mg g^{-1} for MB and 294 mg g^{-1} for Pb^{2+} in a 50 mg L^{-1} MB and Pb^{2+} solution	584
	Pb^{2+}	Metal coordination		
Selenocarrageenan and GO	MB (+)	Electrostatic interaction	168 mg g^{-1} in a 900 mg L^{-1} MB solution	595
	Hg^{2+}	Metal coordination	331 mg g^{-1} in a 100 mg L^{-1} Hg^{2+} solution	
PDA-functionalized graphene hydrogel	RhB (+)	Electrostatic interaction	207 mg g^{-1} in a 600 mg L^{-1} RhB solution, 260 mg g^{-1} in a 400 mg L^{-1} *p*-nitrophenol solution, 336 mg g^{-1} in an 800 mg L^{-1} Pb^{2+} solution, 145 mg g^{-1} in a 500 mg L^{-1} Cd^{2+} solution	591
	p-nitrophenol (+)	Metal coordination		
	Pb^{2+}, Cd^{2+}	Hydrogen bonding		
		$\pi-\pi$ interaction		
In situ polymerized AMPS and AA with the presence of GO nanosheets	MB (+)	Electrostatic interaction	4625 mg g^{-1} (MB), 3194 mg g^{-1} (MV) in a 2000 μmol L^{-1} solution, 643 mg g^{-1} (Ni^{2+}), 1374 mg g^{-1} (Ag^{+}), 1323 mg g^{-1} (Cu^{2+}), 4312 mg g^{-1} (Pb^{2+}) in a 20 mmol L^{-1} solution	585
	MV (+)	Metal coordination		
	Ni^{2+}, Ag^{+}, Cu^{2+}, Pb^{2+}			
GO sheets cross-linked by chitosan chains	MB (+)	Electrostatic interaction	395 mg g^{-1} in a 70 mg L^{-1} MB solution, 326 mg g^{-1} in an 80 mg L^{-1} Eosin Y solution, 70 mg g^{-1} in a 120 mg L^{-1} Cu^{2+} solution, 90 mg g^{-1} in a 110 mg L^{-1} Pb^{2+} solution	589
	Eosin Y (−) Cu^{2+}, Pb^{2+}	Metal coordination		
Gallic acid-functionalized graphene hydrogel	MB (+)	Metal coordination	395 mg g^{-1} in a 10 mg L^{-1} MB solution, 376 mg g^{-1} in a 20 mg L^{-1} MR solution, 305 mg g^{-1} in a 600 mg L^{-1} Cr^{3+} solution	586
	MR (−) Cr^{3+}	$\pi-\pi$ interaction		

https://doi.org/10.1021/acs.chemrev.2c00215
Chem. Rev. XXXX, XXX, XXX−XXX

Table 4. continued

Hydrogel components	Pollutants	Noncovalent interactions for adsorption	Maximum adsorption capacities	Ref
Graphene hydrogel	CIP	Hydrogen bonding $\pi-\pi$ interaction Hydrophobic interaction	~330 mg g^{-1} in a 150 mg L^{-1} CIP solution	609
Egg albumin (ALB) and PEI cross-linked by ECH	DFS	Electrostatic interaction Hydrogen bonding $\pi-\pi$ interaction	233 mg g^{-1} in a 100 mg L^{-1} DFS solution	610
Chitosan grafted PAA, vermiculite	NH_4-N	Electrostatic interaction	78 mg g^{-1} in a ~700 mg L^{-1} NH_4−N solution	606
PVA, tourmaline (Tm) and in situ polymerized AA	NH_4^+	Electrostatic interaction	43 mg g^{-1} in a ~130 mg L^{-1} NH_4^+ solution	607
Chitosan-grafted PAA and rectorite	NH_4^+	Electrostatic interaction	124 mg g^{-1} in a ~1000 mg L^{-1} NH_4^+ solution	608
Chitosan hydrogel beads	$H_2PO_4^-$	Metal coordination	29 mg g^{-1} in a ~100 mg L^{-1} $H_2PO_4^-$ solution	574
Graft copolymerization of AA onto CMC with subsequent being coated on magnetic GO	catechin	Hydrogen bonding Anion-π interaction	27 mg g^{-1} in a 300 mg L^{-1} catechin solution	611
Hydrazide-functionalized pillar[5]arene and 4-aldehydephenyl-functionalized pillar[5]arene	MB (+) MO (−) FS (−) 2,4-DCP BPA 1-NA, Tol	Host−guest interaction	91.5% (MB), 50.4% (MO), 30.1% (FS), 57.8% (2,4-DCP), 86.5% (BPA), 60.4% (1-NA), 63.8% (Tol) in 0.1 mmol L^{-1} pollutant solution with 1 g L^{-1} dry hydrogel	612

https://doi.org/10.1021/acs.chemrev.2c00215
Chem. Rev. XXXX, XXX, XXX−XXX

component 2,4-dichlorophenol (2,4-DCP), polymer products ingredient bisphenol A (BPA), 1-naphthyl amine (1-NA), and common petrochemical material toluene (Tol) are also considered as significant pollutants. Most of these pollutants are known to be harmful to the environment, human beings, and other living organisms because of their toxicity, carcinogenicity, radioactivity, nondegradability, and so on.[568,569] Various techniques have been employed to remove these pollutants from water systems, including chemical precipitation, ion exchange, membrane filtration, coagulation, flocculation, flotation, electrochemical treatment, and adsorption, among which adsorption by hydrogel adsorbents has attracted great attention because of their high efficiency of adsorption and desorption, reusability, free from second-time pollution as well as diverse fabrication methods.[569−571]

Hydrogel adsorbents usually adsorb pollutants via noncovalent interactions between active sites on the hydrogel adsorbents and pollutant molecules, including electrostatic interactions, metal−ligand coordination, hydrogen bonding, $\pi-\pi$ interactions, host−guest interactions, etc. Through modulating types and amounts of active adsorbing sites on the hydrogels, diverse pollutant molecules could be effectively separated and collected from contaminated water resources via single or combinational noncovalent interactions. As listed in Table 4, diversified methods (3D-printed porous structures,[572] hydrogel beads/granules,[570,573−575] incorporation of nanomaterials such as calcium hydroxide nanospherulites,[576−578] GO nanosheets,[575,579] CNTs,[580] etc.) have been adopted to improve the total number of the active adsorbing sites on hydrogel adsorbents. According to the types of pollutants, the main associated noncovalent interacions between the active adsorbing sites and the pollutants in the adsorption process have been summarized, and the corresponding maximum adsorption capacities are listed as a reference. Electrostatic interactions are the principle noncovalent interactions for the adsorption of charged organic dyes. Cationic organic dyes were generally adsorped via negatively charged functional groups in the hydrogel (Figure 36a), including the carboxyl group $-COO^-$,[572,576,578−589] electronegative phenolic group,[590,591] negatively charged montmorillonite (MMT),[590] sulfonic group $-SO_3^-$,[579,585] and negatively charged ionic liquids (1-butyl-3-methylimidazolium bromide (BmImBr)).[573] These negatively charged groups-containing materials such as PAA, 2-acrylamido-2-methyl-1-propanesulfonic acid (AMPSA), alginate, polydopamine, and tannins are easily accessible for the fabrication of hydrogel adsorbents to remove cationic organic dyes. As for the adsorption of anionic organic dyes, positively charged functional groups are frequently utilized (Figure 36b), including amine group $-NH_3^+$,[579] dimethylammonium groups $=N(CH_3)_2^+$ and $-NH(CH_3)_2^+$,[579,592] and triethylamine group $-N(CH_2CH_3)_3^+$.[582] Building materials such as chitosan,[579] quaternized starch,[582] cationic monomers diallyldimethylammonium chloride (DADMAC),[579] and 2-(dimethylamino)ethyl methacrylate (DMAEMA)[592] are usually employed as major components of the hydrogels with positively charged active sites for the adsorption of anionic organic dyes. When oppositely charged functional groups were simultaneously introduced into the hydrogel adsorbents, both cationic and anionic organic dyes could be scavenged via electrostatic interaction between charged functional groups and oppositely charged organic dyes at the same time.[579,582] As hydrogen bonds are ubiquitous in nature, hydrogen bonding can be utilized to enhance the adsorption of hydrogel adsorbents on organic dyes. For example, hydrogen

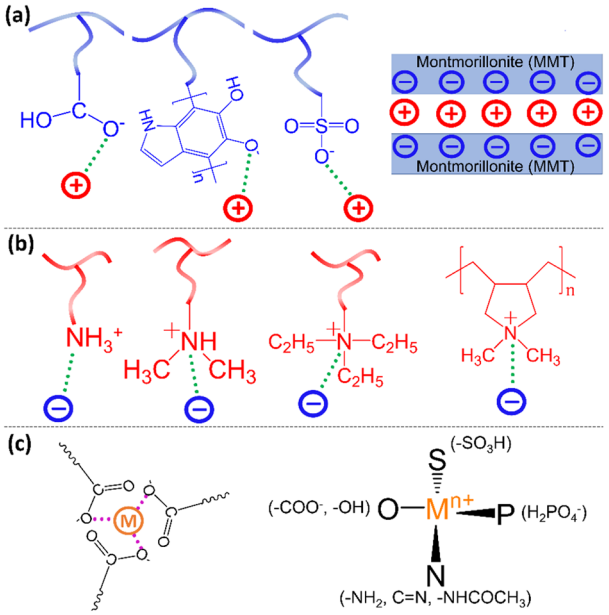

Figure 36. Typical functional groups and ligands in hydrogel absorbents. (a) Functional groups for the adsorption of cationic organic dyes. (b) Functional groups for the adsorption of anionic organic dyes. (c) Typical ligands for the adsorption of pollutant metallic ions.

bonding between the hydrogen atom of hydroxyl groups and the electronegative nitrogen atoms on organic dyes could serve as a minor intermolecular interaction to assist removal of organic dyes.[573,579,580,582,591] The incorporation of nanomaterials like GO nanosheets[579,587,589] and CNTs[580] could reinforce the adsorption capacities of hydrogel adsorbents because of the $\pi-\pi$ interactions between the aromatic ring-abundant nanomaterials and the aromatic ring-included organic dyes. Metal−ligand coordination has been demonstrated as the dominant noncovalent interaction for the adsorption of heavy metal cations. Common ligands generally involve carboxyl group $-COOH$,[575,577,584−586,593−599] hydroxyl group $-OH$,[575,593−596,600−602] amino group $-NH_2$,[575,594,596,600,602−604] and sulfonic group $-SO_3H$[585,595] as well as nitrogen-containing $-NHCOCH_3$ and C=N groups,[605] etc. (Figure 36c). It was demonstrated that metal ions could strongly bond to electron-rich groups via coordination bonds with oxygen or nitrogen atoms. Charged organic dyes and heavy metal cations could be eliminated together through synergy of specific functional groups considering the complexity of actual discharged wastewater.[584−586,589,591,595] Regarding the removal of positively charged inorganic nonmetallic ammonium ions, PAA with abundant negatively charged carboxyl groups $-COO^-$ preferred adsorbing the pollutant via electrostatic interactions.[606−608] For the separation of dihydrogen phosphate $H_2PO_4^-$, the Cu^{2+}-adsorbed chitosan hydrogel beads were secondarily utilized to eliminate dihydrogen phosphate $H_2PO_4^-$ through metal−ligand coordination between Cu^{2+} adsorbed on the hydrogel adsorbent and oxygen atoms of the dihydrogen phosphate.[574] The extraction of CIP was demonstrated to rely on hydrogen bonding, $\pi-\pi$ interactions, and hydrophobic interactions between CIP and the graphene hydrogel adsorbent.[609] The removal of DFS was found to be based on electrostatic interactions, hydrogen bonding, and $\pi-\pi$ interactions between

https://doi.org/10.1021/acs.chemrev.2c00215
Chem. Rev. XXXX, XXX, XXX−XXX

DFS and PEI-modified egg albumin hydrogel.[610] The preconcentration of catechin in water and tea samples was ascribed to the hydrogen-bonding interaction between the electronegative oxygen atoms of the chitosan hydrogel-coated magnetic GO and the hydroxyl groups of catechin as well as the anion−π interaction between the deprotonated carboxyl groups and the aromatic rings of catechin.[611] Huang and co-workers reported that electrically neutral pollutants such as 2,4-DCP, BPA, 1-NA, and Tol could be removed by a pillar[5]arene-based hydrogel adsorbent via host−guest interaction, which concurrently could adsorb both cationic and anionic organic dyes, providing a new approach for the adsorption of pollutants.[612]

4. CONCLUSIONS AND PERSPECTIVES

Noncovalent interactions have long been recognized as binding motifs for the construction of various functional polymers. With the development of state-of-art techniques, the last two decades have witnessed much progress in the fundamental understanding of noncovalent interactions, which promotes the design of advanced functional materials based on these tunable interactions. In this review, we systematically summarize the nanomechanical quantification of different types of noncovalent interactions in polymeric systems, whose binding mechanisms (e.g., ranges, strengths, and time scales of the interactions) are elucidated by direct force measurements conducted at the microscopic, nanoscopic, and molecular levels. The design principles and emerging applications of a series of noncovalently bonded polymeric materials are also discussed, where the mechanical, physicochemical, and biochemical properties of the materials can be modulated by tuning the noncovalent interactions in these systems. Despite considerable achievements in the characterization and manipulation of noncovalent interactions, some challenging issues and opportunities still remain in this field.

For force measurements conducted between two microscopic or nanoscopic surfaces, the detected forces and the interpreted nanomechanical properties of the polymers films are not only dependent on surface chemistry (i.e., the types and numbers of the binding moieties that allow noncovalent interactions) but also affected by surface structure (e.g., roughness, cluster formation, distribution of active sites, orientation of binding groups). For instance, in most molecular and surface force measurements, surfaces or coatings with subnanometer roughness are generally required to allow the accurate determination of the intrinsic interaction force−distance correlation and other information such as molecular or surface deformation and contact area, reducing or even eliminating the influence of surface roughness. Most SFA measurements also require the surfaces or coatings to be transparent or semitransparent. Although AFM allows the detection of rough surfaces, the intrinsic roughness may result in ill-defined contact as surface separation is inferred from the measured force curves. To obtain a complete understanding of the physicochemical principles of the interfacial noncovalent interactions, other surface or structure-sensitive analytical techniques, such as X-ray and neutron reflectometry, X-ray photoelectron spectroscopy, and surface plasmon resonance, should be employed, which can be coupled to force techniques or used separately, to provide a systematic characterization on the composition and topology of the surfaces, facilitating the accurate interpretation of the results from the direct force measurements. For example, an X-ray beam has been coupled with a conventional SFA to determine the structure and molecular orientation of the confined liquids during surface interaction,[615,616] and AFM can also be integrated with infrared or Raman spectroscopy to simultaneously provide topographical and chemical information on a surface.[617] As force-measuring techniques allow the in situ detection of interfacial evolution at the micro- and nanoscales, they have attracted special interest in the characterization of dynamic processes, such as adsorption/desorption of molecules, charge/discharge reactions in batteries, and immune responses of biological systems. These measurements require accurate control of the surrounding environment, where potentiostat/galvanostat can be coupled with the instrument to provide desired electrochemical gradients.[618] The damage of the detected surfaces, especially soft biological tissues, should be prevented by carefully modulating the applied forces.

SMFS is a powerful tool for exploring intramolecular and intermolecular noncovalent interactions between two specific groups, whose energy landscape is usually composed of asymmetric dissociative (from bounded state to transition state) and associative (from separated state to transition state) pathways. In most SMFS studies, only unbinding (i.e., dissociative) dynamics of the complexes are examined because of the explicit characteristics of the force-induced extension of polymers chains, and the binding (i.e., associative) processes are rarely investigated because it is difficult to control the relaxation of immobilized polymer chains, which is a prerequisite for the detection of the binding events. An effective approach is to add a flexible linker between the binding moieties to maintain their proximity and the integrity of the polymer chain, thus the relaxation of the polymers can be governed by the external force similar to the pulling process,[165] holding great promise to reveal the dissociation/association lifetimes and complete energy profiles (e.g., ranges and depths of the energy barriers) of diverse noncovalent interactions.

Although the origin and nature of some types of noncovalent interactions have been illustrated by the quantitative force measurements, the formation of many molecular complexes (e.g., DNA, protein−ligand, polymer−organics) exploits a number of "element interactions", whose contributions are not easy to be differentiated because of the net effect. From an experimental perspective, the distinction of different interaction mechanisms could be achieved by systematic chemical modification of the molecules and careful selection of solvents, which is not feasible in all circumstances. With the development of computational chemistry, many computational approaches, including density functional theory calculations and molecular dynamics simulation, have been successfully combined with the force-measuring techniques to reveal the binding mechanisms of some complex systems,[180,619] which is a promising direction for future study. Up to now, the quantitative measurements of molecular and surface interactions are usually achieved in relatively simple systems with a few model polymers and limited solution conditions. As most biological and engineering processes involve a variety of ions, macromolecules, polymers, particles, and colloidal assemblies, an intriguing research topic is extending the direct force measurements to more complex and realistic systems. Moreover, harsh conditions (e.g., high or low temperature, elevated pressure, high salinity, extremely acid or alkaline solutions) can be encountered in many practical applications, such as energy storage and conversion, sensing, and water treatment, which are expected to influence the physicochemical properties of the polymers and their interaction behaviors. The quantification of polymer−polymer and polymer-surface interaction forces under such conditions is

https://doi.org/10.1021/acs.chemrev.2c00215
Chem. Rev. XXXX, XXX, XXX−XXX

rarely reported because of the difficulties in experiment setup and data interpretation, which requires further investigation.

Although the elucidation, control, and manipulation of many noncovalent interactions have been extensively explored at the micro- and nanoscales, it remains a challenge to directly correlate the nanomechanical properties of the materials to their macroscopic performances. It has been reported that in some noncovalently bonded materials, the force spectroscopy measured between single functional groups agrees well with the mechanical properties of materials.[165,620] For the rational design of functional polymeric materials, more efforts should be devoted to establishing a clear relationship between molecular interactions and bulk properties, where the cooperation of covalent interactions, noncovalent interactions and microstructures should be considered. Another challenge toward the fabrication of materials with programmable structures and functions is to scale up controlled molecular recognition and self-assembly from microscopic to macroscopic world, which can be facilitated by the application of a magnetic/electric field.[621]

Because of the dynamic and reversible nature of noncovalent interactions, supramolecular polymers have been endowed with numerous advantages (e.g., self-healing and adaptive properties), but one major limitation of this type of materials is their mechanical instability, which means they can be damaged or disassembled under a high or continuous mechanical load. One effective strategy to overcome this issue is to combine multiple noncovalent interactions with a broad range of binding affinities in an orthogonal manner, where the strong interactions are used to retain the integrity and robustness of the material while the weak interactions allow the responses to external stimuli. Another approach is to tune the structures of the materials, such as modulating the topologies of polymers, introducing micro/nanofillers, and creating crystalline domains, which can induce synergetic effects of the molecular interactions for mechanical enhancement.

Compared to living organisms that exploit a large variety of noncovalent interactions in an orderly and programmable way, the manipulation of noncovalent interactions in synthetic polymeric materials requires tedious processes and very often lacks precise control. The applications of the relevant functional materials in many emerging fields (e.g., drug delivery, tissue regeneration, sensing) are still in the infant stage. More efforts are needed to truly mimic the compositions, structures, and functions of the biological systems, leading to the development of smarter materials with tunable molecular interactions than those available to date toward clinical practice and engineering applications. For example, although numerous underwater adhesives have been developed by mimicking the key components (e.g., catechol chemistry) of mussel adhesive proteins, their performances are still significantly limited compared to that of marine mussels, especially for load-bearing applications, because the compositional gradients and complex structural features of mussel plaque are generally ignored in the biomimetic translation. For future studies, the investigations of bioinspired adhesives can focus on both the modulation of chemical compositions and the control of the delivery process (e.g., coacervation and surface priming),[398,401] which is essential to achieving superior adhesion and cohesion in practical applications.

AUTHOR INFORMATION

Corresponding Author

Hongbo Zeng − *Department of Chemical and Materials Engineering, University of Alberta, Edmonton, Alberta T6G 1H9, Canada;* orcid.org/0000-0002-1432-5979; Phone: +1-780-492-1044; Email: hongbo.zeng@ualberta.ca; Fax: +1-780-492-2881

Authors

Jingsi Chen − *Department of Chemical and Materials Engineering, University of Alberta, Edmonton, Alberta T6G 1H9, Canada;* orcid.org/0000-0002-8438-6590

Qiongyao Peng − *Department of Chemical and Materials Engineering, University of Alberta, Edmonton, Alberta T6G 1H9, Canada*

Xuwen Peng − *Department of Chemical and Materials Engineering, University of Alberta, Edmonton, Alberta T6G 1H9, Canada*

Hao Zhang − *Department of Chemical and Materials Engineering, University of Alberta, Edmonton, Alberta T6G 1H9, Canada;* orcid.org/0000-0003-4080-3222

Complete contact information is available at: https://pubs.acs.org/10.1021/acs.chemrev.2c00215

Author Contributions

†Jingsi Chen and Qiongyao Peng contributed equally to this work. CRediT: **Jingsi Chen** and **Qiongyao Peng** conceptualization, writing-original draft, writing-review & editing; **Xuwen Peng** writing-review & editing; **Hao Zhang** writing-review & editing; **Hongbo Zeng** conceptualization, funding acquisition, methodology, project administration, supervision, writing-original draft, writing-review & editing.

Notes

The authors declare no competing financial interest.

Biographies

Jingsi Chen obtained her B.Sc. in Materials Science and Engineering from Southeast University in 2012 and received a Ph.D. in Material Engineering from the University of Alberta in 2019. She is currently a postdoctoral researcher at the University of Alberta. Her research interests are mainly focused on the development of supramolecular polymers and functional soft materials toward bioengineering and biomedical applications.

Qiongyao Peng received her B.Sc. in Materials Science and Engineering from Central South University in 2010 and obtained her M.Sc. in Materials Science and Engineering from Shanghai Jiao Tong University in 2014. She received her Ph.D. in Chemical Engineering at the University of Alberta in 2021. She is currently a postdoctoral fellow at the University of Alberta. Her research interests are mainly focused on the development of functional hydrogels and coacervation-inspired wet adhesives for bioengineering and biomedical applications.

Xuwen Peng received a B.Sc. from the University of Shanghai for Science and Technology in 2016. She is currently a Ph.D. candidate in the Department of Chemical and Materials Engineering at the University of Alberta. She is working on coacervation gels and hydrogels with applications in drug delivery, flexible electronics, and human-machine interface.

Hao Zhang is currently a professor in the Department of Chemical and Materials Engineering at the University of Alberta. Before joining the University of Alberta, he was a postdoctoral research associate at

https://doi.org/10.1021/acs.chemrev.2c00215
Chem. Rev. XXXX, XXX, XXX−XXX

Princeton University. He received B.E. and M.S. degrees in Materials Science and Engineering from Tsinghua University and a Ph.D. in Mechanical and Aerospace Engineering from Princeton University. His research focuses on computational and theoretical materials science, with special interest in the static and dynamic properties of defects, and the effects of defects on the physical properties of materials.

Hongbo Zeng obtained his B.Sc. and M.Sc. at Tsinghua University and Ph.D. at the University of California, Santa Barbara. He is a professor in the Department of Chemical and Materials Engineering at the University of Alberta, a Tier 1 Canada Research Chair and a Fellow of the Canadian Academy of Engineering. His research focuses on the intermolecular and surface interactions in polymers, complex fluids, biological systems and engineering processes, and development of advanced functional materials. He has published over 400 peer-reviewed journal papers on related research topics.

ACKNOWLEDGMENTS

This work is supported by the Natural Sciences and Engineering Research Council of Canada (NSERC), the Canada Foundation for Innovation (CFI), and the Canada Research Chairs Program (H. Zeng).

REFERENCES

(1) Lehn, J.-M. Supramolecular Chemistry. *Science* **1993**, *260*, 1762−1764.
(2) Riley, K. E.; Hobza, P. Noncovalent Interactions in Biochemistry. *Wiley Interdiscip. Rev. Comput. Mol. Sci.* **2011**, *1*, 3−17.
(3) Israelachvili, J. N. *Intermolecular and Surface Forces*; Academic press, 2011, 223−250.
(4) Persch, E.; Dumele, O.; Diederich, F. Molecular Recognition in Chemical and Biological Systems. *Angew. Chem., Int. Ed.* **2015**, *54*, 3290−3327.
(5) Fenniri, H.; Mathivanan, P.; Vidale, K. L.; Sherman, D. M.; Hallenga, K.; Wood, K. V.; Stowell, J. G. Helical Rosette Nanotubes: Design, Self-Assembly, and Characterization. *J. Am. Chem. Soc.* **2001**, *123*, 3854−3855.
(6) Spolar, R. S.; Ha, J.-H.; Record, M. T. Hydrophobic Effect in Protein Folding and Other Noncovalent Processes Involving Proteins. *Proc. Natl. Acad. Sci. U.S.A.* **1989**, *86*, 8382−8385.
(7) Williams, D. H.; Stephens, E.; O'Brien, D. P.; Zhou, M. Understanding Noncovalent Interactions: Ligand Binding Energy and Catalytic Efficiency from Ligand-Induced Reductions in Motion within Receptors and Enzymes. *Angew. Chem., Int. Ed.* **2004**, *43*, 6596−6616.
(8) Crespo-Hernández, C. E.; Cohen, B.; Kohler, B. Base Stacking Controls Excited-State Dynamics in A·T DNA. *Nature* **2005**, *436*, 1141−1144.
(9) Young, T.; Abel, R.; Kim, B.; Berne, B. J.; Friesner, R. A. Motifs for Molecular Recognition Exploiting Hydrophobic Enclosure in Protein-Ligand Binding. *Proc. Natl. Acad. Sci. U.S.A.* **2007**, *104*, 808−813.
(10) Lehn, J. M. Supramolecular Polymer Chemistry-Scope and Perspectives. *Polym. Int.* **2002**, *51*, 825−839.
(11) Brunsveld, L.; Folmer, B.; Meijer, E.; Sijbesma, R. Supramolecular Polymers. *Chem. Rev.* **2001**, *101*, 4071−4098.
(12) Bao, C.; Jiang, Y.; Zhang, H.; Lu, X.; Sun, J. Room-Temperature Self-Healing and Recyclable Tough Polymer Composites Using Nitrogen-Coordinated Boroxines. *Adv. Funct. Mater.* **2018**, *28*, 1800560.
(13) Wu, D. Y.; Meure, S.; Solomon, D. Self-Healing Polymeric Materials: A Review of Recent Developments. *Prog. Polym. Sci.* **2008**, *33*, 479−522.
(14) Gong, L.; Xiang, L.; Zhang, J.; Chen, J.; Zeng, H. Fundamentals and Advances on Adhesion of Polymer Surfaces and Thin Films. *Langmuir* **2019**, *35*, 15914−15936.
(15) Waite, J. H.; Andersen, N. H.; Jewhurst, S.; Sun, C. Mussel Adhesion: Finding the Tricks Worth Mimicking. *J. Adhes.* **2005**, *81*, 297−317.
(16) Khan, S.; Lorenzelli, L.; Dahiya, R. S. Technologies for Printing Sensors and Electronics over Large Flexible Substrates: A Review. *IEEE Sens. J.* **2015**, *15*, 3164−3185.
(17) Guo, Q.; Chen, J.; Wang, J.; Zeng, H.; Yu, J. Recent Progress in Synthesis and Application of Mussel-Inspired Adhesives. *Nanoscale* **2020**, *12*, 1307−1324.
(18) Mahadevi, A. S.; Sastry, G. N. Cooperativity in Noncovalent Interactions. *Chem. Rev.* **2016**, *116*, 2775−2825.
(19) Sherrington, D. C.; Taskinen, K. A. Self-Assembly in Synthetic Macromolecular Systems Via Multiple Hydrogen Bonding Interactions. *Chem. Soc. Rev.* **2001**, *30*, 83−93.
(20) Jorgensen, W. L.; Pranata, J. Importance of Secondary Interactions in Triply Hydrogen Bonded Complexes: Guanine-Cytosine vs Uracil-2, 6-Diaminopyridine. *J. Am. Chem. Soc.* **1990**, *112*, 2008−2010.
(21) Murray, T. J.; Zimmerman, S. C. New Triply Hydrogen Bonded Complexes with Highly Variable Stabilities. *J. Am. Chem. Soc.* **1992**, *114*, 4010−4011.
(22) Xia, D.; Wang, P.; Ji, X.; Khashab, N. M.; Sessler, J. L.; Huang, F. Functional Supramolecular Polymeric Networks: The Marriage of Covalent Polymers and Macrocycle-Based Host-Guest Interactions. *Chem. Rev.* **2020**, *120*, 6070−6123.
(23) Del Valle, E. M. Cyclodextrins and Their Uses: A Review. *Process Biochem.* **2004**, *39*, 1033−1046.
(24) Yang, L.; Tan, X.; Wang, Z.; Zhang, X. Supramolecular Polymers: Historical Development, Preparation, Characterization, and Functions. *Chem. Rev.* **2015**, *115*, 7196−7239.
(25) Degen, G. D.; Stow, P. R.; Lewis, R. B.; Andresen Eguiluz, R. C.; Valois, E.; Kristiansen, K.; Butler, A.; Israelachvili, J. N. Impact of Molecular Architecture and Adsorption Density on Adhesion of Mussel-Inspired Surface Primers with Catechol-Cation Synergy. *J. Am. Chem. Soc.* **2019**, *141*, 18673−18681.
(26) Zaccheddu, M.; Filippi, C.; Buda, F. Anion-Π and Π-Π Cooperative Interactions Regulating the Self-Assembly of Nitrate-Triazine-Triazine Complexes. *J. Phys. Chem. A* **2008**, *112*, 1627−1632.
(27) Venkataramana, G.; Sankararaman, S. Synthesis and Spectroscopic Investigation of Aggregation through Cooperative π-π and C-H●●●O Interactions in a Novel Pyrene Octaaldehyde Derivative. *Org. Lett.* **2006**, *8*, 2739−2742.
(28) Yan, X.; Wang, F.; Zheng, B.; Huang, F. Stimuli-Responsive Supramolecular Polymeric Materials. *Chem. Soc. Rev.* **2012**, *41*, 6042−6065.
(29) Willner, I. Stimuli-Controlled Hydrogels and Their Applications. *Acc. Chem. Res.* **2017**, *50*, 657−658.
(30) Webber, M. J.; Appel, E. A.; Meijer, E.; Langer, R. Supramolecular Biomaterials. *Nat. Mater.* **2016**, *15*, 13−26.
(31) Biedermann, F.; Schneider, H.-J. r. Experimental Binding Energies in Supramolecular Complexes. *Chem. Rev.* **2016**, *116*, 5216−5300.
(32) Lu, C.; Liu, Y.; Liu, X.; Wang, C.; Wang, J.; Chu, F. Sustainable Multiple and Multi-Stimuli Shape Memory and Self-Healing Elastomers with Semi-Interpenetrating Network Derived from Biomass Via Bulk Radical Polymerization. *ACS Sustain. Chem. Eng.* **2018**, *6*, 6527−6535.
(33) Dong, L.; Agarwal, A. K.; Beebe, D. J.; Jiang, H. Adaptive Liquid Microlenses Activated by Stimuli-Responsive Hydrogels. *Nature* **2006**, *442*, 551−554.
(34) White, E. M.; Yatvin, J.; Grubbs, J. B., III; Bilbrey, J. A.; Locklin, J. Advances in Smart Materials: Stimuli-Responsive Hydrogel Thin Films. *J. Polym. Sci., Part B: Polym. Phys.* **2013**, *51*, 1084−1099.
(35) Kavanagh, A.; Byrne, R.; Diamond, D.; Fraser, K. J. Stimuli Responsive Ionogels for Sensing Applications - an Overview. *Membranes* **2012**, *2*, 16−39.
(36) Hackelbusch, S.; Rossow, T.; Becker, H.; Seiffert, S. Multi-responsive Polymer Hydrogels by Orthogonal Supramolecular Chain-Cross-Linking. *Macromolecules* **2014**, *47*, 4028−4036.
(37) Yang, J.; Li, Y.; Zhu, L.; Qin, G.; Chen, Q. Double Network Hydrogels with Controlled Shape Deformation: A Mini Review. *J. Polym. Sci., Part B: Polym. Phys.* **2018**, *56*, 1351−1362.

https://doi.org/10.1021/acs.chemrev.2c00215
Chem. Rev. XXXX, XXX, XXX−XXX

(38) Ji, X.; Jie, K.; Zimmerman, S. C.; Huang, F. A Double Supramolecular Crosslinked Polymer Gel Exhibiting Macroscale Expansion and Contraction Behavior and Multistimuli Responsiveness. *Polym. Chem.* **2015**, *6*, 1912−1917.
(39) Hunter, C. A. Quantifying Intermolecular Interactions: Guidelines for the Molecular Recognition Toolbox. *Angew. Chem., Int. Ed.* **2004**, *43*, 5310−5324.
(40) Clark, T.; Murray, J. S.; Politzer, P. A Perspective on Quantum Mechanics and Chemical Concepts in Describing Noncovalent Interactions. *Phys. Chem. Chem. Phys.* **2018**, *20*, 30076−30082.
(41) Müller-Dethlefs, K.; Hobza, P. Noncovalent Interactions: A Challenge for Experiment and Theory. *Chem. Rev.* **2000**, *100*, 143−168.
(42) Dubecky, M.; Mitas, L.; Jurecka, P. Noncovalent Interactions by Quantum Monte Carlo. *Chem. Rev.* **2016**, *116*, 5188−5215.
(43) Christensen, A. S.; Kubar, T.; Cui, Q.; Elstner, M. Semiempirical Quantum Mechanical Methods for Noncovalent Interactions for Chemical and Biochemical Applications. *Chem. Rev.* **2016**, *116*, 5301−5337.
(44) Rezac, J.; Hobza, P. Benchmark Calculations of Interaction Energies in Noncovalent Complexes and Their Applications. *Chem. Rev.* **2016**, *116*, 5038−5071.
(45) Hohenstein, E. G.; Sherrill, C. D. Wavefunction Methods for Noncovalent Interactions. *Wiley Interdiscip. Rev. Comput. Mol. Sci.* **2012**, *2*, 304−326.
(46) Grimme, S. Density Functional Theory with London Dispersion Corrections. *Wiley Interdiscip. Rev. Comput. Mol. Sci.* **2011**, *1*, 211−228.
(47) Riley, K. E.; Pitonák, M.; Jurecka, P.; Hobza, P. Stabilization and Structure Calculations for Noncovalent Interactions in Extended Molecular Systems Based on Wave Function and Density Functional Theories. *Chem. Rev.* **2010**, *110*, 5023−5063.
(48) Handing, K. B.; Niedzialkowska, E.; Shabalin, I. G.; Kuhn, M. L.; Zheng, H.; Minor, W. Characterizing Metal-Binding Sites in Proteins with X-Ray Crystallography. *Nat. Protoc.* **2018**, *13*, 1062−1090.
(49) Palmer, R. A.; Niwa, H. X-Ray Crystallographic Studies of Protein-Ligand Interactions. *Biochem. Soc. Trans.* **2003**, *31*, 973−979.
(50) Gao, Q.; Williams, L. D.; Egli, M.; Rabinovich, D.; Chen, S.-L.; Quigley, G. J.; Rich, A. Drug-Induced DNA Repair: X-Ray Structure of a DNA-Ditercalinium Complex. *Proc. Natl. Acad. Sci. U.S.A.* **1991**, *88*, 2422−2426.
(51) Fraser, J. S.; van den Bedem, H.; Samelson, A. J.; Lang, P. T.; Holton, J. M.; Echols, N.; Alber, T. Accessing Protein Conformational Ensembles Using Room-Temperature X-Ray Crystallography. *Proc. Natl. Acad. Sci. U.S.A.* **2011**, *108*, 16247−16252.
(52) Meyer, B.; Peters, T. Nmr Spectroscopy Techniques for Screening and Identifying Ligand Binding to Protein Receptors. *Angew. Chem., Int. Ed.* **2003**, *42*, 864−890.
(53) Chen, L. X.; Zhang, X.; Shelby, M. Recent Advances on Ultrafast X-Ray Spectroscopy in the Chemical Sciences. *Chem. Sci.* **2014**, *5*, 4136−4152.
(54) Hunt, N. T. 2d-Ir Spectroscopy: Ultrafast Insights into Biomolecule Structure and Function. *Chem. Soc. Rev.* **2009**, *38*, 1837−1848.
(55) Manouchehri, F.; Izadmanesh, Y.; Aghaee, E.; Ghasemi, J. B. Experimental, Computational and Chemometrics Studies of BSA-Vitamin B6 Interaction by UV-Vis, FT-IR, Fluorescence Spectroscopy, Molecular Dynamics Simulation and Hard-Soft Modeling Methods. *Bioorg. Chem.* **2016**, *68*, 124−136.
(56) Macomber, R. S. An Introduction to NMR Titration for Studying Rapid Reversible Complexation. *J. Chem. Educ.* **1992**, *69*, 375−378.
(57) Wang, D.-X.; Wang, M.-X. Anion-π Interactions: Generality, Binding Strength, and Structure. *J. Am. Chem. Soc.* **2013**, *135*, 892−897.
(58) Bujalowski, W.; Jezewska, M. J. Quantitative Thermodynamic Analyses of Spectroscopic Titration Curves. *J. Mol. Struct.* **2014**, *1077*, 40−50.
(59) Chiad, K.; Stelzig, S. H.; Gropeanu, R.; Weil, T.; Klapper, M.; Müllen, K. Isothermal Titration Calorimetry: A Powerful Technique to Quantify Interactions in Polymer Hybrid Systems. *Macromolecules* **2009**, *42*, 7545−7552.
(60) Weidner, T.; Castner, D. G. Sfg Analysis of Surface Bound Proteins: A Route Towards Structure Determination. *Phys. Chem. Chem. Phys.* **2013**, *15*, 12516−12524.
(61) Wang, H.-F. Sum Frequency Generation Vibrational Spectroscopy (SFG-VS) for Complex Molecular Surfaces and Interfaces: Spectral Lineshape Measurement and Analysis Plus Some Controversial Issues. *Prog. Surf. Sci.* **2016**, *91*, 155−182.
(62) Jecklin, M. C.; Schauer, S.; Dumelin, C. E.; Zenobi, R. Label-Free Determination of Protein-Ligand Binding Constants Using Mass Spectrometry and Validation Using Surface Plasmon Resonance and Isothermal Titration Calorimetry. *J. Mol. Recognit.* **2009**, *22*, 319−329.
(63) Derjaguin, B.; Titijevskaia, A.; Abricossova, I.; Malkina, A. Investigations of the Forces of Interaction of Surfaces in Different Media and Their Application to the Problem of Colloid Stability. *Discuss. Faraday Soc.* **1954**, *18*, 24−41.
(64) Ashkin, A.; Dziedzic, J. M.; Bjorkholm, J. E.; Chu, S. Observation of a Single-Beam Gradient Force Optical Trap for Dielectric Particles. *Opt. Lett.* **1986**, *11*, 288−290.
(65) Zeng, H. *Polymer Adhesion, Friction, and Lubrication*; John Wiley & Sons, 2013; pp 45−47.
(66) Israelachvili, J; Min, Y; Akbulut, M; Alig, A; Carver, G; Greene, W; Kristiansen, K; Meyer, E; Pesika, N; Rosenberg, K; Zeng, H Recent Advances in the Surface Forces Apparatus (SFA) Technique. *Rep. Prog. Phys.* **2010**, *73*, 036601.
(67) Israelachvili, J. Direct Measurements of Forces between Surfaces in Liquids at the Molecular Level. *Proc. Natl. Acad. Sci. U. S. A.* **1987**, *84*, 4722−4724.
(68) Vigil, G.; Xu, Z.; Steinberg, S.; Israelachvili, J. Interactions of Silica Surfaces. *J. Colloid Interface Sci.* **1994**, *165*, 367−385.
(69) Merrill, W. W.; Pocius, A. V.; Thakker, B. V.; Tirrell, M. Direct Measurement of Molecular Level Adhesion Forces between Biaxially Oriented Solid Polymer Films. *Langmuir* **1991**, *7*, 1975−1980.
(70) Tabor, D.; Winterton, R. H. S. The Direct Measurement of Normal and Retarded Van Der Waals Forces. *Proc. Math. Phys. Eng.* **1969**, *312*, 435−450.
(71) Xie, L.; Cui, X.; Gong, L.; Chen, J.; Zeng, H. Recent Advances in the Quantification and Modulation of Hydrophobic Interactions for Interfacial Applications. *Langmuir* **2020**, *36*, 2985−3003.
(72) Zeng, H.; Hwang, D. S.; Israelachvili, J. N.; Waite, J. H. Strong Reversible Fe^{3+}-Mediated Bridging between Dopa-Containing Protein Films in Water. *Proc. Natl. Acad. Sci. U.S.A.* **2010**, *107*, 12850−12853.
(73) Tian, Y.; Pesika, N.; Zeng, H.; Rosenberg, K.; Zhao, B.; McGuiggan, P.; Autumn, K.; Israelachvili, J. Adhesion and Friction in Gecko Toe Attachment and Detachment. *Proc. Natl. Acad. Sci. U.S.A.* **2006**, *103*, 19320−19325.
(74) Zeng, H.; Tirrell, M.; Israelachvili, J. Limit Cycles in Dynamic Adhesion and Friction Processes: A Discussion. *J. Adhes.* **2006**, *82*, 933−943.
(75) Giessibl, F. J. Advances in Atomic Force Microscopy. *Rev. Mod. Phys.* **2003**, *75*, 949−978.
(76) Gavara, N. A Beginner's Guide to Atomic Force Microscopy Probing for Cell Mechanics. *Microsc. Res. Technol.* **2017**, *80*, 75−84.
(77) Kappl, M.; Butt, H. J. The Colloidal Probe Technique and Its Application to Adhesion Force Measurements. *Part. Part. Syst. Charact.* **2002**, *19*, 129−143.
(78) Hutter, J. L.; Bechhoefer, J. Calibration of Atomic-Force Microscope Tips. *Rev. Sci. Instrum.* **1993**, *64*, 1868−1873.
(79) Shi, C.; Chan, D. Y.; Liu, Q.; Zeng, H. Probing the Hydrophobic Interaction between Air Bubbles and Partially Hydrophobic Surfaces Using Atomic Force Microscopy. *J. Phys. Chem. C* **2014**, *118*, 25000−25008.
(80) Fréchette, J.; Vanderlick, T. K. Double Layer Forces over Large Potential Ranges as Measured in an Electrochemical Surface Forces Apparatus. *Langmuir* **2001**, *17*, 7620−7627.
(81) Müller, D. J.; Dufrene, Y. F. Atomic Force Microscopy as a Multifunctional Molecular Toolbox in Nanobiotechnology. In *Nanoscience and Technology: A Collection of Reviews from Nature Journals*; Nature Publishing Group, 2010; 269−277.

https://doi.org/10.1021/acs.chemrev.2c00215
Chem. Rev. XXXX, XXX, XXX−XXX

(82) Zhang, W.; Zhang, X. Single Molecule Mechanochemistry of Macromolecules. *Prog. Polym. Sci.* **2003**, *28*, 1271−1295.
(83) Liu, W.; Guo, Y.; Wang, K.; Zhou, X.; Wang, Y.; Lü, J.; Shao, Z.; Hu, J.; Czajkowsky, D. M.; Li, B. Atomic Force Microscopy-Based Single-Molecule Force Spectroscopy Detects DNA Base Mismatches. *Nanoscale* **2019**, *11*, 17206−17210.
(84) Giannotti, M. I.; Vancso, G. J. Interrogation of Single Synthetic Polymer Chains and Polysaccharides by AFM-Based Force Spectroscopy. *ChemPhysChem* **2007**, *8*, 2290−2307.
(85) Oesterhelt, F.; Rief, M.; Gaub, H. Single Molecule Force Spectroscopy by AFM Indicates Helical Structure of Poly (Ethylene-Glycol) in Water. *New J. Phys.* **1999**, *1*, 6.
(86) Evans, E.; Ritchie, K. Dynamic Strength of Molecular Adhesion Bonds. *Biophys. J.* **1997**, *72*, 1541−1555.
(87) Evans, E. Probing the Relation between Force-Lifetime-and Chemistry in Single Molecular Bonds. *Annu. Rev. Biophys. Biomol. Struct.* **2001**, *30*, 105−128.
(88) Friddle, R. W.; Noy, A.; De Yoreo, J. J. Interpreting the Widespread Nonlinear Force Spectra of Intermolecular Bonds. *Proc. Natl. Acad. Sci. U.S.A.* **2012**, *109*, 13573−13578.
(89) Dudko, O. K.; Hummer, G.; Szabo, A. Theory, Analysis, and Interpretation of Single-Molecule Force Spectroscopy Experiments. *Proc. Natl. Acad. Sci. U.S.A.* **2008**, *105*, 15755−15760.
(90) Ashkin, A.; Dziedzic, J. M.; Yamane, T. Optical Trapping and Manipulation of Single Cells Using Infrared Laser Beams. *Nature* **1987**, *330*, 769−771.
(91) Ashkin, A. Optical Trapping and Manipulation of Neutral Particles Using Lasers. *Proc. Natl. Acad. Sci. U.S.A.* **1997**, *94*, 4853−4860.
(92) Neuman, K. C.; Nagy, A. Single-Molecule Force Spectroscopy: Optical Tweezers, Magnetic Tweezers and Atomic Force Microscopy. *Nat. Methods* **2008**, *5*, 491−505.
(93) Visscher, K.; Gross, S. P.; Block, S. M. Construction of Multiple-Beam Optical Traps with Nanometer-Resolution Position Sensing. *IEEE J. Sel. Top. Quantum Electron.* **1996**, *2*, 1066−1076.
(94) Bustamante, C. J.; Chemla, Y. R.; Liu, S.; Wang, M. D. Optical Tweezers in Single-Molecule Biophysics. *Nat. Rev. Dis. Primers* **2021**, *1*, 1−29.
(95) Cecconi, C.; Shank, E. A.; Dahlquist, F. W.; Marqusee, S.; Bustamante, C. Protein-DNA Chimeras for Single Molecule Mechanical Folding Studies with the Optical Tweezers. *Eur. Biophys. J.* **2008**, *37*, 729−738.
(96) Neuman, K. C.; Chadd, E. H.; Liou, G. F.; Bergman, K.; Block, S. M. Characterization of Photodamage to Escherichia Coli in Optical Traps. *Biophys. J.* **1999**, *77*, 2856−2863.
(97) Claesson, P. M.; Dobryden, I.; Li, G.; He, Y.; Huang, H.; Thorén, P.-A.; Haviland, D. B. From Force Curves to Surface Nanomechanical Properties. *Phys. Chem. Chem. Phys.* **2017**, *19*, 23642−23657.
(98) Haviland, D. B.; van Eysden, C. A.; Forchheimer, D.; Platz, D.; Kassa, H. G.; Leclère, P. Probing Viscoelastic Response of Soft Material Surfaces at the Nanoscale. *Soft Matter* **2016**, *12*, 619−624.
(99) Leckband, D.; Israelachvili, J. Intermolecular Forces in Biology. *Q. Rev. Biophys.* **2001**, *34*, 105−267.
(100) Claesson, P. M.; Poptoshev, E.; Blomberg, E.; Dedinaite, A. Polyelectrolyte-Mediated Surface Interactions. *Adv. Colloid Interface Sci.* **2005**, *114*, 173−187.
(101) Zhou, H.-X.; Pang, X. Electrostatic Interactions in Protein Structure, Folding, Binding, and Condensation. *Chem. Rev.* **2018**, *118*, 1691−1741.
(102) Szilagyi, I.; Trefalt, G.; Tiraferri, A.; Maroni, P.; Borkovec, M. Polyelectrolyte Adsorption, Interparticle Forces, and Colloidal Aggregation. *Soft Matter* **2014**, *10*, 2479−2502.
(103) Boudou, T.; Crouzier, T.; Ren, K.; Blin, G.; Picart, C. Multiple Functionalities of Polyelectrolyte Multilayer Films: New Biomedical Applications. *Adv. Mater.* **2010**, *22*, 441−467.
(104) Poptoshev, E.; Rutland, M. W.; Claesson, P. Surface Forces in Aqueous Polyvinylamine Solutions. I. Glass Surfaces. *Langmuir* **1999**, *15*, 7789−7794.
(105) Finessi, M.; Sinha, P.; Szilágyi, I.; Popa, I.; Maroni, P.; Borkovec, M. Charge Reversal of Sulfate Latex Particles by Adsorbed Linear Poly (Ethylene Imine) Probed by Multiparticle Colloidal Probe Technique. *J. Phys. Chem. B* **2011**, *115*, 9098−9105.
(106) Popa, I.; Gillies, G.; Papastavrou, G.; Borkovec, M. Attractive Electrostatic Forces between Identical Colloidal Particles Induced by Adsorbed Polyelectrolytes. *J. Phys. Chem. B* **2009**, *113*, 8458−8461.
(107) Popa, I.; Papastavrou, G.; Borkovec, M. Charge Regulation Effects on Electrostatic Patch-Charge Attraction Induced by Adsorbed Dendrimers. *Phys. Chem. Chem. Phys.* **2010**, *12*, 4863−4871.
(108) Lowack, K.; Helm, C. Molecular Mechanisms Controlling the Self-Assembly Process of Polyelectrolyte Multilayers. *Macromolecules* **1998**, *31*, 823−833.
(109) Blomberg, E.; Poptoshev, E.; Claesson, P. M.; Caruso, F. Surface Interactions During Polyelectrolyte Multilayer Buildup. 1. Interactions and Layer Structure in Dilute Electrolyte Solutions. *Langmuir* **2004**, *20*, 5432−5438.
(110) Pincus, P. Colloid Stabilization with Grafted Polyelectrolytes. *Macromolecules* **1991**, *24*, 2912−2919.
(111) Murakami, D.; Takenaka, A.; Kobayashi, M.; Jinnai, H.; Takahara, A. Measurement of the Electrostatic Interaction between Polyelectrolyte Brush Surfaces by Optical Tweezers. *Langmuir* **2013**, *29*, 16093−16097.
(112) Raftari, M.; Zhang, Z. J.; Carter, S. R.; Leggett, G. J.; Geoghegan, M. Nanoscale Contact Mechanics between Two Grafted Polyelectrolyte Surfaces. *Macromolecules* **2015**, *48*, 6272−6279.
(113) Balastre, M.; Li, F.; Schorr, P.; Yang, J.; Mays, J. W.; Tirrell, M. V. A Study of Polyelectrolyte Brushes Formed from Adsorption of Amphiphilic Diblock Copolymers Using the Surface Forces Apparatus. *Macromolecules* **2002**, *35*, 9480−9486.
(114) Han, L.; Yan, B.; Zhang, L.; Wu, M.; Wang, J.; Huang, J.; Deng, Y.; Zeng, H. Tuning Protein Adsorption on Charged Polyelectrolyte Brushes Via Salinity Adjustment. *Colloids Surf. A: Physicochem. Eng. Asp.* **2018**, *539*, 37−45.
(115) Willott, J. D.; Murdoch, T. J.; Webber, G. B.; Wanless, E. J. Nature of the Specific Anion Response of a Hydrophobic Weak Polyelectrolyte Brush Revealed by AFM Force Measurements. *Macromolecules* **2016**, *49*, 2327−2338.
(116) Yu, J.; Mao, J.; Yuan, G.; Satija, S.; Jiang, Z.; Chen, W.; Tirrell, M. Structure of Polyelectrolyte Brushes in the Presence of Multivalent Counterions. *Macromolecules* **2016**, *49*, 5609−5617.
(117) Ma, L.; Gaisinskaya-Kipnis, A.; Kampf, N.; Klein, J. Origins of Hydration Lubrication. *Nat. Commun.* **2015**, *6*, 1−6.
(118) Raviv, U.; Giasson, S.; Kampf, N.; Gohy, J.-F.; Jérôme, R.; Klein, J. Lubrication by Charged Polymers. *Nature* **2003**, *425*, 163−165.
(119) Yu, J.; Jackson, N.; Xu, X.; Morgenstern, Y.; Kaufman, Y.; Ruths, M.; De Pablo, J.; Tirrell, M. Multivalent Counterions Diminish the Lubricity of Polyelectrolyte Brushes. *Science* **2018**, *360*, 1434−1438.
(120) Butt, H.-J. Measuring Local Surface Charge Densities in Electrolyte Solutions with a Scanning Force Microscope. *Biophys. J.* **1992**, *63*, 578−582.
(121) Rossell, J.; Allen, S.; Davies, M.; Roberts, C.; Tendler, S.; Williams, P. Electrostatic Interactions Observed When Imaging Proteins with the Atomic Force Microscope. *Ultramicroscopy* **2003**, *96*, 37−46.
(122) Medalsy, I. D.; Müller, D. J. Nanomechanical Properties of Proteins and Membranes Depend on Loading Rate and Electrostatic Interactions. *ACS Nano* **2013**, *7*, 2642−2650.
(123) Valle-Delgado, J.; Molina-Bolivar, J.; Galisteo-Gonzalez, F.; Galvez-Ruiz, M.; Feiler, A.; Rutland, M. W. Adhesion Forces between Protein Layers Studied by Means of Atomic Force Microscopy. *Langmuir* **2006**, *22*, 5108−5114.
(124) Dong, Y.; Laaksonen, A.; Cao, W.; Ji, X.; Lu, X. AFM Study of pH-Dependent Adhesion of Single Protein to TiO_2 Surface. *Adv. Mater. Interfaces* **2019**, *6*, 1900411.
(125) Zheng, P.; Cao, Y.; Bu, T.; Straus, S. K.; Li, H. Single Molecule Force Spectroscopy Reveals That Electrostatic Interactions Affect the Mechanical Stability of Proteins. *Biophys. J.* **2011**, *100*, 1534−1541.

https://doi.org/10.1021/acs.chemrev.2c00215
Chem. Rev. XXXX, XXX, XXX−XXX

(126) Dobrawa, R.; Würthner, F. Metallosupramolecular Approach toward Functional Coordination Polymers. *J. Polym. Sci., Part A: Polym. Chem.* **2005**, *43*, 4981−4995.
(127) Pearson, R. G. Hard and Soft Acids and Bases. *J. Am. Chem. Soc.* **1963**, *85*, 3533−3539.
(128) Gohy, J.-F. Metallo-Supramolecular Block Copolymer Micelles. *Coord. Chem. Rev.* **2009**, *253*, 2214−2225.
(129) Kuppuraj, G.; Dudev, M.; Lim, C. Factors Governing Metal-Ligand Distances and Coordination Geometries of Metal Complexes. *J. Phys. Chem. B* **2009**, *113*, 2952−2960.
(130) Zielenkiewicz, W.; Lebedeva, N. S.; Antina, E.; Vyugin, A.; Kamiński, M. Titration Calorimetric Investigation of Interactions of Zinc (II), Nickel (II), and Copper (II) Tetraphenylporphine Complexes with Pyridine in Three Solvents. *J. Solution Chem.* **1998**, *27*, 879−886.
(131) Yamasaki, K.; Yasuda, M. Stability of Zinc and Cadmium Complexes with 2, 2'-Bipyridine and 1, 10-Phenanthroline. *J. Am. Chem. Soc.* **1956**, *78*, 1324−1324.
(132) Goze, C.; Ulrich, G.; Charbonnière, L.; Cesario, M.; Prangé, T.; Ziessel, R. Cation Sensors Based on Terpyridine-Functionalized Boradiazaindacene. *Chem. Eur. J.* **2003**, *9*, 3748−3755.
(133) Harrington, M. J.; Masic, A.; Holten-Andersen, N.; Waite, J. H.; Fratzl, P. Iron-Clad Fibers: A Metal-Based Biological Strategy for Hard Flexible Coatings. *Science* **2010**, *328*, 216−220.
(134) Yang, B.; Lim, C.; Hwang, D. S.; Cha, H. J. Switch of Surface Adhesion to Cohesion by Dopa-Fe^{3+} Complexation, in Response to Microenvironment at the Mussel Plaque/Substrate Interface. *Chem. Mater.* **2016**, *28*, 7982−7989.
(135) Li, Y.; Wen, J.; Qin, M.; Cao, Y.; Ma, H.; Wang, W. Single-Molecule Mechanics of Catechol-Iron Coordination Bonds. *ACS Biomater. Sci. Eng.* **2017**, *3*, 979−989.
(136) Mesko, M.; Xiang, L.; Bohle, S.; Hwang, D. S.; Zeng, H.; Harrington, M. J. Catechol-Vanadium Binding Enhances Cross-Linking and Mechanics of a Mussel Byssus Coating Protein. *Chem. Mater.* **2021**, *33*, 6530−6540.
(137) Lee, H.; Scherer, N. F.; Messersmith, P. B. Single-Molecule Mechanics of Mussel Adhesion. *Proc. Natl. Acad. Sci. U.S.A.* **2006**, *103*, 12999−13003.
(138) Yu, J.; Wei, W.; Menyo, M. S.; Masic, A.; Waite, J. H.; Israelachvili, J. N. Adhesion of Mussel Foot Protein-3 to TiO^2 Surfaces: The Effect of pH. *Biomacromolecules* **2013**, *14*, 1072−1077.
(139) Reinecke, A.; Bertinetti, L.; Fratzl, P.; Harrington, M. J. Cooperative Behavior of a Sacrificial Bond Network and Elastic Framework in Providing Self-Healing Capacity in Mussel Byssal Threads. *J. Struct. Biol.* **2016**, *196*, 329−339.
(140) Schmidt, S.; Reinecke, A.; Wojcik, F.; Pussak, D.; Hartmann, L.; Harrington, M. J. Metal-Mediated Molecular Self-Healing in Histidine-Rich Mussel Peptides. *Biomacromolecules* **2014**, *15*, 1644−1652.
(141) Cao, Y.; Yoo, T.; Li, H. Single Molecule Force Spectroscopy Reveals Engineered Metal Chelation Is a General Approach to Enhance Mechanical Stability of Proteins. *Proc. Natl. Acad. Sci. U.S.A.* **2008**, *105*, 11152−11157.
(142) Sun, W.; Xue, B.; Fan, Q.; Tao, R.; Wang, C.; Wang, X.; Li, Y.; Qin, M.; Wang, W.; Chen, B.; Cao, Y. Molecular Engineering of Metal Coordination Interactions for Strong, Tough, and Fast-Recovery Hydrogels. *Sci. Adv.* **2020**, *6*, No. eaaz9531.
(143) Kersey, F. R.; Yount, W. C.; Craig, S. L. Single-Molecule Force Spectroscopy of Bimolecular Reactions: System Homology in the Mechanical Activation of Ligand Substitution Reactions. *J. Am. Chem. Soc.* **2006**, *128*, 3886−3887.
(144) Kudera, M.; Eschbaumer, C.; Gaub, H. E.; Schubert, U. S. Analysis of Metallo-Supramolecular Systems Using Single-Molecule Force Spectroscopy. *Adv. Funct. Mater.* **2003**, *13*, 615−620.
(145) Hao, X.; Zhu, N.; Gschneidtner, T.; Jonsson, E. Ö.; Zhang, J.; Moth-Poulsen, K.; Wang, H.; Thygesen, K. S.; Jacobsen, K. W.; Ulstrup, J.; Chi, Q. Direct Measurement and Modulation of Single-Molecule Coordinative Bonding Forces in a Transition Metal Complex. *Nat. Commun.* **2013**, *4*, 1−10.
(146) Zheng, P.; Li, H. Highly Covalent Ferric-Thiolate Bonds Exhibit Surprisingly Low Mechanical Stability. *J. Am. Chem. Soc.* **2011**, *133*, 6791−6798.
(147) Zheng, P.; Arantes, G. M.; Field, M. J.; Li, H. Force-Induced Chemical Reactions on the Metal Centre in a Single Metalloprotein Molecule. *Nat. Commun.* **2015**, *6*, 1−9.
(148) Li, J.; Li, H. Single Molecule Force Spectroscopy Reveals That a Two-Coordinate Ferric Site Is Critical for the Folding of Holo-Rubredoxin. *Nanoscale* **2020**, *12*, 22564−22573.
(149) Armstrong, G.; Buggy, M. Hydrogen-Bonded Supramolecular Polymers: A Literature Review. *J. Mater. Sci.* **2005**, *40*, 547−559.
(150) Lee, G. U.; Chrisey, L. A.; Colton, R. J. Direct Measurement of the Forces between Complementary Strands of DNA. *Science* **1994**, *266*, 771−773.
(151) Boland, T.; Ratner, B. Direct Measurement of Hydrogen Bonding in DNA Nucleotide Bases by Atomic Force Microscopy. *Proc. Natl. Acad. Sci. U.S.A.* **1995**, *92*, 5297−5301.
(152) Rief, M.; Clausen-Schaumann, H.; Gaub, H. E. Sequence-Dependent Mechanics of Single DNA Molecules. *Nat. Struct. Biol.* **1999**, *6*, 346−349.
(153) Bockelmann, U.; Thomen, P.; Essevaz-Roulet, B.; Viasnoff, V.; Heslot, F. Unzipping DNA with Optical Tweezers: High Sequence Sensitivity and Force Flips. *Biophys. J.* **2002**, *82*, 1537−1553.
(154) Binazadeh, M.; Faghihnejad, A.; Unsworth, L. D.; Zeng, H. Understanding the Effect of Secondary Structure on Molecular Interactions of Poly-L-Lysine with Different Substrates by SFA. *Biomacromolecules* **2013**, *14*, 3498−3508.
(155) Marszalek, P. E.; Lu, H.; Li, H.; Carrion-Vazquez, M.; Oberhauser, A. F.; Schulten, K.; Fernandez, J. M. Mechanical Unfolding Intermediates in Titin Modules. *Nature* **1999**, *402*, 100−103.
(156) Brockwell, D. J.; Paci, E.; Zinober, R. C.; Beddard, G. S.; Olmsted, P. D.; Smith, D. A.; Perham, R. N.; Radford, S. E. Pulling Geometry Defines the Mechanical Resistance of a β-Sheet Protein. *Nat. Struct. Mol. Biol.* **2003**, *10*, 731−737.
(157) Jagannathan, B.; Elms, P. J.; Bustamante, C.; Marqusee, S. Direct Observation of a Force-Induced Switch in the Anisotropic Mechanical Unfolding Pathway of a Protein. *Proc. Natl. Acad. Sci. U.S.A.* **2012**, *109*, 17820−17825.
(158) Zhang, Q.; Jaroniec, J.; Lee, G.; Marszalek, P. E. Direct Detection of Inter-Residue Hydrogen Bonds in Polysaccharides by Single-Molecule Force Spectroscopy. *Angew. Chem., Int. Ed.* **2005**, *44*, 2723−2727.
(159) Qian, L.; Bao, Y.; Duan, W.; Cui, S. Effects of Water Content of the Mixed Solvent on the Single-Molecule Mechanics of Amylose. *ACS Macro Lett.* **2018**, *7*, 672−676.
(160) Giannotti, M. I.; Rinaudo, M.; Vancso, G. J. Force Spectroscopy of Hyaluronan by Atomic Force Microscopy: From Hydrogen-Bonded Networks toward Single-Chain Behavior. *Biomacromolecules* **2007**, *8*, 2648−2652.
(161) Sijbesma, R. P.; Beijer, F. H.; Brunsveld, L.; Folmer, B. J.; Hirschberg, J. K.; Lange, R. F.; Lowe, J. K.; Meijer, E. Reversible Polymers Formed from Self-Complementary Monomers Using Quadruple Hydrogen Bonding. *Science* **1997**, *278*, 1601−1604.
(162) Faghihnejad, A.; Feldman, K. E.; Yu, J.; Tirrell, M. V.; Israelachvili, J. N.; Hawker, C. J.; Kramer, E. J.; Zeng, H. Adhesion and Surface Interactions of a Self-Healing Polymer with Multiple Hydrogen-Bonding Groups. *Adv. Funct. Mater.* **2014**, *24*, 2322−2333.
(163) Zou, S.; Schönherr, H.; Vancso, G. J. Force Spectroscopy of Quadruple H-Bonded Dimers by AFM: Dynamic Bond Rupture and Molecular Time-Temperature Superposition. *J. Am. Chem. Soc.* **2005**, *127*, 11230−11231.
(164) Chen, J.; Wu, M.; Gong, L.; Zhang, J.; Yan, B.; Liu, J.; Zhang, H.; Thundat, T.; Zeng, H. Mechanistic Understanding and Nanomechanics of Multiple Hydrogen-Bonding Interaction in Aqueous Environment. *J. Phys. Chem. C* **2019**, *123*, 4540−4548.
(165) Chung, J.; Kushner, A. M.; Weisman, A. C.; Guan, Z. Direct Correlation of Single-Molecule Properties with Bulk Mechanical Performance for the Biomimetic Design of Polymers. *Nat. Mater.* **2014**, *13*, 1055−1062.

https://doi.org/10.1021/acs.chemrev.2c00215
Chem. Rev. XXXX, XXX, XXX−XXX

(166) Hosono, N.; Kushner, A. M.; Chung, J.; Palmans, A. R.; Guan, Z.; Meijer, E. W. Forced Unfolding of Single-Chain Polymeric Nanoparticles. *J. Am. Chem. Soc.* **2015**, *137*, 6880−6888.
(167) Chang, S. K.; Hamilton, A. D. Molecular Recognition of Biologically Interesting Substrates: Synthesis of an Artificial Receptor for Barbiturates Employing Six Hydrogen Bonds. *J. Am. Chem. Soc.* **1988**, *110*, 1318−1319.
(168) Liang, C. K.; Dubacheva, G. V.; Buffeteau, T.; Cavagnat, D.; Hapiot, P.; Fabre, B.; Tucker, J. H.; Bassani, D. M. Reversible Control over Molecular Recognition in Surface-Bound Photoswitchable Hydrogen-Bonding Receptors: Towards Read-Write-Erase Molecular Printboards. *Chem. Eur. J.* **2013**, *19*, 12748−12758.
(169) Naranjo, T.; Cerrón, F.; Nieto-Ortega, B.; Latorre, A.; Somoza, Á.; Ibarra, B.; Pérez, E. M. Mechanical Measurement of Hydrogen Bonded Host-Guest Systems under Non-Equilibrium, near-Physiological Conditions. *Chem. Sci.* **2017**, *8*, 6037−6041.
(170) Ahn, B. K.; Lee, D. W.; Israelachvili, J. N.; Waite, J. H. Surface-Initiated Self-Healing of Polymers in Aqueous Media. *Nat. Mater.* **2014**, *13*, 867−872.
(171) Bao, Y.; Huang, X.; Xu, J.; Cui, S. Effect of Intramolecular Hydrogen Bonds on the Single-Chain Elasticity of Poly (Vinyl Alcohol): Evidencing the Synergistic Enhancement Effect at the Single-Molecule Level. *Macromolecules* **2021**, *54*, 7314−7320.
(172) Cai, W.; Xu, D.; Zhang, F.; Wei, J.; Lu, S.; Qian, L.; Lu, Z.; Cui, S. Intramolecular Hydrogen Bonds in a Single Macromolecule: Strength in High Vacuum Versus Liquid Environments. *Nano Res.* **2021**, *15*, 1−7.
(173) Lyu, X.; Song, Y.; Feng, W.; Zhang, W. Direct Observation of Single-Molecule Stick-Slip Motion in Polyamide Single Crystals. *ACS Macro Lett.* **2018**, *7*, 762−766.
(174) Thakuria, R.; Nath, N. K.; Saha, B. K. The Nature and Applications of π-π Interactions: A Perspective. *Cryst. Growth Des.* **2019**, *19*, 523−528.
(175) Claessens, C. G.; Stoddart, J. F. π-π Interactions in Self-Assembly. *J. Phys. Org. Chem.* **1997**, *10*, 254−272.
(176) Hunter, C. A.; Sanders, J. K. The Nature of π-π Interactions. *J. Am. Chem. Soc.* **1990**, *112*, 5525−5534.
(177) Kim, K. S.; Tarakeshwar, P.; Lee, J. Y. Molecular Clusters of π-Systems: Theoretical Studies of Structures, Spectra, and Origin of Interaction Energies. *Chem. Rev.* **2000**, *100*, 4145−4186.
(178) Steuber, H.; Heine, A.; Klebe, G. Structural and Thermodynamic Study on Aldose Reductase: Nitro-Substituted Inhibitors with Strong Enthalpic Binding Contribution. *J. Mol. Biol.* **2007**, *368*, 618−638.
(179) Zhang, Y.; Liu, C.; Shi, W.; Wang, Z.; Dai, L.; Zhang, X. Direct Measurements of the Interaction between Pyrene and Graphite in Aqueous Media by Single Molecule Force Spectroscopy: Understanding the π-π Interactions. *Langmuir* **2007**, *23*, 7911−7915.
(180) Zhang, J.; Lu, X.; Shi, C.; Yan, B.; Gong, L.; Chen, J.; Xiang, L.; Xu, H.; Liu, Q.; Zeng, H. Unraveling the Molecular Interaction Mechanism between Graphene Oxide and Aromatic Organic Compounds with Implications on Wastewater Treatment. *Chem. Eng. J.* **2019**, *358*, 842−849.
(181) Manohar, S.; Mantz, A. R.; Bancroft, K. E.; Hui, C.-Y.; Jagota, A.; Vezenov, D. V. Peeling Single-Stranded DNA from Graphite Surface to Determine Oligonucleotide Binding Energy by Force Spectroscopy. *Nano Lett.* **2008**, *8*, 4365−4372.
(182) Iliafar, S.; Wagner, K.; Manohar, S.; Jagota, A.; Vezenov, D. Quantifying Interactions between DNA Oligomers and Graphite Surface Using Single Molecule Force Spectroscopy. *J. Phys. Chem. C* **2012**, *116*, 13896−13903.
(183) Iliafar, S.; Mittal, J.; Vezenov, D.; Jagota, A. Interaction of Single-Stranded DNA with Curved Carbon Nanotube Is Much Stronger Than with Flat Graphite. *J. Am. Chem. Soc.* **2014**, *136*, 12947−12957.
(184) Lai, J.; Zhou, H.; Wang, M.; Chen, Y.; Jin, Z.; Li, S.; Yang, J.; Jin, X.; Liu, H.; Zhao, W. Recyclable, Stretchable and Conductive Double Network Hydrogels Towards Flexible Strain Sensors. *Journal of Materials Chemistry C* **2018**, *6*, 13316−13324.
(185) Cai, W.; Xu, D.; Qian, L.; Wei, J.; Xiao, C.; Qian, L.; Lu, Z.-y.; Cui, S. Force-Induced Transition of π-π Stacking in a Single Polystyrene Chain. *J. Am. Chem. Soc.* **2019**, *141*, 9500−9503.
(186) Stauffer, D. A.; Barrans, R. E., Jr.; Dougherty, D. A. Biomimetic Catalysis of an Sn_2 Reaction Resulting from a Novel Form of Transition-State Stabilization. *Angew. Chem., Int. Ed.* **1990**, *29*, 915−918.
(187) Cubero, E.; Luque, F. J.; Orozco, M. Is Polarization Important in Cation-π Interactions? *Proc. Natl. Acad. Sci. U.S.A.* **1998**, *95*, 5976−5980.
(188) Ma, J. C.; Dougherty, D. A. The Cation-π Interaction. *Chem. Rev.* **1997**, *97*, 1303−1324.
(189) Kearney, P. C.; Mizoue, L. S.; Kumpf, R. A.; Forman, J. E.; McCurdy, A.; Dougherty, D. A. Molecular Recognition in Aqueous Media. New Binding Studies Provide Further Insights into the Cation-π Interaction and Related Phenomena. *J. Am. Chem. Soc.* **1993**, *115*, 9907−9919.
(190) Lu, Q.; Oh, D. X.; Lee, Y.; Jho, Y.; Hwang, D. S.; Zeng, H. Nanomechanics of Cation-π Interactions in Aqueous Solution. *Angew. Chem.* **2013**, *125*, 4036−4040.
(191) Gebbie, M. A.; Wei, W.; Schrader, A. M.; Cristiani, T. R.; Dobbs, H. A.; Idso, M.; Chmelka, B. F.; Waite, J. H.; Israelachvili, J. N. Tuning Underwater Adhesion with Cation-π Interactions. *Nat. Chem.* **2017**, *9*, 473−479.
(192) Xiang, L.; Zhang, J.; Wang, W.; Gong, L.; Zhang, L.; Yan, B.; Zeng, H. Nanomechanics of π-Cation-π Interaction with Implications for Bio-Inspired Wet Adhesion. *Acta Biomater.* **2020**, *117*, 294−301.
(193) Hwang, D. S.; Zeng, H.; Lu, Q.; Israelachvili, J.; Waite, J. H. Adhesion Mechanism in a Dopa-Deficient Foot Protein from Green Mussels. *Soft Matter* **2012**, *8*, 5640−5648.
(194) Kim, S.; Faghihnejad, A.; Lee, Y.; Jho, Y.; Zeng, H.; Hwang, D. S. Cation-π Interaction in Dopa-Deficient Mussel Adhesive Protein Mfp-1. *J. Mater. Chem. B* **2015**, *3*, 738−743.
(195) Shin, M.; Park, Y.; Jin, S.; Jung, Y. M.; Cha, H. J. Two Faces of Amine-Catechol Pair Synergy in Underwater Cation-π Interactions. *Chem. Mater.* **2021**, *33*, 3196−3206.
(196) Chang, H.; Adibnia, V.; Li, C.; Su, R.; Qi, W.; Banquy, X. Short-Sequence Superadhesive Peptides with Topologically Enhanced Cation-π Interactions. *Chem. Mater.* **2021**, *33*, 5168−5176.
(197) Mascal, M.; Armstrong, A.; Bartberger, M. D. Anion-Aromatic Bonding: A Case for Anion Recognition by π-Acidic Rings. *J. Am. Chem. Soc.* **2002**, *124*, 6274−6276.
(198) Quiñonero, D.; Garau, C.; Rotger, C.; Frontera, A.; Ballester, P.; Costa, A.; Deyà, P. M. Anion-π Interactions: Do They Exist? *Angew. Chem.* **2002**, *114*, 3539−3542.
(199) Berryman, O. B.; Bryantsev, V. S.; Stay, D. P.; Johnson, D. W.; Hay, B. P. Structural Criteria for the Design of Anion Receptors: The Interaction of Halides with Electron-Deficient Arenes. *J. Am. Chem. Soc.* **2007**, *129*, 48−58.
(200) Schottel, B. L.; Chifotides, H. T.; Dunbar, K. R. Anion-π Interactions. *Chem. Soc. Rev.* **2008**, *37*, 68−83.
(201) Zhang, J.; Xiang, L.; Yan, B.; Zeng, H. Nanomechanics of Anion-π Interaction in Aqueous Solution. *J. Am. Chem. Soc.* **2020**, *142*, 1710−1714.
(202) Akamatsu, M.; Kimura, A.; Yamanaga, K.; Sakai, K.; Sakai, H. Anion-π Interaction at the Solid/Water Interfaces. *Chem. Commun.* **2021**, *57*, 4650−4653.
(203) Zeng, H.; Shi, C.; Huang, J.; Li, L.; Liu, G.; Zhong, H. Recent Experimental Advances on Hydrophobic Interactions at Solid/Water and Fluid/Water Interfaces. *Biointerphases* **2016**, *11*, 018903.
(204) Meyer, E. E.; Rosenberg, K. J.; Israelachvili, J. Recent Progress in Understanding Hydrophobic Interactions. *Proc. Natl. Acad. Sci. U.S.A.* **2006**, *103*, 15739−15746.
(205) Tyrrell, J. W.; Attard, P. Images of Nanobubbles on Hydrophobic Surfaces and Their Interactions. *Phys. Rev. Lett.* **2001**, *87*, 176104.
(206) Podgornik, R. Electrostatic Correlation Forces between Surfaces with Surface Specific Ionic Interactions. *J. Chem. Phys.* **1989**, *91*, 5840−5849.

https://doi.org/10.1021/acs.chemrev.2c00215
Chem. Rev. XXXX, XXX, XXX−XXX

(207) Israelachvili, J.; Pashley, R. The Hydrophobic Interaction Is Long Range, Decaying Exponentially with Distance. *Nature* **1982**, *300*, 341−342.
(208) Faghihnejad, A.; Zeng, H. Hydrophobic Interactions between Polymer Surfaces: Using Polystyrene as a Model System. *Soft Matter* **2012**, *8*, 2746−2759.
(209) Cui, X.; Liu, J.; Xie, L.; Huang, J.; Liu, Q.; Israelachvili, J. N.; Zeng, H. Modulation of Hydrophobic Interaction by Mediating Surface Nanoscale Structure and Chemistry, Not Monotonically by Hydrophobicity. *Angew. Chem.* **2018**, *130*, 12079−12084.
(210) Donaldson, S. H., Jr; Røyne, A.; Kristiansen, K.; Rapp, M. V.; Das, S.; Gebbie, M. A.; Lee, D. W.; Stock, P.; Valtiner, M.; Israelachvili, J. Developing a General Interaction Potential for Hydrophobic and Hydrophilic Interactions. *Langmuir* **2015**, *31*, 2051−2064.
(211) Ma, C. D.; Wang, C.; Acevedo-Vélez, C.; Gellman, S. H.; Abbott, N. L. Modulation of Hydrophobic Interactions by Proximally Immobilized Ions. *Nature* **2015**, *517*, 347−350.
(212) Shi, C.; Yan, B.; Xie, L.; Zhang, L.; Wang, J.; Takahara, A.; Zeng, H. Long-Range Hydrophilic Attraction between Water and Polyelectrolyte Surfaces in Oil. *Angew. Chem., Int. Ed.* **2016**, *55*, 15017−15021.
(213) Li, I. T.; Walker, G. C. Interfacial Free Energy Governs Single Polystyrene Chain Collapse in Water and Aqueous Solutions. *J. Am. Chem. Soc.* **2010**, *132*, 6530−6540.
(214) Li, I. T.; Walker, G. C. Signature of Hydrophobic Hydration in a Single Polymer. *Proc. Natl. Acad. Sci. U.S.A.* **2011**, *108*, 16527−16532.
(215) Di, W.; Gao, X.; Huang, W.; Sun, Y.; Lei, H.; Liu, Y.; Li, W.; Li, Y.; Wang, X.; Qin, M.; Zhu, Z.; Cao, Y.; Wang, W. Direct Measurement of Length Scale Dependence of the Hydrophobic Free Energy of a Single Collapsed Polymer Nanosphere. *Phys. Rev. Lett.* **2019**, *122*, 047801.
(216) Bao, Y.; Qian, H.-j.; Lu, Z.-y.; Cui, S. Revealing the Hydrophobicity of Natural Cellulose by Single-Molecule Experiments. *Macromolecules* **2015**, *48*, 3685−3690.
(217) Waite, J. H.; Tanzer, M. L. Polyphenolic Substance of Mytilus Edulis: Novel Adhesive Containing L-Dopa and Hydroxyproline. *Science* **1981**, *212*, 1038−1040.
(218) Lu, Q.; Danner, E.; Waite, J. H.; Israelachvili, J. N.; Zeng, H.; Hwang, D. S. Adhesion of Mussel Foot Proteins to Different Substrate Surfaces. *J. Royal Soc. Interface* **2013**, *10*, 20120759.
(219) Yu, J.; Kan, Y.; Rapp, M.; Danner, E.; Wei, W.; Das, S.; Miller, D. R.; Chen, Y.; Waite, J. H.; Israelachvili, J. N. Adaptive Hydrophobic and Hydrophilic Interactions of Mussel Foot Proteins with Organic Thin Films. *Proc. Natl. Acad. Sci. U.S.A.* **2013**, *110*, 15680−15685.
(220) Utzig, T.; Stock, P.; Valtiner, M. Resolving Non-Specific and Specific Adhesive Interactions of Catechols at Solid/Liquid Interfaces at the Molecular Scale. *Angew. Chem., Int. Ed.* **2016**, *55*, 9524−9528.
(221) Xie, L.; Gong, L.; Zhang, J.; Han, L.; Xiang, L.; Chen, J.; Liu, J.; Yan, B.; Zeng, H. A Wet Adhesion Strategy Via Synergistic Cation-π and Hydrogen Bonding Interactions of Antifouling Zwitterions and Mussel-Inspired Binding Moieties. *J. Mater. Chem. A* **2019**, *7*, 21944−21952.
(222) Maier, G. P.; Rapp, M. V.; Waite, J. H.; Israelachvili, J. N.; Butler, A. Adaptive Synergy between Catechol and Lysine Promotes Wet Adhesion by Surface Salt Displacement. *Science* **2015**, *349*, 628−632.
(223) Rapp, M. V.; Maier, G. P.; Dobbs, H. A.; Higdon, N. J.; Waite, J. H.; Butler, A.; Israelachvili, J. N. Defining the Catechol-Cation Synergy for Enhanced Wet Adhesion to Mineral Surfaces. *J. Am. Chem. Soc.* **2016**, *138*, 9013−9016.
(224) Tiu, B. D. B.; Delparastan, P.; Ney, M. R.; Gerst, M.; Messersmith, P. B. Cooperativity of Catechols and Amines in High-Performance Dry/Wet Adhesives. *Angew. Chem., Int. Ed.* **2020**, *59*, 16616−16624.
(225) Lim, C.; Huang, J.; Kim, S.; Lee, H.; Zeng, H.; Hwang, D. S. Nanomechanics of Poly (Catecholamine) Coatings in Aqueous Solutions. *Angew. Chem., Int. Ed.* **2016**, *55*, 3342−3346.
(226) Zhang, C.; Xiang, L.; Zhang, J.; Gong, L.; Han, L.; Xu, Z.-K.; Zeng, H. Tough and Alkaline-Resistant Mussel-Inspired Wet Adhesion with Surface Salt Displacement Via Polydopamine/Amine Synergy. *Langmuir* **2019**, *35*, 5257−5263.
(227) Ji, X.; Ahmed, M.; Long, L.; Khashab, N. M.; Huang, F.; Sessler, J. L. Adhesive Supramolecular Polymeric Materials Constructed from Macrocycle-Based Host-Guest Interactions. *Chem. Soc. Rev.* **2019**, *48*, 2682−2697.
(228) Schönherr, H.; Beulen, M. W.; Bügler, J.; Huskens, J.; van Veggel, F. C.; Reinhoudt, D. N.; Vancso, G. J. Individual Supramolecular Host-Guest Interactions Studied by Dynamic Single Molecule Force Spectroscopy. *J. Am. Chem. Soc.* **2000**, *122*, 4963−4967.
(229) Auletta, T.; de Jong, M. R.; Mulder, A.; van Veggel, F. C. J. M.; Huskens, J.; Reinhoudt, D. N.; Zou, S.; Zapotoczny, S.; Schonherr, H.; Vancso, G. J.; Kuipers, L. β-Cyclodextrin Host-Guest Complexes Probed under Thermodynamic Equilibrium: Thermodynamics and AFM Force Spectroscopy. *J. Am. Chem. Soc.* **2004**, *126*, 1577−1584.
(230) Yasuda, S.; Suzuki, I.; Shinohara, K.-i.; Shigekawa, H. Single Molecular Anatomy of Solvophobic Effects in Host-Guest Interactions Based on Surface Tension Using Atomic Force Microscopy. *Phys. Rev. Lett.* **2006**, *96*, 228303.
(231) Pandey, S.; Xiang, Y.; Walpita Kankanamalage, D. V.; Jayawickramarajah, J.; Leng, Y.; Mao, H. Measurement of Single-Molecule Forces in Cholesterol and Cyclodextrin Host-Guest Complexes. *J. Phys. Chem. B* **2021**, *125*, 11112−11121.
(232) Liu, S.; Ruspic, C.; Mukhopadhyay, P.; Chakrabarti, S.; Zavalij, P. Y.; Isaacs, L. The Cucurbit[n]uril Family: Prime Components for Self-Sorting Systems. *J. Am. Chem. Soc.* **2005**, *127*, 15959−15967.
(233) Zhang, M.; Gong, Z.; Yang, W.; Jin, L.; Liu, S.; Chang, S.; Liang, F. Regulating Host-Guest Interactions between Cucurbit[7]uril and Guests on Gold Surfaces for Rational Engineering of Gold Nanoparticles. *ACS Appl. Nano Mater.* **2020**, *3*, 4283−4291.
(234) Pandey, S.; Kankanamalage, D. V. W.; Zhou, X.; Hu, C.; Isaacs, L.; Jayawickramarajah, J.; Mao, H. Chaperone-Assisted Host-Guest Interactions Revealed by Single-Molecule Force Spectroscopy. *J. Am. Chem. Soc.* **2019**, *141*, 18385−18389.
(235) González-Urbina, L.; Baert, K.; Kolaric, B.; Pérez-Moreno, J.; Clays, K. Linear and Nonlinear Optical Properties of Colloidal Photonic Crystals. *Chem. Rev.* **2012**, *112*, 2268−2285.
(236) Vogel, N.; Retsch, M.; Fustin, C. A.; del Campo, A.; Jonas, U. Advances in Colloidal Assembly: The Design of Structure and Hierarchy in Two and Three Dimensions. *Chem. Rev.* **2015**, *115*, 6265−6311.
(237) Tao, Y.; Zheng, D.; Zhao, J.; Liu, K.; Liu, J.; Lei, J.; Wang, L. Self-Assembling pH-Responsive Nanoparticle Platform Based on Pectin-Doxorubicin Conjugates for Codelivery of Anticancer Drugs. *ACS Omega* **2021**, *6*, 9998−10004.
(238) Son, S.; Rao, N. V.; Ko, H.; Shin, S.; Jeon, J.; Han, H. S.; Nguyen, V. Q.; Thambi, T.; Suh, Y. D.; Park, J. H. Carboxymethyl Dextran-Based Hypoxia-Responsive Nanoparticles for Doxorubicin Delivery. *Int. J. Biol. Macromol.* **2018**, *110*, 399−405.
(239) Kulkarni, P.; Haldar, M. K.; You, S.; Choi, Y.; Mallik, S. Hypoxia-Responsive Polymersomes for Drug Delivery to Hypoxic Pancreatic Cancer Cells. *Biomacromolecules* **2016**, *17*, 2507−2513.
(240) Fomina, N.; McFearin, C.; Sermsakdi, M.; Edigin, O.; Almutairi, A. UV and Near-IR Triggered Release from Polymeric Nanoparticles. *J. Am. Chem. Soc.* **2010**, *132*, 9540−9542.
(241) Ramírez-García, P. D.; Retamal, J. S.; Shenoy, P.; Imlach, W.; Sykes, M.; Truong, N.; Constandil, L.; Pelissier, T.; Nowell, C. J.; Khor, S. Y.; et al. A pH-Responsive Nanoparticle Targets the Neurokinin 1 Receptor in Endosomes to Prevent Chronic Pain. *Nat. Nanotechnol.* **2019**, *14*, 1150−1159.
(242) Thambi, T.; Deepagan, V. G.; Yoon, H. Y.; Han, H. S.; Kim, S. H.; Son, S.; Jo, D. G.; Ahn, C. H.; Suh, Y. D.; Kim, K.; et al. Hypoxia-Responsive Polymeric Nanoparticles for Tumor-Targeted Drug Delivery. *Biomaterials* **2014**, *35*, 1735−1743.
(243) Zhao, Z.; Han, Z.; Naveena, K.; Lei, G.; Qiu, S.; Li, X.; Li, T.; Shi, X.; Zhuang, W.; Li, Y.; et al. ROS-Responsive Nanoparticle as a Berberine Carrier for OHC-Targeted Therapy of Noise-Induced Hearing Loss. *ACS Appl. Mater. Interfaces* **2021**, *13*, 7102−7114.

https://doi.org/10.1021/acs.chemrev.2c00215
Chem. Rev. XXXX, XXX, XXX−XXX

(244) Chen, H.; Liu, Z.; Wei, B.; Huang, J.; You, X.; Zhang, J.; Yuan, Z.; Tang, Z.; Guo, Z.; Wu, J. Redox Responsive Nanoparticle Encapsulating Black Phosphorus Quantum Dots for Cancer Theranostics. *Bioact. Mater.* **2021**, *6*, 655−665.
(245) Zong, Z.; Hua, L.; Wang, Z.; Xu, H.; Ye, C.; Pan, B.; Zhao, Z.; Zhang, L.; Lu, J.; Liu, H.; et al. Self-Assembled Angiopep-2 Modified Lipid-Poly (Hypoxic Radiosensitized Polyprodrug) Nanoparticles Delivery TMZ for Glioma Synergistic TMZ and RT Therapy. *Drug Delivery* **2019**, *26*, 34−44.
(246) Li, Y.; Lu, A.; Long, M.; Cui, L.; Chen, Z.; Zhu, L. Nitroimidazole Derivative Incorporated Liposomes for Hypoxia-Triggered Drug Delivery and Enhanced Therapeutic Efficacy in Patient-Derived Tumor Xenografts. *Acta Biomater.* **2019**, *83*, 334−348.
(247) Zhang, Y.; Wang, H.; Stewart, S.; Jiang, B.; Ou, W.; Zhao, G.; He, X. Cold-Responsive Nanoparticle Enables Intracellular Delivery and Rapid Release of Trehalose for Organic-Solvent-Free Cryopreservation. *Nano Lett.* **2019**, *19*, 9051−9061.
(248) Zhang, Y.; Cai, L.; Li, D.; Lao, Y. H.; Liu, D.; Li, M.; Ding, J.; Chen, X. Tumor Microenvironment-Responsive Hyaluronate-Calcium Carbonate Hybrid Nanoparticle Enables Effective Chemotherapy for Primary and Advanced Osteosarcomas. *Nano Research* **2018**, *11*, 4806−4822.
(249) Liu, L.; Zhang, Y.; Yu, S.; Yang, Z.; He, C.; Chen, X. Dual Stimuli-Responsive Nanoparticle-Incorporated Hydrogels as an Oral Insulin Carrier for Intestine-Targeted Delivery and Enhanced Paracellular Permeation. *ACS Biomater. Sci. Eng.* **2018**, *4*, 2889−2902.
(250) Kim, J. H.; Lee, S.; Park, K.; Nam, H. Y.; Jang, S. Y.; Youn, I.; Kim, K.; Jeon, H.; Park, R. W.; Kim, I. S.; et al. Protein-Phosphorylation-Responsive Polymeric Nanoparticles for Imaging Protein Kinase Activities in Single Living Cells. *Angew. Chem., Int. Ed.* **2007**, *46*, 5779−5782.
(251) Knight, F. C.; Gilchuk, P.; Kumar, A.; Becker, K. W.; Sevimli, S.; Jacobson, M. E.; Suryadevara, N.; Wang-Bishop, L.; Boyd, K. L.; Crowe, J. E.; Joyce, S.; Wilson, J. T. Mucosal Immunization with a pH-Responsive Nanoparticle Vaccine Induces Protective $CD8^+$ Lung-Resident Memory T Cells. *ACS Nano* **2019**, *13*, 10939−10960.
(252) Wilson, J. T.; Keller, S.; Manganiello, M. J.; Cheng, C.; Lee, C. C.; Opara, C.; Convertine, A.; Stayton, P. S. pH-Responsive Nanoparticle Vaccines for Dual-Delivery of Antigens and Immunostimulatory Oligonucleotides. *ACS Nano* **2013**, *7*, 3912−3925.
(253) Wang, W.; Li, X.; Wang, Z.; Zhang, J.; Dong, X.; Wu, Y.; Fang, C.; Zhou, A.; Wu, Y. A Novel "Mosaic-Type" Nanoparticle for Selective Drug Release Targeting Hypoxic Cancer Cells. *Nanoscale* **2019**, *11*, 2211−2222.
(254) Xu, X.; Wu, J.; Liu, S.; Saw, P. E.; Tao, W.; Li, Y.; Krygsman, L.; Yegnasubramanian, S.; De Marzo, A. M.; Shi, J.; et al. Redox-Responsive Nanoparticle-Mediated Systemic RNAi for Effective Cancer Therapy. *Small* **2018**, *14*, 1802565.
(255) Rao, W.; Zhang, W.; Poventud-Fuentes, I.; Wang, Y.; Lei, Y.; Agarwal, P.; Weekes, B.; Li, C.; Lu, X.; Yu, J.; et al. Thermally Responsive Nanoparticle-Encapsulated Curcumin and Its Combination with Mild Hyperthermia for Enhanced Cancer Cell Destruction. *Acta Biomater.* **2014**, *10*, 831−842.
(256) Dong, Z.; Kang, Y.; Yuan, Q.; Luo, M.; Gu, Z. H_2O_2-Responsive Nanoparticle Based on the Supramolecular Self-Assemble of Cyclodextrin. *Front. Pharmacol.* **2018**, *9*, 552.
(257) Kang, Y.; Ju, X.; Wang, L.; Ding, L. S.; Liu, G. T.; Zhang, S.; Li, B. J. pH and Glutathione Dual-Triggered Supramolecular Assemblies as Synergistic and Controlled Drug Release Carriers. *Polym. Chem.* **2017**, *8*, 7260−7270.
(258) Hadi, M. M.; Nesbitt, H.; Masood, H.; Sciscione, F.; Patel, S.; Ramesh, B. S.; Emberton, M.; Callan, J. F.; MacRobert, A.; McHale, A. P.; et al. Investigating the Performance of a Novel pH and Cathepsin B Sensitive, Stimulus-Responsive Nanoparticle for Optimised Sonodynamic Therapy in Prostate Cancer. *J. Controlled Release* **2021**, *329*, 76−86.
(259) Zhang, Y.; Lu, Y.; Wang, F.; An, S.; Zhang, Y.; Sun, T.; Zhu, J.; Jiang, C. ATP/pH Dual Responsive Nanoparticle with D-[des-Arg^{10}]Kallidin Mediated Efficient In Vivo Targeting Drug Delivery. *Small* **2017**, *13*, 1602494.
(260) Zhang, C.; Zhang, J.; Shi, G.; Song, H.; Shi, S.; Zhang, X.; Huang, P.; Wang, Z.; Wang, W.; Wang, C.; et al. A Light Responsive Nanoparticle-Based Delivery System Using Pheophorbide A Graft Polyethylenimine for Dendritic Cell-Based Cancer Immunotherapy. *Mol. Pharmaceutics* **2017**, *14*, 1760−1770.
(261) Aliprandi, A.; Mauro, M.; De Cola, L. Controlling and Imaging Biomimetic Self-Assembly. *Nat. Chem.* **2016**, *8*, 10−15.
(262) Tian, Z.; Yang, C.; Wang, W.; Yuan, Z. Shieldable Tumor Targeting Based on pH Responsive Self-Assembly/Disassembly of Gold Nanoparticles. *ACS Appl. Mater. Interfaces* **2014**, *6*, 17865−17876.
(263) Lee, C. W.; Takagi, C.; Truong, T.; Chen, Y. C.; Ostafin, A. Luminescent Au Nanoparticles with a pH-Responsive Nanoparticle-Supported Molecular Brush. *J. Phys. Chem. C* **2010**, *114*, 12459−12468.
(264) Olson, M. A.; Coskun, A.; Klajn, R.; Fang, L.; Dey, S. K.; Browne, K. P.; Grzybowski, B. A.; Stoddart, J. F. Assembly of Polygonal Nanoparticle Clusters Directed by Reversible Noncovalent Bonding Interactions. *Nano Lett.* **2009**, *9*, 3185−3190.
(265) Tian, D.; Qin, F.; Zhao, H.; Zhang, C.; Wang, H.; Liu, N.; Ai, Y. Bio-Responsive Nanoparticle for Tumor Targeting and Enhanced Photo-Immunotherapy. *Colloids Surf., B* **2021**, *202*, 111681.
(266) Zhao, J.; Su, H.; Vansuch, G. E.; Liu, Z.; Salaita, K.; Dyer, R. B. Localized Nanoscale Heating Leads to Ultrafast Hydrogel Volume-Phase Transition. *ACS Nano* **2019**, *13*, 515−525.
(267) Ramey-Ward, A. N.; Su, H.; Salaita, K. Mechanical Stimulation of Adhesion Receptors Using Light-Responsive Nanoparticle Actuators Enhances Myogenesis. *ACS Appl. Mater. Interfaces* **2020**, *12*, 35903−35917.
(268) Torres, L., Jr; Daristotle, J. L.; Ayyub, O. B.; Bellato Meinhardt, B. M.; Garimella, H.; Margaronis, A.; Seifert, S.; Bedford, N. M.; Woehl, T. J.; Kofinas, P. Structurally Colored Protease Responsive Nanoparticle Hydrogels with Degradation-Directed Assembly. *Nanoscale* **2019**, *11*, 17904−17912.
(269) Zhang, M.; Xu, C.; Wen, L.; Han, M. K.; Xiao, B.; Zhou, J.; Zhang, Y.; Zhang, Z.; Viennois, E.; Merlin, D. A Hyaluronidase-Responsive Nanoparticle-Based Drug Delivery System for Targeting Colon Cancer Cells. *Cancer Res.* **2016**, *76*, 7208−7218.
(270) Xiao, D.; Jia, H. Z.; Zhang, J.; Liu, C. W.; Zhuo, R. X.; Zhang, X. Z. A Dual-Responsive Mesoporous Silica Nanoparticle for Tumor-Triggered Targeting Drug Delivery. *Small* **2014**, *10*, 591−598.
(271) Low, S. C.; Ng, Q. H.; Tan, L. S. Study of Magnetic-Responsive Nanoparticle on the Membrane Surface as a Membrane Antifouling Surface Coating. *J. Polym. Res.* **2019**, *26*, 70.
(272) Guryanov, I.; Naumenko, E.; Konnova, S.; Lagarkova, M.; Kiselev, S.; Fakhrullin, R. Spatial Manipulation of Magnetically-Responsive Nanoparticle Engineered Human Neuronal Progenitor Cells. *Nanomed. Nanotechnol. Biol. Med.* **2019**, *20*, 102038.
(273) Nash, M. A.; Yager, P.; Hoffman, A. S.; Stayton, P. S. Mixed Stimuli-Responsive Magnetic and Gold Nanoparticle System for Rapid Purification, Enrichment, and Detection of Biomarkers. *Bioconjugate Chem.* **2010**, *21*, 2197−2204.
(274) Nash, M. A.; Waitumbi, J. N.; Hoffman, A. S.; Yager, P.; Stayton, P. S. Multiplexed Enrichment and Detection of Malarial Biomarkers Using a Stimuli-Responsive Iron Oxide and Gold Nanoparticle Reagent System. *ACS Nano* **2012**, *6*, 6776−6785.
(275) Rittikulsittichai, S.; Kolhatkar, A. G.; Sarangi, S.; Vorontsova, M. A.; Vekilov, P. G.; Brazdeikis, A.; Lee, T. R. Multi-Responsive Hybrid Particles: Thermo-, pH-, Photo-, and Magneto-Responsive Magnetic Hydrogel Cores with Gold Nanorod Optical Triggers. *Nanoscale* **2016**, *8*, 11851−11861.
(276) Mosquera, J.; Zhao, Y.; Jang, H. J.; Xie, N.; Xu, C.; Kotov, N. A.; Liz-Marzán, L. M. Plasmonic Nanoparticles with Supramolecular Recognition. *Adv. Funct. Mater.* **2020**, *30*, 1902082.
(277) Zhang, H. Molecularly Imprinted Nanoparticles for Biomedical Applications. *Adv. Mater.* **2020**, *32*, 1806328.
(278) Peng, H.; Qin, Y. T.; He, X. W.; Li, W. Y.; Zhang, Y. K. Epitope Molecularly Imprinted Polymer Nanoparticles for Chemo-/Photo-

https://doi.org/10.1021/acs.chemrev.2c00215
Chem. Rev. XXXX, XXX, XXX−XXX

dynamic Synergistic Cancer Therapy Guided by Targeted Fluorescence Imaging. *ACS Appl. Mater. Interfaces* **2020**, *12*, 13360−13370.
(279) Wang, J.; Qiu, H.; Shen, H.; Pan, J.; Dai, X.; Yan, Y.; Pan, G.; Sellergren, B. Molecularly Imprinted Fluorescent Hollow Nanoparticles as Sensors for Rapid and Efficient Detection λ-Cyhalothrin in Environmental Water. *Biosens. Bioelectron.* **2016**, *85*, 387−394.
(280) Carrasco, S.; Benito-Peña, E.; Navarro-Villoslada, F.; Langer, J.; Sanz-Ortiz, M. N.; Reguera, J.; Liz-Marzán, L. M.; Moreno-Bondi, M. C. Multibranched Gold-Mesoporous Silica Nanoparticles Coated with a Molecularly Imprinted Polymer for Label-Free Antibiotic Surface-Enhanced Raman Scattering Analysis. *Chem. Mater.* **2016**, *28*, 7947−7954.
(281) Wu, Y.; Liu, X.; Meng, M.; Lv, P.; Yan, M.; Wei, X.; Li, H.; Yan, Y.; Li, C. Bio-Inspired Adhesion: Fabrication of Molecularly Imprinted Nanocomposite Membranes by Developing a Hybrid Organic-Inorganic Nanoparticles Composite Structure. *J. Membr. Sci.* **2015**, *490*, 169−178.
(282) Zhao, P.; Hao, J. Tert-Butylhydroquinone Recognition of Molecular Imprinting Electrochemical Sensor Based on Core-Shell Nanoparticles. *Food Chem.* **2013**, *139*, 1001−1007.
(283) Xia, Z.; Lin, Z.; Xiao, Y.; Wang, L.; Zheng, J.; Yang, H.; Chen, G. Facile Synthesis of Polydopamine-Coated Molecularly Imprinted Silica Nanoparticles for Protein Recognition and Separation. *Biosens. Bioelectron.* **2013**, *47*, 120−126.
(284) Cao, Y.; Hu, X.; Zhao, T.; Mao, Y.; Fang, G.; Wang, S. A Core-Shell Molecularly Imprinted Optical Sensor Based on the Upconversion Nanoparticles Decorated with Zinc-Based Metal-Organic Framework for Selective and Rapid Detection of Octopamine. *Sens. Actuators, B* **2021**, *326*, 128838.
(285) Zhu, H.; Yao, H.; Xia, K.; Liu, J.; Yin, X.; Zhang, W.; Pan, J. Magnetic Nanoparticles Combining Teamed Boronate Affinity and Surface Imprinting for Efficient Selective Recognition of Glycoproteins under Physiological pH. *Chem. Eng. J.* **2018**, *346*, 317−328.
(286) Li, Y.; Ding, M. J.; Wang, S.; Wang, R. Y.; Wu, X. L.; Wen, T. T.; Yuan, L. H.; Dai, P.; Lin, Y. H.; Zhou, X. M. Preparation of Imprinted Polymers at Surface of Magnetic Nanoparticles for the Selective Extraction of Tadalafil from Medicines. *ACS Appl. Mater. Interfaces* **2011**, *3*, 3308−3315.
(287) Mao, Y.; Bao, Y.; Han, D.; Li, F.; Niu, L. Efficient One-Pot Synthesis of Molecularly Imprinted Silica Nanospheres Embedded Carbon Dots for Fluorescent Dopamine Optosensing. *Biosens. Bioelectron.* **2012**, *38*, 55−60.
(288) Stöber, W.; Fink, A.; Bohn, E. Controlled Growth of Monodisperse Silica Spheres in the Micron Size Range. *J. Colloid Interface Sci.* **1968**, *26*, 62−69.
(289) Edwardson, T. G. W.; Lau, K. L.; Bousmail, D.; Serpell, C. J.; Sleiman, H. F. Transfer of Molecular Recognition Information from DNA Nanostructures to Gold Nanoparticles. *Nat. Chem.* **2016**, *8*, 162−170.
(290) Sun, W.; Lu, Y.; Mao, J.; Chang, N.; Yang, J.; Liu, Y. Multidimensional Sensor for Pattern Recognition of Proteins Based on DNA-Gold Nanoparticles Conjugates. *Anal. Chem.* **2015**, *87*, 3354−3359.
(291) Yang, X.; Li, J.; Pei, H.; Li, D.; Zhao, Y.; Gao, J.; Lu, J.; Shi, J.; Fan, C.; Huang, Q. Pattern Recognition Analysis of Proteins Using DNA-Decorated Catalytic Gold Nanoparticles. *Small* **2013**, *9*, 2844−2849.
(292) Jiang, Y.; Zhao, H.; Lin, Y.; Zhu, N.; Ma, Y.; Mao, L. Colorimetric Detection of Glucose in Rat Brain Using Gold Nanoparticles. *Angew. Chem.* **2010**, *122*, 4910−4914.
(293) Imene, B.; Cui, Z.; Zhang, X.; Gan, B.; Yin, Y.; Tian, Y.; Deng, H.; Li, H. 4-Amino-3-Mercaptobenzoic Acid Functionalized Gold Nanoparticles: Synthesis, Selective Recognition and Colorimetric Detection of Cyhalothrin. *Sens. Actuators, B* **2014**, *199*, 161−167.
(294) Kim, C.; Agasti, S. S.; Zhu, Z.; Isaacs, L.; Rotello, V. M. Recognition-Mediated Activation of Therapeutic Gold Nanoparticles inside Living Cells. *Nat. Chem.* **2010**, *2*, 962−966.
(295) Song, G.; Xu, C.; Li, B. Visual Chiral Recognition of Mandelic Acid Enantiomers with L-Tartaric Acid-Capped Gold Nanoparticles as Colorimetric Probes. *Sens. Actuators, B* **2015**, *215*, 504−509.
(296) Wang, D.; Liu, B.; Ma, Y.; Wu, C.; Mou, Q.; Deng, H.; Wang, R.; Yan, D.; Zhang, C.; Zhu, X. A Molecular Recognition Approach To Synthesize Nucleoside Analogue Based Multifunctional Nanoparticles for Targeted Cancer Therapy. *J. Am. Chem. Soc.* **2017**, *139*, 14021−14024.
(297) Figueroa, S. M.; Fleischmann, D.; Beck, S.; Tauber, P.; Witzgall, R.; Schweda, F.; Goepferich, A. Nanoparticles Mimicking Viral Cell Recognition Strategies Are Superior Transporters into Mesangial Cells. *Adv. Sci.* **2020**, *7*, 1903204.
(298) Karawdeniya, B. I.; Damry, A. M.; Murugappan, K.; Manjunath, S.; Bandara, Y. M. N. D. Y.; Jackson, C. J.; Tricoli, A.; Neshev, D. Surface Functionalization and Texturing of Optical Metasurfaces for Sensing Applications. *Chem. Rev.* **2022**, DOI: 10.1021/acs.chemrev.1c00990.
(299) Chouirfa, H.; Bouloussa, H.; Migonney, V.; Falentin-Daudré, C. Review of Titanium Surface Modification Techniques and Coatings for Antibacterial Applications. *Acta Biomater.* **2019**, *83*, 37−54.
(300) Amani, H.; Arzaghi, H.; Bayandori, M.; Dezfuli, A. S.; Pazoki-Toroudi, H.; Shafiee, A.; Moradi, L. Controlling Cell Behavior through the Design of Biomaterial Surfaces: A Focus on Surface Modification Techniques. *Adv. Mater. Interfaces* **2019**, *6*, 1900572.
(301) Zoppe, J. O.; Ataman, N. C.; Mocny, P.; Wang, J.; Moraes, J.; Klok, H. A. Surface-Initiated Controlled Radical Polymerization: State-of-the-Art, Opportunities, and Challenges in Surface and Interface Engineering with Polymer Brushes. *Chem. Rev.* **2017**, *117*, 1105−1318.
(302) Queffélec, C.; Petit, M.; Janvier, P.; Knight, D. A.; Bujoli, B. Surface Modification Using Phosphonic Acids and Esters. *Chem. Rev.* **2012**, *112*, 3777−3807.
(303) Qiu, Z. Y.; Chen, C.; Wang, X. M.; Lee, I. S. Advances in the Surface Modification Techniques of Bone-Related Implants for Last 10 Years. *Regener. Biomater.* **2014**, *1*, 67−79.
(304) Decher, G. Fuzzy Nanoassemblies: Toward Layered Polymeric Multicomposites. *Science* **1997**, *277*, 1232−1237.
(305) Caruso, F.; Caruso, R. A.; Möhwald, H. Nanoengineering of Inorganic and Hybrid Hollow Spheres by Colloidal Templating. *Science* **1998**, *282*, 1111−1114.
(306) Zhao, S.; Caruso, F.; Dähne, L.; Decher, G.; De Geest, B. G.; Fan, J.; Feliu, N.; Gogotsi, Y.; Hammond, P. T.; Hersam, M. C.; et al. The Future of Layer-by-Layer Assembly: A Tribute to ACS Nano Associate Editor Helmuth Mohwald. *ACS Nano* **2019**, *13*, 6151−6169.
(307) Richardson, J. J.; Björnmalm, M.; Caruso, F. Multilayer Assembly. Technology-Driven Layer-by-Layer Assembly of Nanofilms. *Science* **2015**, *348*, aaa2491.
(308) Borges, J.; Mano, J. F. Molecular Interactions Driving the Layer-by-Layer Assembly of Multilayers. *Chem. Rev.* **2014**, *114*, 8883−8942.
(309) Matsusaki, M.; Ajiro, H.; Kida, T.; Serizawa, T.; Akashi, M. Layer-by-layer Assembly Through Weak Interactions and Their Biomedical Applications. *Adv. Mater.* **2012**, *24*, 454−474.
(310) Saurer, E. M.; Flessner, R. M.; Sullivan, S. P.; Prausnitz, M. R.; Lynn, D. M. Layer-by-Layer Assembly of DNA- and Protein-Containing Films on Microneedles for Drug Delivery to the Skin. *Biomacromolecules* **2010**, *11*, 3136−3143.
(311) Cheng, G.; Yin, C.; Tu, H.; Jiang, S.; Wang, Q.; Zhou, X.; Xing, X.; Xie, C.; Shi, X.; Du, Y.; et al. Controlled Co-delivery of Growth Factors through Layer-by-Layer Assembly of Core-Shell Nanofibers for Improving Bone Regeneration. *ACS Nano* **2019**, *13*, 6372−6382.
(312) Wilson, J. T.; Cui, W.; Chaikof, E. L. Layer-by-Layer Assembly of a Conformal Nanothin PEG Coating for Intraportal Islet Transplantation. *Nano Lett.* **2008**, *8*, 1940−1948.
(313) Zeng, G.; Xing, Y.; Gao, J.; Wang, Z.; Zhang, X. Unconventional Layer-by-Layer Assembly of Graphene Multilayer Films for Enzyme-Based Glucose and Maltose Biosensing. *Langmuir* **2010**, *26*, 15022−15026.
(314) Liu, Y.; Liu, Y.; Feng, H.; Wu, Y.; Joshi, L.; Zeng, X.; Li, J. Layer-by-Layer Assembly of Chemical Reduced Graphene and Carbon

https://doi.org/10.1021/acs.chemrev.2c00215
Chem. Rev. XXXX, XXX, XXX−XXX

Nanotubes for Sensitive Electrochemical Immunoassay. *Biosens. Bioelectron.* **2012**, *35*, 63−68.
(315) Tian, Y.; He, Q.; Cui, Y.; Li, J. Fabrication of Protein Nanotubes Based on Layer-by-Layer Assembly. *Biomacromolecules* **2006**, *7*, 2539−2542.
(316) Tang, Z.; Kotov, N. A.; Magonov, S.; Ozturk, B. Nanostructured Artificial Nacre. *Nat. Mater.* **2003**, *2*, 413−418.
(317) Podsiadlo, P.; Paternel, S.; Rouillard, J. M.; Zhang, Z.; Lee, J.; Lee, J. W.; Gulari, E.; Kotov, N. A. Layer-by-Layer Assembly of Nacre-like Nanostructured Composites with Antimicrobial Properties. *Langmuir* **2005**, *21*, 11915−11921.
(318) Finnemore, A.; Cunha, P.; Shean, T.; Vignolini, S.; Guldin, S.; Oyen, M.; Steiner, U. Biomimetic Layer-by-Layer Assembly of Artificial Nacre. *Nat. Commun.* **2012**, *3*, 966.
(319) Kang, K.; Lee, K. H.; Han, Y.; Gao, H.; Xie, S.; Muller, D. A.; Park, J. Layer-by-Layer Assembly of Two-Dimensional Materials into Wafer-Scale Heterostructures. *Nature* **2017**, *550*, 229−233.
(320) dos Santos, F. A.; Vieira, N. C. S.; Zambianco, N. A.; Janegitz, B. C.; Zucolotto, V. The Layer-by-Layer Assembly of Reduced Graphene Oxide Films and Their Application as Solution-Gated Field-Effect Transistors. *Appl. Surf. Sci.* **2021**, *543*, 148698.
(321) Li, H.; Pang, S.; Wu, S.; Feng, X.; Mullen, K.; Bubeck, C. Layer-by-Layer Assembly and UV Photoreduction of Graphene-Polyoxometalate Composite Films for Electronics. *J. Am. Chem. Soc.* **2011**, *133*, 9423−9429.
(322) Osada, N.; Bucur, C. B.; Aso, H.; Muldoon, J. The Design of Nanostructured Sulfur Cathodes Using Layer by Layer Assembly. *Energy Environ. Sci.* **2016**, *9*, 1668−1673.
(323) Li, P.; Jiang, Y.; Song, R. B.; Zhang, J. R.; Zhu, J. J. Layer-by-Layer Assembly of Au and CdS Nanoparticles on the Surface of Bacterial Cells for Photo-Assisted Bioanodes in Microbial Fuel Cells. *J. Mater. Chem. B* **2021**, *9*, 1638−1646.
(324) Wang, Z.; Ouyang, L.; Li, H.; Wågberg, L.; Hamedi, M. M. Layer-by-Layer Assembly of Strong Thin Films with High Lithium Ion Conductance for Batteries and Beyond. *Small* **2021**, *17*, 2100954.
(325) Carosio, F.; Fontaine, G.; Alongi, J.; Bourbigot, S. Starch-Based Layer by Layer Assembly: Efficient and Sustainable Approach to Cotton Fire Protection. *ACS Appl. Mater. Interfaces* **2015**, *7*, 12158−12167.
(326) Fang, Y.; Sun, W.; Li, J.; Liu, H.; Liu, X. Eco-Friendly Flame Retardant and Dripping-Resistant of Polyester/Cotton Blend Fabrics Through Layer-by-Layer Assembly Fully Bio-Based Chitosan/Phytic Acid Coating. *Int. J. Biol. Macromol.* **2021**, *175*, 140−146.
(327) Carosio, F.; Alongi, J.; Malucelli, G. α-Zirconium Phosphate-Based Nanoarchitectures on Polyester Fabrics Through Layer-by-Layer Assembly. *J. Mater. Chem.* **2011**, *21*, 10370−10376.
(328) Carosio, F.; Laufer, G.; Alongi, J.; Camino, G.; Grunlan, J. C. Layer-by-Layer Assembly of Silica-Based Flame Retardant Thin Film on PET Fabric. *Polym. Degrad. Stab.* **2011**, *96*, 745−750.
(329) Jang, W. S.; Rawson, I.; Grunlan, J. C. Layer-by-Layer Assembly of Thin Film Oxygen Barrier. *Thin Solid Films* **2008**, *516*, 4819−4825.
(330) Li, Y.; Tang, Z.; Wang, W.; Huang, X.; Lv, Y.; Qian, F.; Cheng, Y.; Wang, H. Improving Air Barrier, Water Vapor Permeability Properties of Cellulose Paper by Layer-by-Layer Assembly of Graphene Oxide. *Carbohydr. Polym.* **2021**, *253*, 117227.
(331) Xie, L.; Liu, F.; Liu, J.; Zeng, H. A Nanomechanical Study on Deciphering the Stickiness of SARS-CoV-2 on Inanimate Surfaces. *ACS Appl. Mater. Interfaces* **2020**, *12*, 58360−58368.
(332) Cerkez, I.; Kocer, H. B.; Worley, S. D.; Broughton, R. M.; Huang, T. S. N-halamine Biocidal Coatings via a Layer-by-Layer Assembly Technique. *Langmuir* **2011**, *27*, 4091−4097.
(333) Shchukin, D. G.; Zheludkevich, M.; Yasakau, K.; Lamaka, S.; Ferreira, M. G. S.; Möhwald, H. Layer-by-Layer Assembled Nanocontainers for Self-Healing Corrosion Protection. *Adv. Mater.* **2006**, *18*, 1672−1678.
(334) Li, S.; Wang, D.; Xiao, H.; Zhang, H.; Cao, S.; Chen, L.; Ni, Y.; Huang, L. Ultra-Low Pressure Cellulose-Based Nanofiltration Membrane Fabricated on Layer-by-Layer Assembly for Efficient Sodium Chloride Removal. *Carbohydr. Polym.* **2021**, *255*, 117352.
(335) Woo, Y. C.; Kim, Y.; Yao, M.; Tijing, L. D.; Choi, J. S.; Lee, S.; Kim, S. H.; Shon, H. K. Hierarchical Composite Membranes with Robust Omniphobic Surface Using Layer-By-Layer Assembly Technique. *Environ. Sci. Technol.* **2018**, *52*, 2186−2196.
(336) Hu, M.; Mi, B. Layer-by-Layer Assembly of Graphene Oxide Membranes via Electrostatic Interaction. *J. Membr. Sci.* **2014**, *469*, 80−87.
(337) Saren, Q.; Qiu, C. Q.; Tang, C. Y. Synthesis and Characterization of Novel Forward Osmosis Membranes Based on Layer-by-Layer Assembly. *Environ. Sci. Technol.* **2011**, *45*, 5201−5208.
(338) Du, N.; Zhang, H.; Chen, B.; Ma, X.; Liu, Z.; Wu, J.; Yang, D. Porous Indium Oxide Nanotubes: Layer-by-Layer Assembly on Carbon-Nanotube Templates and Application for Room-Temperature NH3 Gas Sensors. *Adv. Mater.* **2007**, *19*, 1641−1645.
(339) Yu, H.; Cao, T.; Zhou, L.; Gu, E.; Yu, D.; Jiang, D. Layer-by-Layer Assembly and Humidity Sensitive Behavior of Poly(ethyleneimine)/Multiwall Carbon Nanotube Composite Films. *Sens. Actuators, B* **2006**, *119*, 512−515.
(340) Zou, J.; Kim, F. Diffusion Driven Layer-by-Layer Assembly of Graphene Oxide Nanosheets into Porous Three-Dimensional Macrostructures. *Nat. Commun.* **2014**, *5*, 5254.
(341) Lee, H.; Lee, Y.; Statz, A. R.; Rho, J.; Park, T. G.; Messersmith, P. B. Substrate-Independent Layer-by-Layer Assembly by Using Mussel-Adhesive-Inspired Polymers. *Adv. Mater.* **2008**, *20*, 1619−1623.
(342) Shim, B. S.; Podsiadlo, P.; Lilly, D. G.; Agarwal, A.; Lee, J.; Tang, Z.; Ho, S.; Ingle, P.; Paterson, D.; Lu, W.; et al. Nanostructured Thin Films Made by Dewetting Method of Layer-By-Layer Assembly. *Nano Lett.* **2007**, *7*, 3266−3273.
(343) Zhao, N.; Shi, F.; Wang, Z.; Zhang, Xi. Combining Layer-by-Layer Assembly with Electrodeposition of Silver Aggregates for Fabricating Superhydrophobic Surfaces. *Langmuir* **2005**, *21*, 4713−4716.
(344) Lee, H.; Mensire, R.; Cohen, R. E.; Rubner, M. F. Strategies for Hydrogen Bonding Based Layer-by-Layer Assembly of Poly(vinyl alcohol) with Weak Polyacids. *Macromolecules* **2012**, *45*, 347−355.
(345) Zhang, X.; Xu, Y.; Zhang, X.; Wu, H.; Shen, J.; Chen, R.; Xiong, Y.; Li, J.; Guo, S. Progress on the Layer-by-Layer Assembly of Multilayered Polymer Composites: Strategy, Structural Control and Applications. *Prog. Polym. Sci.* **2019**, *89*, 76−107.
(346) Wang, F.; Ma, N.; Chen, Q.; Wang, W.; Wang, L. Halogen Bonding as a New Driving Force for Layer-by-Layer Assembly. *Langmuir* **2007**, *23*, 9540−9542.
(347) Li, L.; Xu, Z.; Sun, W.; Chen, J.; Dai, C.; Yan, B.; Zeng, H. Bio-Inspired Membrane with Adaptable Wettability for Smart Oil/Water Separation. *J. Membr. Sci.* **2020**, *598*, 117661.
(348) Orrego, S.; Chen, Z.; Krekora, U.; Hou, D.; Jeon, S. Y.; Pittman, M.; Montoya, C.; Chen, Y.; Kang, S. H. Bioinspired Materials with Self-Adaptable Mechanical Properties. *Adv. Mater.* **2020**, *32*, 1906970.
(349) Wei, Z.; Thanneeru, S.; Margaret Rodriguez, E.; Weng, G.; He, J. Adaptable Eu-Containing Polymeric Films with Dynamic Control of Mechanical Properties in Response to Moisture. *Soft Matter* **2020**, *16*, 2276−2284.
(350) Zhang, X.; Liu, C.; Yang, J.; Huang, X. J.; Xu, Z. K. Wettability Switchable Membranes for Separating Both Oil-in-Water and Water-in-Oil Emulsions. *J. Membr. Sci.* **2021**, *624*, 118976.
(351) Cölfen, H. Biomineralization: A Crystal-Clear View. *Nat. Mater.* **2010**, *9*, 960−961.
(352) Zhou, X.; Wang, L.; Wei, Z.; Weng, G.; He, J. An Adaptable Tough Elastomer with Moisture-Triggered Switchable Mechanical and Fluorescent Properties. *Adv. Funct. Mater.* **2019**, *29*, 1903543.
(353) Han, L.; Gong, L.; Chen, J.; Zhang, J.; Xiang, L.; Zhang, L.; Wang, Q.; Yan, B.; Zeng, H. Universal Mussel-Inspired Ultrastable Surface-Anchoring Strategy via Adaptive Synergy of Catechol and Cations. *ACS Appl. Mater. Interfaces* **2018**, *10*, 2166−2173.
(354) Netzer, L.; Sagiv, J. A New Approach to Construction of Artificial Monolayer Assemblies. *J. Am. Chem. Soc.* **1983**, *105*, 674−676.

https://doi.org/10.1021/acs.chemrev.2c00215
Chem. Rev. XXXX, XXX, XXX−XXX

(355) Lee, H.; Dellatore, S. M.; Miller, W. M.; Messersmith, P. B. Mussel-Inspired Surface Chemistry for Multifunctional Coatings. *Science* **2007**, *318*, 426−430.
(356) Lee, H. A.; Park, E.; Lee, H. Polydopamine and Its Derivative Surface Chemistry in Material Science: A Focused Review for Studies at KAIST. *Adv. Mater.* **2020**, *32*, 1907505.
(357) Hong, S.; Na, Y. S.; Choi, S.; Song, I. T.; Kim, W. Y.; Lee, H. Non-Covalent Self-Assembly and Covalent Polymerization Co-Contribute to Polydopamine Formation. *Adv. Funct. Mater.* **2012**, *22*, 4711−4717.
(358) Guo, Q.; Chen, J.; Wang, J.; Zeng, H.; Yu, J. Recent Progress in Synthesis and Application of Mussel-Inspired Adhesives. *Nanoscale* **2020**, *12*, 1307−1324.
(359) Lee, H.; Rho, J.; Messersmith, P. B. Facile Conjugation of Biomolecules onto Surfaces via Mussel Adhesive Protein Inspired Coatings. *Adv. Mater.* **2009**, *21*, 431−434.
(360) Zhang, J.; Zhang, L.; Cui, X.; Gong, L.; Xiang, L.; Shi, C.; Hu, W.; Zeng, H. Scalable Polyzwitterion-Polydopamine Coating for Regenerable Oil/Water Separation and Underwater Self-Cleaning of Stubborn Heavy Oil Fouling without Pre-Hydration. *Chem. Commun.* **2018**, *54*, 9734−9737.
(361) Luo, C.; Liu, W.; Luo, B.; Tian, J.; Wen, W.; Liu, M.; Zhou, C. Antibacterial Activity and Cytocompatibility of Chitooligosaccharide-Modified Polyurethane Membrane via Polydopamine Adhesive Layer. *Carbohydr. Polym.* **2017**, *156*, 235−243.
(362) Yang, K.; Lee, J. S.; Kim, J.; Lee, Y. B.; Shin, H.; Um, S. H.; Kim, J. B.; Park, K. I.; Lee, H.; Cho, S. W. Polydopamine-Mediated Surface Modification of Scaffold Materials for Human Neural Stem Cell Engineering. *Biomater.* **2012**, *33*, 6952−6964.
(363) Ryu, J.; Ku, S. H.; Lee, H.; Park, C. B. Mussel-Inspired Polydopamine Coating as a Universal Route to Hydroxyapatite Crystallization. *Adv. Funct. Mater.* **2010**, *20*, 2132−2139.
(364) Kang, S. M.; Hwang, N. S.; Yeom, J.; Park, S. Y.; Messersmith, P. B.; Choi, I. S.; Langer, R.; Anderson, D. G.; Lee, H. One-Step Multipurpose Surface Functionalization by Adhesive Catecholamine. *Adv. Funct. Mater.* **2012**, *22*, 2949−2955.
(365) Han, L.; Xiang, L.; Zhang, J.; Chen, J.; Liu, J.; Yan, B.; Zeng, H. Biomimetic Lubrication and Surface Interactions of Dopamine-Assisted Zwitterionic Polyelectrolyte Coatings. *Langmuir* **2018**, *34*, 11593−11601.
(366) Lee, H. A.; Ma, Y.; Zhou, F.; Hong, S.; Lee, H. Material-Independent Surface Chemistry beyond Polydopamine Coating. *Acc. Chem. Res.* **2019**, *52*, 704−713.
(367) Shin, M.; Park, E.; Lee, H. Plant-Inspired Pyrogallol-Containing Functional Materials. *Adv. Funct. Mater.* **2019**, *29*, 1903022.
(368) Kang, S. M.; Rho, J.; Choi, I. S.; Messersmith, P. B.; Lee, H. Norepinephrine: Material-Independent, Multifunctional Surface Modification Reagent. *J. Am. Chem. Soc.* **2009**, *131*, 13224−13225.
(369) Li, L.; Yan, B.; Zhang, L.; Tian, Y.; Zeng, H. Mussel-Inspired Antifouling Coatings Bearing Polymer Loops. *Chem. Commun.* **2015**, *51*, 15780−15783.
(370) Lee, Y.; Lee, H.; Kim, Y. B.; Kim, J.; Hyeon, T.; Park, H.; Messersmith, P. B.; Park, T. G. Bioinspired Surface Immobilization of Hyaluronic Acid on Monodisperse Magnetite Nanocrystals for Targeted Cancer Imaging. *Adv. Mater.* **2008**, *20*, 4154−4157.
(371) Yang, W.; Pan, M.; Zhang, J.; Zhang, L.; Lin, F.; Liu, X.; Huang, C.; Chen, X. Z.; Wang, J.; Yan, B.; et al. A Universal Strategy for Constructing Robust and Antifouling Cellulose Nanocrystal Coating. *Adv. Funct. Mater.* **2022**, *32*, 2109989.
(372) Koga, S.; Williams, D. S.; Perriman, A. W.; Mann, S. Peptide-Nucleotide Microdroplets as a Step Towards a Membrane-Free Protocell Model. *Nat. Chem.* **2011**, *3*, 720−724.
(373) Okihana, H.; Ponnamperuma, C. A Protective Function of the Coacervates against UV Light on the Primitive Earth. *Nature* **1982**, *299*, 347−349.
(374) Tan, Y.; Hoon, S.; Guerette, P. A.; Wei, W.; Ghadban, A.; Hao, C.; Miserez, A.; Waite, J. H. Infiltration of Chitin by Protein Coacervates Defines the Squid Beak Mechanical Gradient. *Nat. Chem. Biol.* **2015**, *11*, 488−495.
(375) Sun, Y.; Lim, Z. W.; Guo, Q.; Yu, J.; Miserez, A. Liquid-Liquid Phase Separation of Proteins and Peptides Derived from Biological Materials: Discovery, Protein Engineering, and Emerging Applications. *MRS Bull.* **2020**, *45*, 1039−1047.
(376) Stewart, R. J.; Wang, C. S.; Song, I. T.; Jones, J. P. The Role of Coacervation and Phase Transitions in the Sandcastle Worm Adhesive System. *Adv. Colloid Interface Sci.* **2017**, *239*, 88−96.
(377) Shin, Y.; Brangwynne, C. P. Liquid Phase Condensation in Cell Physiology and Disease. *Science* **2017**, *357*, No. eaaf4382.
(378) Yeo, G. C.; Keeley, F. W.; Weiss, A. S. Coacervation of Tropoelastin. *Adv. Colloid Interface Sci.* **2011**, *167*, 94−103.
(379) Basu, S.; Bhattacharya, G. Some Aspects of the Phenomenon of Coacervation. *Science* **1952**, *115*, 544−545.
(380) Elbaum-Garfinkle, S.; Kim, Y.; Szczepaniak, K.; Chen, C. C.; Eckmann, C. R.; Myong, S.; Brangwynne, C. P. The Disordered P Granule Protein LAF-1 Drives Phase Separation into Droplets with Tunable Viscosity and Dynamics. *Proc. Natl. Acad. Sci. U.S.A.* **2015**, *112*, 7189−7194.
(381) Schuster, B. S.; Reed, E. H.; Parthasarathy, R.; Jahnke, C. N.; Caldwell, R. M.; Bermudez, J. G.; Ramage, H.; Good, M. C.; Hammer, D. A. Controllable Protein Phase Separation and Modular Recruitment to Form Responsive Membraneless Organelles. *Nat. Commun.* **2018**, *9*, 2985.
(382) Drobot, B.; Iglesias-Artola, J. M.; Le Vay, K.; Mayr, V.; Kar, M.; Kreysing, M.; Mutschler, H.; Tang, T. D. Compartmentalised RNA Catalysis in Membrane-Free Coacervate Protocells. *Nat. Commun.* **2018**, *9*, 3643.
(383) Gobbo, P.; Tian, L.; Pavan Kumar, B.; Turvey, S.; Cattelan, M.; Patil, A. J.; Carraro, M.; Bonchio, M.; Mann, S. Catalytic Processing in Ruthenium-Based Polyoxometalate Coacervate Protocells. *Nat. Commun.* **2020**, *11*, 41.
(384) Muiznieks, L. D.; Cirulis, J. T.; van der Horst, A.; Reinhardt, D. P.; Wuite, G. J.; Pomès, R.; Keeley, F. W. Modulated Growth, Stability and Interactions of Liquid-Like Coacervate Assemblies of Elastin. *Matrix Biol.* **2014**, *36*, 39−50.
(385) Tatsubo, D.; Suyama, K.; Miyazaki, M.; Maeda, I.; Nose, T. Stepwise Mechanism of Temperature-Dependent Coacervation of the Elastin-like Peptide Analogue Dimer, $(C(WPGVG)_3)_2$. *Biochem.* **2018**, *57*, 1582−1590.
(386) Annabi, N.; Zhang, Y.-N.; Assmann, A.; Sani, E. S.; Cheng, G.; Lassaletta, A. D.; Vegh, A.; Dehghani, B.; Ruiz-Esparza, G. U.; Wang, X.; Gangadharan, S.; Weiss, A. S.; Khademhosseini, A. Engineering a Highly Elastic Human Protein-Based Sealant for Surgical Applications. *Sci. Transl. Med.* **2017**, *9*, No. eaai7466.
(387) Gourgas, O.; Muiznieks, L. D.; Bello, D. G.; Nanci, A.; Sharpe, S.; Cerruti, M. Cross-Linked Elastin-like Polypeptide Membranes as a Model for Medial Arterial Calcification. *Biomacromolecules* **2019**, *20*, 2625−2636.
(388) Navon, Y.; Zhou, M.; Matson, J. B.; Bitton, R. Dendritic Elastin-like Peptides: The Effect of Branching on Thermoresponsiveness. *Biomacromolecules* **2016**, *17*, 262−270.
(389) McDaniel, J. R.; Callahan, D. J.; Chilkoti, A. Drug Delivery to Solid Tumors by Elastin-Like Polypeptides. *Adv. Drug Delivery Rev.* **2010**, *62*, 1456−1467.
(390) Miserez, A.; Schneberk, T.; Sun, C.; Zok, F. W.; Waite, J. H. The Transition from Stiff to Compliant Materials in Squid Beaks. *Science* **2008**, *319*, 1816−1819.
(391) Gabryelczyk, B.; Cai, H.; Shi, X.; Sun, Y.; Swinkels, P. J. M.; Salentinig, S.; Pervushin, K.; Miserez, A. Hydrogen Bond Guidance and Aromatic Stacking Drive Liquid-Liquid Phase Separation of Intrinsically Disordered Histidine-Rich Peptides. *Nat. Commun.* **2019**, *10*, 5465.
(392) Lee, B. P.; Messersmith, P. B.; Israelachvili, J. N.; Waite, J. H. Mussel-Inspired Adhesives and Coatings. *Annu. Rev. Mater. Res.* **2011**, *41*, 99−132.
(393) Stewart, R. J.; Wang, C. S.; Shao, H. Complex Coacervates as a Foundation for Synthetic Underwater Adhesives. *Adv. Colloid Interface Sci.* **2011**, *167*, 85−93.

https://doi.org/10.1021/acs.chemrev.2c00215
Chem. Rev. XXXX, XXX, XXX−XXX

(394) Zhao, H.; Sun, C.; Stewart, R. J.; Waite, J. H. Cement Proteins of the Tube-Building Polychaete Phragmatopoma Californica. *J. Biol. Chem.* **2005**, *280*, 42938−42944.
(395) Shao, H.; Stewart, R. J. Biomimetic Underwater Adhesives with Environmentally Triggered Setting Mechanisms. *Adv. Mater.* **2010**, *22*, 729−733.
(396) Kaur, S.; Weerasekare, G. M.; Stewart, R. J. Multiphase Adhesive Coacervates Inspired by the Sandcastle Worm. *ACS Appl. Mater. Interfaces* **2011**, *3*, 941−944.
(397) Wei, W.; Tan, Y.; Martinez Rodriguez, N. R.; Yu, J.; Israelachvili, J. N.; Waite, J. H. A Mussel-Derived One Component Adhesive Coacervate. *Acta Biomater.* **2014**, *10*, 1663−1670.
(398) Ahn, B. K.; Das, S.; Linstadt, R.; Kaufman, Y.; Martinez-Rodriguez, N. R.; Mirshafian, R.; Kesselman, E.; Talmon, Y.; Lipshutz, B. H.; Israelachvili, J. N.; et al. High-Performance Mussel-Inspired Adhesives of Reduced Complexity. *Nat. Commun.* **2015**, *6*, 8663.
(399) Kim, S.; Huang, J.; Lee, Y.; Dutta, S.; Yoo, H. Y.; Jung, Y. M.; Jho, Y.; Zeng, H.; Hwang, D. S. Complexation and Coacervation of Like-Charged Polyelectrolytes Inspired by Mussels. *Proc. Natl. Acad. Sci. U.S.A.* **2016**, *113*, E847−E853.
(400) Kim, S.; Yoo, H. Y.; Huang, J.; Lee, Y.; Park, S.; Park, Y.; Jin, S.; Jung, Y. M.; Zeng, H.; Hwang, D. S.; et al. Salt Triggers the Simple Coacervation of an Underwater Adhesive When Cations Meet Aromatic π Electrons in Seawater. *ACS Nano* **2017**, *11*, 6764−6772.
(401) Zhao, Q.; Lee, D. W.; Ahn, B. K.; Seo, S.; Kaufman, Y.; Israelachvili, J. N.; Waite, J. H. Underwater Contact Adhesion and Microarchitecture in Polyelectrolyte Complexes Actuated by Solvent Exchange. *Nat. Mater.* **2016**, *15*, 407−412.
(402) Wei, C.; Zhu, X.; Peng, H.; Chen, J.; Zhang, F.; Zhao, Q. Facile Preparation of Lignin-Based Underwater Adhesives with Improved Performances. *ACS Sustainable Chem. Eng.* **2019**, *7*, 4508−4514.
(403) Kim, K.; Shin, M.; Koh, M. Y.; Ryu, J. H.; Lee, M. S.; Hong, S.; Lee, H. Tape: A Medical Adhesive Inspired by a Ubiquitous Compound in Plants. *Adv. Funct. Mater.* **2015**, *25*, 2402−2410.
(404) Peng, Q.; Wu, Q.; Chen, J.; Wang, T.; Wu, M.; Yang, D.; Peng, X.; Liu, J.; Zhang, H.; Zeng, H. Coacervate-Based Instant and Repeatable Underwater Adhesive with Anticancer and Antibacterial Properties. *ACS Appl. Mater. Interfaces* **2021**, *13*, 48239−48251.
(405) Xu, J.; Li, X.; Li, J.; Li, X.; Li, B.; Wang, Y.; Wu, L.; Li, W. Wet and Functional Adhesives from One-Step Aqueous Self-Assembly of Natural Amino Acids and Polyoxometalates. *Angew. Chem., Int. Ed.* **2017**, *56*, 8731−8735.
(406) Peng, Q.; Chen, J.; Zeng, Z.; Wang, T.; Xiang, L.; Peng, X.; Liu, J.; Zeng, H. Adhesive Coacervates Driven by Hydrogen-Bonding Interaction. *Small* **2020**, *16*, 2004132.
(407) Peng, Q.; Chen, J.; Wang, T.; Gong, L.; Peng, X.; Wu, M.; Ma, Y.; Wu, F.; Yang, D.; Zhang, H.; et al. Coacervation-Driven Instant Paintable Underwater Adhesives with Tunable Optical and Electrochromic Properties. *J. Mater. Chem. A* **2021**, *9*, 12988−13000.
(408) Lee, D.; Hwang, H.; Kim, J. S.; Park, J.; Youn, D.; Kim, D.; Hahn, J.; Seo, M.; Lee, H. VATA: A Poly(vinyl alcohol)- and Tannic Acid-Based Nontoxic Underwater Adhesive. *ACS Appl. Mater. Interfaces* **2020**, *12*, 20933−20941.
(409) Chen, J.; Peng, Q.; Thundat, T.; Zeng, H. Stretchable, Injectable, and Self-Healing Conductive Hydrogel Enabled by Multiple Hydrogen Bonding Toward Wearable Electronics. *Chem. Mater.* **2019**, *31*, 4553−4563.
(410) Sun, J. Y.; Zhao, X.; Illeperuma, W. R.; Chaudhuri, O.; Oh, K. H.; Mooney, D. J.; Vlassak, J. J.; Suo, Z. Highly Stretchable and Tough Hydrogels. *Nature* **2012**, *489*, 133−136.
(411) Yang, Y.; Urban, M. W. Self-Healing Polymeric Materials. *Chem. Soc. Rev.* **2013**, *42*, 7446−7467.
(412) Zheng, N.; Xu, Y.; Zhao, Q.; Xie, T. Dynamic Covalent Polymer Networks: A Molecular Platform for Designing Functions Beyond Chemical Recycling and Self-healing. *Chem. Rev.* **2021**, *121*, 1716−1745.
(413) Wu, M.; Chen, J.; Huang, W.; Yan, B.; Peng, Q.; Liu, J.; Chen, L.; Zeng, H. Injectable and Self-Healing Nanocomposite Hydrogels with Ultrasensitive pH-Responsiveness and Tunable Mechanical Properties: Implications for Controlled Drug Delivery. *Biomacromolecules* **2020**, *21*, 2409−2420.
(414) Xia, D.; Wang, P.; Ji, X.; Khashab, N. M.; Sessler, J. L.; Huang, F. Functional Supramolecular Polymeric Betworks: The Marriage of Covalent Polymers and Macrocycle-Based Host-Guest Interactions. *Chem. Rev.* **2020**, *120*, 6070−6123.
(415) Yang, L.; Tan, X.; Wang, Z.; Zhang, X. Supramolecular Polymers: Historical Development, Preparation, Characterization, and Functions. *Chem. Rev.* **2015**, *115*, 7196−7239.
(416) Brunsveld, L.; Folmer, B. J. B.; Meijer, E. W.; Sijbesma, R. P. Supramolecular Polymers. *Chem. Rev.* **2001**, *101*, 4071−4097.
(417) Zhao, J.; Gong, J.; Wang, G.; Zhu, K.; Ye, K.; Yan, J.; Cao, D. A Self-Healing Hydrogel Electrolyte for Flexible Solid-State Supercapacitors. *Chem. Eng. J.* **2020**, *401*, 125456.
(418) Huang, S.; Wan, F.; Bi, S.; Zhu, J.; Niu, Z.; Chen, J. A Self-Healing Integrated All-in-One Zinc-Ion Battery. *Angew. Chem., Int. Ed.* **2019**, *58*, 4313−4317.
(419) Wang, J.; Liu, F.; Tao, F.; Pan, Q. Rationally Designed Self-Healing Hydrogel Electrolyte toward a Smart and Sustainable Supercapacitor. *ACS Appl. Mater. Interfaces* **2017**, *9*, 27745−27753.
(420) Wei, P.; Chen, T.; Chen, G.; Liu, H.; Mugaanire, I. T.; Hou, K.; Zhu, M. Conductive Self-Healing Nanocomposite Hydrogel Skin Sensors with Antifreezing and Thermoresponsive Properties. *ACS Appl. Mater. Interfaces* **2020**, *12*, 3068−3079.
(421) Ahn, B. K.; Lee, D. W.; Israelachvili, J. N.; Waite, J. H. Surface-Initiated Self-Healing of Polymers in Aqueous Media. *Nat. Mater.* **2014**, *13*, 867−872.
(422) Getachew, B. A.; Kim, S. R.; Kim, J. H. Self-healing hydrogel pore-filled water filtration membranes. *Environ. Sci. Technol.* **2017**, *51*, 905−913.
(423) Wang, W.; Narain, R.; Zeng, H. Rational Design of Self-Healing Tough Hydrogels: A Mini Review. *Front. Chem.* **2018**, *6*, 497.
(424) Gong, Z.; Zhang, G.; Zeng, X.; Li, J.; Li, G.; Huang, W.; Sun, R.; Wong, C. High-Strength, Tough, Fatigue Resistant, and Self-Healing Hydrogel Based on Dual Physically Cross-Linked Network. *ACS Appl. Mater. Interfaces* **2016**, *8*, 24030−24037.
(425) Liu, J.; Song, G.; He, C.; Wang, H. Self-Healing in Tough Graphene Oxide Composite Hydrogels. *Macromol. Rapid Commun.* **2013**, *34*, 1002−1007.
(426) Phadke, A.; Zhang, C.; Arman, B.; Hsu, C. C.; Mashelkar, R. A.; Lele, A. K.; Tauber, M. J.; Arya, G.; Varghese, S. Rapid Self-Healing Hydrogels. *Proc. Natl. Acad. Sci. U.S.A.* **2012**, *109*, 4383−4388.
(427) Jiang, H.; Duan, L.; Ren, X.; Gao, G. Hydrophobic Association Hydrogels with Excellent Mechanical and Self-Healing Properties. *Eur. Polym. J.* **2019**, *112*, 660−669.
(428) Tuncaboylu, D. C.; Sari, M.; Oppermann, W.; Okay, O. Tough and Self-Healing Hydrogels Formed via Hydrophobic Interactions. *Macromolecules* **2011**, *44*, 4997−5005.
(429) Tuncaboylu, D. C.; Argun, A.; Sahin, M.; Sari, M.; Okay, O. Structure Optimization of Self-Healing Hydrogels Formed via Hydrophobic Interactions. *Polymer* **2012**, *53*, 5513−5522.
(430) Yang, W.; Shao, B.; Liu, T.; Zhang, Y.; Huang, R.; Chen, F.; Fu, Q. Robust and mechanically and electrically self-healing hydrogel for efficient electromagnetic interference shielding. *ACS Appl. Mater. Interfaces* **2018**, *10*, 8245−8257.
(431) Owusu-Nkwantabisah, S.; Gillmor, J. R.; Switalski, S. C.; Slater, G. L. An Autonomous Self-Healing Hydrogel Based on Surfactant-Free Hydrophobic Association. *J. Appl. Polym. Sci.* **2017**, *134*, 44800.
(432) Owusu-Nkwantabisah, S.; Gillmor, J.; Switalski, S.; Mis, M. R.; Bennett, G.; Moody, R.; Antalek, B.; Gutierrez, R.; Slater, G. Synergistic Thermoresponsive Optical Properties of a Composite Self-Healing Hydrogel. *Macromolecules* **2017**, *50*, 3671−3679.
(433) Loebel, C.; Rodell, C. B.; Chen, M. H.; Burdick, J. A. Shear-Thinning and Self-Healing Hydrogels as Injectable Therapeutics and for 3D-Printing. *Nat. Protoc.* **2017**, *12*, 1521−1541.
(434) Highley, C. B.; Rodell, C. B.; Burdick, J. A. Direct 3D Printing of Shear-Thinning Hydrogels into Self-Healing Hydrogels. *Adv. Mater.* **2015**, *27*, 5075−5079.

https://doi.org/10.1021/acs.chemrev.2c00215
Chem. Rev. XXXX, XXX, XXX−XXX

(435) Jalalvandi, E.; Shavandi, A. Shear Thinning/Self-Healing Hydrogel Based on Natural Polymers with Secondary Photocrosslinking for Biomedical Applications. *J. Mech. Behav. Biomed. Mater.* **2019**, *90*, 191−201.
(436) Jia, Y.; Zhu, X. X. Self-Healing Supramolecular Hydrogel Made of Polymers Bearing Cholic Acid and β-Cyclodextrin Pendants. *Chem. Mater.* **2015**, *27*, 387−393.
(437) Chen, H.; Ma, X.; Wu, S.; Tian, H. A Rapidly Self-Healing Supramolecular Polymer Hydrogel with Photostimulated Room-Temperature Phosphorescence Responsiveness. *Angew. Chem., Int. Ed.* **2014**, *53*, 14149−14152.
(438) Kakuta, T.; Takashima, Y.; Nakahata, M.; Otsubo, M.; Yamaguchi, H.; Harada, A. Preorganized Hydrogel: Self-Healing Properties of Supramolecular Hydrogels Formed by Polymerization of Host-Guest-Monomers that Contain Cyclodextrins and Hydrophobic Guest Groups. *Adv. Mater.* **2013**, *25*, 2849−2853.
(439) Yang, Q.; Wang, P.; Zhao, C.; Wang, W.; Yang, J.; Liu, Q. Light-Switchable Self-Healing Hydrogel Based on Host-Guest Macro-Crosslinking. *Macromol. Rapid Commun.* **2017**, *38*, 1600741.
(440) Wang, Z.; Ren, Y.; Zhu, Y.; Hao, L.; Chen, Y.; An, G.; Wu, H.; Shi, X.; Mao, C. A Rapidly Self-Healing Host-Guest Supramolecular Hydrogel with High Mechanical Strength and Excellent Biocompatibility. *Angew. Chem., Int. Ed.* **2018**, *57*, 9008−9012.
(441) Miyamae, K.; Nakahata, M.; Takashima, Y.; Harada, A. Self-Healing, Expansion-Contraction, and Shape-Memory Properties of a Preorganized Supramolecular Hydrogel through Host-Guest Interactions. *Angew. Chem., Int. Ed.* **2015**, *54*, 8984−8987.
(442) Appel, E. A.; Loh, X. J.; Jones, S. T.; Biedermann, F.; Dreiss, C. A.; Scherman, O. A. Ultrahigh-Water-Content Supramolecular Hydrogels Exhibiting Multistimuli Responsiveness. *J. Am. Chem. Soc.* **2012**, *134*, 11767−11773.
(443) McKee, J. R.; Appel, E. A.; Seitsonen, J.; Kontturi, E.; Scherman, O. A.; Ikkala, O. Healable, Stable and Stiff Hydrogels: Combining Conflicting Properties Using Dynamic and Selective Three-Component Recognition with Reinforcing Cellulose Nanorods. *Adv. Funct. Mater.* **2014**, *24*, 2706−2713.
(444) Liu, J.; Tan, C. S. Y.; Yu, Z.; Li, N.; Abell, C.; Scherman, O. A. Tough Supramolecular Polymer Networks with Extreme Stretchability and Fast Room-Temperature Self-Healing. *Adv. Mater.* **2017**, *29*, 1605325.
(445) Zeng, H.; Hwang, D. S.; Israelachvili, J. N.; Waite, J. H. Strong Reversible Fe^{3+}-Mediated Bridging between Dopa-Containing Protein Films in Water. *Proc. Natl. Acad. Sci. U.S.A.* **2010**, *107*, 12850−12853.
(446) Holten-Andersen, N.; Harrington, M. J.; Birkedal, H.; Lee, B. P.; Messersmith, P. B.; Lee, K. Y.; Waite, J. H. pH-Induced Metal-Ligand Cross-Links Inspired by Mussel Yield Self-Healing Polymer Networks with Near-Covalent Elastic Moduli. *Proc. Natl. Acad. Sci. U.S.A.* **2011**, *108*, 2651−2655.
(447) Krogsgaard, M.; Behrens, M. A.; Pedersen, J. S.; Birkedal, H. Self-Healing Mussel-Inspired Multi-pH-Responsive Hydrogels. *Biomacromolecules* **2013**, *14*, 297−301.
(448) Azevedo, S.; Costa, A. M. S.; Andersen, A.; Choi, I. S.; Birkedal, H.; Mano, J. F. Bioinspired Ultratough Hydrogel with Fast Recovery, Self-Healing, Injectability and Cytocompatibility. *Adv. Mater.* **2017**, *29*, 1700759.
(449) Jing, X.; Mi, H.-Y.; Peng, X.-F.; Turng, L.-S. Biocompatible, Self-Healing, Highly Stretchable Polyacrylic Acid/Reduced Graphene Oxide Nanocomposite Hydrogel Sensors via Mussel-Inspired Chemistry. *Carbon* **2018**, *136*, 63−72.
(450) Wei, Z.; He, J.; Liang, T.; Oh, H.; Athas, J.; Tong, Z.; Wang, C.; Nie, Z. Autonomous Self-Healing of Poly(acrylic acid) Hydrogels Induced by the Migration of Ferric Ions. *Polym. Chem.* **2013**, *4*, 4601−4605.
(451) Darabi, M. A.; Khosrozadeh, A.; Mbeleck, R.; Liu, Y.; Chang, Q.; Jiang, J.; Cai, J.; Wang, Q.; Luo, G.; Xing, M. Skin-Inspired Multifunctional Autonomic-Intrinsic Conductive Self-Healing Hydrogels with Pressure Sensitivity, Stretchability, and 3D Printability. *Adv. Mater.* **2017**, *29*, 1700533.
(452) Chen, Y. M.; Sun, L.; Yang, S. A.; Shi, L.; Zheng, W. J.; Wei, Z.; Hu, C. Self-Healing and Photoluminescent Carboxymethyl Cellulose-Based Hydrogels. *Eur. Polym. J.* **2017**, *94*, 501−510.
(453) Qin, H.; Zhang, T.; Li, N.; Cong, H. P.; Yu, S. H. Anisotropic and Self-Healing Hydrogels with Multi-Responsive Actuating Capability. *Nat. Commun.* **2019**, *10*, 2202.
(454) Mao, X.; Cheng, R.; Zhang, H.; Bae, J.; Cheng, L.; Zhang, L.; Deng, L.; Cui, W.; Zhang, Y.; Santos, H. A.; et al. Self-Healing and Injectable Hydrogel for Matching Skin Flap Regeneration. *Adv. Sci.* **2019**, *6*, 1801555.
(455) Chen, H.; Cheng, R.; Zhao, X.; Zhang, Y.; Tam, A.; Yan, Y.; Shen, H.; Zhang, Y. S.; Qi, J.; Feng, Y.; Liu, L.; Pan, G.; Cui, W.; Deng, L. An Injectable Self-Healing Coordinative Hydrogel with Antibacterial and Angiogenic Properties for Diabetic Skin Wound Repair. *NPG Asia Mater.* **2019**, *11*, 3.
(456) Qin, H.; Zhang, T.; Li, H. N.; Cong, H. P.; Antonietti, M.; Yu, S. H. Dynamic Au-Thiolate Interaction Induced Rapid Self-Healing Nanocomposite Hydrogels with Remarkable Mechanical Behaviors. *Chem.* **2017**, *3*, 691−705.
(457) Shi, L.; Wang, F.; Zhu, W.; Xu, Z.; Fuchs, S.; Hilborn, J.; Zhu, L.; Ma, Q.; Wang, Y.; Weng, X.; et al. Self-Healing Silk Fibroin-Based Hydrogel for Bone Regeneration: Dynamic Metal-Ligand Self-Assembly Approach. *Adv. Funct. Mater.* **2017**, *27*, 1700591.
(458) Han, J.; Xie, C.; Huang, Y. S.; Wagner, M.; Liu, W.; Zeng, X.; Liu, J.; Sun, S.; Koynov, K.; Butt, H. J.; et al. Ru-Se Coordination: A New Dynamic Bond for Visible-Light-Responsive Materials. *J. Am. Chem. Soc.* **2021**, *143* (32), 12736−12744.
(459) Luo, F.; Sun, T. L.; Nakajima, T.; Kurokawa, T.; Zhao, Y.; Sato, K.; Ihsan, A. B.; Li, X.; Guo, H.; Gong, J. P. Oppositely Charged Polyelectrolytes form Tough, Self-Healing, and Rebuildable Hydrogels. *Adv. Mater.* **2015**, *27*, 2722−2727.
(460) Keplinger, C.; Sun, J. Y.; Foo, C. C.; Rothemund, P.; Whitesides, G. M.; Suo, Z. Stretchable, Transparent, Ionic Conductors. *Science* **2013**, *341*, 984−987.
(461) Ihsan, A. B.; Sun, T. L.; Kurokawa, T.; Karobi, S. N.; Nakajima, T.; Nonoyama, T.; Roy, C. K.; Luo, F.; Gong, J. P. Self-Healing Behaviors of Tough Polyampholyte Hydrogels. *Macromolecules* **2016**, *49*, 4245−4252.
(462) Fan, H.; Wang, J.; Tao, Z.; Huang, J.; Rao, P.; Kurokawa, T.; Gong, J. P. Adjacent Cationic-Aromatic Sequences Yield Strong Electrostatic Adhesion of Hydrogels in Seawater. *Nat. Commun.* **2019**, *10*, 5127.
(463) Fan, H.; Wang, J.; Gong, J. P. Barnacle Cement Proteins-Inspired Tough Hydrogels with Robust, Long-Lasting, and Repeatable Underwater Adhesion. *Adv. Funct. Mater.* **2021**, *31*, 2009334.
(464) Roy, S.; Baral, A.; Banerjee, A. An Amino-Acid-Based Self-Healing Hydrogel: Modulation of the Self-Healing Properties by Incorporating Carbon-Based Nanomaterials. *Chem. Eur. J.* **2013**, *19*, 14950−14957.
(465) Sun, J. Y.; Keplinger, C.; Whitesides, G. M.; Suo, Z. Ionic Skin. *Adv. Mater.* **2014**, *26*, 7608−7614.
(466) Cheng, S.; Narang, Y. S.; Yang, C.; Suo, Z.; Howe, R. D. Stick-On Large-Strain Sensors for Soft Robots. *Adv. Mater. Interfaces* **2019**, *6*, 1900985.
(467) Li, S.; Zhou, X.; Dong, Y.; Li, J. Flexible Self-Repairing Materials for Wearable Sensing Applications: Elastomers and Hydrogels. *Macromol. Rapid Commun.* **2020**, *41*, 2000444.
(468) Tan, M. W. M.; Thangavel, G.; Lee, P. S. Rugged Soft Robots using Tough, Stretchable, and Self-Healable Adhesive Elastomers. *Adv. Funct. Mater.* **2021**, *31*, 2103097.
(469) Guo, H.; Han, Y.; Zhao, W.; Yang, J.; Zhang, L. Universally Autonomous Self-Healing Elastomer with High Stretchability. *Nat. Commun.* **2020**, *11*, 2037.
(470) Parida, K.; Thangavel, G.; Cai, G.; Zhou, X.; Park, S.; Xiong, J.; Lee, P. S. Extremely Stretchable and Self-Healing Conductor based on Thermoplastic Elastomer for All-Three-Dimensional Printed Triboelectric Nanogenerator. *Nat. Commun.* **2019**, *10*, 2158.
(471) Zhang, Q.; Niu, S.; Wang, L.; Lopez, J.; Chen, S.; Cai, Y.; Du, R.; Liu, Y.; Lai, J. C.; Liu, L.; et al. An Elastic Autonomous Self-Healing

https://doi.org/10.1021/acs.chemrev.2c00215
Chem. Rev. XXXX, XXX, XXX−XXX

Capacitive Sensor Based on a Dynamic Dual Crosslinked Chemical System. *Adv. Mater.* **2018**, *30*, 1801435.
(472) Wang, Y.; Huang, F.; Chen, X.; Wang, X. W.; Zhang, W. B.; Peng, J.; Li, J.; Zhai, M. Stretchable, Conductive, and Self-Healing Hydrogel with Super Metal Adhesion. *Chem. Mater.* **2018**, *30*, 4289−4297.
(473) Deng, Z.; Guo, Y.; Zhao, X.; Ma, P. X.; Guo, B. Multifunctional Stimuli-Responsive Hydrogels with Self-Healing, High Conductivity, and Rapid Recovery through Host-Guest Interactions. *Chem. Mater.* **2018**, *30*, 1729−1742.
(474) Jeon, I.; Cui, J.; Illeperuma, W. R.; Aizenberg, J.; Vlassak, J. J. Extremely Stretchable and Fast Self-Healing Hydrogels. *Adv. Mater.* **2016**, *28*, 4678−4683.
(475) Peng, Q.; Chen, J.; Wang, T.; Peng, X.; Liu, J.; Wang, X.; Wang, J.; Zeng, H. Recent Advances in Designing Conductive Hydrogels for Flexible Electronics. *InfoMat* **2020**, *2*, 843−865.
(476) Su, G.; Yin, S.; Guo, Y.; Zhao, F.; Guo, Q.; Zhang, X.; Zhou, T.; Yu, G. Balancing the Mechanical, Electronic, and Self-Healing Properties in Conductive Self-Healing Hydrogel for Wearable Sensor Applications. *Mater. Horiz.* **2021**, *8*, 1795−1804.
(477) Ge, G.; Lu, Y.; Qu, X.; Zhao, W.; Ren, Y.; Wang, W.; Wang, Q.; Huang, W.; Dong, X. Muscle-Inspired Self-Healing Hydrogels for Strain and Temperature Sensor. *ACS Nano* **2020**, *14*, 218−228.
(478) Gong, J. P.; Katsuyama, Y.; Kurokawa, T.; Osada, Y. Double-Network Hydrogels with Extremely High Mechanical Strength. *Adv. Mater.* **2003**, *15*, 1155−1158.
(479) Tang, H.; Sun, J.; Shu, X.; Zhao, Y.; Nie, J.; Zhu, X. Fabrication of a Surface Adhesion Layer for Hydrogel Sensors via Photografting. *ACS Appl. Polym. Mater.* **2020**, *2*, 4140−4148.
(480) Nam, S.; Mooney, D. Polymeric Tissue Adhesives. *Chem. Rev.* **2021**, *121*, 11336−11384.
(481) Zhang, F. X.; Liu, P.; Ding, W.; Meng, Q. B.; Su, D. H.; Zhang, Q. C.; Lian, R. X.; Yu, B. Q.; Zhao, M. D.; Dong, J.; et al. Injectable Mussel-Inspired Highly Adhesive Hydrogel with Exosomes for Endogenous Cell Recruitment and Cartilage Defect Regeneration. *Biomaterials* **2021**, *278*, 121169.
(482) Zheng, Z.; Bian, S.; Li, Z.; Zhang, Z.; Liu, Y.; Zhai, X.; Pan, H.; Zhao, X. Catechol Modified Quaternized Chitosan Enhanced Wet Adhesive and Antibacterial Properties of Injectable Thermo-Sensitive Hydrogel for Wound Healing. *Carbohydr. Polym.* **2020**, *249*, 116826.
(483) Ryu, J. H.; Choi, J. S.; Park, E.; Eom, M. R.; Jo, S.; Lee, M. S.; Kwon, S. K.; Lee, H. Chitosan Oral Patches Inspired by Mussel Adhesion. *J. Controlled Release* **2020**, *317*, 57−66.
(484) Park, E.; Lee, J.; Huh, K. M.; Lee, S. H.; Lee, H. Toxicity-Attenuated Glycol Chitosan Adhesive Inspired by Mussel Adhesion Mechanisms. *Adv. Healthcare Mater.* **2019**, *8*, 1900275.
(485) Yang, B.; Song, J.; Jiang, Y.; Li, M.; Wei, J.; Qin, J.; Peng, W.; Lasaosa, F. L.; He, Y.; Mao, H.; et al. Injectable Adhesive Self-Healing Multicross-Linked Double-Network Hydrogel Facilitates Full-Thickness Skin Wound Healing. *ACS Appl. Mater. Interfaces* **2020**, *12*, 57782−57797.
(486) Shin, J.; Lee, J. S.; Lee, C.; Park, H. J.; Yang, K.; Jin, Y.; Ryu, J. H.; Hong, K. S.; Moon, S. H.; Chung, H. M.; et al. Tissue Adhesive Catechol-Modified Hyaluronic Acid Hydrogel for Effective, Minimally Invasive Cell Therapy. *Adv. Funct. Mater.* **2015**, *25*, 3814−3824.
(487) Zhu, W.; Iqbal, J.; Wang, D. A. A Dopa-Functionalized Chondroitin Sulfate-Based Adhesive Hydrogel as a Promising Multi-Functional Bioadhesive. *J. Mater. Chem. B* **2019**, *7*, 1741−1752.
(488) Zhou, Y.; Zhao, J.; Sun, X.; Li, S.; Hou, X.; Yuan, X.; Yuan, X. Rapid Gelling Chitosan/Polylysine Hydrogel with Enhanced Bulk Cohesive and Interfacial Adhesive Force: Mimicking Features of Epineurial Matrix for Peripheral Nerve Anastomosis. *Biomacromolecules* **2016**, *17*, 622−630.
(489) Maier, G. P.; Rapp, M. V.; Waite, J. H.; Israelachvili, J. N.; Butler, A. Adaptive Synergy between Catechol and Lysine Promotes Wet Adhesion by Surface Salt Displacement. *Science* **2015**, *349*, 628−632.
(490) Zhang, X.; Chen, J.; He, J.; Bai, Y.; Zeng, H. Mussel-Inspired Adhesive and Conductive Hydrogel with Tunable Mechanical Properties for Wearable Strain Sensors. *J. Colloid Interface Sci.* **2021**, *585*, 420−432.
(491) Lu, S.; Zhang, X.; Tang, Z.; Xiao, H.; Zhang, M.; Liu, K.; Chen, L.; Huang, L.; Ni, Y.; Wu, H. Mussel-Inspired Blue-Light-Activated Cellulose-Based Adhesive Hydrogel with Fast Gelation, Rapid Haemostasis and Antibacterial Property for Wound Healing. *Chem. Eng. J.* **2021**, *417*, 129329.
(492) Fan, X.; Fang, Y.; Zhou, W.; Yan, L.; Xu, Y.; Zhu, H.; Liu, H. Mussel Foot Protein Inspired Tough Tissue-Selective Underwater Adhesive Hydrogel. *Mater. Horiz.* **2021**, *8*, 997−1007.
(493) Liang, S.; Zhang, Y.; Wang, H.; Xu, Z.; Chen, J.; Bao, R.; Tan, B.; Cui, Y.; Fan, G.; Wang, W.; et al. Paintable and Rapidly Bondable Conductive Hydrogels as Therapeutic Cardiac Patches. *Adv. Mater.* **2018**, *30*, 1704235.
(494) Shao, Z.; Hu, X.; Cheng, W.; Zhao, Y.; Hou, J.; Wu, M.; Xue, D.; Wang, Y. Degradable Self-Adhesive Epidermal Sensors Prepared from Conductive Nanocomposite Hydrogel. *Nanoscale* **2020**, *12*, 18771−18781.
(495) Jung, H.; Kim, M. K.; Lee, J. Y.; Choi, S. W.; Kim, J. Adhesive Hydrogel Patch with Enhanced Strength and Adhesiveness to Skin for Transdermal Drug Delivery. *Adv. Funct. Mater.* **2020**, *30*, 2004407.
(496) Acome, E.; Mitchell, S. K.; Morrissey, T. G.; Emmett, M. B.; Benjamin, C.; King, M.; Radakovitz, M.; Keplinger, C. Hydraulically Amplified Self-Healing Electrostatic Actuators with Muscle-Like Performance. *Science* **2018**, *359*, 61−65.
(497) Liang, Y.; Zhao, X.; Hu, T.; Chen, B.; Yin, Z.; Ma, P. X.; Guo, B. Adhesive Hemostatic Conducting Injectable Composite Hydrogels with Sustained Drug Release and Photothermal Antibacterial Activity to Promote Full-Thickness Skin Regeneration during Wound Healing. *Small* **2019**, *15*, 1900046.
(498) Jing, X.; Mi, H. Y.; Lin, Y. J.; Enriquez, E.; Peng, X. F.; Turng, L. S. Highly Stretchable and Biocompatible Strain Sensors Based on Mussel-Inspired Super-Adhesive Self-Healing Hydrogels for Human Motion Monitoring. *ACS Appl. Mater. Interfaces* **2018**, *10*, 20897−20909.
(499) Han, L.; Lu, X.; Liu, K.; Wang, K.; Fang, L.; Weng, L. T.; Zhang, H.; Tang, Y.; Ren, F.; Zhao, C.; et al. Mussel-Inspired Adhesive and Tough Hydrogel Based on Nanoclay Confined Dopamine Polymerization. *ACS Nano* **2017**, *11*, 2561−2574.
(500) Shao, C.; Wang, M.; Meng, L.; Chang, H.; Wang, B.; Xu, F.; Yang, J.; Wan, P. Mussel-Inspired Cellulose Nanocomposite Tough Hydrogels with Synergistic Self-Healing, Adhesive, and Strain-Sensitive Properties. *Chem. Mater.* **2018**, *30*, 3110−3121.
(501) Fan, H.; Wang, J.; Jin, Z. Tough, Swelling-resistant, Self-healing, and Adhesive Dual-Cross-linked Hydrogels Based on Polymer-Tannic Acid Multiple Hydrogen Bonds. *Macromolecules* **2018**, *51*, 1696−1705.
(502) Han, N.; Xu, Z.; Cui, C.; Li, Y.; Zhang, D.; Xiao, M.; Fan, C.; Wu, T.; Yang, J.; Liu, W. A Fe^{3+}-crosslinked Pyrogallol-Tethered Gelatin Adhesive Hydrogel with Antibacterial Activity for Wound Healing. *Biomater. Sci.* **2020**, *8*, 3164−3172.
(503) Abebe, M. W.; Appiah-Ntiamoah, R.; Kim, H. Gallic Acid Modified Alginate Self-Adhesive Hydrogel for Strain Responsive Transdermal Delivery. *Int. J. Biol. Macromol.* **2020**, *163*, 147−155.
(504) Oh, D. X.; Kim, S.; Lee, D.; Hwang, D. S. Tunicate-Mimetic Nanofibrous Hydrogel Adhesive with Improved Wet Adhesion. *Acta Biomater.* **2015**, *20*, 104−112.
(505) Gan, D.; Xing, W.; Jiang, L.; Fang, J.; Zhao, C.; Ren, F.; Fang, L.; Wang, K.; Lu, X. Plant-Inspired Adhesive and Tough Hydrogel Based on Ag-Lignin Nanoparticles-Triggered Dynamic Redox Catechol Chemistry. *Nat. Commun.* **2019**, *10*, 1487.
(506) Pearce, T. R.; Waybrant, B.; Kokkoli, E. The Role of Spacers on the Self-Assembly of DNA Aptamer-Amphiphiles into Micelles and Nanotapes. *Chem. Commun.* **2014**, *50*, 210−212.
(507) Chen, J.; Wu, M.; Gong, L.; Zhang, J.; Yan, B.; Liu, J.; Zhang, H.; Thundat, T.; Zeng, H. Mechanistic Understanding and Nanomechanics of Multiple Hydrogen-Bonding Interactions in Aqueous Environment. *J. Phys. Chem. C* **2019**, *123*, 4540−4548.

https://doi.org/10.1021/acs.chemrev.2c00215
Chem. Rev. XXXX, XXX, XXX−XXX

(508) Liu, X.; Zhang, Q.; Gao, Z.; Hou, R.; Gao, G. Bioinspired Adhesive Hydrogel Driven by Adenine and Thymine. *ACS Appl. Mater. Interfaces* **2017**, *9*, 17645−17652.
(509) Liu, X.; Zhang, Q.; Gao, G. Bioinspired Adhesive Hydrogels Tackified by Nucleobases. *Adv. Funct. Mater.* **2017**, *27*, 1703132.
(510) Pei, X.; Zhang, H.; Zhou, Y.; Zhou, L.; Fu, J. Stretchable, Self-Healing and Tissue-Adhesive Zwitterionic Hydrogels as Strain Sensors for Wireless Monitoring of Organ motions. *Mater. Horiz.* **2020**, *7*, 1872−1882.
(511) Chen, J.; Wang, D.; Wang, L. H.; Liu, W.; Chiu, A.; Shariati, K.; Liu, Q.; Wang, X.; Zhong, Z.; Webb, J.; et al. An Adhesive Hydrogel with "Load-Sharing" Effect as Tissue Bandages for Drug and Cell Delivery. *Adv. Mater.* **2020**, *32*, 2001628.
(512) Li, Z. Y.; Liu, Y. Y.; Li, Y. J.; Wang, W.; Song, Y.; Zhang, J.; Tian, H. High-Preservation Single-Cell Operation Through a Photo-Responsive Hydrogel-Nanopipette System. *Angew. Chem., Int. Ed.* **2021**, *60*, 5157−5161.
(513) Xiang, Y.; Lu, X.; Yue, J.; Zhang, Y.; Sun, X.; Zhang, G.; Cai, D.; Wu, Z. Stimuli-Responsive Hydrogel as Carrier for Controlling the Release and Leaching Behavior of Hydrophilic Pesticide. *Sci. Total Environ.* **2020**, *722*, 137811.
(514) Han, Z.; Wang, P.; Mao, G.; Yin, T.; Zhong, D.; Yiming, B.; Hu, X.; Jia, Z.; Nian, G.; Qu, S.; et al. Dual pH-Responsive Hydrogel Actuator for Lipophilic Drug delivery. *ACS Appl. Mater. Interfaces* **2020**, *12*, 12010−12017.
(515) Werzer, O.; Tumphart, S.; Keimel, R.; Christian, P.; Coclite, A. M. Drug Release from Thin Films Encapsulated by a Temperature-Responsive Hydrogel. *Soft Matter* **2019**, *15*, 1853−1859.
(516) Gawade, P. M.; Shadish, J. A.; Badeau, B. A.; DeForest, C. A. Logic-Based Delivery of Site-Specifically Modified Proteins from Environmentally Responsive Hydrogel Biomaterials. *Adv. Mater.* **2019**, *31*, 1902462.
(517) Park, S. H.; Shin, H. S.; Park, S. N. A Novel pH-Responsive Hydrogel Based on Carboxymethyl Cellulose/2-Hydroxyethyl Acrylate for Transdermal Delivery of Naringenin. *Carbohydr. Polym.* **2018**, *200*, 341−352.
(518) Hou, X.; Li, Y.; Pan, Y.; Jin, Y.; Xiao, H. Controlled Release of Agrochemicals and Heavy Metal Ion Capture Dual-Functional Redox-Responsive Hydrogel for Soil Remediation. *Chem. Commun.* **2018**, *54*, 13714−13717.
(519) Chen, Y.; Gao, Y.; da Silva, L. P.; Pirraco, R. P.; Ma, M.; Yang, L.; Reis, R. L.; Chen, J. A Thermo-/pH-Responsive Hydrogel (PNIPAM-PDMA-PAA) with Diverse Nanostructures and Gel Behaviors as a General Drug Carrier for Drug Release. *Polym. Chem.* **2018**, *9*, 4063−4072.
(520) Liu, D.; Jia, S.; Zhang, H.; Ma, Y.; Guan, Z.; Li, J.; Zhu, Z.; Ji, T.; Yang, C. J. Integrating Target-Responsive Hydrogel with Pressuremeter Readout Enables Simple, Sensitive, User-Friendly, Quantitative Point-of-Care Testing. *ACS Appl. Mater. Interfaces* **2017**, *9*, 22252−22258.
(521) Kureha, T.; Aoki, D.; Hiroshige, S.; Iijima, K.; Aoki, D.; Takata, T.; Suzuki, D. Decoupled Thermo- and pH-responsive Hydrogel Microspheres Cross-Linked by Rotaxane Networks. *Angew. Chem., Int. Ed.* **2017**, *56*, 15393−15396.
(522) Koetting, M. C.; Guido, J. F.; Gupta, M.; Zhang, A.; Peppas, N. A. pH-Responsive and Enzymatically-Responsive Hydrogel Microparticles for the Oral Delivery of Therapeutic Proteins: Effects of Protein size, Crosslinking Density, and Hydrogel Degradation on Protein Delivery. *J. Controlled Release* **2016**, *221*, 18−25.
(523) Ma, C.; Shi, Y.; Pena, D. A.; Peng, L.; Yu, G. Thermally Responsive Hydrogel Blends: A General Drug Carrier Model for Controlled Drug Release. *Angew. Chem., Int. Ed.* **2015**, *54*, 7376−7380.
(524) Liu, Z.; Yao, P. Injectable Thermo-responsive Hydrogel Composed of Xanthan Gum and Methylcellulose Double Networks With Shear-thinning Property. *Carbohydr. Polym.* **2015**, *132*, 490−498.
(525) Lim, D.; Lee, E.; Kim, H.; Park, S.; Baek, S.; Yoon, J. Multi Stimuli-Responsive Hydrogel Microfibers Containing Magnetite Nanoparticles Prepared Using Microcapillary Devices. *Soft Matter* **2015**, *11*, 1606−1613.
(526) Gajanayake, T.; Olariu, R.; Leclere, F. M.; Dhayani, A.; Yang, Z.; Bongoni, A. K.; Banz, Y.; Constantinescu, M. A.; Karp, J. M.; Vemula, P. K.; Rieben, R.; Vogelin, E. A Single Localized Dose of Enzyme-Responsive Hydrogel Improves Long-Term Survival of a Vascularized Composite Allograft. *Sci. Transl. Med.* **2014**, *6*, 249ra110.
(527) Popescu, M. T.; Mourtas, S.; Pampalakis, G.; Antimisiaris, S. G.; Tsitsilianis, C. pH-Responsive Hydrogel/Liposome Soft Nanocomposites for Tuning Drug Release. *Biomacromolecules* **2011**, *12*, 3023−3030.
(528) Mi, P.; Ju, X. J.; Xie, R.; Wu, H. G.; Ma, J.; Chu, L. Y. A Novel Stimuli-Responsive Hydrogel for K^+-induced Controlled-Release. *Polymer* **2010**, *51*, 1648−1653.
(529) Dadsetan, M.; Liu, Z.; Pumberger, M.; Giraldo, C. V.; Ruesink, T.; Lu, L.; Yaszemski, M. J. A Stimuli-Responsive Hydrogel for Doxorubicin Delivery. *Biomaterials* **2010**, *31*, 8051−8062.
(530) Zhang, X.; Dong, C.; Huang, W.; Wang, H.; Wang, L.; Ding, D.; Zhou, H.; Long, J.; Wang, T.; Yang, Z. Rational Design of a Photo-Responsive UVR8-derived Protein and a Self-Assembling Peptide-Protein Conjugate for Responsive Hydrogel Formation. *Nanoscale* **2015**, *7*, 16666−16670.
(531) Luo, W.; Cui, Q.; Fang, K.; Chen, K.; Ma, H.; Guan, J. Responsive Hydrogel-Based Photonic Nanochains for Microenvironment Sensing and Imaging in Real Time and High Resolution. *Nano Lett.* **2020**, *20*, 803−811.
(532) Bhat, A.; Amanor-Boadu, J. M.; Guiseppi-Elie, A. Toward Impedimetric Measurement of Acidosis with a pH-Responsive Hydrogel Sensor. *ACS Sens.* **2020**, *5*, 500−509.
(533) Wang, R.; Zhang, M.; Guan, Y.; Chen, M.; Zhang, Y. A CO_2-Responsive Hydrogel Film for Optical Sensing of Dissolved CO_2. *Soft Matter* **2019**, *15*, 6107−6115.
(534) Li, Z.; Tang, C.; Huang, D.; Qin, W.; Luo, F.; Wang, J.; Guo, L.; Qiu, B.; Lin, Z. Sensitive Hyaluronidase Biosensor Based on Target-Responsive Hydrogel Using Electronic Balance as Readout. *Anal. Chem.* **2019**, *91*, 11821−11826.
(535) Li, Y.; Ma, Y.; Jiao, X.; Li, T.; Lv, Z.; Yang, C. J.; Zhang, X.; Wen, Y. Control of Capillary Behavior Through Target-Responsive Hydrogel Permeability Alteration for Sensitive Visual Quantitative Detection. *Nat. Commun.* **2019**, *10*, 1036.
(536) Yoshida, K.; Nakajima, S.; Kawano, R.; Onoe, H. Spring-Shaped Stimuli-Responsive Hydrogel Actuator with Large Deformation. *Sens. Actuators, B* **2018**, *272*, 361−368.
(537) Huang, Y.; Fang, L.; Zhu, Z.; Ma, Y.; Zhou, L.; Chen, X.; Xu, D.; Yang, C. Design and Synthesis of Target-Responsive Hydrogel for Portable Visual Quantitative Detection of Uranium with a Microfluidic Distance-Based Readout Device. *Biosens. Bioelectron.* **2016**, *85*, 496−502.
(538) Zhu, Z.; Guan, Z.; Jia, S.; Lei, Z.; Lin, S.; Zhang, H.; Ma, Y.; Tian, Z. Q.; Yang, C. J. Au@Pt Nanoparticle Encapsulated Target-Responsive Hydrogel with Volumetric Bar-Chart Chip Readout for Quantitative Point-of-Care Testing. *Angew. Chem., Int. Ed.* **2014**, *53*, 12503−12507.
(539) Glazer, P. J.; Leuven, J.; An, H.; Lemay, S. G.; Mendes, E. Multi-Stimuli Responsive Hydrogel Cilia. *Adv. Funct. Mater.* **2013**, *23*, 2964−2970.
(540) Zhao, Y.; Lo, C.; Ruan, L.; Pi, C.; Kim, C.; Alsaid, Y.; Frenkel, I.; Rico, R.; Tsao, T.; He, X. Somatosensory Actuator Based on Stretchable Conductive Photothermally Responsive Hydrogel. *Sci. Rob.* **2021**, *6*, No. eabd5483.
(541) Zhang, X.; Xu, X.; Chen, L.; Zhang, C.; Liao, L. Multi-responsive Hydrogel Actuator with Photo-switchable Color Changing Behaviors. *Dyes Pigm.* **2020**, *174*, 108042.
(542) Rotjanasuworapong, K.; Thummarungsan, N.; Lerdwijitjarud, W.; Sirivat, A. Facile Formation of Agarose Hydrogel and Electro-mechanical Responses as Electro-Responsive Hydrogel Materials in Actuator Applications. *Carbohydr. Polym.* **2020**, *247*, 116709.
(543) Jiang, H.; Fan, L.; Yan, S.; Li, F.; Li, H.; Tang, J. Tough and Electro-Responsive Hydrogel Actuators with Bidirectional Bending Behavior. *Nanoscale* **2019**, *11*, 2231−2237.

https://doi.org/10.1021/acs.chemrev.2c00215
Chem. Rev. XXXX, XXX, XXX−XXX

(544) Gao, G.; Wang, Z.; Xu, D.; Wang, L.; Xu, T.; Zhang, H.; Chen, J.; Fu, J. Snap-Buckling Motivated Controllable Jumping of Thermo-Responsive Hydrogel Bilayers. *ACS Appl. Mater. Interfaces* **2018**, *10*, 41724−41731.
(545) Nakajima, S.; Kawano, R.; Onoe, H. Stimuli-Responsive Hydrogel Microfibers with Controlled Anisotropic Shrinkage and Cross-Sectional Geometries. *Soft Matter* **2017**, *13*, 3710−3719.
(546) Morales, D.; Bharti, B.; Dickey, M. D.; Velev, O. D. Bending of Responsive Hydrogel Sheets Guided by Field-Assembled Microparticle Endoskeleton Structures. *Small* **2016**, *12*, 2283−2290.
(547) Jiang, T.; Zhao, X.; Yin, X.; Yang, R.; Tan, G. Dynamically Adaptive Window Design with Thermo-Responsive Hydrogel for Energy Efficiency. *Appl. Energy* **2021**, *287*, 116573.
(548) Zhou, Y.; Cai, Y.; Hu, X.; Long, Y. Temperature-Responsive Hydrogel with Ultra-Large Solar Modulation and High Luminous Transmission for "Smart Window" Applications. *J. Mater. Chem. A* **2014**, *2*, 13550−13555.
(549) Mok, S.; Al Habyan, S.; Ledoux, C.; Lee, W.; MacDonald, K. N.; McCaffrey, L.; Moraes, C. Mapping Cellular-Scale Internal Mechanics in 3D Tissues with Thermally Responsive Hydrogel Probes. *Nat. Commun.* **2020**, *11*, 4757.
(550) Downs, F. G.; Lunn, D. J.; Booth, M. J.; Sauer, J. B.; Ramsay, W. J.; Klemperer, R. G.; Hawker, C. J.; Bayley, H. Multi-Responsive Hydrogel Structures from Patterned Droplet Networks. *Nat. Chem.* **2020**, *12*, 363−371.
(551) Karis, D. G.; Ono, R. J.; Zhang, M.; Vora, A.; Storti, D.; Ganter, M. A.; Nelson, A. Cross-Linkable Multi-Stimuli Responsive Hydrogel Inks for Direct-Write 3D Printing. *Polym. Chem.* **2017**, *8*, 4199−4206.
(552) Wang, J.; Tang, F.; Wang, Y.; Liu, S.; Li, L. Tunable Single-Molecule White-Light Emission in Stimuli-Responsive Hydrogel. *Adv. Opt. Mater.* **2020**, *8*, 1901571.
(553) Han, D.; Li, Y.; Liu, X.; Li, B.; Han, Y.; Zheng, Y.; Yeung, K. W. K.; Li, C.; Cui, Z.; Liang, Y.; et al. Rapid bacteria Trapping and Killing of Metal-Organic Frameworks Strengthened Photo-Responsive Hydrogel for Rapid Tissue Repair of Bacterial Infected Wounds. *Chem. Eng. J.* **2020**, *396*, 125194.
(554) Li, W.; Dong, K.; Ren, J.; Qu, X. A β-Lactamase-Imprinted Responsive Hydrogel for the Treatment of Antibiotic-Resistant Bacteria. *Angew. Chem., Int. Ed.* **2016**, *55*, 8049−8053.
(555) Zhu, Y.; Matsumura, Y.; Velayutham, M.; Foley, L. M.; Hitchens, T. K.; Wagner, W. R. Reactive Oxygen Species Scavenging with a Biodegradable, Thermally Responsive Hydrogel Compatible with Soft Tissue Injection. *Biomaterials* **2018**, *177*, 98−112.
(556) Xiao, H.; Lu, W.; Le, X.; Ma, C.; Li, Z.; Zheng, J.; Zhang, J.; Huang, Y.; Chen, T. A Multi-responsive Hydrogel with a Triple Shape Memory Effect Based on Reversible Switches. *Chem. Commun.* **2016**, *52*, 13292−13295.
(557) Lv, S. W.; Liu, Y.; Xie, M.; Wang, J.; Yan, X. W.; Li, Z.; Dong, W. G.; Huang, W. H. Near-Infrared Light-Responsive Hydrogel for Specific Recognition and Photothermal Site-Release of Circulating Tumor Cells. *ACS Nano* **2016**, *10*, 6201−6210.
(558) Guo, B.; Pan, G.; Guo, Q.; Zhu, C.; Cui, W.; Li, B.; Yang, H. Saccharides and Temperature Dual-Responsive Hydrogel Layers for Harvesting Cell Sheets. *Chem. Commun.* **2015**, *51*, 644−647.
(559) Pan, G.; Guo, Q.; Ma, Y.; Yang, H.; Li, B. Thermo-Responsive Hydrogel Layers Imprinted with Rgds Peptide: A System for Harvesting Cell Sheets. *Angew. Chem., Int. Ed.* **2013**, *52*, 6907−6911.
(560) Ye, Y.; Mao, Y.; Wang, H.; Ren, Z. Hybrid Structure of pH-Responsive Hydrogel and Carbon Nanotube Array with Super-wettability. *J. Mater. Chem.* **2012**, *22*, 2449−2455.
(561) Chen, L.; Liu, M.; Lin, L.; Zhang, T.; Ma, J.; Song, Y.; Jiang, L. Thermal-Responsive Hydrogel Surface: Tunable Wettability and Adhesion to Oil at the Water/Solid Interface. *Soft Matter* **2010**, *6*, 2708−2712.
(562) Chen, J.; Peng, Q.; Peng, X.; Han, L.; Wang, X.; Wang, J.; Zeng, H. Recent Advances in Mechano-Responsive Hydrogels for Biomedical Applications. *ACS Appl. Polym. Mater.* **2020**, *2*, 1092−1107.
(563) Best, J. P.; Neubauer, M. P.; Javed, S.; Dam, H. H.; Fery, A.; Caruso, F. Mechanics of pH-Responsive Hydrogel Capsules. *Langmuir* **2013**, *29*, 9814−9823.
(564) Park, J.; Pramanick, S.; Park, D.; Yeo, J.; Lee, J.; Lee, H.; Kim, W. J. Therapeutic-Gas-Responsive Hydrogel. *Adv. Mater.* **2017**, *29*, 1702859.
(565) Guo, Y.; Bae, J.; Fang, Z.; Li, P.; Zhao, F.; Yu, G. Hydrogels and Hydrogel-Derived Materials for Energy and Water Sustainability. *Chem. Rev.* **2020**, *120*, 7642−7707.
(566) Li, L.; Yan, B.; Yang, J.; Chen, L.; Zeng, H. Novel Mussel-Inspired Injectable Self-Healing Hydrogel with Anti-Biofouling Property. *Adv. Mater.* **2015**, *27*, 1294−1299.
(567) Kureha, T.; Shibamoto, T.; Matsui, S.; Sato, T.; Suzuki, D. Investigation of Changes in the Microscopic Structure of Anionic Poly(*N*-isopropylacrylamide-*co*-Acrylic acid) Microgels in the Presence of Cationic Organic Dyes toward Precisely Controlled Uptake/release of Low-Molecular-Weight Chemical Compound. *Langmuir* **2016**, *32*, 4575−4585.
(568) Van Tran, V.; Park, D.; Lee, Y. C. Hydrogel Applications for Adsorption of Contaminants in Water and Wastewater Treatment. *Environ. Sci. Pollut. Res. Int.* **2018**, *25*, 24569−24599.
(569) Jing, G.; Wang, L.; Yu, H.; Amer, W. A.; Zhang, L. Recent Progress on Study of Hybrid Hydrogels for Water treatment. *Colloids Surf., A* **2013**, *416*, 86−94.
(570) Zheng, Y.; Wang, A. Superadsorbent with Three-Dimensional Networks: From Bulk Hydrogel to Granular hydrogel. *Eur. Polym. J.* **2015**, *72*, 661−686.
(571) Mu, R.; Liu, B.; Chen, X.; Wang, N.; Yang, J. Hydrogel Adsorbent in Industrial Wastewater Treatment and Ecological Environment Protection. *Environ. Technol. Innovation* **2020**, *20*, 101107.
(572) Yuan, J.; Yi, C.; Jiang, H.; Liu, F.; Cheng, G. J. Direct Ink Writing of Hierarchically Porous Cellulose/Alginate Monolithic Hydrogel as a Highly Effective Adsorbent for Environmental Applications. *ACS Appl. Polym. Mater.* **2021**, *3*, 699−709.
(573) Karimi-Maleh, H.; Ranjbari, S.; Tanhaei, B.; Ayati, A.; Orooji, Y.; Alizadeh, M.; Karimi, F.; Salmanpour, S.; Rouhi, J.; Sillanpaa, M.; et al. Novel 1-butyl-3-methylimidazolium Bromide Impregnated Chitosan Hydrogel Beads Nanostructure as an Efficient Nanobio-adsorbent for Cationic Dye Removal: Kinetic Study. *Environ. Res.* **2021**, *195*, 110809.
(574) Dai, J.; Yang, H.; Yan, H.; Shangguan, Y.; Zheng, Q.; Cheng, R. Phosphate Adsorption from Aqueous Solutions by Disused Adsorbents: Chitosan Hydrogel Beads after the Removal of Copper(II). *Chem. Eng. J.* **2011**, *166*, 970−977.
(575) Arshad, F.; Selvaraj, M.; Zain, J.; Banat, F.; Haija, M. A. Polyethylenimine Modified Graphene Oxide Hydrogel Composite as an Efficient Adsorbent for Heavy Metal Ions. *Sep. Purif. Technol.* **2019**, *209*, 870−880.
(576) Tang, Z.; Hu, X.; Ding, H.; Li, Z.; Liang, R.; Sun, G. Villi-like Poly(acrylic acid) Based Hydrogel Adsorbent with Fast and Highly Efficient Methylene Blue Removing Ability. *J. Colloid Interface Sci.* **2021**, *594*, 54−63.
(577) Lv, Q.; Hu, X.; Zhang, X.; Huang, L.; Liu, Z.; Sun, G. Highly Efficient Removal of Trace Metal Ions by Using Poly(acrylic acid) Hydrogel Adsorbent. *Mater. Des.* **2019**, *181*, 107934.
(578) Hu, X. S.; Liang, R.; Sun, G. Super-Adsorbent Hydrogel for Removal of Methylene Blue Dye from Aqueous Solution. *J. Mater. Chem. A* **2018**, *6*, 17612−17624.
(579) Mittal, H.; Al Alili, A.; Morajkar, P. P.; Alhassan, S. M. Go Crosslinked Hydrogel Nanocomposites of Chitosan/Carboxymethyl Cellulose-A Versatile Adsorbent for the Treatment of Dyes Contaminated Wastewater. *Int. J. Biol. Macromol.* **2021**, *167*, 1248−1261.
(580) Mallakpour, S.; Tabesh, F. Green and Plant-Based Adsorbent From Tragacanth Gum and Carboxyl-Functionalized Carbon Nanotube Hydrogel Bionanocomposite for the Super Removal of Methylene Blue Dye. *Int. J. Biol. Macromol.* **2021**, *166*, 722−729.

https://doi.org/10.1021/acs.chemrev.2c00215
Chem. Rev. XXXX, XXX, XXX−XXX

(581) Sharma, B.; Thakur, S.; Mamba, G.; Prateek; Gupta, R. K.; Gupta, V. K.; Thakur, V. K. Titania Modified Gum Tragacanth Based Hydrogel Nanocomposite for Water Remediation. *J. Environ. Chem. Eng.* **2021**, *9*, 104608.
(582) Sarmah, D.; Karak, N. Double Network Hydrophobic Starch Based Amphoteric Hydrogel as an Effective Adsorbent for Both Cationic and Anionic Dyes. *Carbohydr. Polym.* **2020**, *242*, 116320.
(583) Pandey, S.; Do, J. Y.; Kim, J.; Kang, M. Fast and Highly Efficient Removal of Dye from Aqueous Solution Using Natural Locust Bean Gum Based Hydrogels as Adsorbent. *Int. J. Biol. Macromol.* **2020**, *143*, 60−75.
(584) Kamel, S.; El-Gendy, A. A.; Hassan, M. A.; El-Sakhawy, M.; Kelnar, I. Carboxymethyl Cellulose-Hydrogel Embedded with Modified Magnetite Nanoparticles and Porous Carbon: Effective Environmental Adsorbent. *Carbohydr. Polym.* **2020**, *242*, 116402.
(585) Song, X.; An, J.; He, C.; Zhou, J.; Xu, Y.; Ji, H.; Yang, L.; Yin, J.; Zhao, W.; Zhao, C. A Bioinspired Strategy Towards Super-Adsorbent Hydrogel Spheres via Self-Sacrificing Micro-Reactors for Robust Wastewater Remediation. *J. Mater. Chem. A* **2019**, *7*, 21386−21403.
(586) Liu, G.; Yu, R.; Lan, T.; Liu, Z.; Zhang, P.; Liang, R. Gallic Acid-functionalized Graphene Hydrogel as Adsorbent for Removal of Chromium (III) and Organic Dye Pollutants from Tannery Wastewater. *RSC Adv.* **2019**, *9*, 27060−27068.
(587) Soleimani, K.; Tehrani, A. D.; Adeli, M. Bioconjugated Graphene Oxide Hydrogel as an Effective Adsorbent for Cationic Dyes Removal. *Ecotoxicol. Environ. Saf.* **2018**, *147*, 34−42.
(588) Sun, X. F.; Liu, B.; Jing, Z.; Wang, H. Preparation and Adsorption Property of Xylan/Poly(acrylic acid) Magnetic Nanocomposite Hydrogel Adsorbent. *Carbohydr. Polym.* **2015**, *118*, 16−23.
(589) Chen, Y.; Chen, L.; Bai, H.; Li, L. Graphene Oxide-Chitosan Composite Hydrogels as Broad-Spectrum Adsorbents for Water Purification. *J. Mater. Chem. A* **2013**, *1*, 1992−2001.
(590) Qi, X.; Zeng, Q.; Tong, X.; Su, T.; Xie, L.; Yuan, K.; Xu, J.; Shen, J. Polydopamine/Montmorillonite-Embedded Pullulan Hydrogels as Efficient Adsorbents for Removing Crystal Violet. *J. Hazard. Mater.* **2021**, *402*, 123359.
(591) Gao, H.; Sun, Y.; Zhou, J.; Xu, R.; Duan, H. Mussel-Inspired Synthesis of Polydopamine-Functionalized Graphene Hydrogel as Reusable Adsorbents for Water Purification. *ACS Appl. Mater. Interfaces* **2013**, *5*, 425−432.
(592) Karthika, J. S.; Vishalakshi, B. Novel Stimuli Responsive Gellan Gum-graft-Poly(dmaema) Hydrogel as Adsorbent for Anionic Dye. *Int. J. Biol. Macromol.* **2015**, *81*, 648−655.
(593) Li, T. T.; Wang, Z.; Ren, H. T.; Peng, H. K.; Zhang, X.; Jiang, Q.; Lou, C. W.; Lin, J. H. Recyclable and Degradable Nonwoven-Based Double-Network Composite Hydrogel Adsorbent for Efficient Removal of Pb(II) and Ni(II) from Aqueous Solution. *Sci. Total Environ.* **2021**, *758*, 143640.
(594) Jiang, H.; Yang, Y.; Lin, Z.; Zhao, B.; Wang, J.; Xie, J.; Zhang, A. Preparation of a Novel Bio-Adsorbent of Sodium Alginate Grafted Polyacrylamide/Graphene Oxide Hydrogel for the Adsorption of Heavy Metal Ion. *Sci. Total Environ.* **2020**, *744*, 140653.
(595) Zhuang, Y. T.; Jiang, R.; Wu, D. F.; Yu, Y. L.; Wang, J. H. Selenocarrageenan-Inspired Hybrid Graphene Hydrogel as Recyclable Adsorbent for Efficient Scavenging of Dyes and Hg^{2+} in Water Environment. *J. Colloid Interface Sci.* **2019**, *540*, 572−578.
(596) Zhu, J.; Zhang, H.; Chen, R.; Liu, Q.; Liu, J.; Yu, J.; Li, R.; Zhang, M.; Wang, J. An Anti-Algae Adsorbent for Uranium Extraction: L-Arginine Functionalized Graphene Hydrogel Loaded with Ag Nanoparticles. *J. Colloid Interface Sci.* **2019**, *543*, 192−200.
(597) Zhou, G.; Luo, J.; Liu, C.; Chu, L.; Crittenden, J. Efficient Heavy Metal Removal from Industrial Melting Effluent Using Fixed-Bed Process Based on Porous Hydrogel Adsorbents. *Water Res.* **2018**, *131*, 246−254.
(598) Zhu, Y.; Wang, W.; Zheng, Y.; Wang, F.; Wang, A. Rapid Enrichment of Rare-Earth Metals by Carboxymethyl Cellulose-Based Open-Cellular hydrogel Adsorbent from Hipes Template. *Carbohydr. Polym.* **2016**, *140*, 51−58.
(599) Jiang, L.; Liu, P. Design of Magnetic Attapulgite/Fly Ash/Poly(acrylic acid) Ternary Nanocomposite Hydrogels and Performance Evaluation as Selective Adsorbent for Pb^{2+} Ion. *ACS Sustainable Chem. Eng.* **2014**, *2*, 1785−1794.
(600) Ma, J.; Li, T.; Liu, Y.; Cai, T.; Wei, Y.; Dong, W.; Chen, H. Rice Husk Derived Double Network Hydrogel as Efficient Adsorbent for Pb(II), Cu(II) and Cd(II) Removal in Individual and Multicomponent Systems. *Bioresour. Technol.* **2019**, *290*, 121793.
(601) Zhang, M.; Song, L.; Jiang, H.; Li, S.; Shao, Y.; Yang, J.; Li, J. Biomass Based Hydrogel as an Adsorbent for the Fast Removal of Heavy Metal Ions From Aqueous Solutions. *J. Mater. Chem. A* **2017**, *5*, 3434−3446.
(602) Xu, R.; Zhou, G.; Tang, Y.; Chu, L.; Liu, C.; Zeng, Z.; Luo, S. New Double Network Hydrogel Adsorbent: Highly Efficient Removal of Cd(II) and Mn(II) Ions in Aqueous Solution. *Chem. Eng. J.* **2015**, *275*, 179−188.
(603) Godiya, C. B.; Liang, M.; Sayed, S. M.; Li, D.; Lu, X. Novel Alginate/Polyethyleneimine Hydrogel Adsorbent for Cascaded Removal and Utilization of Cu^{2+} and Pb^{2+} Ions. *J. Environ. Manage.* **2019**, *232*, 829−841.
(604) Zhou, G.; Liu, C.; Chu, L.; Tang, Y.; Luo, S. Rapid and Efficient Treatment of Wastewater with High-Concentration Heavy Metals Using a New Type of Hydrogel-Based Adsorption Process. *Bioresour. Technol.* **2016**, *219*, 451−457.
(605) Wang, X.; Deng, W.; Xie, Y.; Wang, C. Selective Removal of Mercury ions Using a Chitosan-Poly(vinyl alcohol) Hydrogel Adsorbent with Three-Dimensional Network Structure. *Chem. Eng. J.* **2013**, *228*, 232−242.
(606) Zheng, Y.; Xie, Y.; Wang, A. Rapid and Wide pH-Independent Ammonium-Nitrogen Removal Using a Composite Hydrogel with Three-Dimensional Networks. *Chem. Eng. J.* **2012**, *179*, 90−98.
(607) Zheng, Y.; Liu, Y.; Wang, A. Fast Removal of Ammonium Ion Using a Hydrogel Optimized with Response Surface Methodology. *Chem. Eng. J.* **2011**, *171*, 1201−1208.
(608) Zheng, Y.; Wang, A. Evaluation of Ammonium Removal Using a Chitosan-*g*-Poly (acrylic acid)/Rectorite Hydrogel Composite. *J. Hazard. Mater.* **2009**, *171*, 671−677.
(609) Yu, F.; Sun, Y.; Yang, M.; Ma, J. Adsorption Mechanism and Effect of Moisture Contents on Ciprofloxacin Removal by Three-Dimensional Porous Graphene Hydrogel. *J. Hazard. Mater.* **2019**, *374*, 195−202.
(610) Godiya, C. B.; Kumar, S.; Xiao, Y. Amine Functionalized Egg Albumin Hydrogel with Enhanced Adsorption Potential for Diclofenac Sodium in water. *J. Hazard. Mater.* **2020**, *393*, 122417.
(611) Sereshti, H.; Samadi, S.; Asgari, S.; Karimi, M. Preparation and Application of Magnetic Graphene Oxide Coated with a Modified Chitosan Ph-sensitive Hydrogel: An Efficient Biocompatible Adsorbent for Catechin. *RSC Adv.* **2015**, *5*, 9396−9404.
(612) Ju, H.; Zhou, X.; Shi, B.; Kong, X.; Xing, H.; Huang, F. A Pillar[5]arene-Based Hydrogel Adsorbent in Aqueous Environments for Organic Micropollutants. *Polym. Chem.* **2019**, *10*, 5821−5828.
(613) Fang, R.; He, W.; Xue, H.; Chen, W. Synthesis and Characterization of a High-Capacity Cationic Hydrogel Adsorbent and Its Application in the Removal of Acid Black 1 from Aqueous Solution. *React. Funct. Polym.* **2016**, *102*, 1−10.
(614) Isobe, N.; Chen, X.; Kim, U. J.; Kimura, S.; Wada, M.; Saito, T.; Isogai, A. Tempo-Oxidized Cellulose Hydrogel as a High-Capacity and Reusable Heavy Metal Ion Adsorbent. *J. Hazard. Mater.* **2013**, *260*, 195−201.
(615) Idziak, S. H. J.; Safinya, C. R.; Hill, R. S.; Kraiser, K. E.; Ruths, M.; Warriner, H. E.; Steinberg, S.; Liang, K. S.; Israelachvili, J. N. The X-ray Surface Forces Apparatus: Structure of A Thin Smectic Liquid Crystal Film Under Confinement. *Science* **1994**, *264*, 1915−1918.
(616) Weiss, H.; Cheng, H. W.; Mars, J.; Li, H.; Merola, C.; Renner, F. U.; Honkimäki, V.; Valtiner, M.; Mezger, M. Structure and Dynamics of Confined Liquids: Challenges and Perspectives for the X-Ray Surface Forces Apparatus. *Langmuir* **2019**, *35*, 16679−16692.

https://doi.org/10.1021/acs.chemrev.2c00215
Chem. Rev. XXXX, XXX, XXX−XXX

(617) Dazzi, A.; Prater, C. B. AFM-IR: Technology and Applications in Nanoscale Infrared Spectroscopy and Chemical Imaging. *Chem. Rev.* **2017**, *117*, 5146−5173.
(618) Lang, S. Y.; Shi, Y.; Guo, Y. G.; Wang, D.; Wen, R.; Wan, L. J. Insight into the Interfacial Process and Mechanism in Lithium-Sulfur Batteries: An In Situ AFM Study. *Angew. Chem., Int. Ed.* **2016**, *55*, 15835−15839.
(619) Tian, F.; Li, G.; Zheng, B.; Liu, Y.; Shi, S.; Deng, Y.; Zheng, P. Verification of Sortase for Protein Conjugation by Single-Molecule Force Spectroscopy and Molecular Dynamics Simulations. *Chem. Commun.* **2020**, *56*, 3943−3946.
(620) Xing, H.; Li, Z.; Wang, W.; Liu, P.; Liu, J.; Song, Y.; Wu, Z. L.; Zhang, W.; Huang, F. Mechanochemistry of an Interlocked Poly[2]-catenane: From Single Molecule to Bulk Gel. *CCS Chem.* **2020**, *2*, 513−523.
(621) Zhang, Q.; Sun, Y.; He, C.; Shi, F.; Cheng, M. Fabrication of 3D Ordered Structures with Multiple Materials via Macroscopic Supramolecular Assembly. *Adv. Sci.* **2020**, *7*, 2002025.

https://doi.org/10.1021/acs.chemrev.2c00215
Chem. Rev. XXXX, XXX, XXX−XXX